

Diffusion kinetics and phase formation in  
Ag/Al and Ru/Al multilayer thin films

---

Dissertation

zur Erlangung des Grades  
des Doktors der Ingenieurwissenschaften  
der Naturwissenschaftlich-Technischen Fakultät  
der Universität des Saarlandes

von

**HISHAM AHMED NABIL ABOULFADL**

Saarbrücken - 2017

<b>Tag des Kolloquiums:</b>	07.12.2017
<b>Dekan:</b>	Prof. Dr. G. Kickelbick
<b>Berichterstatter/in:</b>	Prof. Dr.-Ing. F. Mücklich Prof. Dr. R. Busch Prof. Dr. G. Wilde
<b>Vorsitzende/r:</b>	Prof. Dr.-Ing. D. Bähre
<b>Akad. Mitarbeiter/in:</b>	Dr.-Ing. F. Aubertin

“There are really no objects in the world at all, only vibrations of energy, and relationships.”

Dr. Eben Alexander

# Table of Contents

<u>ACKNOWLEDGMENTS</u>	<u>V</u>
<u>ABSTRACT</u>	<u>VI</u>
<u>KURZZUSAMMENFASSUNG</u>	<u>VII</u>
<u>LIST OF UNITS, ABBREVIATIONS AND SYMBOLS</u>	<u>VIII</u>
<u>1. LITERATURE REVIEW</u>	<u>1</u>
1.1. THIN-FILM TECHNOLOGY OVERVIEW	1
1.2. THE CURRENT STAGE OF THIN FILM TECHNOLOGY	3
1.3. CHEMICAL REACTIONS IN THIN FILMS VERSUS BULK MATERIALS	4
1.4. NUCLEATION IN MISCIBLE MULTILAYER THIN FILMS	17
1.4.1. NUCLEATION IN A CONCENTRATION GRADIENT	18
1.4.2. NUCLEATION BY INTERFACIAL MASS TRANSPORT	22
1.5. TWO-STEP GROWTH PROCESS	25
1.6. PHASE FORMATION AND PHASE SEQUENCE DEPENDENCY ON PERIOD THICKNESS	27
1.7. DIFFUSION KINETICS IN THIN FILM STRUCTURES	29
1.7.1. INTERDIFFUSION IN BILAYER FILMS	30
1.7.2. GRAIN BOUNDARY DIFFUSION AND KINETIC REGIMES	31
1.7.3. EFFECTIVE DIFFUSIVITY	34
1.8. THIN FILM GROWTH BY PHYSICAL VAPOR DEPOSITION	34
1.9. SUMMARY OF THE LITERATURE-REVIEW	40
1.10. MOTIVATIONS AND OBJECTIVES	40
1.11. THE AG/AL SYSTEM	41
1.12. THE RU/AL SYSTEM	42
<u>2. EXPERIMENTAL METHODS</u>	<u>45</u>
2.1. MATERIAL SYNTHESIS	45
2.1.1. MAGNETRON SPUTTERING	45
2.2. THERMAL ANALYSIS	48
2.2.1. POWER COMPENSATED DIFFERENTIAL SCANNING CALORIMETRY (DSC)	48
2.3. MICROSTRUCTURAL ANALYSIS	49
2.3.1. X-RAY DIFFRACTION (XRD)	49
2.3.2. SCANNING ELECTRON MICROSCOPY/FOCUSED ION BEAM (SEM/FIB)	51
2.3.3. TRANSMISSION ELECTRON MICROSCOPY (TEM)	54
2.3.4. SCANNING TRANSMISSION ELECTRON MICROSCOPY (STEM)	55
2.3.5. TRANSMISSION KIKUCHI DIFFRACTION (TKD)	55
2.3.6. ATOM PROBE TOMOGRAPHY (APT)	57
<u>3. RESULTS</u>	<u>59</u>
3.1. AG/AL SYSTEM	59
3.1.1. AS-DEPOSITED FILMS	59
3.1.1.1. PERIOD INVESTIGATION	59
3.1.1.2. SPUTTERING POWER INVESTIGATION	62
3.1.1.3. APT ANALYSES	66
3.1.1.4. SPUTTERING GAS PRESSURE INVESTIGATION	72

3.1.1.5. COMPOSITION INVESTIGATION IN THE 10 NM PERIODS	75
3.1.1.6. APT ANALYSES	78
3.1.2. THERMALLY TREATED FILMS	84
3.1.2.1. PERIOD AND SPUTTERING POWER INVESTIGATION	84
3.1.2.2. PHASE FORMATION IN THE 100 NM PERIODS	86
3.1.2.3. PHASE FORMATION IN THE 10 NM PERIODS	93
3.2. RU/AL SYSTEM	108
3.2.1. AS-DEPOSITED FILMS	108
3.2.1.1. MULTILAYER THIN FILMS	108
3.2.1.2. LOCAL MAGNIFICATION EFFECTS	110
3.2.1.3. TRILAYER THIN FILMS	111
3.2.2. THERMALLY TREATED FILMS	113
<u>4. DISCUSSIONS</u>	<u>117</u>
4.1. AG/AL INVESTIGATION	117
4.2. RU/AL INVESTIGATION	127
<u>5. CONCLUSIONS</u>	<u>129</u>
<u>APPENDIX A1 – STRESS EFFECTS ON CONCENTRATION GRADIENTS IN THIN FILMS</u>	<u>132</u>
<u>REFERENCES</u>	<u>135</u>

## **Acknowledgments**

I would like to thank my supervisor Prof. Dr.-Ing. Frank Mücklich (Chair of Functional Materials, Department of Material Science, Saarland University) for giving me the opportunity to do my doctoral study at his institute. I would like to thank Prof. Dr. rer. nat. Ralf Busch (Chair of Metallic Materials, Department of Material Science, Saarland University) for the fruitful discussions on this work.

I greatly acknowledge the AME-Lab and the DFG for providing funding to my research work. I am grateful to Dr. Isabella Gallino for the DSC measurements and her collaborations. I would also like to thank Dr. Karsten Woll for the discussions at the beginning of my doctoral studies. I am very thankful as well to Dr. Naureen Ghafoor and Dr. Peter Leibenguth for their help with TEM analyses. Moreover, I would deeply like to thank my colleague Christoph Pauly for his help with FIB, discussions, and the German translation of the abstract. I also send my thanks to my colleague Sebastian Slawik for the XRD measurements and I appreciate the feedback for this work provided by my colleague Dr. Sebastian Suarez.

Finally, I would like to thank my beloved family and friends for giving me continuous support and love throughout my academic studies.

## **Abstract**

Thin films demonstrate peculiar mass-transport and chemical reactions, which is a manifestation of their unique microstructure properties compared to bulk. High interfacial densities found in multilayer thin films induce various effects on the kinetics and thermodynamics which require further attention. Multilayers deposited by DC magnetron sputtering undergo calorimetric and microstructural analyses. The microstructure is extensively studied on the atomic scale to provide quantitative information on concentration gradients, grain boundary segregations and reaction mechanisms. Two multilayer thin films systems of miscible elements are chosen for the investigation, namely, Ag/Al and Ru/Al, analyzed in as-deposited and annealed conditions, respectively. The interdiffusion in the Ag/Al films is studied under different deposition conditions and period thicknesses. The magnitude of interdiffusion is found to be inversely proportional to the period thickness and reduced using low sputtering power. Layer thicknesses in Ag/Al below 6 nm have revealed the influence of the interfacial gradient energy on enhancing interdiffusion. Metastable phases were detected in Ag/Al reactions which form as transient or product phases. Asymmetric interdiffusion is detected in Ru/Al multilayers, related to non-equilibrium segregations during deposition.

## **Kurzzusammenfassung**

Dünnschichten zeigen Besonderheiten im Stofftransport und bei chemischen Reaktionen, was ein Ausdruck ihrer einzigartigen Gefügeeigenschaften im Vergleich zu Bulk-Materialien ist. Die hohe Grenzflächendichte in Multischichten hat verschiedene Auswirkungen auf Thermodynamik und Kinetik, was besondere Aufmerksamkeit verdient. Mittels DC-Magnetronspütern abgeschiedene Multischichten werden kalorimetrisch und mikrostrukturell analysiert. Eingehende Gefügeuntersuchungen auf der atomaren Skala liefern quantitative Informationen über Konzentrationsgradienten, Korngrenzensegregation und Reaktionsmechanismen. Zwei verschiedene Multilagensysteme miteinander mischbarer Elemente, Ag/Al und Ru/Al, werden für die Untersuchungen ausgewählt und sowohl nach der Abscheidung, als auch nach Wärmebehandlung analysiert. Die Interdiffusion in Ag/Al-Schichten wird als Funktion der Abscheidebedingungen und Bilayerdicke untersucht, wobei sich ihr Ausmaß als umgekehrt proportional zur Bilayerdicke erweist und bei geringerer Sputterleistung weniger ausgeprägt ist. Einzellagedicken von weniger als 6 nm in Ag/Al zeigen den Einfluss der Grenzflächengradientenenergie auf die Interdiffusion. Die intermetallische  $\gamma$ -Phase nukleiert durch lokale Übersättigung in wärmebehandelten Ag/Al-Schichten. Metastabile Phasen wurden sowohl als Zwischen-, als auch als Endprodukte von Ag/Al-Reaktionen gefunden. Asymmetrische Interdiffusion als Folge von Ungleichgewichtssegregationen wurde in Ru/Al-Multilagen nachgewiesen.

## List of units, abbreviations and symbols

<b>Units</b>	<b>Description</b>	<b>Abbreviations</b>	<b>Description</b>
Pa	Pascal	CVD	Chemical vapor deposition
m	meter	PVD	Physical vapor deposition
s	second	GMR	Giant-magneto resistance
K	Kelvin	MEMS	Microelectromechanical systems
J	Joule	SF	Stacking fault
Hz	Hertz	TB	Twin boundary
eV	Electron Volt	GB	Grain boundary
°C	Celsius degree	LAGB	Low angle grain boundary
W	Watt	SID	Stress induced diffusion
V	Volt	DSC	Differential scanning calorimetry
bar	bar	XRD	X-ray diffraction
Torr	Torr	SEM	Scanning electron microscopy
mol	mole	FIB	Focused ion beam
g	gram	EDX	Energy dispersive X-ray spectroscopy
		TEM	Transmission electron microscopy
		STEM	Scanning transmission electron microscopy
		BF	Bright field
		DF	Dark field
		HAADF	High-angle annular dark field
		TKD	Transmission Kikuchi diffraction
		EBSD	Electron backscattered diffraction
		APT	Atom probe tomography
		LEAP	Local electrode atom probe
		TAP	Tomographic atom probe
		TOF	Time-of-flight
		SDM	Spatial distribution map
		Proxigram	Proximity-histogram
		DC	Direct current
		fcc	Face-centered cubic
		bcc	Base-centered cubic
		hcp	Hexagonal close-packed

<b>Symbols</b>	<b>Description</b>
$Q$	Activation energy
$\dot{Q}$	Heat flow
$Q_o$	Ionization energy
$E$	Energy
$P$	Pressure
$T$	Temperature
$T_M$	Melting point temperature

$T_S$	Substrate temperature
$T_H$	Homologous temperature
$V$	Volume
$V_{at}$	Atomic volume
$J$	Diffusion flux
$c$	Concentration
$x$	Distance
$m$	Mass
$X$	Average mole fraction
$X_{GB}$	Volume fraction of grain boundaries
$d$	Distance between vertical grain boundaries (intercept length)
$d_{hkl}$	Spacing between diffraction planes
$\bar{d}$	Average interplanar spacing
$v$	Velocity
$r$	Diffusion flux ratio
$R_{tip}$	End-tip radius
$D$	Lattice (bulk) diffusion coefficient
$\tilde{D}$	Interdiffusion coefficient
$D^{eff}$	Effective diffusion coefficient
$D_s$	Surface diffusion coefficient
$D_{GB}$	Grain boundary diffusion coefficient
$D_{TD}$	Topographic defect diffusion coefficient
$D_{TJ}$	Triple junction diffusion coefficient
$D_{LAGB}$	Low angle grain boundary diffusion coefficient
$D_{disl.}$	Dislocation diffusion coefficient
$D_{\Lambda}$	Interdiffusivity in a multilayer thin film
$t$	Time
$\tau$	Time for interfacial transport
$F$	Total free energy
$F_{elect.}$	Applied field on a tip
$N_v$	Number of atoms per unit volume
$k_f$	Tip shape factor
$\kappa$	Interfacial gradient energy
$\kappa^{eff}$	Effective interfacial reaction barrier
$\sigma_{sp}$	Specific interfacial free energy
$f_0$	Local free energy
$\mu$	Chemical potential
$\Lambda$	Individual film layer thickness
$\Lambda_s$	Sublimation energy
$\lambda$	Bilayer period thickness
$\lambda_x$	X-ray beam wavelength
$f$	Helmholtz free energy
$a$	Lattice parameter
$\theta_{eq}$	Groove angle

$\theta_{inc.}$	Incident angle
$\theta_{hkl}$	Diffraction Bragg angle
$\gamma_{GB}$	Grain boundary free energy
$\gamma_{int}$	Interfacial free energy
$T_i$	Kinetic coefficient
$W$	Composition constant
$J^I$	Interfacial diffusion flux
$m^I$	Interfacial lateral mobility
$L^I$	Interfacial decay length
$L$	Bulk decay length
$G$	Gibbs free energy
$G^I$	Interfacial free energy
$\emptyset$	Wetting angle
$\emptyset_e$	Work function
$s$	Segregation factor
$\delta$	Initial grain boundary thickness
$\gamma$	Surface energy
$\gamma^*$	Film-substrate interfacial energy
$C_s$	Specific heat capacity

# 1. Literature review

## 1.1. Thin-film technology overview

Thin films existed far before our modern time, dating back to the middle-bronze age. The processing and application of inorganic thin films has a long history of up to about 5000 years. The early Egyptians were the first practitioners of the art of gold beating and gliding, where a sequence of chemical and mechanical processes produced thin films which were used for decorations and protection purposes, such as statuary, royal crowns and coffin cases. Gold leafs from Luxor dating to the Eighteenth Dynasty (1567 – 1320 BC) measured  $\sim 0.3 \mu\text{m}$  in thickness [1], also found in earlier stone pyramids (2600 BC) in Saqqara, Egypt. Later, a process called “cold mercury” gliding was developed where liquid mercury is rubbed onto thin surfaces (ex. Copper and Bronze) creating mirror-like surfaces, and sometimes used as an interfacial layer for Gold leaf to be press-bonded on top, representing what can be known today as film/substrate adhesion layer. The practice of cold mercury was later used by artisans for many centuries in different civilizations, although there were mental and physical toxicity effects known of mercury. Sumerians in the region later known as Mesopotamia (in modern Iraq), developed brazing of thin films materials used as interfacial layers for joining two metal parts together, which dates to almost 3400 BC [2]. Electroless plating was developed further on by Moche Indians in Peru ( $\sim 100$  BC) which was based solely on a chemical process (mercury-free) where it offered joining of gold and silver thin films to copper substrates offering coating thicknesses of  $\sim 0.2 \mu\text{m}$  [3]. Archaeological evidences were found for thin-film deposition by electroplating within the last few centuries BC and the first few AD years in Mesopotamia which used common food acids as electrolytes and produced copper thin films. Such techniques marked the first golden age of thin-film technology.

The second golden age of thin film technology was approximately between the late 1700s to the early 1900s where several thin film processing techniques were invented and developed. This was possible due to the developments in vacuum technology, electricity, crystallography, and surface science. Vacuum was necessary for providing proper synthesis conditions for clean and controlled growth of thin films. Pressures of  $10^{-3} - 10^{-4}$  Torr in small evacuated chambers was sufficient to provide ballistic environments for deposition processes. Pulsed and dc power supply were essential for several thin film deposition techniques, however some techniques were discovered through the development of electricity, such as electrochemical batteries developed by Count Alessandro Volta in

1800 [4] and William Grove in 1852 [5], where electrodeposition and sputter deposition techniques were established. The advances in the science of crystallography starting from Kepler (1611) up to the Miller indices (1839) has helped in the understanding of the crystal orientations and epitaxial relationships of the thin films. The progress of surface science starting by the Young theory in 1805 [6] for the wetting angle of a liquid droplet on a solid substrate and its relationship with the interfacial energies per area has contributed majorly in the physical-chemistry description of the heterogeneous capillary model of thin film nucleation and provided a basis of film growth understanding. Some spectroscopic characterization techniques were available during this era, such as optical emission spectroscopy, which has contributed significantly in the characterization of the chemical species of the thin films. Optical microscopes were also used to study the morphologies of the deposited films. Such characterization techniques nonetheless provided limited chemical resolution as well as very limited structural information of the films. The common deposition techniques developed during this period were electrodeposition, sol-gel processing, sputter deposition, arc deposition, chemical vapor deposition (CVD), and thermal evaporation. Amongst these techniques sputter deposition was unique in offering high quality films with substantial lifetime. The progress of thin film deposition techniques was mostly driven by curiosity and motives for fundamental scientific understanding, but through time has attracted a lot of attention for practical applications. Several industrial applications have benefited from the thin film technology during that era, such as single and multilayer metal films for mirrors and optical antireflective coatings on telescope lenses and eyepieces [7]. Using sol-gel processing various composites were possible to be synthesized as well as monolithic films for optical lenses. Moreover, web-coating via sputter deposition was developed in the 1930s and was used to produce shiny decorative designs on various textile, wood and leather products by gold [2].

We are now living in the third golden age of thin film technology, which is between the late 1950's up to our present day. In the past few decades, deposition techniques were further developed offering thin films with high purity and more controlled microstructure, wider possibilities of thin film characterizations became available having extremely high resolution down to the atomic scale, as well as accessibility to material modeling and simulation tools which offer very close agreements with experiments. Thin films of high quality became easier to produce, far better characterized experimentally, and more understood in terms of structure and growth behavior. Highly advanced physical vapor deposition (PVD) technology allowed producing wide range of elements and compounds as constituents of thin films with controlled thicknesses down to single monolayer films. Furthermore, in the past few decades there was even a stronger commercial interest in the usage of

thin films, especially in microelectronic components and aerospace engineering. Thin films became more integrated in essential applications due to a general motive for product miniaturization, reducing costs of expensive raw materials in devices, added also to interesting new physical effects which were discovered by means of artificially modulated thin film layers. The giant magnetoresistance (GMR) effect, revealed in metallic multilayer thin films in 1988 [8], has led to a massive wave of research and development due to its application as magnetic field sensors used to read data in microelectromechanical systems (MEMS) and hard disk drives. A Nobel prize in physics was awarded later in 2007 to Albert Fert and Peter Grünberg for the discovery of GMR. Other physical effects were also discovered between 1980's and 1990's using periodically stacked layers of thin films such as perpendicular magnetic anisotropy, superlattice effects, and antiferromagnetic coupling effects [9]. All such effects arise primarily due to the distinctive role of interfaces in thin films. Moreover, thin films provided a platform to design materials with unique features compared to bulk, such as metastable phases exhibiting high temperature stability or surface-initiated spinodal decomposition at far reduced temperatures, both of which are attractive properties for high temperature materials applications. Modulated thin film layers have also shown to be very useful for applications such as wear resistant coatings or wafer bonding materials by self-propagating reactions. This third era of thin film technology is thus by far the most exciting one and is continuously showing a clear impact on industrial applications which enhance the quality of our daily life.

## **1.2. The current stage of thin film technology**

The main goal nowadays is to further refine the synthesis of thin films and reach atom-by-atom control of film growth to attain specific desired properties from thin films as well as discovering other interesting physical effects in multilayer thin films. Indeed, it requires intensive research and development to reach such synthesis precision, and to precisely control every atom species and their arrangements in a thin film structure. Nevertheless, it is essential that such research is supported by numerical models and mature understanding of the atomic re-arrangements, chemical reactions, and diffusion kinetics possible to occur in film thicknesses of a few nanometers or less, under various synthesis conditions, pressure, and temperatures. Solid state reactions in thin films are drastically different compared to bulk, and till today this area remains not fully understood and requires more attention. Current models that describe thin film reactions need further development with the aid of in-depth experimental studies conducted at the atomic scale. The present understanding for the relationship of the microstructure properties to the behavior of thin films reactions needs to be further expanded which is the main motivation for this work.

### **1.3. Chemical reactions in thin films versus bulk materials**

Thin films exhibit specific set of properties which results in unique chemical reactions that are usually far from equilibrium conditions. Chemical reactions producing compound phases in thin films are a result of an interplay between diffusion, nucleation, and phase growth. The microstructure of polycrystalline thin films differs very much in comparison to bulk materials which plays a huge role on the kinetics and thermodynamic behaviors. The ways in which thin films are distinct and how these distinctions affect diffusion and solid state reactions can be briefly explained as follows:

#### **A. Lattice defects**

In thin film deposition, the mechanisms on which target atoms arrive onto a substrate, condense, nucleate, and grow together as crystals induces a significant amount of lattice defects compared to bulk. Lattice defects could be ‘frozen-in’ during growth, or formed in order to release the strain in the films. A high density of point defects (vacancies and interstitials) in the interior of the crystallites is very common in thin films which results in increased volume diffusivity [10], leading to lattice diffusion in thin films to be usually higher than in bulk. Line defects such as dislocations, stacking faults (SF) and twin boundaries (TB) are also found in higher concentration and usually attract solute atom segregations. Moreover, diffusion along dislocations is generally enhanced by pipe diffusion mechanism, causing them to act as fast diffusion paths in the microstructure. However, grain boundaries (GBs) are the most contributing lattice defects in enhancing the diffusivity in polycrystalline thin films [11]. Deposition conditions and deposition parameters can be tuned to control the grain size. Nevertheless, in most cases, thin films are nanostructured with a fine GB network which act as fast-diffusion paths for diffusing elements. It is generally understood that vacancy diffusion is the main interdiffusion mechanism in metallic thin films [12]. By thermal annealing of the films, GBs become quickly occupied with the diffusing species, due to their higher concentration of vacancies, while lattice diffusion results in atom transport within the grains, and across the interfaces leading to thickening of interfaces (lowering the concentration gradient) in the case of layered structures. It is also possible that significant interdiffusion in the lattice defects can occur during film growth which strongly depends on the deposition conditions and the material deposited.

#### **B. Interfacial roughness and topographic defects**

During thin film growth, target atoms arrive on a substrate where the surface conditions of the substrate majorly affect the morphology of the interface created. Surface preparation is therefore very important if abrupt interfaces are desired. Other factors can also give rise to interfacial roughness such as low incident particle energy or low substrate temperature. However, when the substrate surface is rough, the thin film/substrate interface will consequently be rough and interfacial voids would form. This is significant when there is an epitaxial relationship between the substrate and thin film, where the morphology and texture of the substrate grains are influencing the morphology and texture of the thin film grains, the same applies for an epitaxial relationship between two metals in a multilayer stack. In the case of multilayers, slight roughness in the first few layers can increase exponentially with the number of layers deposited, meaning a roughness increase along the growth direction. If the rough spots are not filled in with target atoms during growth a high density of interfacial voids and pinholes would be present and the adhesion between the layers would become weak. Nevertheless, concerning the kinetics, in multilayer thin film structures, high interfacial roughness can lead to a collapse of the multilayer ordered structure at some local regions, which can be referred to as *topographical defects*. Above a critical value of interfacial roughness, the continuous lateral connection of the individual layers becomes disturbed, where topographical defects begin to appear (see schematic in Figure 1). Such regions act as pipelines connecting the layers together and serve as fast-diffusion paths. These pipelines are similar to inter-agglomerate boundaries or void networks found in nanocrystallites prepared from powder, where it is understood that the diffusivity there can be several orders of magnitude higher than GB diffusion, approaching surface diffusion [13], [14].

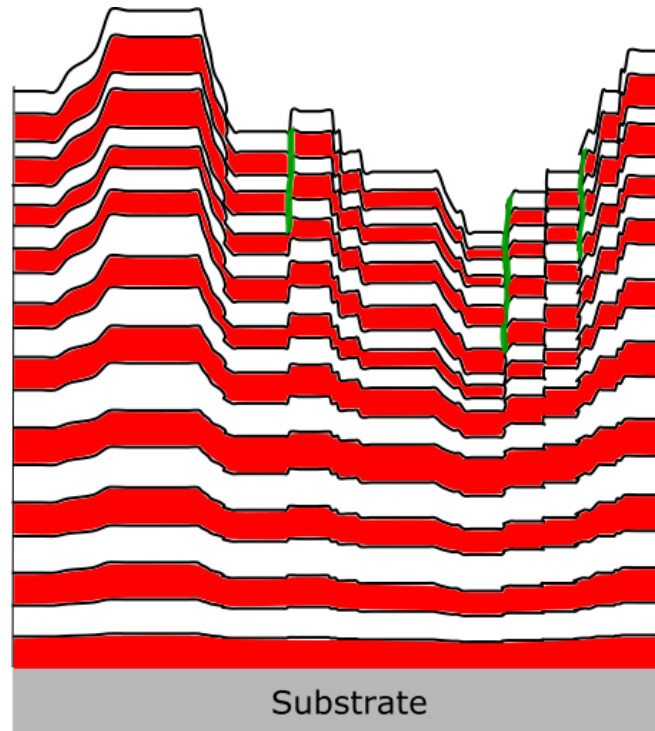


**Figure 1** Schematic for the development of interfacial roughness in a multilayer thin film structure (metal A in red, metal B in white). Topographic defects are marked with green color.

### C. Stresses and stress gradients

Stresses in thin films are very common, and they can impose a strong influence on the arrangements of atoms and the chemical reactions. There are several sources that can lead to stresses building up in thin films since generally the films are deposited under non-equilibrium conditions and the growth behavior is constrained by the substrate as well as the target atoms flux properties. The sources of the stresses can be mainly divided into two parts, intrinsic stresses which are related to stresses developed as a result of the film growth dynamics, and extrinsic stresses related to external forces such as thermal stresses. The stresses in the films are divided into volumetric and interfacial stresses, where volumetric stresses can be tensile or compressive, which are anisotropic [15]. Tensile stresses can commonly arise from matrix atoms ‘frozen-in’ at the surface during growth and positioned at spacing greater than they should, while point defects in films create compressive stresses as matrix atoms are positioned closer together [16]. Tension or compression forces could also build up in the films due to crystallite coalescence during growth or surface stress effects at the proximity of the phase boundary interfaces, respectively, and such stresses are known to vary with film thickness [15]. Moreover, since film deposition is usually carried out at elevated temperatures, differences in the thermal coefficient of expansion between the deposited film and the substrate creates compressive or tensile stresses in the layers. Micro-cracks that sometimes appear in thin films are typically formed

due to such differences in thermal coefficients of expansion [17]. Interfacial stresses develop as a result of two dissimilar materials deposited on each other. Coherent, semi-coherent or incoherent phase boundaries are created depending on the structural properties of the phases deposited. Coherent phase boundaries are formed when both phases have similar structures and a lattice mismatch less than about 5 %. The structure of one phase at the proximity of the interface is stretched in order to create a coherent boundary generating misfit strains (where misfit dislocations are formed) inducing what is usually referred to as coherency stresses. For phases with different structures or lattice mismatch greater than about 5% semi-coherent or incoherent phase boundaries are produced. In semi-coherent phase boundaries, a combination of vacancies and misfit dislocations are present at the interface, whereas for incoherent phase boundaries a rigid contact is created between the phases which normally exhibit significantly higher surface energies [18]. Interfacial stresses therefore exist due to the disturbed lattice symmetry at these interfaces, and strongly depend on the nature of the interface. Both interfacial and volumetric stresses thus build stress gradients in thin films, and certainly, the contribution of the interfacial stresses increases with the number of film layers deposited per volume. Therefore, for multilayers, the interface to volume ratio can become significant, especially for small bi-layer periods, that can induce substantial amount of stresses in the films (in the order of several GPa, for example in Au/Ni multilayers [19]).

The implication of stresses on solid state reactions in thin films is by the relationship of stresses on diffusion in solids. It is well known that when neighboring phases exhibit compositional changes their volumes change, and consequently they can act mechanically on each other. The same applies in reverse, meaning; internal stresses can induce compositional changes. The activation energy for diffusion ( $Q$ ) is dependent on the stresses as follows [20]:

$$\left(\frac{\partial Q}{\partial P}\right)_T = V_{\text{at}} \quad (1)$$

where  $P$  is the pressure applied, representing a uniform stress. The  $V_{\text{at}}$  is approximately the atomic volume, which can be much reduced along GBs and phase boundaries due to their confined volumes. The effect of uniform stress on diffusion in the interior of a grain is relatively straight-forward and purely kinetic, but for the cases of non-uniform stresses and multi-phases the situation becomes more complex which can have important effects on the concentration gradients at the phase boundaries. F. Larché and J. Cahn [21] have calculated the effects of non-uniform stresses on the concentration gradients in a semi-infinite diffusion couple and displayed the influence on the equilibrium state of the interface and the free energies for both phases (see Appendix A1). This area has received little attention. Most experimental studies on stress induced diffusion (SID) for thin films have focused on

measuring the total stresses in the films due to interdiffusion and/or nucleation triggered by thermal annealing (for example in Ref. [22]), but not on interdiffusion caused by intrinsic stresses existent in the films in the as-deposited state, which is more difficult to quantify. Stresses alter the driving force for diffusion which directly impacts the thermodynamics in the films, and of course imposes a greater effect when the density of interfaces per volume is relatively high (Ex. ultrathin multilayer films).

#### **D. Reduced diffusion distances**

Since diffusion obeys continuity and conservation laws, it is a function of distance as well as time. According to Fick's first law of diffusion [23], the diffusion flux can be described as:

$$J = -D \frac{\partial c}{\partial x} \quad (2)$$

where  $c$  is concentration ( $\text{mol/m}^3$ ),  $x$  is distance (m) in one dimension, and  $D$  is the diffusion coefficient ( $\text{m}^2/\text{s}$ ), assuming a constant value. The negative sign means that diffusion occurs in the direction opposite to the increasing concentration gradient. The concentration profile however will change with time, which is described by Fick's second law of diffusion, where the change in concentration with time is expressed as:

$$\frac{\partial c}{\partial t} = D \frac{\partial^2 c}{\partial x^2} \quad (3)$$

In thin films having small individual layer thicknesses the decay in the concentration of one phase layer during annealing, due to the diffusion outwards, becomes more influenced by the diffusion fluxes of other close neighboring phases, therefore forcing the tendency for homogenization of the layers to occur more rapidly, compared to a diffusion couple case with layers of several micrometers thick. Interdiffusion could be even more enhanced with the existence of any fast diffusion paths in the microstructure. Hence, the individual layer thickness in thin films is a very important parameter that can significantly speed up reaction kinetics between two miscible metals. More theory on diffusion kinetics in thin films is given in section 1.7.

#### **E. Interfacial gradient energy effects**

Binary systems composed of multi-phase components consist of compositional fluctuations where the local free energy per volume depends on the local composition as well as the composition of the surrounding volume. According to Cahn-Hilliard theory [24] for non-uniform systems, the local free energy can be expanded in a Taylor series of local composition derivatives to represent the total free energy. The model considers that the interfaces between two phases are accompanied by a chemical “gradient energy”, defined as  $\kappa(\nabla c)^2$  which depends on the square of the local composition gradient, and  $\kappa$  is the gradient energy coefficient. The total free energy of a volume  $V$  can be expressed as:

$$F = N_V \int (f_0 + \kappa(\nabla c)^2 + \dots) dV \quad (4)$$

where  $N_V$  is the number of atoms per unit volume and  $f_0$  is the local free energy for a uniform solid solution. The specific interfacial free energy ( $\sigma_{sp}$ ) can be therefore defined as the difference per unit area of interface between the actual free energy of the system and that which it would have if the solid solution was homogenous, and can be written as:

$$\sigma_{sp} = N_V \int_{-\infty}^{+\infty} \left[ \left( \Delta f(c) + \kappa \left( \frac{dc}{dx} \right)^2 \right) \right] dx \quad (5)$$

with

$$\Delta f(c) = f_0(c) - [c \mu_B(e) + (1 - c)\mu_A(e)] \quad (6)$$

where  $x$  is the distance across the interface,  $\mu_A(e)$  and  $\mu_B(e)$  are the chemical potentials per molecule of the species A and B in two phases at equilibrium forming an interface. The equilibrium state therefore occurs at the minimum of the specific interfacial free energy, where a relatively diffused interface corresponds to a small contribution of the gradients energy term  $\kappa(dc/dx)^2$  to the specific interfacial energy, and a sharp interface corresponds to a large contribution. The relationship to the interdiffusivity in a multilayer thin film with an individual layer thickness of  $\Lambda$  can then be expressed as:

$$D_\Lambda = D \left( 1 + \frac{8\pi^2}{\Lambda^2 f''} \kappa \right) \quad (7)$$

where  $D$  is the lattice diffusion coefficient and  $f$  is the Helmholtz free energy per unit volume, with  $f'' = (\partial^2 f / \partial c^2)$ . Therefore, for very small values of  $\Lambda$  (very short diffusion distances)  $D_\Lambda$

increases significantly compared to  $D_0$ , where  $\kappa$  would have a strong impact on the interdiffusion. The influence of  $\kappa$  begins to induce a significant effect on the film composition at  $\Lambda$  values below 10 nm thickness [20], [25]. It is thereby a common question if the compositions of the very thin films layers remain pure when a multilayer stack has periodicity of less than 10 nm. The constant  $\kappa$  can be measured using diffusion measurements on a bilayer films at different annealing temperatures, or estimated using a regular solution models [25]. It is worth mentioning however that the Cahn-Hilliard model was developed for describing inhomogeneous solid solutions exhibiting phase separation (positive heat of mixing) where  $\kappa$  has a positive value and  $f''$  is either positive or negative depending on the temperature and composition. Cook et al. [26] have refined the Cahn-Hilliard model to be applied for a discrete lattice where  $\kappa$  can have any value, which can be applied to miscible and immiscible systems and valid for modulations of all wavelengths. The total free energy of a certain domain can be given as:

$$F = (1/N_V) \sum_p \left[ f(p) + (\kappa/2a^2) \sum_u [c(p+u) - c(p)]^2 \right] \quad (8)$$

where  $a$  ( $= |a_i|$ ) is the lattice parameter,  $u$  represents the three numbers  $u_1$ ,  $u_2$  and  $u_3$  determined from the vector  $x(u)$  from site ( $p$ ) to one of the nearest-neighbor lattice sites, in which  $x(p) = p_1a_1 + p_2a_2 + p_3a_3$ , and  $a_i$  are the lattice translation vectors.

## F. Interface characteristic and interfacial stability issues

Apart from intermixing in thin films caused by chemical energies, residual stresses or high interfacial roughness, intermixing is also dependent on the interfacial free energies, which can either stabilize or destabilize a multilayer thin film structure. In polycrystalline multilayer thin films the ratio of the GB free energies and interfacial free energies determine the equilibrium groove angle at the triple point where GBs intersect the phase boundary interfaces [27]. The relationship is:

$$2 \cos \theta_{eq} = \frac{\gamma_{GB}}{\gamma_{int}} \quad (9)$$

where  $\theta_{eq}$  is the groove angle,  $\gamma_{GB}$  is the GB free energy, and  $\gamma_{int}$  is the interfacial free energy. The larger the groove angles the less local penetrations there is between the two layers, i.e. the more stable the multilayer structure, whereas small groove angles correspond to deeper local penetrations,

i.e. the less stable the structure. In the case of miscible systems, small groove angles induce more local intermixing between the layers. These free energies vary with the orientation of each grain, thus for a polycrystalline structure the groove angle would vary according to the texture of the film and nature of GBs. An example for this is shown in Figure 2. Interfacial free energies in crystalline phases consists of two contributions: The first contribution is related to the chemical interaction energy and the second contribution is related to elastic strain at the interface which is higher for semi-coherent and incoherent interfaces compared to coherent interfaces [28]. Therefore, the interface nature is generally involved in the stability of the interface and it is very important to mention that interfacial free energy terms are hardly known, especially for polycrystalline thin films. Due to the high density of interfaces and the complexity of polycrystalline structures in layered thin films situation, interfacial free energies play a vital role in chemical reactions which differs to bulk reactions. It is critical to mention that incoherent interfaces can act as a sources or sinks for thermal vacancies [28], where atomic transport can occur through the interface which further enhances the significance of high interfacial densities on the effective diffusion in thin films (diffusion kinetics more discussed in section 1.7). Little attention has been given to the influence of the interfacial nature upon the mass transport across and through the interface, which can be due to difficulties in experimental characterization of such effects.

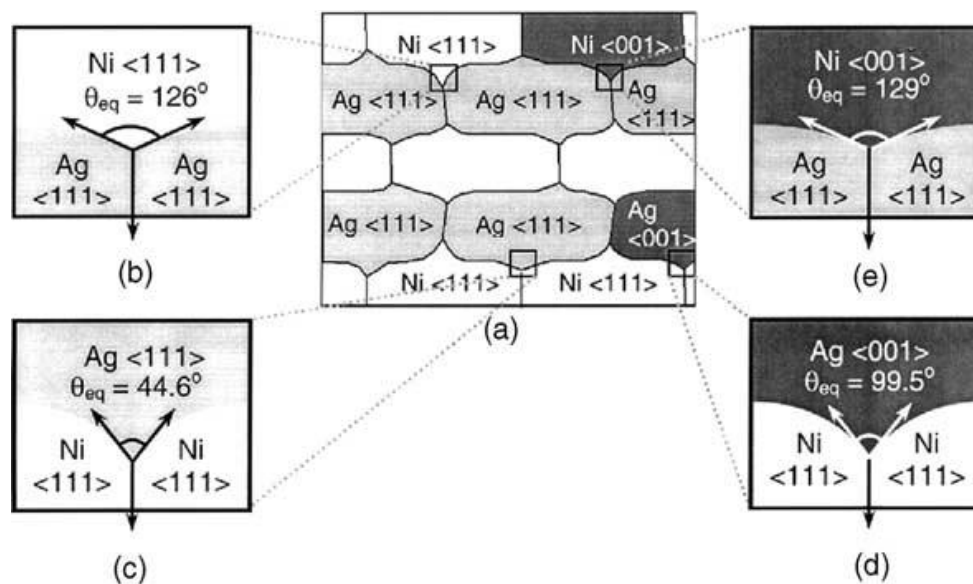


**Figure 2** An example for groove angles in a polycrystalline Ag/Ni (immiscible) multilayer thin film system. (a) Schematic overview of the microstructure. (b)-(d) The different resulting groove angles depending on the orientation of each grain at the triple junction. Taken from Ref. [27].

## G. Competitive nucleation and competitive growth

In thin films, unique intermetallic phases can appear which are uncommon or even impossible to form in bulk, where such phases can be sometimes metastable or amorphous. They form by thermal treatment of the films or directly in the as-deposited case (phase formations during film growth is explained in section 1.8). In diffusion couples having individual layer thicknesses of several micrometers all phases allowed by the phase diagram eventually form via annealing where the phase layer growth obeys a parabolic law [29]. Contrariwise, in thin films the parabolic growth of the intermetallic layers is generally not observed, this is primarily due to the limited volume of reactants surrounding the growing intermetallic phase(s) [30]. The formation of specific phases and the distinctive sequence of phases produced in thin films are understood to be a result of competition between different phases' nuclei at the diffused regions. The competition in the nucleation is also combined with competition in the growth of these phases. A series of studies have investigated these issues and developed some numerical models to explain the phase selection criteria in thin films. F. d'Heurle [31] in a simple early model has suggested that all possible phases within the diffusive region of thin films are likely to nucleate and grow, but the first phase that grows is the one which has the maximum diffusivity, and as it grows it dominates ("*fast is the first*"), making other phases grow even slower than they would grow alone, and thus become difficult to be experimentally detected. Another model by Gösel et al. [32] suggested that the nucleation and growth of the phases with slower diffusivities can become totally suppressed. They introduced the concept of a critical thickness of the new phase growing between two parent phases, above which other slower phases can shrink till they disappear. The decay and consumption of the slower phases by the fast, dominating phase has also given an explanation to the disagreements commonly found for the diffusive zone composition and the expected equilibrium values in the phase diagrams. In other words, the composition of the dominating phase usually exhibits off-stoichiometric values to the expected equilibrium values, which is explained to possibly be due to the existence of other decaying phases within in the diffused region [33].

It is important to note that growth kinetics can be diffusion controlled, where the layer thickness increases proportionally with the square root of time, or can be interface controlled, where the layer thickness increases linearly with time. In thin films, it is usually the combination of both, and obviously, the influence of interface controlled reactions increases with the interfacial density. The growth of a single compound layer is determined by the combination of two processes: 1- Mass transport in the compound layer where the diffusion flux slows down with the increasing new phase layer thickness. 2- Rearrangements of the atoms at the interface as well as atomic transport occurring

through the phase boundaries (interfaces) required for the growth of the compound layer, which can involve reaction barriers. The atomic transport at the interfaces can be divided into three successive steps: (a) detachment of atoms from the lattice of phase A, (b) transition through the A/B interface, (c) attachment of atoms to the lattice of phase B. Each of these steps happens within a certain time frame. The transition time is estimated to be  $\tau_1 \sim h^2/D_B$ , where  $D_B$  is the diffusivity in phase B (considering transport to phase B) and  $h \sim 5 \times 10^{-10}$  m [29]. The detachment and attachment times ( $\tau_2$ ) are similar and are estimated to be  $d_x^2/D_B$ , where  $d_x$  is a few atomic distances. Assuming parabolic law of phase growth of an individual intermetallic layer, the time of transfer through the layer can approximately be expressed as:

$$\tau_{dif} \sim \frac{\Delta x}{v} \sim \frac{\Delta x}{\frac{D^{eff} \Delta c}{\Delta x}} \sim \frac{\Delta x^2}{D^{eff} \Delta c} \quad (10)$$

where  $\Delta x$  is the change in layer thickness,  $\Delta c$  is the difference in composition across the layer and  $D^{eff}$  is the effective interdiffusion coefficient in the layer. Therefore, the phase boundary (interface) can become rate limiting in the case of  $\tau_1 + 2\tau_2 > \tau_{dif}$ , and the growth kinetics becomes more interface controlled, whereas if  $\tau_1 + 2\tau_2 < \tau_{dif}$  the growth kinetics becomes more diffusion controlled [29].

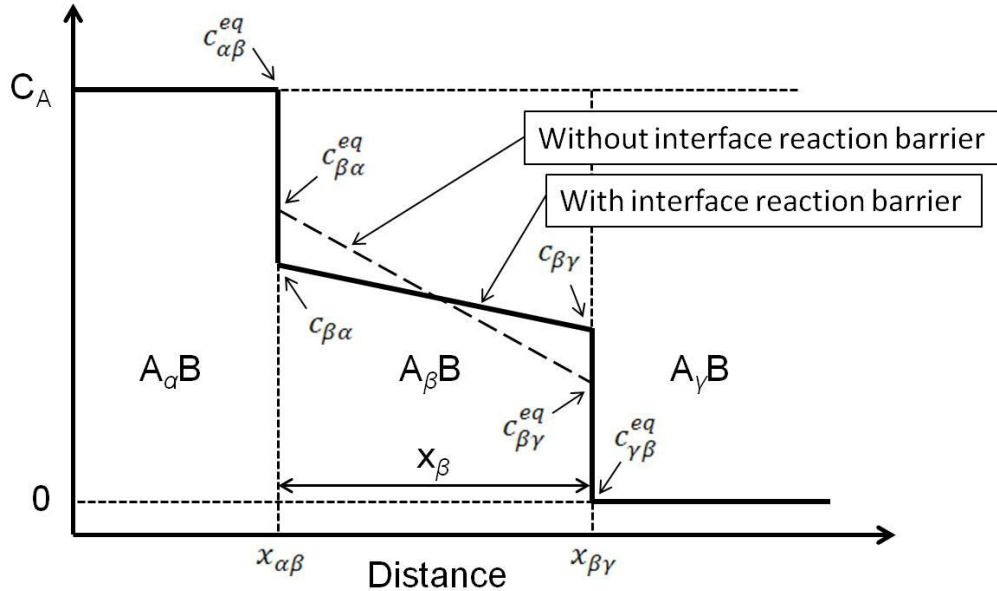


**Figure 3** Schematic representation of a concentration profile for A atoms across  $A_\alpha B/A_\beta B/A_\gamma B$  phases showing the influence of interface reaction barrier on the concentration gradient of the  $A_\beta B$  phase.

The model of Gösel et al. [32] is the most known one for describing the suppression/growth criteria in thin film reactions. First, the model demonstrates the effect of interface reaction barriers (interface controlled kinetics) on the concentration profiles and growth of an intermetallic phase between two metals. Figure 3 shows a schematic concentration profile across layers  $A_\alpha B$  (pure A atoms concentration) and  $A_\gamma B$  (pure B atoms concentration) with an intermetallic phase  $A_\beta B$  in between, where the effect of interface reaction barriers on the concentration gradient across the  $A_\beta B$  phase is highlighted. Assuming a constant interdiffusion coefficient and no interfacial barriers, the composition of the diffusive regions fits to equilibrium phase diagram. According to G. Kidson [34], the change of the positions of the two interfaces of  $A_\beta B$  phase can be described as:

$$\left(c_{\alpha\beta}^{eq} - c_{\beta\alpha}\right) \frac{dx_{\alpha\beta}}{dt} = D_\beta^{eff} \left(\frac{dc_\beta^A}{dx}\right)_{\beta\alpha} \quad (11)$$

$$\left(c_{\beta\gamma} - c_{\gamma\beta}^{eq}\right) \frac{dx_{\beta\gamma}}{dt} = -D_\beta^{eff} \left(\frac{dc_\beta^A}{dx}\right)_{\beta\gamma} \quad (12)$$

where  $c_\beta^A$  refers to the concentration of element A in the  $A_\beta B$  phase and  $D_\beta^{eff}$  is the effective diffusion coefficient in  $A_\beta B$ . Assuming a steady state flux according to Fick's diffusion law, the diffusion flux of A atoms in the  $A_\beta B$  phase is therefore:

$$j_\beta^A = \kappa_{\beta\alpha} \left(c_{\beta\alpha}^{eq} - c_{\beta\alpha}\right) \quad (13)$$

or

$$j_\beta^A = \kappa_{\beta\gamma} \left(c_{\beta\gamma} - c_{\beta\gamma}^{eq}\right) \quad (14)$$

where  $\kappa_{\beta\alpha}$  and  $\kappa_{\beta\gamma}$  represent the reaction constants due to the interfacial reaction barriers. The thickness change of the  $A_\beta B$  can be thus expressed as:

$$\frac{dx_\beta}{dt} = \frac{W_\beta \cdot \Delta c_\beta^{eq} \cdot \kappa_\beta^{eff}}{\left(1 + \frac{x_\beta + \kappa_\beta^{eff}}{D_\beta^{eff}}\right)} \quad (15)$$

where  $W_\beta$  is a constant determined by the composition of the three phases ( $A_\alpha B/A_\beta B/A_\gamma B$ ) and the atomic volume for A and B atoms,  $\Delta c_\beta^{eq} = c_{\beta\alpha}^{eq} - c_{\beta\gamma}^{eq}$ , and  $\kappa_\beta^{eff}$  represents the effective interfacial reaction barrier across the  $A_\beta B$  phase, where  $1/\kappa_\beta^{eff} = 1/\kappa_{\beta\alpha} + 1/\kappa_{\beta\gamma}$ . Hence, based on this thickness change equation above, a critical changeover thickness  $x_\beta^*$  exists ( $x_\beta^* = D_\beta^{eff}/\kappa_\beta^{eff}$ ) where the growth kinetics switches from diffusion controlled to interface controlled, therefore:

$$x_\beta \sim t, \text{ if } x_\beta \ll x_\beta^* \quad (16)$$

or

$$x_\beta \sim \sqrt{t}, \text{ if } x_\beta \gg x_\beta^* \quad (17)$$

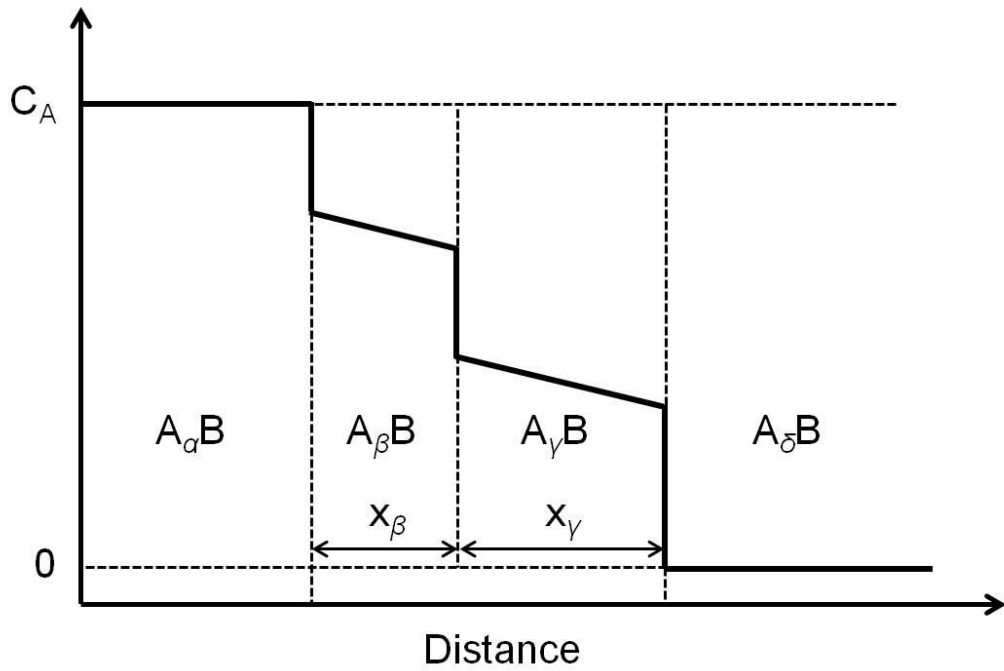


**Figure 4** Schematic representation of a concentration profile for A atoms across  $A_\alpha B/A_\beta B/A_\gamma B/A_\delta B$  phase. The schematic represents two phases competing within the diffusive zone.

The model of Gösel et al. [32] further considers such effects on the competition between of a number of potential phases in the diffusive zone. It predicts that more than one phase can exist in the diffused region between two metals in layer geometry. For simplicity, the model presents only two phases, namely,  $A_\beta B$  and  $A_\gamma B$ , between two pure phases  $A_\alpha B$  (pure A atoms concentration) and  $A_\delta B$

(pure B atoms concentration), as shown in Figure 4. The change in the thickness of  $A_\beta B$  and  $A_\gamma B$  phases can be expressed as:

$$\frac{dx_\beta}{dt} = W_\beta \cdot j_\beta^A - W_{\beta\gamma} \cdot j_\gamma^A \quad (18)$$

$$\frac{dx_\gamma}{dt} = W_\gamma \cdot j_\gamma^A - W_{\gamma\beta} \cdot j_\beta^A \quad (19)$$

where the quantities  $W_\beta, W_{\beta\gamma}, W_\gamma,$  and  $W_{\gamma\beta}$  account for the change in composition at the phase boundary interfaces (note that  $W_{\beta\gamma} = W_{\gamma\beta}$ ). The model then considers an interesting case, which closely resembles thin film reactions, in which one phase is taken to be diffusion controlled, for instance the phase  $A_\gamma B$ , and the other phase ( $A_\beta B$ ) is interface controlled. Thus,  $j_\gamma^A$  and  $j_\beta^A$  can be written as:

$$j_\gamma^A = -\tilde{D}_\beta \frac{\Delta c_\beta}{x_\beta} \quad (20)$$

$$j_\beta^A = \frac{\Delta c_\gamma^{eq} \kappa_\gamma^{eff}}{\left(1 + \frac{x_\gamma \kappa_\gamma^{eff}}{D_\gamma^{eff}}\right)} \quad (21)$$

The growth  $A_\beta B$  layer ( $dx_\beta/dt > 0$ ) can be expressed by the ratio of the diffusion fluxes  $r = j_\beta^A/j_\gamma^A$  in which  $r_1 = W_{\beta\gamma}/W_\beta$  and  $r_2 = W_\gamma/W_{\gamma\beta}$  (note that  $r_2 > r_1$ ). The growth of phase  $A_\beta B$  requires the condition of  $r > r_1$  whereas the growth of  $A_\gamma B$  requires  $r < r_2$ . If the  $r$  ratio is outside the  $r_1$  to  $r_2$  range, one phase will shrink and the other phase will grow in expense, while a value between the  $r_1$  to  $r_2$  range means that both phases will grow simultaneously. The flux ratio  $r$  changes by time, meaning that growth and suppression behaviors dynamically vary with time. In Figure 5 an illustration is presented for the different regimes as a function of the flux ratio  $r$ . The blue line represents a case, in which  $A_\beta B$  phase shrinks while the  $A_\gamma B$  grows. This condition holds as long as  $x_\gamma$  is so small that  $r$  remains less than  $r_1$ . Therefore, it can be predicted that  $A_\beta B$  will be suppressed if  $x_\gamma$  is below a critical thickness (marked in Figure 5). This agrees well with the theory of nucleation within a concentration gradient (discussed in section 1.4.1). At later stages where  $x_\gamma$  exceeds the critical thickness ( $r > r_1$ ) the  $A_\beta B$  begins to grow along with the  $A_\gamma B$  phase proportional to  $\sqrt{t}$ , assuming no growth barriers and an unlimited supply of reactants.

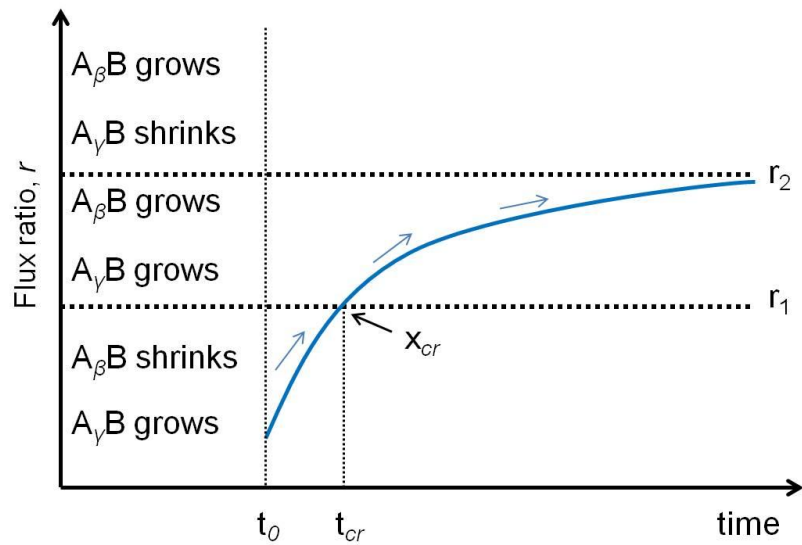


**Figure 5** Schematic for the growth and shrinkage regimes of the  $A_\gamma B$  and  $A_\beta B$  phases showing their dependence on the flux ratio  $r$ . The blue line represents the case explained in the text. The critical thickness  $x_{cr}$  of phase  $A_\gamma B$  is marked, which is at the intersection of the curve with the  $r_1$  value.

Based on the seven issues mentioned above, chemical reactions in thin films are unique and considered sometimes ambiguous to fully understand since they can be influenced by several factors simultaneously. It is extremely important to note that the studies which explain phase competition such as the ones mentioned above focus primarily on what happens at the phase boundary, i.e. nucleation and growth in the diffused zone at the phase boundary where concentration gradients thus play a crucial role on the thermodynamics. Such models do not consider the leakage of diffusing species in lattice defects within the microstructure, especially GBs. Hence, numerical models for nucleation and phase growth in the concentration gradients should be treated with some care, since they do not represent a general case for thin film reactions.

#### 1.4. Nucleation in miscible multilayer thin films

The conditions of nucleation in a diffused region between two phases in a layered geometry is to some extent different compared to the classical nucleation theory (explained in [31]) used to describe nucleation in bulk materials. The situation is more complicated due to that fact that the nucleus forms in a composition which is strongly inhomogeneous, i.e. nucleation at regions with chemical potential gradients and concentration gradients. Moreover, the change in the surface energy by nucleation does not need to be always positive, due to the likelihood that the summation of the surface energies for the two new interfaces ( $\alpha/\beta$  and  $\beta/\gamma$ ) created by the formation of a new intermediate phase ( $A_\beta B$ )

formed between two parent phases ( $A_\alpha B$  and  $A_\gamma B$ ) could be smaller than the surface energy of the consumed  $\alpha/\gamma$  interface (assuming high interfacial tension between  $A_\alpha B$  and  $A_\gamma B$  phases) [31]. Furthermore, due to the leakage of atoms to interfaces, defects, and phase boundaries, diffused zones can be located at local sites where nucleation can be described as heterogeneous, thus a significant increase in the surface energy is not necessarily escorted with the nucleation in thin films.

The new phase normally appears in the diffusive zones, where the nucleation can be a result of two possibilities:

1. Formation of diffused zones at the phase boundaries interfaces after a concentration preparation period
2. Formation of local interdiffused regions due to segregations to microstructural defects (ex. GBs)

For each of these two cases the possible modes of nucleation will be described shortly, keeping in mind, that nature would normally take the pathway with the lowest nucleation barrier, requiring the lowest energy for phase formation, which can also be a combination of several nucleation modes simultaneously [35].

#### **1.4.1. Nucleation in a concentration gradient**

In most conditions, nucleation in thin films happens much before full homogenization of the two parent phases is reached where the nucleation is strongly influenced by the diffusion fluxes between parent phases as well as embryos of competing intermediate phases in the diffusive zone. The nucleation here is therefore dissimilar to the classical theory from the thermodynamic aspect, as well as the kinetic. Three different modes of nucleation are ascribed at the concentration gradient. Each mode basically varies in the sense of how the nucleus is formed and how the chemical composition is distributed within the nuclei.

##### **I. Polymorphic mode**

According to Gusak and Gurov [36], it is considered in this mode that interdiffusion at the phase boundary interface will lead to lowering of the concentration gradient, which is referred to as a *concentration preparation period*. The interdiffused region is treated as a metastable

parent solution with a sharp concentration profile which has a wide solubility range overlapping with the two parent phases. Nucleation will happen in this metastable phase when the concentration gradient is lowered sufficiently to allow space for a stable compound nucleus to form. The nucleus will form by a reconstruction of the atomic structure in the metastable phase without suddenly changing the concentration profile. Consequently, the composition of the newly born nucleus is inhomogeneous from the very beginning as it consists of a concentration gradient within. It is important to note that the composition of the metastable phase overlaps, to some extent, with the composition of new intermediate phase shortly before nucleation happens, this stage is necessary in building up a chemical driving force for the transformation to take place. The relationship between the width of the interdiffused zone and the nucleation therefore becomes obvious, where under sharp concentration gradients the nucleation is forbidden (nucleation barrier). However, the formation of a stable nucleus at the concentration gradient depends on the shape of the nucleus. Assuming ellipsoidal nucleus rather than a spherical nucleus, Gusak [29] has shown that the nucleation barrier can become considerably reduced, which was also supported by Monte Carlo (MC) simulations. An illustration for this nucleation on Gibbs free energy curves is shown in Figure 6.

## **II. Transversal mode**

According to Desré and Yavari [37], this mode considers that a nucleus forming in the diffused zone at the phase boundary interface is composed of several thin slices in the direction perpendicular to the unidirectional concentration gradient. Diffusion is fed in the nucleus along this perpendicular direction where each slice is treated as a decomposition of the parent phases. The distribution of components inside each slice is considered unlimited and independent on the other slices, thus here the composition in the nucleus (all the slices) is generally composed of a compositional gradient. Again, the diffused zone is assumed here to be a metastable phase with a wide solubility range. The concentration of the nucleus  $c_{\text{new}}$  is determined by the concentration of the metastable  $c_{\text{old}}$  phase in the proximity of the nucleus according to the parallel tangent rule (see Figure 6). To note, the popular ‘common tangents’ rule is the reduction of the parallel tangent rule if supersaturation is prohibited [29]. The application of the parallel tangent rule leads to a maximum chemical driving force for each slice, since it is assumed that the concentration surrounding the nucleation zone of each slice remains unchanged, acting as a reservoir for the chemical potential at each slice. This mode

of nucleation shares some similarities to the polymorphic mode in the sense that it also exhibits a nucleation barrier above a critical concentration gradient, and is also dependent on the shape of the nucleus, i.e. the flatter the defined nucleus shape, the lower the nucleation barrier.

### **III. Total mixing (longitudinal) mode**

According to Hodaj and Desré [38], this mode considers that the slices within the diffusive zone mix together (total mixing) during the nucleation and the atoms redistribute inside the nucleus forming the new phase. In this case, there is no concentration gradient found in the nucleus and the process of nucleation does not require diffusion from the surrounding. Therefore, it is understood that in such case the concentration gradient assists the nucleation, meaning that higher concentration gradient is more favorable for nucleation. This mode is therefore in contradiction with the other two modes in sense of some forbiddance for nucleation above a critical concentration gradient. Although this mode may offer the lowest nucleation barrier, from the thermodynamic aspect, compared to the other modes, it can be kinetically suppressed. The chance for this mode to be active necessitates that the atomic mobility in the new phase must be much higher than in the parent phase. An illustration for this nucleation on Gibbs free energy curves is shown in Figure 6.

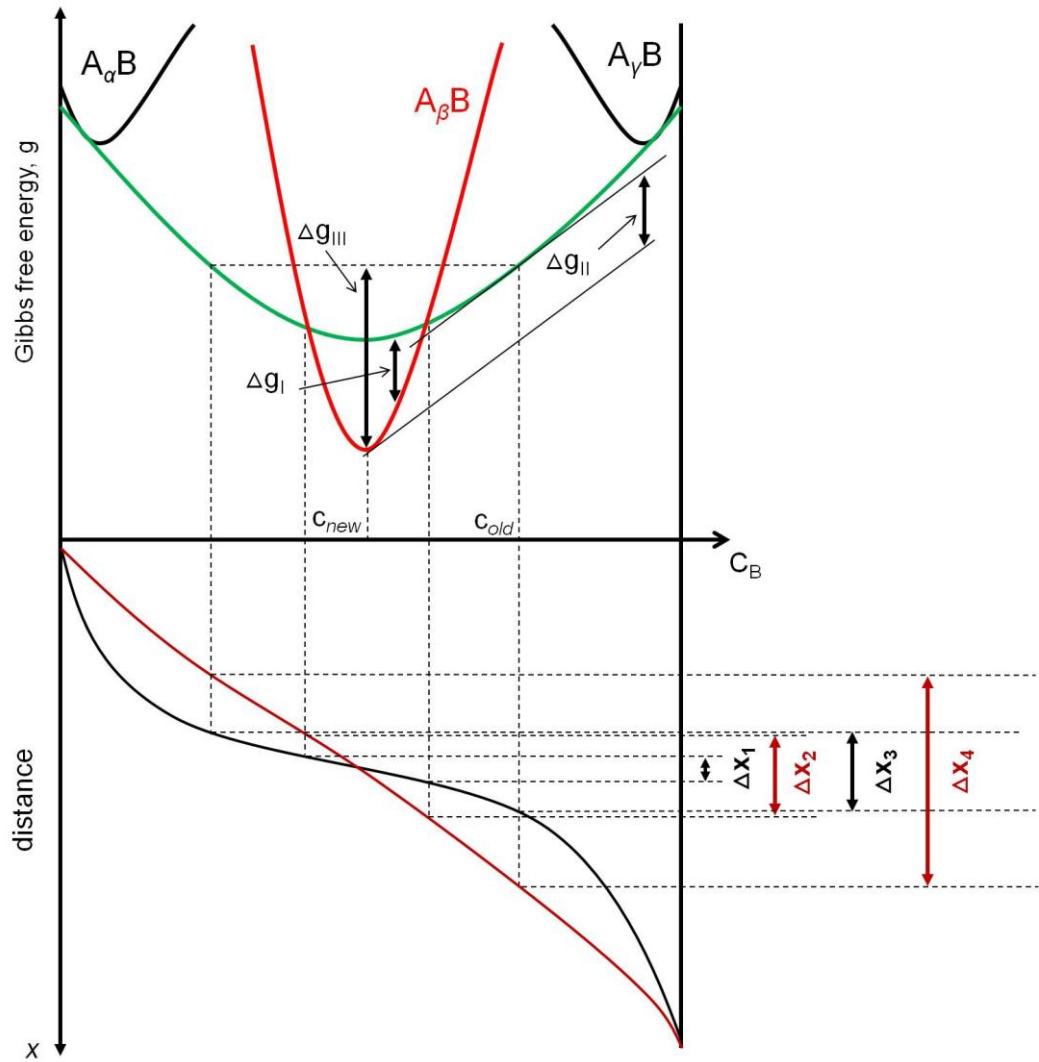


**Figure 6** A schematic illustration of the Gibbs free energy curves showing the driving force  $\Delta g$  for the three different modes of nucleation explained in the text ( $\Delta g_I$  polymorphic,  $\Delta g_{II}$  transversal, and  $\Delta g_{III}$  longitudinal). The green curve represents a metastable phase (wide solubility range) at the diffusive zone, and the red curve is the new intermetallic phase. At the bottom, two concentration profiles are shown with two different concentration gradients. The influence of the concentration gradient on the thickness of the region containing a concentration range of the intermetallic phase is illustrated.  $\Delta x_1$  and  $\Delta x_2$  represent the favorable nucleation regions for the polymorphic mode, while  $\Delta x_3$  and  $\Delta x_4$  represent the favorable nucleation regions for the transversal mode.

It is important to note that all the three modes mentioned treat the diffusive zone at the phase boundary interface as a metastable phase with broad concentration range overlapping with the parent phases and the new intermetallic phase. If the solubility between the parent phases is more confined, the concentration gradient will be sharper and the diffused zone would be consequently reduced leading to a smaller favorable region for nucleation. This issue is illustrated in Figure 7. Therefore, in

such case, the concentration gradient (or more precisely the chemical potential gradients) would have a greater influence on suppressing nucleation [35].

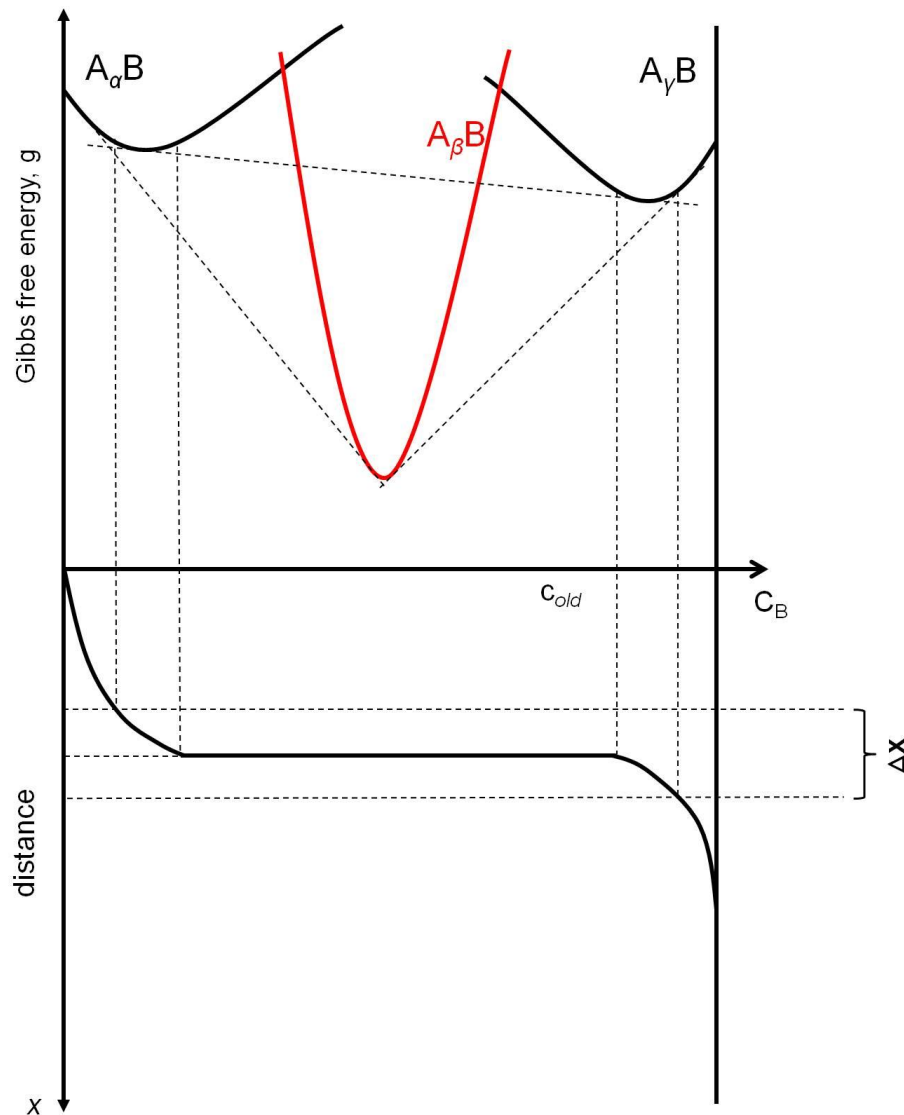


**Figure 7** A schematic illustration of the Gibbs free energy curves of two phases with limited mutual solubility. The red curve is the new intermetallic phase. At the bottom, the corresponding concentration profiles based on the solubility of  $A_\alpha B$  and  $A_\gamma B$  phases is shown. The favorable nucleation region is represented by  $\Delta x$  (for any nucleation mode).

#### 1.4.2. Nucleation by interfacial mass transport

In polycrystalline multilayer thin films mass transport can be significant in the GBs, as well as through the phase boundaries. Interdiffusion at the interfaces changes their chemical potentials which can act as the main driving force for nucleation. Coffey and Barmak [39] have developed a model

that describes a mechanism of nucleation solely dependent on the interfacial free energies. As a result, the model provides an explanation for the phase selection process which combines thermodynamical aspects as well as microstructural based kinetics, named as a *grain boundary diffusion controlled precipitation* model suitable to be applied on multilayer thin films reactions. The differences in the chemical potentials of the phases and the chemical potentials of the interfaces (GBs and phase boundaries) are explained to drive three processes: 1- Lattice diffusion (atom transport across the interfaces) 2- GB and phase boundary diffusion (atom transport through the interfaces) 3- Chemical reactions at the interfaces leading to heterogeneous nucleation. The flux density of atoms crossing the interface from  $\alpha$  to  $\beta$  phase can be expressed as:

$$J_i^{\alpha-\beta} = T_i^{\alpha-\beta} (\mu_i^\alpha - \mu_i^\beta) \quad (22)$$

where  $T_i^{\alpha-\beta}$  is a kinetic coefficient ( $\text{atoms}^2/\text{cm}^2 \cdot \text{s} \cdot \text{eV}$ ) for the atom transfer process from phase  $\alpha$  to phase  $\beta$  ( $i$  can be A or B atoms).  $\mu_i^\alpha$  and  $\mu_i^\beta$  are the chemical potentials ( $\text{eV}/\text{atom}$ ) of  $\alpha$  grain and  $\beta$  grain, respectively. The flux density ( $\text{atoms}/\text{cm} \cdot \text{s}$ ) through the interface is described as:

$$J_i^I = -m_i^I \left( \frac{d\mu_i^I}{dx} \right) \quad (23)$$

where  $m_i^I$  is the lateral mobility in the interface ( $\text{atoms}^2/\text{s} \cdot \text{eV}$ ),  $\mu_i^I$  is the chemical potential in the interface, which differs from the chemical potentials inside the grains. Considering two phases  $\alpha$  and  $\beta$  with a common phase boundary interface, the flux density into and out of the phase boundary interface can be represented as:

$$J_i^{\alpha-I} = T_i^{\alpha-I} (\mu_i^\alpha - \mu_i^I) \quad (24)$$

$$J_i^{I-\beta} = T_i^{I-\beta} (\mu_i^I - \mu_i^\beta) \quad (25)$$

where  $T_i^{\alpha-I}$  and  $T_i^{I-\beta}$  are kinetic coefficients for the atom transfer process from phase  $\alpha$  to the interface and from the interface to phase  $\beta$ , respectively. The model assumes no thickness of the interface (no volume) and resolves the transport only in two dimensions, assuming similar dependences in both dimensions. Moreover, the model does not consider stress development by interdiffusion. The flux in the interface is therefore balanced of the flux in and out of the interface as:

$$\frac{dJ_i^I}{dx} = J_i^{\alpha-I} - J_i^{I-\beta} \quad (26)$$

Solving a differential equation for the dependency of these two modes of mass transport as a function of two dimensional space leads to a definition of a characteristic length  $L_i^I$  which represents the decay length for  $\mu_i^I$  ( $i$  can be A or B atoms), given as:

$$L_i^I = \sqrt{\left[ \frac{m_i^I}{(T_i^{\alpha-I} + T_i^{I-\beta})} \right]} \quad (27)$$

This decay length scale is not a time dependent variable, as for bulk diffusion decay lengths ( $L = \sqrt{Dt}$ ). In fact, it is a fundamental quantity dependent on the diffusivity characteristics of the interface (phase boundary or GB), which relates the interface diffusivity to the interfacial reaction rate. It is a length over which interdiffusion can occur between two phases through fast diffusion paths. In thin films with grain structures of a few hundreds of nanometers,  $L_i^I$  can be comparable to the grain size. When the grain sizes are significantly larger than the decay length, the transport across the interfaces does not compete with the transport in the interfaces and a metastable equilibrium is quickly achieved ( $\mu_i^\alpha = \mu_i^I = \mu_i^\beta$ ). Whereas, if the grain sizes are much smaller than the decay length, the interfacial chemical potential will be constant around each grain and will thus dominate the atomic transport and preferential sites for nucleation, related to type C diffusion (diffusion kinetics discussed in section 1.7.2). The free energy for an interface as a function of the composition along a certain path  $x$  can be defined as:

$$G^I = c\mu_A^I(x) + (1 - c)\mu_B^I(x) \quad (28)$$

where  $c$  represents the composition of a metastable phase  $A_cB_{1-c}$  (solid solution at the interface). This interfacial free energy can be conceptually similar to free energy curves of defined phases used to determine driving forces for nucleation. The interfacial free energy curve varies across the distance of the interface, it also changes when interdiffusion is allowed through the interface (time-dependent). Therefore, as interdiffusion proceeds in the interface the free energy curve becomes more positive and it can intersect with the free energy curves of intermediate phases, where phase selection and nucleation can become possible, as shown in Figure 8. The likelihood of a phase to

form is therefore not required to be the one having the highest free energy value (most negative), but rather the one having a free energy below the interfacial free energy curve. Once a new phase is nucleated it can act as a sink for A and B atoms which will induce a new balance for the chemical potentials between the three phases, that would thus govern the phase selection criteria of a following intermediate phase to form. This model provides a promising basis for understanding nucleation in polycrystalline thin films. Nevertheless, values for the interfacial chemical potentials are difficult to be known for a specific system since they depend on various factors such as surface and strain energies.

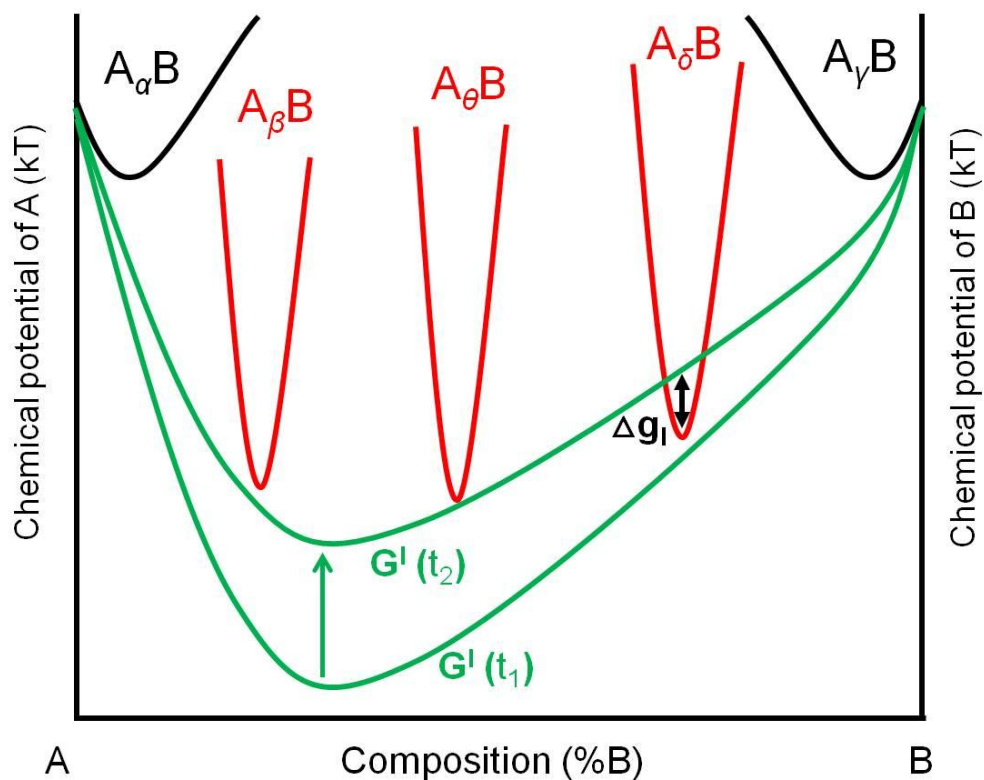


**Figure 8** A schematic illustration of the interfacial free energy according to Coffey and Barmak model [39]. The green curves represent the interfacial free energy at times  $t_1$  and  $t_2$  during annealing where interdiffusion takes place ( $t_2 > t_1$ ) where the free energy curve becomes more positive moving upwards. The red curves represent the free energy curves for three intermediate phases. At  $t_2$  the free energy curve for the intermetallic phase  $A_\delta B$  becomes lower than the interfacial free energy curve, where nucleation becomes possible with a chemical driving force of  $\Delta g_i$ . Such phase may possibly be metastable and unlikely to form in bulk conditions.

### 1.5. Two-step growth process

Apart from phase competitions and the unique selectivity for phase formations known for thin film reactions, phase growth in many miscible metallic multilayer thin films exhibits a special mutual behavior explained in an earlier model by Coffey et al. [40]. The growth of the early compound phase that forms between two parent layers is described to grow in two stages, corresponding to two consecutive heat releases commonly detected by differential scanning calorimetry (DSC) during ramp-annealing, both of which correspond to formation and growth of one compound phase. This two heat release behavior has been reported in several transition metal-aluminide systems such as Ru/Al [41], Co/Al [42], Nb/Al, Ni/Al, Ag/Al, Hf/Al and Ti/Al (all are reviewed in Ref. [43]) as well as in transition metal-silicide systems such as V/a-Si, Ni/a-Si, and Ti/Si. The model explains that the first stage is a lateral growth of the new phase in the plane of the phase boundary interface which forms a coalescent and continuous layer. The second stage is a growth of this new phase in the normal direction to the interface. The first stage is considered to be interface controlled (growth behaves linearly with time), that is assisted also by diffusion in the moving boundaries of the new phase (similar to diffusion induced grain boundary migration [44]). While the second stage is considered to be diffusion controlled exhibiting a parabolic growth behavior [29]. The amount of heat released by the first and second step can vary according to the film thickness (multilayer period). For small periods, almost all the reaction occurs in a single heat release representing the first stage, intermediate periods show a typical two successive heat releases, whereas for the large periods the first heat release is extremely low and most of the DSC signal is detected for the second stage. A schematic illustration is displayed in Figure 9. Michaelsen et al. [45] have shown that the DSC experimental results studied for Nb/Al and Ti/Al fit very well to simulations of the heat releases according to the two-stage model [40]. Based on the phase growth characteristics described by the model the period dependence behavior is quite reasonable. Small periods exhibit higher density of interfaces inducing strong interfacial reactions and the distance for the second step growth is significantly short, whereas larger periods hold relatively lower interfacial densities leading to fewer interface controlled reactions while having more volume for the type of growth in the second step. Another interesting and noticeable behavior, in the metallic multilayer systems displaying the two successive heat releases for the first phase, is the shift in reaction temperatures of the heat releases as a function of the period, showing reaction temperatures to be proportional to the period thickness. Two possible reasons could explain this, first, small periods exhibit much shorter diffusion distances therefore requiring less amount of heat to be applied to the system for complete growth of the compound phases, however, another possibility could be that small periods exhibit higher or thicker initial interdiffusion (diffused zones) between the layers, thus requiring lower heat for nucleation to start (less concentration gradient preparation time).

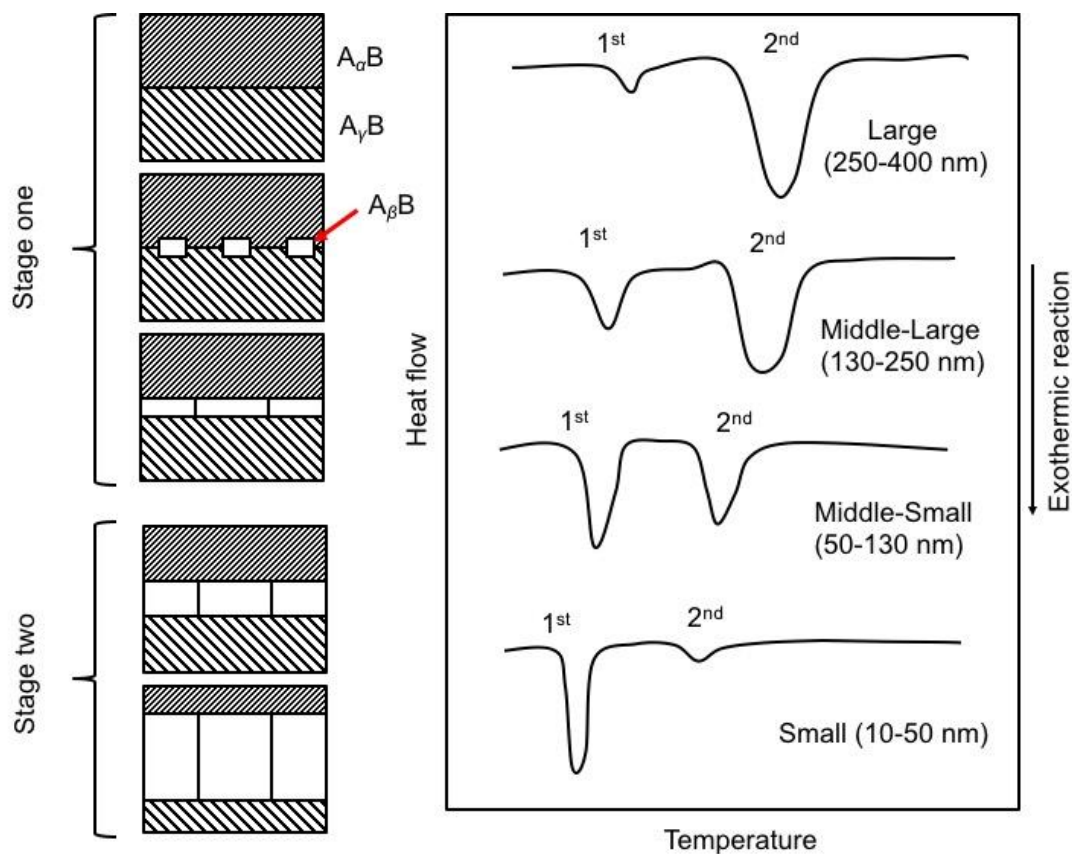


**Figure 9** Schematic for the two-stage phase growth behavior of the phase  $A_\beta B$  in  $A_\alpha B/A_\gamma B$  multilayer structure. The DSC scans show an example of a typical period behavior for different period thickness (typical period ranges given). The reaction temperature increases with the period thickness.

Using high resolution imaging techniques Jeske et al. [46] have studied the phase formation in Ni/Al thin film bilayers synthesized using two different deposition techniques. They reported that the formation of the new compound phase as a continuous layer is observed in samples with large grain sizes deposited using electron-beam evaporation agreeing with the two-stage growth mechanism. Whereas, for films of small grain sizes deposited by sputter deposition, the early compound phase did not nucleate and grow as a continuous layer, rather along the GBs, showing different results to the Coffey model [40]. Such results highlight the influence of the microstructure and the effective diffusivity upon the nucleation and phase growth characteristics, respectively.

### 1.6. Phase formation and phase sequence dependency on period thickness

Several features change in multilayer thin films by varying the period thickness, such as: grain size, diffusion distances, roughness, texture, stresses, interfacial density, as well as the volume of parent phases surrounding a growing compound phase during chemical reaction. Moreover, the effect of the gradient energy can become significant in very thin periods (ultrathin multilayers). The influence of these physical properties can be directly seen studies on the early phase formations and phase sequence of miscible metallic multilayer thin films with various period thicknesses, such as in Ni/Al [47], [48] for example, where different phase sequence and early phase formations are reported as a function of the period thickness.

The reaction in the small periods is the most interesting one because of their peculiar kinetics. In many miscible metallic multilayers, annealing small periods show a direct formation of the product phase at relatively lower reaction temperatures. For instance, annealing Ni/Al multilayers with periods less than 15 nm and a composition range near 50:50, will directly lead to the formation of the B2-NiAl phase [47]. This is usually explained to be caused by increased interdiffusion, as well as shallow concentration gradients due to the higher influence of the gradient energy effect, leading to larger nucleation favored diffused regions for the desired final phase to form directly. Diffusion coefficients in ultra-fine grain structures are normally 2-3 orders of magnitude higher than GB diffusion coefficients [49]. Assuming Johnson-Mehl Avrami kinetics (diffusion controlled reactions) it has been shown by Barmak et al. [50] for Ni/Al and by Illeková et al. [51] for Ti/Al that small periods result in almost 3 times higher Avrami exponents compared to larger periods, suggesting different nucleation mechanisms in small and large periods, respectively. It is very important to note that direct phase formation behavior is not a general case, since in some miscible metallic multilayers, such as Mo/Se, annealing small periods lead to the interfaces dissolving and a formation of an amorphous homogenous phase, followed by the nucleation of the crystalline product phase at relatively higher temperatures [52].

Regarding amorphous phase formations, it is very important to mention here that in some material combinations the system has a high tendency to form an early amorphous phase from the reaction of the two parent phases. This is commonly seen for noble metals (Au, Pd, Cu) as well as the combinations of early transition metals (Zr, Nb, Hf, Ti) and late transition metals (Fe, Ni, Co, Pd) [1], [53]. Greer [20] has shown that the formation of a crystalline compound, amorphous phase, or a solid solution as the early phase is highly dependent on the amount of heat of mixing ( $\Delta H_{\text{mix}}$ ) produced as well as the ratio of atomic radius for both elements, reflecting the diffusivity in the

system. Binary systems with large negative heat of mixing (larger than approximately -30 kJ/mol) and small radius ratio ( $r_{\text{small}}/r_{\text{large}}$  less than approximately 0.85) usually exhibit amorphous phase formations. It is nevertheless very interesting that amorphous phase formation can be dependent on the period thickness, as seen for Mo/Se multilayers [52].

For middle-to-large periods (typically 50-500 nm) a phase sequence is commonly detected (several intermediate phases nucleate and grow) during annealing before the final stoichiometric phase forms. Amorphous or metastable phases may appear as the first intermetallic phases, which are commonly discussed to be a result of suppression of crystalline phases to nucleate at the early stages [35]. The first phase to nucleate is very important, since it determines the phase selectively criteria for the formation of the subsequent phase(s) to form (explained above in section 1.4.2).

In a specific multilayer system, it is common to find contradictory phase sequences and early phase formations reported in literature. This is primarily due to differences in the synthesis of the multilayer films, where different deposition techniques can result in different microstructures, as well as different level of impurities in the films. Moreover, under some deposition conditions, the first phase to form, be metastable or not, could already exist in the as-deposited condition, thus the thermal treatment would only be inducing further growth of the compound phase. The role of deposition on the microstructure and interdiffusion is discussed in section 1.8.

### **1.7. Diffusion kinetics in thin film structures**

It is necessary to point out that the real driving force for diffusion is not the concentration gradient, nor the mobility of a certain phase, but rather the chemical potential gradient between the phases in contact with each other. Components always diffuse down the chemical potential gradient which in some cases could actually be against the concentration gradient (uphill diffusion), for example in phases exhibiting a miscibility gap. Therefore, diffusion kinetics based on Fick's laws can sometimes be limiting in some applications. The interconnection between thermodynamics and kinetics is always strongly evident in chemical reactions, either in diffusion couples or thin films. The diffusion kinetics in thin films is however more complicated since the mass transport can be heavily influenced by other microstructural factors such as lattice/topographic defects, interfacial transport and stresses.

As mentioned above in section 1.3, according to Zotov et al. [12], vacancy diffusion best describes the atomic mechanism of mass transport in a wide range of miscible metallic multilayer thin films.

Therefore, any regions with high vacancy concentrations mediate diffusion to reach higher rates, such as GBs, voids, and topographic defects, as well as phase boundary interfaces which have strong disturbance in the lattice symmetry and can act as sink for diffusion [46]. Moreover, interfaces and lattice defects act as sources and sinks for vacancies which intensifies their contributions in the mass transport [30].

### 1.7.1. Interdiffusion in bilayer films

In the continuum approach of treating diffusion, the interdiffusion coefficient between two metals with a wide homogeneity range can be calculated from the compositional profile across the phase boundary interface. The interdiffusivity depends on the mobility of each phase as well as the composition, where diffusion coefficients in most cases do not have constant values, meaning that they can vary with the composition. Several methods are used for the calculation of interdiffusion, such as the Darken and the Nerst-Planck equations [23]:

$$\tilde{D}_D = X_\alpha D_\beta + X_\beta D_\alpha \quad (29)$$

$$\tilde{D}_{NP} = \frac{D_\beta \cdot D_\alpha}{X_\beta D_\beta + X_\alpha D_\alpha} \quad (30)$$

$D_\alpha$  and  $D_\beta$  are the lattice diffusion coefficients for phase  $\alpha$  and  $\beta$ , respectively, with  $X_\alpha$  and  $X_\beta$  as the average mole fractions of each phase. The interdiffusion coefficient,  $\tilde{D}_D$ , based on the Darken calculation, offers a good estimate for the interdiffusivity on a macroscopic level which assumes a local thermal equilibrium of vacancies (sinks and sources) across the interface. On the other hand, the interdiffusion coefficient,  $\tilde{D}_{NP}$ , based on the Nerst-Planck (same as the Nazarov-Gurov method), offers a more detailed description on the mesoscopic scale for the interdiffusion, which can be influenced by non-equilibrium vacancy distribution across the interface that affects the mobility of both phases [29]. It is important to note that in the case when the mobility of both phases in contact vary significantly, leading to the formation of asymmetric concentration profiles. In these conditions, the balance in the effective sources and sinks created across the interface, which assist in the migration of atoms, rapidly vanishes, and in some diffusion couples, it results to the appearance of voids close to the interface. This is known as the Kirkendall effect [28]. Strong variations in the mobility of reactant phases together, as well as their diffusion rates in the compound phases plays a

vital role in the concentration gradients between the phases [54] as well as the growth rate of intermetallic phases.

As mentioned in sections 1.3 and 1.4.2, in thin films, the slow atomic exchange mechanism of lattice diffusion can sometimes be considered almost ‘frozen-in’, where lattice defects in the microstructure dominate the interdiffusion between two phases. The contribution of the transport along fast-diffusion paths is highly dependent on the microstructure, and as discussed in section 1.6, it can be also dependent on the period thickness in a multilayer structure.

### 1.7.2. Grain boundary diffusion and kinetic regimes

In polycrystalline materials, a hierarchy of fast diffusion paths can be found in the microstructure which plays a key role in interdiffusion of thin films. Activation energies for GB diffusion,  $Q_{GB}$ , are typically about 0.4-0.6 the activation energies for volume diffusion (lattice),  $Q_V$ , leading to GB diffusion rates reaching four to six orders of magnitude higher compared to volume diffusion [28]. Diffusion rates in low-angle grain boundaries (LAGB) are normally slightly slower than GB diffusion, due to their more constricted open structure, which can be similar to diffusion rates found at dislocations. Diffusivities in high angle GBs can also vary according to the structural characteristics of the GBs (misorientation and tilt angles). Thus, random GB networks in thin films can exhibit fast and slow diffusion pathways, which was recently proved experimentally [11]. The fastest type of GBs diffusion is along triple junctions (TJs), where higher vacancy concentrations exist due to their more open structure, where diffusivities can exceed high angle GBs by up to three orders of magnitude [55]. TJs therefore serve as a special type of GB diffusion. Moreover, regarding fast diffusion paths, depending on the roughness in thin films, especially multilayers, topographic defects can build up (discussed in section 1.3), which are principally agglomerations of voids within the structure. The diffusion in these pathways can be comparable that to surface diffusion (or slightly less), in which activation energies for surface diffusion,  $Q_s$ , are about 0.1-0.3 activation energies for volume diffusion [28]. Hence, the diffusion rates in topographic defects ( $D_{TD}$ ) are higher than diffusion rates in any lattice defects within the microstructure. The hierarchy of diffusion rates is:

$$D_s \geq D_{TD} > D_{TJ} > D_{GB} > (D_{LAGB} \text{ or } D_{disl.}) > D \quad (31)$$

GB diffusion can exhibit different regimes where the ratio between the contribution of the lattice and GB diffusion can vary. A certain regime can dominate depending on the annealing temperature,

annealing time, grain size, as well as the characteristics of the lattice and GBs [23]. The dependency of the regime on the grain size is a very important aspect, which is of great interest in the work here, since grain sizes vary with the period thickness in multilayer thin film structures which should therefore influence the GB kinetic regime. The different GB kinetic regimes, according to Harrison's classification [23], [56], can be defined as follows:

**i. Type A diffusion**

In this regime, lattice diffusion has a significant contribution in the effective diffusion, and the diffusion front appears almost planar with slight penetrations at the GB regions. This regime is generally observed at high annealing temperatures, and/or long annealing times, and/or materials with fine grains. The diffusion length for lattice diffusion ( $D \cdot t^{1/2}$ ) is usually larger than or equal to the spacing between GBs ( $d$ ). Since GBs exhibit segregation of the solute elements during diffusion, the actual thickness is therefore defined by the product of the segregation factor and the initial GB thickness, which equal,  $s \cdot \delta$ . The actual thickness of the segregated GBs is much smaller than the lattice diffusion length, hence, in type A conditions:

$$s \cdot \delta \ll (d/0.8) \leq \sqrt{D \cdot t} \quad (32)$$

**ii. Type B diffusion**

In this regime, lattice diffusion has a lower contribution in the effective diffusion, and the diffusion front appears as long extensions of diffusion along the GBs followed by GB diffusion tails. The formation of the tails is due to the leakage of diffusant atoms from the boundary into the interior of the grains, where the GB acts as a source for such diffusion path. This regime is usually observed after annealing at low temperatures, and/or short annealing times, and/or in materials having large grains. Here, the lattice diffusion length ( $D \cdot t^{1/2}$ ) is much smaller than the spacing  $d$ , but still much larger than the segregated GB thickness. Therefore, in type B conditions:

$$s \cdot \delta \ll \sqrt{D \cdot t} \ll d \quad (33)$$

**iii. Type C diffusion**

In this regime, lattice diffusion is theoretically absent, where diffusion only proceeds along the GBs, without leakage of atoms into the grain interiors. Therefore, no GB diffusion tails exist. This regime is usually observed at low temperature anneals, and/or very short annealing times, and/or nanostructured crystalline materials. The lattice diffusion length is therefore smaller than the segregated GB thickness:

$$\sqrt{D \cdot t} \ll s \cdot \delta \ll d \quad (34)$$

Since the diffusion here is only localized at the GBs ( $\delta \sim 0.5$  nm), diffusion studies using tracer elements or radioactive isotopes are very difficult to be carried out (limited diffuser amount to be detected). However, this regime is very common in thin film structures [39], which emphasizes the key role of GBs in the interdiffusion in thin films. The different types of GB regimes are illustrated in Figure 10.

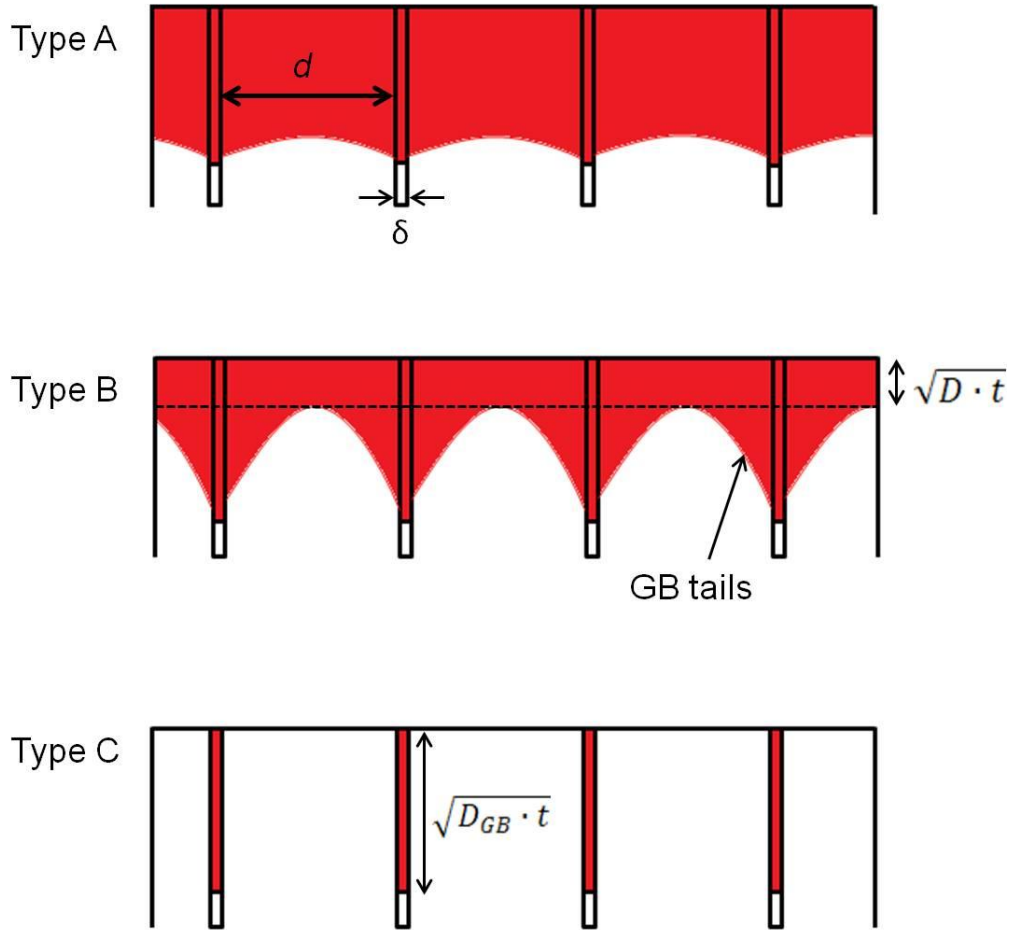


**Figure 10** Illustration for the main diffusion regimes according to Harrison’s classification [23] in five grains positioned parallel to the diffusion direction. The red color represents the diffuser element.

### 1.7.3. Effective diffusivity

The volume fraction of GBs in the microstructure therefore influences the contribution of the GB diffusion to the total diffusivity in the material, which is referred to as the *effective diffusivity*. The effective diffusivity for solute atoms can be estimated by the Hart-Morlock relationship [57] for a simple microstructure with GBs in parallel direction with the diffuser (as seen in Figure 10) as:

$$D_{eff} = \frac{sX_{GB}D_{GB} + (1 - X_{GB})D}{1 - X_{GB} + sX_{GB}} \quad (35)$$

where  $s$  is the segregation factor for solute atoms and  $X_{GB}$  is the volume fraction of GBs.

## 1.8. Thin film growth by physical vapor deposition

The process of thin film growth by PVD is an extremely non-equilibrium process, where the heterogeneous nucleation of vapor atoms on a substrate occurs at significantly high levels of supersaturation [58]. High concentrations of point and line defects in the lattice structure formed during deposition generally leads to different film properties compared to bulk properties [10]. Thin film formation is composed of several steps: Condensation, nucleation, nuclei growth, coalescence, interface formation, and film growth. Vapor atoms arrive on the substrate and condense on the surface, bonding directly with substrate atoms or with neighboring atoms on the surface (that can include impurity atoms). The atom is thus considered to be chemisorbed to the surface. As atoms condense on the substrate surface certain energy is released by this chemical reaction, referred to as the condensation energy, which gives rise to the substrate temperature. At high deposition rates, appreciable substrate heating can occur which can trigger interdiffusion and phase transformations during film deposition. Before the chemical bonding occurs, the atom can have some mobility on the surface, referred to as surface mobility. This mobility depends on the incident energy of the deposited atom, the strength of atom-surface interactions (chemical bonding), as well as the substrate temperature [16]. A mobile atom on the surface is referred to as an adatom. At low surface mobilities, the atoms bond quickly at the area in which they arrive, whereas at high surface mobilities, adatoms can move more freely on the surface and bond at preferential nucleation sites. The surface properties of the substrate greatly influence the characteristics of the film created on top, in which a topographic relationship is built between both layers, where surface roughness affects the morphology of the interface created between them. Moreover, thin films can have a structural relationship with crystalline substrates, which is known as epitaxial growth.

Nucleation occurs when several deposited atoms bond together and form a stable nucleus on the surface. The nuclei can then start growing on the substrate. While growing they may rotate and align to preferential crystallographic orientations. The growth can occur in three main different modes, depending on the interaction energies of the surface atoms and thin film atoms [58]. Young's wetting equation provides the physical concept for the existence of the different modes during nuclei growth in terms of the surface energies (see Figure 11). The three different modes are:

#### A. 2D growth

In this mode, a layered growth occurs, referred to as the *Frank-van der Merwe* mode, where the deposited film monolayers grow on top of each other. The interaction with the substrate or

adjacent films is strong with low extent of agglomerations of the deposited atoms. Here  $\emptyset \approx 0$ , which requires  $\gamma_B > \gamma_A + \gamma^*$ .

### B. 3D growth

In this mode, three-dimensional clusters form on the surface and grow together, referred to as the *Volmer-Weber* mode, where the deposited atoms agglomerate together in the form of clusters. The interaction with the substrate or adjacent films is weak compared to interactions of the deposited atoms together. Here  $\emptyset > 0$ , which requires  $\gamma_B < \gamma_A + \gamma^*$ .

### C. 2D plus 3D growth

In this mode, a two-dimensional growth occurs followed by three-dimensional growth, referred to as the *Stranski-Krastanov* mode. This occurs due to an increase in the interfacial energy by the deposition of a few monolayers which shifts the growth mode. This mode is a dynamic one representing both modes described above occurring simultaneously, which is commonly found in metal-on-metal deposition at low surface mobilities [59].

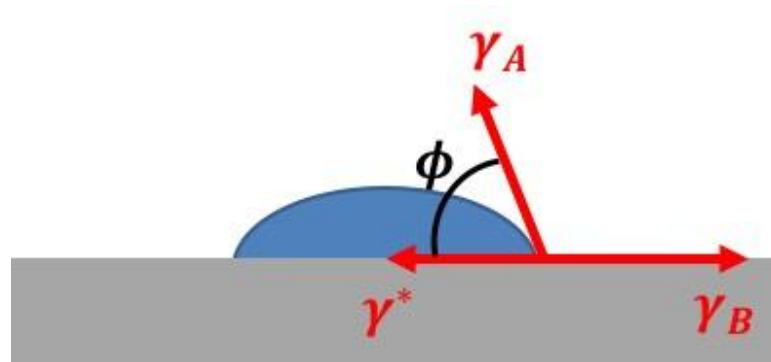


**Figure 11** Schematic illustration for the Young's equation ( $\gamma_B = \gamma^* + \gamma_A \cos \emptyset$ ) of a liquid nucleus on a substrate.  $\emptyset$  describes the wetting angle,  $\gamma^*$  is the interface energy of the film-substrate,  $\gamma_B$  is the surface energy of the substrate, and  $\gamma_A$  is the surface energy of the film material.

As the nuclei grow they form islands on the substrate surface. The islands then grow until they connect and form a continuous thin film layer. This process is known as coalescence. The formation of a continuous layer is very important for obtaining low roughness of the thin film layer. As the islands connect they can form a GB between them or fuse together to form a single island. Mass transport during this growth occurs by surface and lattice diffusion, which is influenced by the

surface energies and supersaturation, respectively. It is worth noting that in extreme cases of limited diffusion and bond saturation, an amorphous layer can be built during the growth of the islands [16].

As adatoms condense, nucleate and grow into islands, an interface gets formed with the substrate which can be hugely influenced by the deposition parameters. Generally, the interface can be abrupt or somewhat diffused, based on the solubility of the film and substrate together, which is a pure thermodynamic effect (as explained in section 1.4.1). Abrupt interfaces formed due to limited solubility could be synthesized to be more diffused, which can be achieved by depositing atoms with high incident energies that allows them to penetrate deeper into the surface of the substrate or the metal surface. In multilayers, diffused interfaces can also be achieved by degrading the deposition flux from one material to the other, which is called a pseudodiffusion interface [16]. A diffused interface between layers with mutual solubility can become further diffused if the substrate temperature is elevated during deposition or by long deposition times with high substrate temperatures. As mentioned above, diffusion due to elevated substrate surface temperatures could allow the formation of compound phase at the interface. Compound interphases are commonly found in metal-metal systems that are moderately or highly reactive, such as Al-Pd or Al-Zr [60], [61]. In cases of rough substrate surface, a rough interface will be created which include surface grooves that become filled in by the deposited materials. The deposition on rough surface morphology can create inhomogeneous distribution of the film on the surface due to geometrical shadowing effects which can also generate voids and porosities at the interface. As islands connect together and the film starts growing in thickness, the material deposited, the substrate used, as well as the deposition conditions, are primary variables that control the microstructure of the thin film. Structural zone models are used to describe the resulting microstructure based on the mentioned variables. The structural models estimate three main zones depending on the ratio of the substrate temperature ( $T_s$ ) to the melting temperature of the material deposited ( $T_m$ ). Since activation energies for diffusion in most metals can be linked to the melting temperature of the material, therefore the homologous temperature,  $T_h$ , that is [62]:

$$T_h = \frac{T_s}{T_m} \quad (36)$$

which provides an indication for the mobility of adatoms on the surface during deposition. For low adatom mobilities, atoms condense quickly and islands do not easily fuse together during growth, leading to a fine grain structure. At very low adatom mobilities it can lead to the formation of a porous structure with high interfacial roughness. In the Thornton model for structure zone diagrams

[63], the regime of low adatom mobility can be generally defined as zone 1, with  $T_h < 0.3$ . At higher homologous temperatures, typically  $0.3 < T_h < 0.5$ , surface diffusion sets in, leading to the formation of columnar grains with larger grain sizes and reduced defect density, defined as zone 2. At even higher homologous temperatures,  $T_h > 0.5$ , bulk diffusion sets in leading to denser films with even larger and equiaxed grain structures, defined as zone 3. It is important to note that the substrate temperature is used here as an estimate for the film temperature. Since the homologous temperature is related to the mobility of adatoms, it is also understood to influence the film growth modes, as reported by Thompson [59].

In sputter deposition, the adatom mobility can be influenced by changing the incident energy of the sputtered atoms via the sputter gas pressure. At low sputter gas pressures, the sputtered atoms collide less with the sputter gas atoms during their pathway from the target to the substrate, and thus do not lose much of their kinetic energy. On the contrary, at high sputter gas pressures, the sputtered atoms collide more with the gas atoms, which reduces their kinetic energies further, leading to lower energy distribution when they arrive at the surface, i.e. lower adatom mobility [62]. Moreover, the sputtering power can also alter the degree of interdiffusion and the grain structure, since the sputtering power is directly proportional to the surface mobility of adatoms during deposition and the substrate temperature [17]. Details on sputter deposition technique are given in section 2.1. Therefore, the structure zone can be defined using the homologous temperature and the sputter gas pressure, which is presented in the structure zone model shown in Figure 12.

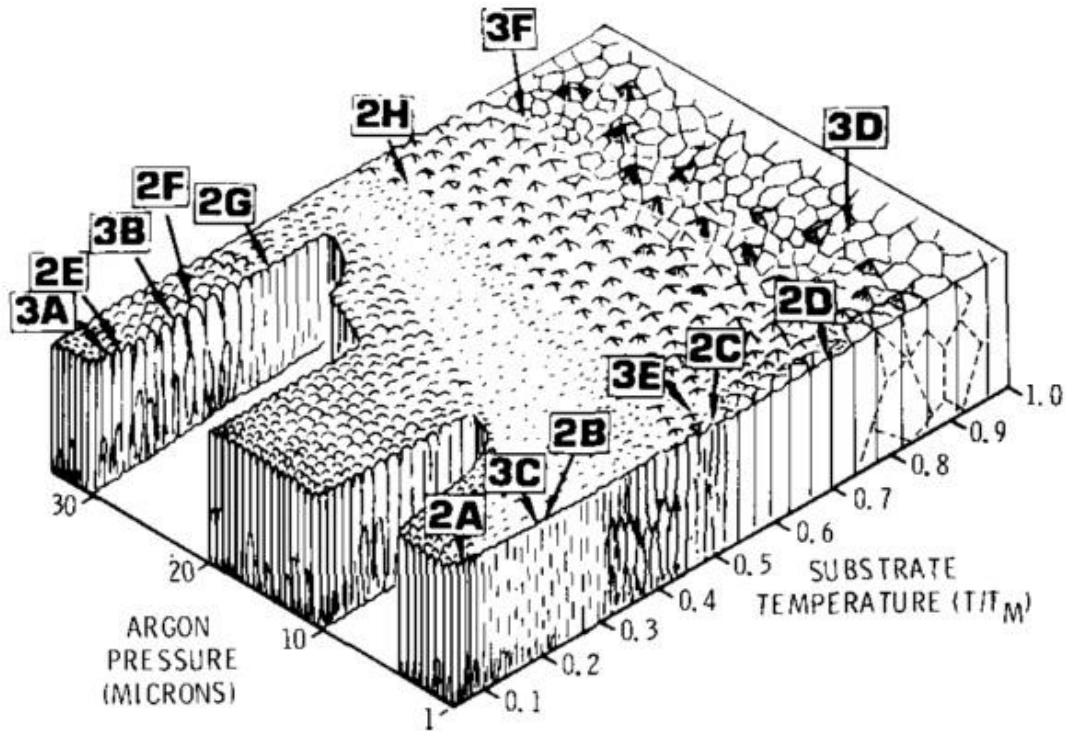


**Figure 12** Structure zone model by Thornton [63] showing structural variation as a function of the homologous temperature and sputter gas pressure (Argon). The labels shown refer to microstructural examples presented in Ref. [63].

Other parameters can be also adjusted to control the grain size, such as substrate cooling, substrate biasing, as well as the substrate-target distance [17], [64]. For metals, the average range of kinetic energy of the deposited atoms differs for each deposition technique, following the sequence (typically): vapor deposition < electron-beam evaporation < magnetron sputtering < ion-beam deposition [12].

Hence, at this point, the significance of the synthesis process in the design of the thin film microstructures and interfaces becomes obvious. For any metallic system, concentration gradients at phase boundaries, initial interdiffusion, grain sizes, texture, and defect density can be generally controlled during the synthesis procedure. Consequently, the effects of the diffusion kinetics in a thin film structure are extremely tunable by the deposition conditions. Contradictory results found in literature on early phase formation and phase sequence for specific multilayer thin film systems (discussed in section 1.6) highlights the role of synthesis and deposition parameters on the thin film chemical reactions.

## **1.9. Summary of the literature-review**

The fundamental differences between bulk and thin film materials in terms of kinetics and thermodynamics have been briefly presented here in order to highlight the complexity of thin film reactions, but also to justify the necessity for further research in this direction. In multilayer thin films, it is elucidated why the period thickness is a crucial design parameter that can influence diffusion regimes, phase competitions, and phase sequence by thermal treatment. Better understanding of thin film chemical reactions and their relationships to the microstructure is essential for the development of highly engineered thin films exhibiting physical properties that can be precisely controlled. Deposition conditions allow particularly interesting possibilities to modify the mechanical, structural, and chemical stability of the thin films. As individual film layer thicknesses reach a few nanometers, fine variations in deposition settings can have major effects on the thin film properties.

## **1.10. Motivations and objectives**

The work here is focused on investigating interdiffusion as well as phase formation mechanisms in miscible metallic multilayer thin films using experimental techniques with resolution down to the sub-nanometer scale level combined with calorimetry analyses. Atom probe tomography (APT) technique is implemented extensively in this work to provide atomistic analyses of the chemical composition in the thin films. Improved understanding of interchangeable effective diffusivity as well as variations in the mechanism of phase formation as a function of the period thickness is a main objective. The goal is to provide a clearer scientific perspective on the relationship between microstructural based kinetics and the period thickness, which is directly related to the processes of nucleation and growth of the early compound phases. Concentration gradients measurements across phase boundaries and diffusion along fast-diffusion paths are of main interest in the investigation. Thin film characterization is performed on as-deposited condition as well as thermally treated thin films at different temperature ranges, carried out in a systematic approach, in order to study the microstructural evolution as well as the phase sequence in different periods. The influence of the composition in the multilayers is also of interest in this study, specifically in small multilayer periods due to their extremely unusual kinetics.

A further motivation for this work is to investigate the effects of deposition conditions on the interdiffusion and microstructural based kinetics. Two deposition conditions are investigated,

namely, the sputtering power and the sputter gas pressure, respectively. As described above, these parameters influence the adatom mobility and substrate temperature during film growth, which is known to have a direct impact on the microstructure and kinetics of the system. Segregations at GBs and the enthalpy of the chemical reactions in different film conditions are evaluated. Complementary microscopy techniques are combined to illustrate the diffusion kinetics using relatively low and high sputtering power as well as low and high sputter gas pressure.

To enhance the understanding of the complex physical phenomena at hand, simple systems are highly preferable. Amongst miscible metallic multilayer thin film systems displaying the common calorimetric behaviors of period dependent reactions, the work here primarily focuses on Ag/Al multilayer thin films used a model system. The experimental investigation is extended to study interdiffusion and phase formation in Ru/Al multilayer thin films, representing a more technically relevant system used in industrial applications, nevertheless, a more complicated one regarding thermodynamic, structural, and synthesis aspects.

### **1.11. The Ag/Al system**

Multilayer thin films of Ag/Al have several physical properties which make them attractive for the investigation here. To begin with, both silver and aluminum have face-centered cubic (fcc) crystal structures and exhibit almost identical lattice constants: 408 and 405 pm, respectively. Consequently, the lattice mismatch between both crystals is less than 1%. Therefore, depositing layers of Ag and Al on top of each other leads to strong epitaxial film growth and formation of coherent interfaces with negligible coherency stresses. This is advantageous for two main reasons. First, it allows varying deposition parameters and layer thickness within a wide range, without significantly affecting the interfacial roughness and the mechanical stability of the multilayer. Second, to understand interdiffusion based on chemical interactions of both layers, minimizing the influence of film stresses on interdiffusion is highly beneficial. Furthermore, the Ag-Al system exhibits only two equilibrium phases: Ag<sub>3</sub>Al (with  $\mu$  of complex cubic  $\beta$ -Mn structure at low temperatures and  $\beta$  of base-centered cubic (bcc) structure at high temperatures) and Ag<sub>2</sub>Al (with  $\gamma$  of hcp structure), respectively [65]. Therefore, the phase diagram of Ag-Al system is relatively simple as shown in Figure 13. Moreover, it has been reported that Ag/Al multilayer thin films display the typical two successive heat releases measured by DSC for the formation and growth of the Ag<sub>2</sub>Al compound phase [66]. Hence, the system offers interesting characteristics for the type of investigation in this study. Additionally, regarding APT analyses, Ag and Al exhibit very similar field evaporation values [67] which results in

particularly high quality datasets which is greatly beneficial for the type of analysis required in this work. Details of APT technique and measurement artifacts are discussed in sections 2.3.6 and 3.2.1.2.

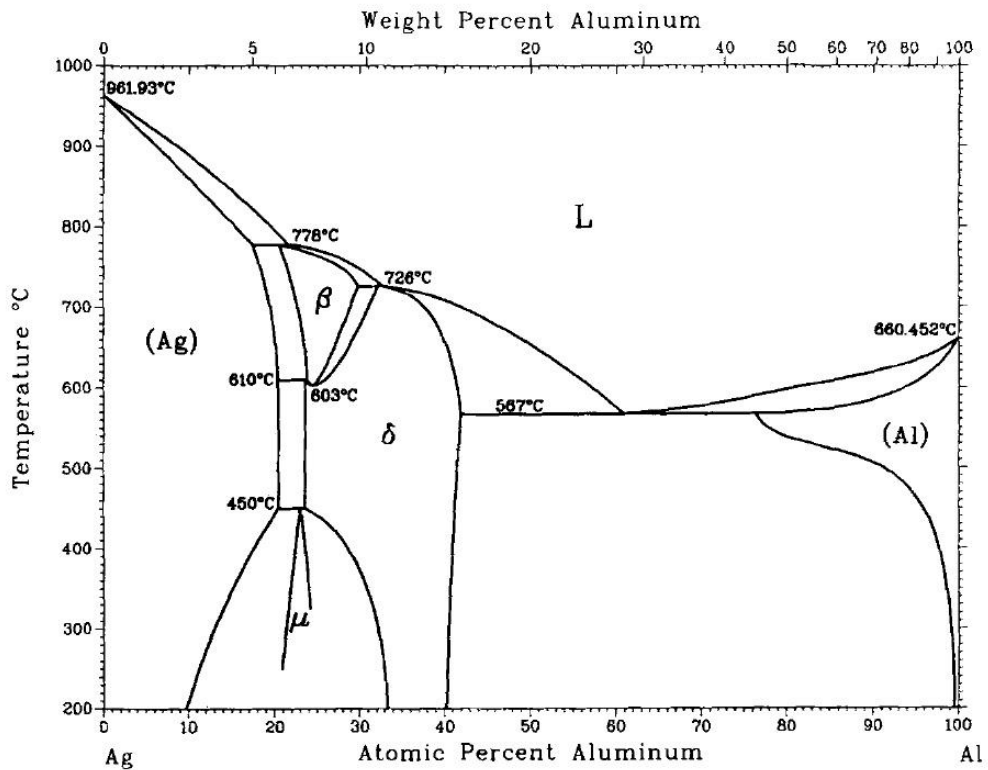


**Figure 13** Ag-Al phase diagram according to McAlister [65].

It is worth noting that the Ag-Al system is long known for its ability to form Guinier-Preston (GP) zones [68], which is used to strengthen aluminum alloys. Low contents of Ag are added to pure Al, and under quenching conditions Ag-rich clusters start forming which develop into GP zones by further annealing. The GP zones are reported to have various crystal structures and metastable compositions, which under sufficient annealing time form stable silver rich  $\gamma$  with hcp structure [69]. The formation of GP zones is driven by the miscibility gap found in the Al-rich region of the phase diagram, where phase decomposition occurs.

### 1.12. The Ru/Al system

The intermetallic RuAl phase with B2 crystal structure has distinctive combinations of high thermal stability with a melting point of 2050 °C, high ductility at room temperature due to its five independent slip systems, as well as high corrosion and oxidation resistance [70], [71]. These properties make this alloy very promising for functional coatings of high temperature stressed

components. It also exhibits high thermal conductivity and good electrical conductivity, comparable to other intermetallics such as NiAl, FeAl, or CoAl [72], [73]. However, the production of homogenous single-phase RuAl is extremely difficult using conventional synthesis techniques such as casting or mechanical alloying. This is mainly due to the large difference in the Ru and Al melting points ( $\Delta T_M=1674$  °C). Formation of RuAl phase via annealing of multilayer thin films offers a more promising solution due to the reduced temperature of phase transformations in thin films compared to bulk, added to the extremely faster kinetics. To produce coating films, this technique requires significantly lower weight of the reactants and thus lower costs compared to other conventional synthesis techniques. Moreover, by varying the individual layer thickness of Ru and Al, the stoichiometry of the final compound product after annealing can be precisely controlled. Ideally, to form RuAl phase directly, small bilayer periods are preferable (typically  $\lambda < 10$  nm) [41], [74]. However, it is also possible to form single phase RuAl using larger periods but after the formation and annihilation of intermediate Ru-rich intermetallic phases during annealing [75]. In bilayer periods typically above 22 nm, formation of intermediate phase(s) occur before the RuAl nucleates, in which RuAl<sub>6</sub> is commonly the first phase to nucleate, and is suggested to nucleate by Al diffusion in the Ru layers [76], [77]. Several phases may form before the RuAl phase nucleates, which appear more clearly in larger periods (for example in  $\lambda = 178$  nm [75]). Interdiffusion and phase formation in this system is therefore of great interest in order to explain the mechanism of early nucleation and its relationship to the period thickness. Ru/Al multilayers represent a classical example for the period behavior in miscible metallic multilayer thin films. Though, chemical reactions in this system are far less studied, in comparison to other systems, such as Ni/Al, Ti/Al, or Nb/Al.

Ru/Al multilayer thin films exhibit self-propagating reactions when ignited which display unique interesting physical properties compared to other systems such as Ni/Al or Pt/Al [77]. In that case, the films are ignited via fast heating rates ( $\sim 10^6$  K/s) which induce the layers to react vigorously together releasing a substantial amount of heat (above 1000 °C) used for local bonding applications. The mechanism for phase formation in this case is drastically different compared to slow heating conditions (typically 0.1 – 5 K/s), and is not in the scope of the work here. Nevertheless, in the self-propagation reaction, the maximum temperature reached, the amount of heat released and the velocity of the reaction are dependent on the amount of the initial interdiffusion in the multilayers. Ideally, the maximum heat released and fastest reaction velocity occurs in conditions of minimal intermixing [75]. Therefore, for development of Ru/Al multilayers used in self-propagation reaction applications, it is also of interest to understand the amount as well as the distribution of interdiffusion

in the as-deposited multilayer thin films. Tuning the properties of the self-propagation reactions can be achieved by controlling the initial interdiffusion of the as-deposited films.

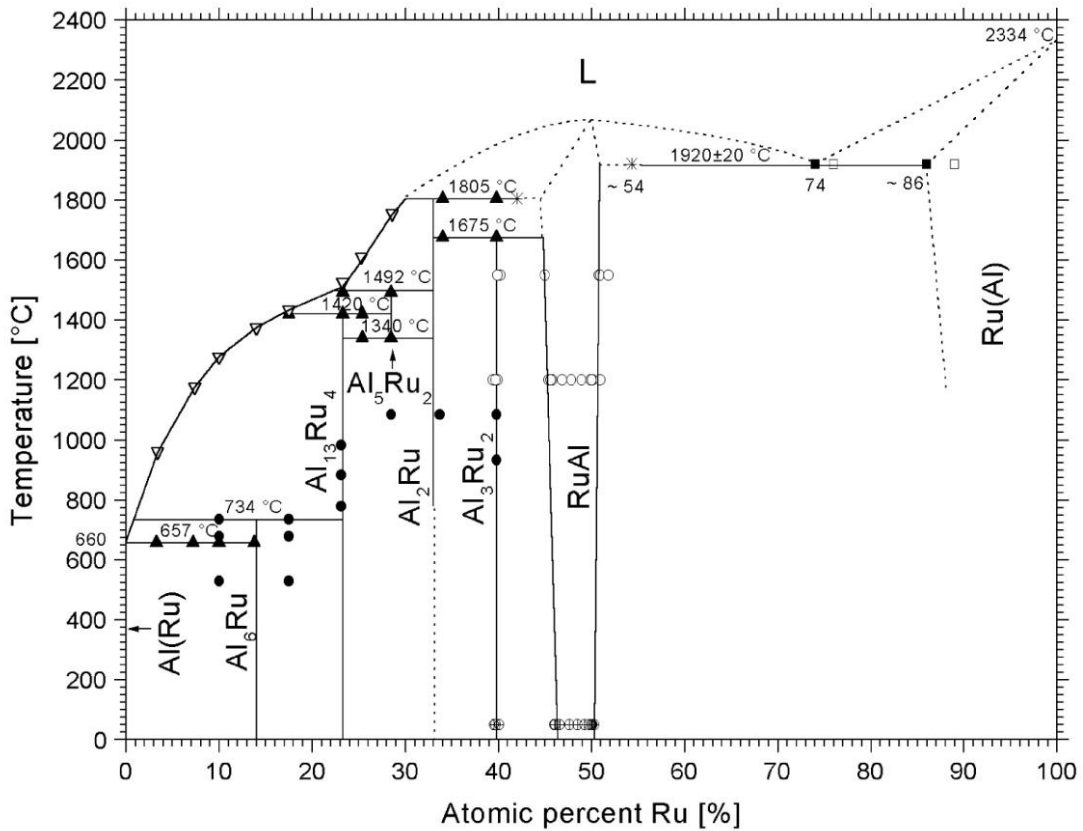


**Figure 14** Ru-Al phase diagram according to Mücklich et al. [70].

This alloy exhibits a relatively complicated phase diagram, in which five intermetallic compounds exist, as shown in Figure 14. However, all the intermetallic phases are in the Al-rich side, as no equilibrium Ru-rich phases are known to form [78]. Ru and Al exhibit different crystal structures, where Ru has an hcp structure with lattice constants:  $a = 270$  pm,  $c = 428$  pm. Using PVD, Ru in general grow along the  $\langle 0001 \rangle$  direction with no epitaxial relationship with Al layers and formation of incoherent phase boundary interfaces [41]. Hence, in comparison to Ag/Al, this system is different from structural and thermodynamic aspects. Moreover, Ru and Al exhibit extremely different field evaporation values which raises a lot of challenges for carrying out successful APT analyses. Therefore, the range of investigation of chemical reactions for this system in this work is much narrower compared to Ag/Al.

## **2. Experimental methods**

### **2.1. Material synthesis**

#### **2.1.1. Magnetron sputtering**

Sputtering is the process of vaporization of target atoms by momentum transfer via the bombardment of energetic particles onto a target surface. The energetic particles are generally atoms of an inert gas that get ionized and accelerated to hit the target surface, due to an electric field located at the proximity of the target. Plasma is thus produced due to the ionization of the gas in the electric field. Magnetron sputtering includes the addition of a magnetic field to the electric field applied. This results in denser plasma at low gas pressures and higher sputtering rates which offers improved quality of thin films, and is widely used in metal deposition as well for some dielectrics. However, a drawback to this technology is that using planar magnets the plasma is non-uniform, which leads to inhomogeneous sputter rate across the target [16]. The sputtering target is usually actively cooled since it heats up during operation. In magnetron sputtering the target has a negative potential and is surrounded by an anode ring with a positive potential. The substrate is positioned on a plate which is usually grounded, but can have a negative biased potential as an optional setting. As described above in section 1.8, substrate temperatures rise during film growth, hence in some systems it is possible to reduce the substrate temperature by cooling of the plates. A schematic of a magnetron sputtering apparatus is shown in Figure 15.

The sputtering yield is the ratio of the number of target atoms ejected to the number of bombarding particles hitting the target. The yield also depends on the chemical bonding of the target atoms and the energy transferred by the particle-atom collision [17]. Therefore, for every type of inert gas used and target material, the sputtering yield can vary. Argon is the commonly used inert gas for metal deposition, which under default settings gives a sputtering yield typically in the range of 1-2. Target atoms get sputtered and leave the target surface with energies ranging from a few eV to several

hundred eV, depending on the relative mass of the target element and the energy of the bombarding ions [16]. The target atoms leaving the target are usually neutrally charged but can get ionized in the plasma, which is referred to as post-vaporization ionization. As the target atoms travel towards the substrate they collide with the gas atoms in the chamber which reduces their incident energy. The target atoms become *thermalized* to the ambient energy of the sputtering gas in the chamber. It is therefore possible to vary the incident energies of the target atoms by changing the gas pressure (high pressure causes more collisions, thus lower incident energies). From Laws of Conservation of Energy and Conservation of Momentum, the energy transferred by the collision is given by [16]:

$$\frac{E_t}{E_g} = 4m_t m_g \frac{\cos^2 \theta_{inc.}}{(m_g + m_t)^2} \quad (37)$$

where  $E_t$ ,  $E_g$  and  $m_t$ ,  $m_g$  are the energies and masses of the target atom and incident gas atom, respectively, and  $\theta_{inc.}$  is the incident angle. The incident energy has vital effects on the film growth since it is directly related to the adatom surface mobility as discussed in section 1.8. Increasing the sputtering power leads to higher deposition rates and higher energy flux, this results in more substrate heating as well as additional thermal radiations.

However, it is important to note that the effect of the sputtering power on the incident energy per deposited target atom should not necessarily be directly proportional, since gas rarefaction effects at high sputtering powers increases the impedance of the plasma which affects the current-voltage characteristics of the discharge and reduces the contribution of charge carriers to the total energy of the target atom [64]. Therefore, in magnetron sputtering the incident energy per deposited target atom generally decreases with higher sputtering power, but the substrate temperature increases, which has important effects on interdiffusion and thin film growth. The influence of the incident energy on thin film growth behavior is a very crucial aspect on the interfacial mixing which can require numerical simulations of the thin film growth combined with atomistic characterization techniques on the thin films in order to be better understood, as carried out for example in Ref. [79].

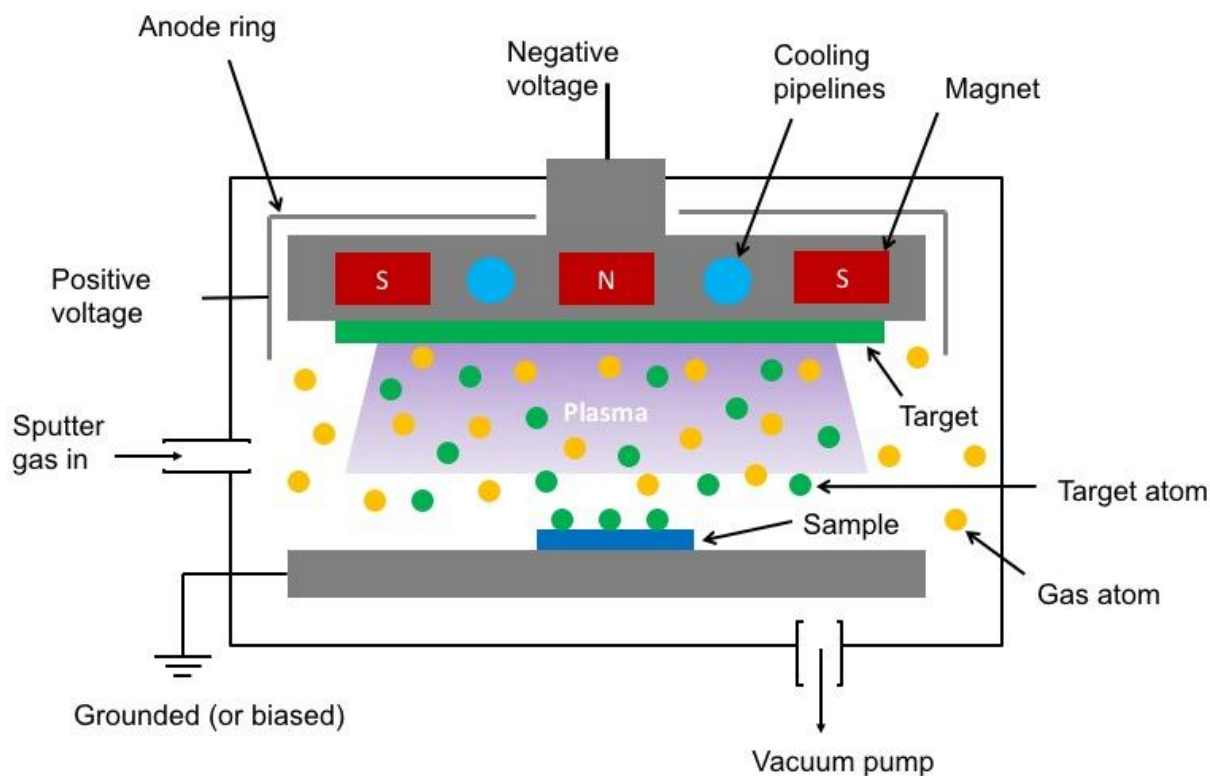


**Figure 15** Schematic for a magnetron sputtering system.

### ❖ Experimental

Deposition of the thin films was carried out in a DC magnetron of von Ardenne PPS-A 200 system. The target to substrate distance is 10 cm and the target sizes used are of 20.3 cm diameter. The substrates were positioned on a moving stage with an active shutter system. The binary multilayer thin film deposition was carried out by changing the substrate position from underneath each target. During the deposition of one target, the other target was switched off with its shutter closed, therefore “cross-talk” between both targets during deposition was avoided. The targets used were of high purity (purity > 99.95 at. %) with a base pressure of  $10^{-6}$  mbar. Single crystal Si wafers (100) were used for all cases with sizes ranging from 2-4 cm<sup>2</sup> and the substrates were positioned approximately in the same spot on the plates to minimize vapor flux inhomogeneity to influence the film composition.

For the Ag/Al multilayer thin films, three different argon gas pressures were used: 0.003, 0.01, and 0.06 mbar. Two sputtering powers were used for Ag and Al targets, 50 and 100 W, producing power densities of 0.15 and 0.30 W/cm<sup>2</sup>, respectively, which are referred to later in the manuscript as “low” and “high” sputtering power, respectively. Temperature gauge strips were attached near the substrates to measure the substrate temperatures during deposition, which showed ~25 C° (~298 K)

and  $\sim 50\text{ C}^\circ$  ( $\sim 323\text{ K}$ ) for the low and high sputtering powers (under Ar pressure of 0.003 mbar), respectively. Ag and Al exhibit a moderately negative heat of mixing, so that power densities above  $0.30\text{ W/cm}^2$  induce intermetallic phase formations during deposition, which was undesirable here. Ag is the first layer deposited on the Si substrates, but in some samples a  $5\text{ }\mu\text{m}$  under-layer was deposited between the substrate and the multilayers. Bi-layer period thicknesses ( $\lambda$ ) of 10, 50, 100, 200 and 400 nm were produced with a total multilayer thickness of  $4\text{ }\mu\text{m}$ . A constant composition ratio Ag:Al of 2:1 was used for all periods, except for the 10 nm period which was deposited in two other Ag:Al composition ratios of 1:2 and near 1:1, respectively. The films of 1:1 composition ratio have shown slightly more Al concentrations when checked with energy dispersive X-ray spectroscopy (approx. 55 at.% Al), therefore the term “near 50:50” is used in the text. The films were stored in a cooled chamber of  $-20\text{ C}^\circ$  ( $253\text{ K}$ ) temperature directly after deposition to avoid room temperature diffusion.

For the Ru/Al thin films, 0.003 mbar argon gas pressure was used in all cases. Sputtering power for Ru and Al targets were 200 and 100 W, producing power densities of  $0.60$  and  $0.30\text{ W/cm}^2$ , respectively. Two sets of samples were prepared, multilayer thin films and trilayer thin films, respectively.  $50\text{ nm}$  thick Ti layer was deposited between the film and the substrate for improved adhesion. For the multilayers, different bilayer periods were produced, having 44, 66 and 88 nm thicknesses with Al:Ru composition ratio of 1:1 (layer thickness ratio Al/Ru is 1.224), and a total film thickness of  $2\text{ }\mu\text{m}$ . For the trilayer thin films,  $400\text{ nm}$  thick Ru layer was deposited directly on the Si substrate, followed by  $80\text{ nm}$  thick Al layer, then  $400\text{ nm}$  thick Ru layer on top (Al layer sandwiched between two thicker layers of Ru).

## **2.2. Thermal analysis**

### **2.2.1. Power compensated differential scanning calorimetry (DSC)**

A DSC is an instrument which provides quantitative thermodynamic and kinetic information about the physical and chemical changes that undergo in a material subjected to heat. A sample and a reference are placed in two micro-furnaces that are thermally insulated from each other, and both micro-furnaces are equipped with a platinum resistance thermometer. By application of heat to both, the energy absorbed or released by the sample is compensated by adding or subtracting an equivalent amount of electrical current to the heater located in the sample holder. The exact amount of current

applied to the sample is known by comparing the signal from both resistance thermometers and automatically adjusting the temperature difference between the sample and the reference holder to be at zero level (“null-balance” principle) [45]. The resistance thermometers require to be precisely calibrated for each heating rate, since any deviations due to thermal lags can induce large errors in the data. The heat flow (Watts) thus is given by the equation:

$$\dot{Q} = mC_s \frac{dT}{dt} \quad (38)$$

where  $m$  is the mass,  $C_s$  is the sample’s specific heat capacity and  $dT/dt$  represents the heating rate.

## ❖ Experimental

DSC analysis was carried out only for Ag/Al multilayer thin films. Free standing films were attained by dissolving the samples with the Cu under-layer using a solution of ammonium peroxydisulfate. The films were cleaned using ethanol and placed in Al pans where each DSC sample weighted about 5-10 mg and consisted of about 10-20 foils. The measurements were performed in a power compensated DSC system of Perking Elmer Hyper-DSC 8500 type. The measurements were carried out within the range of 253 to 573 K and using heating rates of 0.33, 1, 1.5 and 2 K.s<sup>-1</sup> with a constant flow of high purity argon gas. The baselines were produced by repeating the measurements in a second up-scan of the reacted material under identical conditions without removing the sample and by subtracting them from the first up-scan. The DSC temperature and the enthalpy of transformation were calibrated for each heating rate using n-decane (C<sub>10</sub>H<sub>22</sub>), indium and zinc as standards.

## 2.3. Microstructural analysis

### 2.3.1. X-ray diffraction (XRD)

Diffraction of an X-ray beam targeted on a material allows to study periodic structures within the material. In the case of crystalline materials, the periodic atomic arrangements induce a scattering of the electromagnetic wave forming a constructive interference when the Bragg’s condition is fulfilled, in which the condition is described as:

$$2d_{hkl} \sin \theta_{hkl} = n\lambda_x \quad (39)$$

where  $d_{hkl}$  is the spacing between diffracting planes,  $\theta_{hkl}$  is the incidence angle of the beam,  $n$  is an integer, and  $\lambda_x$  is the X-ray wavelength. The position and intensity of the diffraction peaks collected on a diffractometer detector are determined by the crystal structure, i.e. representing the distance between parallel planes of atoms (d-spacing). The process is illustrated in Figure 16.

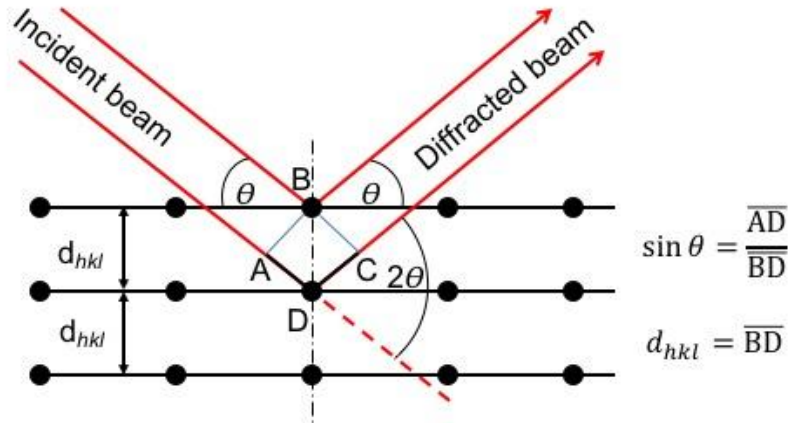


**Figure 16** Illustration for constructive interference of an X-ray beam on a crystalline material with periodic arrangement of atoms.  $\overline{ADC}$  represent the optical path difference.

Depending on the mass absorption coefficient, the density of the material analyzed, and the diffractometer setup implemented, the penetration depth of the beam in the material can vary, which can be a few micrometers up to a several hundred micrometers [80]. Measuring d-spacings within a relatively large irradiated volume provides rich statistical data on the crystal structure of the material. XRD is a very powerful technique for structural analysis of bulk materials, powders, and polycrystalline thin films, where phase identification, crystal orientation relationships, texture, as well stresses can be precisely characterized.

### ❖ Experimental

For the XRD analysis carried out here the Bragg-Brentano geometry was used in a  $\theta$ - $\theta$  goniometer. In this configuration, the sample is kept stable while both the X-ray source and the detector rotate with respect to the goniometer axis, both having the same angle with respect to the sample surface. An illustration of the setup is shown in Figure 17. In all the measurements, an offset angle of  $3^\circ$  was used to eliminate the signal from the strongly textured Si substrate (off-axis measurement).

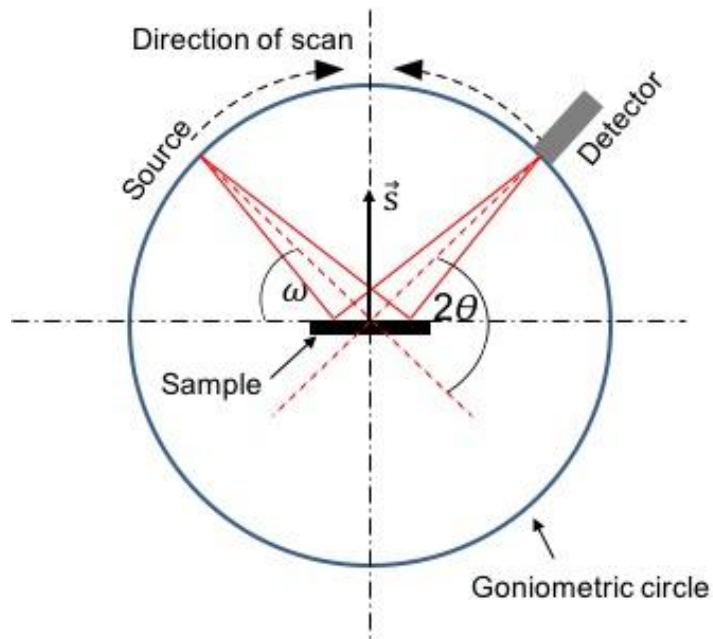


**Figure 17** Bragg-Brentano configuration.  $\omega$  represents the incident angle,  $\vec{s}$  represents the diffraction vector perpendicular to the sample surface, and  $2\theta$  is the diffraction angle.

XRD analyses were performed on Ag/Al films in as-deposited and annealed conditions to identify the phases as well as to study texture effects. The measurements were carried out at room temperature with Cu-K $\alpha$  radiation ( $\lambda_x=0.1542$  nm) at 40 kV and 40 mA using PANalytical X'Pert Pro MPD with a diffraction angle ( $2\theta$ ) range of 30 to 90 degrees and slit optics.

### 2.3.2. Scanning Electron Microscopy/Focused Ion Beam (SEM/FIB)

Scanning electron microscope (SEM) uses a focused beam of electrons to image a sample surface which offers a spatial resolution down to (typically) few nanometers (2-4 nm). The electron beam interacts with an electrically conducting sample producing secondary electrons, auger electrons, backscattered electrons, and X-rays [1]. Secondary and backscattered electrons are mainly used for imaging the sample. SEM imaging raster scans the sample surface using one of both modes to provide images that display the topography and the Z-contrast of the sample in high resolution. Different contrast in SEM images can provide qualitative information on the composition since the interaction volume of the electrons varies according to the mean atomic number of the sample or specific phases appearing at the sample surface. A focused ion beam microscope (FIB) operates in a similar way to SEM but uses gallium ions (typically Ga is used) instead of electrons, which is generated in a liquid metal ion source (typically liquid metal ion source is used). The fine beam raster scans the sample surface releasing secondary electrons for imaging, but more importantly it sputters

away the material being observed which can be applied to local regions of interest. This localized milling capability offers a range of possibilities for characterizing the material and for cutting out segments from the sample for further characterizations. In modern equipment both SEM and FIB are combined in a dual beam system, as illustrated in Figure 18.

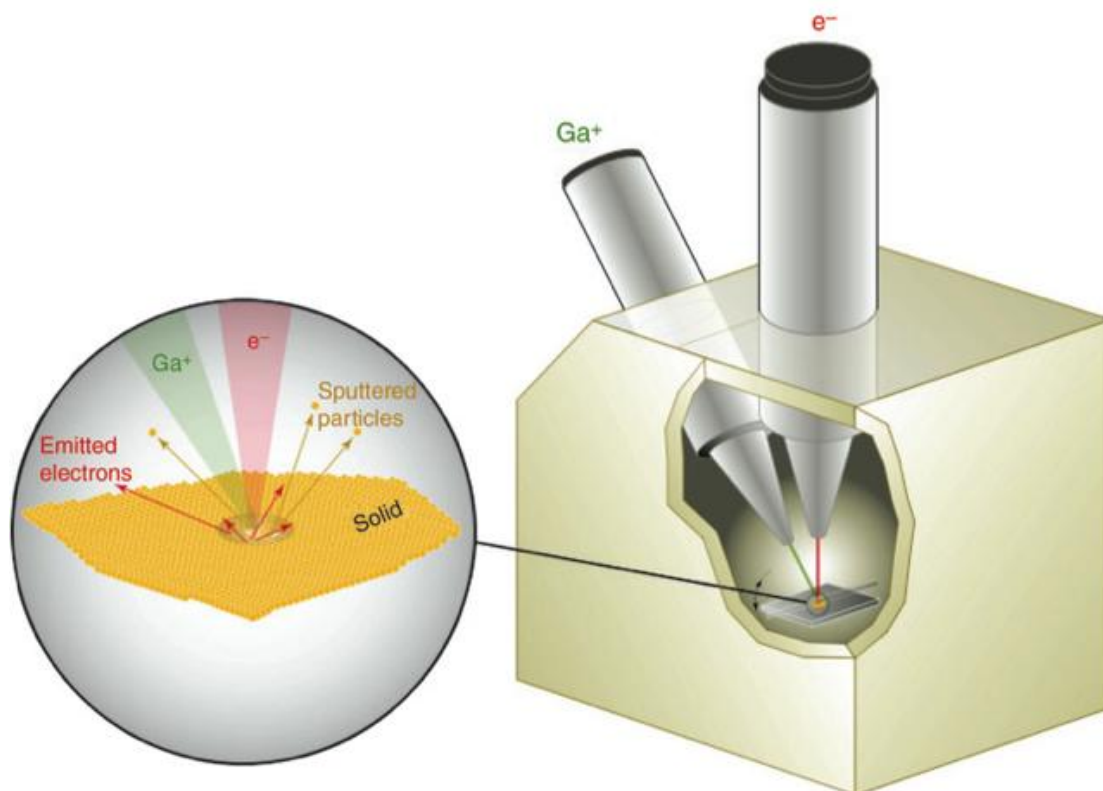


**Figure 18** Schematic illustration for a dual beam FIB/SEM instrument. The magnified image shows the electrons and ions interacting with the sample surface. Taken from Ref. [81].

### ❖ Experimental

FIB/SEM dual beam instrument was used to prepare lamella samples for transmission electron microscope (TEM), transmission kichuchi diffraction (TKD), as well as for APT samples preparation. Samples for TKD and TEM are identical in shape, whereas for APT sample preparation a needle shape tip prepared from the thin film samples. The early stages of these sample preparations are similar, in the sense that they require extracting out a region of interest from the main sample using ion-milling and a micromanipulator to remove and transport a small lamella/wedge inside the instrument chamber. Prior to the milling process, a platinum thin protective layer is deposited on top the samples using electron beam deposition in the microscope (1  $\mu\text{m}$  thick for the lamella sample preparation and 200 nm thick for APT sample preparation). For TEM/TKD sample preparation, an

automatic-running wizard is used to cut out a lamella with a thickness of about 1  $\mu\text{m}$ . The lamella has a rectangular shape, with a width of 12-20  $\mu\text{m}$  and depth of about 8  $\mu\text{m}$ . The lamella is then attached to the micromanipulator, transported, and then attached to a Cu grid which serves as TEM sample carrier. The attachment is done using platinum FIB deposition. The lamella is then thinned down using  $\text{Ga}^+$  ions till the required electron-transparency thickness is reached (below 100 nm). For APT sample preparation, a wedge shape with a triangular cross section is cut out from thin film samples, referred to as the liftout technique [82]. The wedge has a width of about 20  $\mu\text{m}$  and depth of about 4  $\mu\text{m}$ , which can produce 6-8 tips for APT. The wedge is attached to the micromanipulator and transported to a Si microtip array. About 2-3  $\mu\text{m}$  thick segments are sliced off from the wedge using the ion beam and attached to the Si posts of the microtip array via platinum FIB deposition. The sample pieces attached on the Si posts are then sharpened into needle-shape tips using the ion beam. An acceleration voltage of 2 kV is used for the ion-beam in the final steps of tip shaping to reduce Ga induced damage. The APT tips have a sharp geometry with an end-radius below 50 nm. An overview of the sample preparations is shown in Figure 19. All the preparation for APT tips were done having the multilayers perpendicular to the main axis of the tips. All sample preparations were carried out in an FEI Helios NanoLab 600 DualBeam instrument equipped with an OmniProbe 100 micromanipulator.

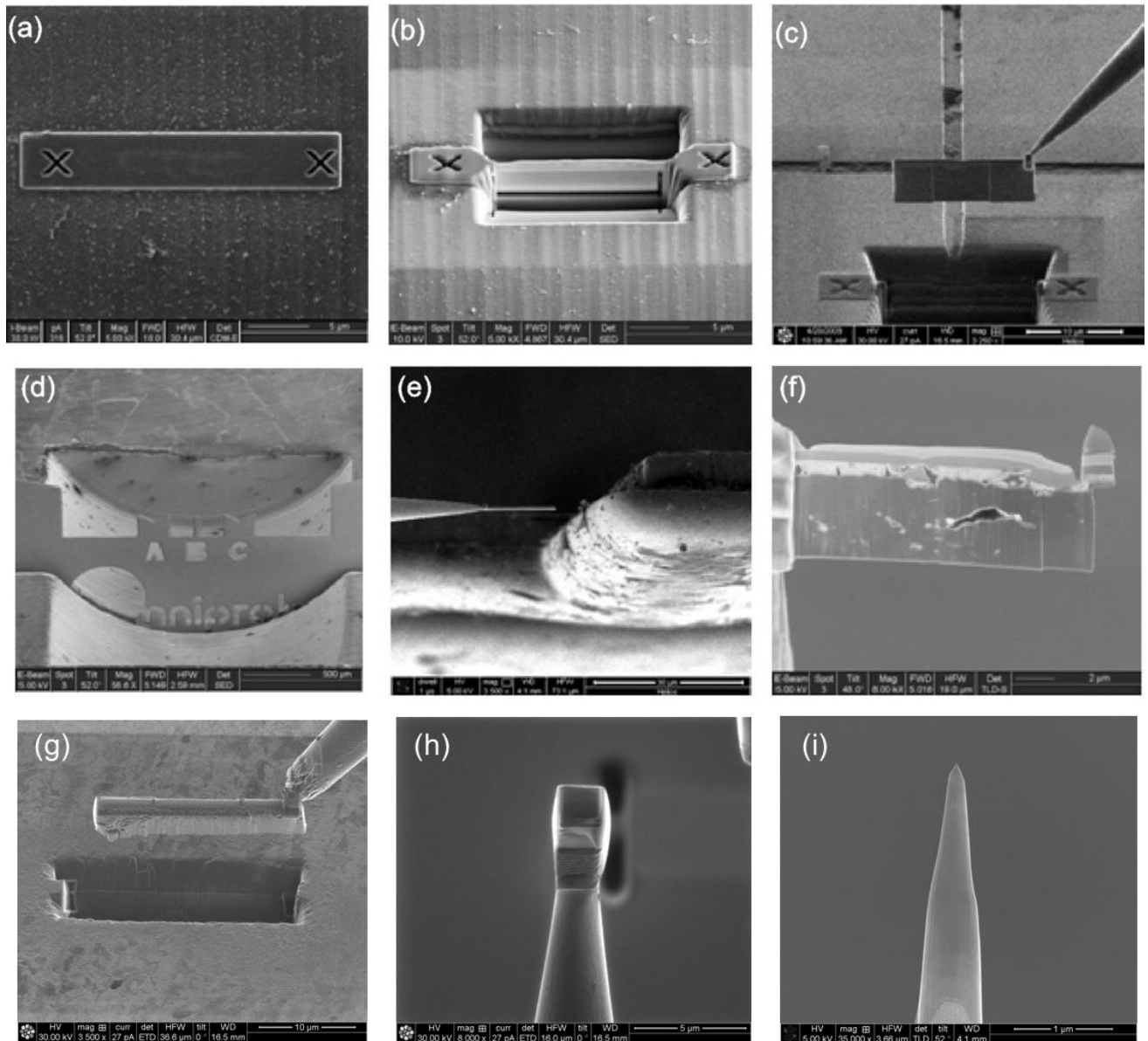


**Figure 19** Stages of sample preparations using SEM/FIB. (a)-(f) shows TEM sample preparation stages. (a) Pt deposited on the sample surface, (b) lamella prepared using auto-wizard, (c)-(e) transfer of the wedge to the Cu grid by the micromanipulator, and (f) shows the final TEM lamella after thinning. (g)-(i) shows APT sample preparation stages. (g) extraction of the wedge by the micromanipulator, (h) a segment of the wedge is attached to a Si post and cut from the wedge, and (i) shows the sample after thinning it to a needle shape.

### 2.3.3. Transmission electron microscopy (TEM)

Transmission electron microscopy (TEM) offers a higher spatial resolution compared to SEM, which depending on the instrument can reach down to the atomic level. As the name implies, the structural imaging is obtained by detecting highly accelerated electrons effectively transmitted through a

specimen having very low thickness ( $<100$  nm). The transmitted electrons are projected onto post-specimen lens or a detector. Elastic scattering of the electrons provides diffraction patterns that reveal localized structural information for crystalline samples, whereas inelastic scattering provides high resolution images of the sample. Details regarding TEM imaging and analytical methods can be found elsewhere [83].

#### ❖ **Experimental**

Ag/Al and Ru/Al TEM samples were prepared using FIB. Two TEM instruments were used, a JEOL 2010 equipped with LaB<sub>6</sub> filament as electron source with acceleration voltage of 200 kV, and a FEI Tecnai G2 F20 UT equipped with a field emission gun with acceleration voltage of 200 kV.

#### **2.3.4. Scanning transmission electron microscopy (STEM)**

Scanning transmission electron microscopy is a type of TEM where the beam of electrons is focused on a fine spot on the sample and raster scans across its surface. This technique offers high resolution imaging and is complementary to TEM.

#### ❖ **Experimental**

Ag/Al and Ru/Al TEM samples were prepared using FIB and analyzed in the dual beam FIB/SEM instrument mentioned earlier in section 2.3.2. The instrument is equipped with a multisegment STEM detector which allows bright-field (BF), dark field (DF), and high-angle annular dark field (HAADF) imaging. The STEM analysis in this instrument is carried out at relatively low acceleration voltage of 30 kV.

#### **2.3.5. Transmission Kikuchi diffraction (TKD)**

Electron back-scattered diffraction (EBSD) is a common technique used to carry out crystallographic analysis on crystalline samples using a SEM instrument equipped with an EBSD detector. Inelastically scattered electrons from the sample that satisfy the Bragg's condition (see section 2.3.1) form paired high-angle cones of electrons (referred to as Kossel cones). Imaging these Kossel cones on a phosphor screen of an EBSD detector displays Kikuchi bands that correspond to each diffraction

plane. Thus, from the Kikuchi bands a crystallographic information from the sample can be acquired. Transmission Kikuchi diffraction (TKD), also sometimes referred to as transmission EBSD (t-EBSD), is considered an extension to the conventional EBSD method, since it offers a higher spatial resolution (down to a few nanometers) for Kikuchi diffraction analysis using transmitted forward scattered electrons from a TEM sample [84]. In this mode, the crystallographic information of the diffraction patterns is derived from the last 10-20 nm of the thin TEM foil sample before the electrons totally transmit the sample [85]. The improved resolution is mainly due to the reduction of diffuse scattering, which is typical for bulk samples, in other words, for TEM foils a large part of the interaction volume is cut away [86]. This thus allows the analysis of nanoparticles and grains of a few tens of nanometers in size, using the same SEM instrument. Therefore, TKD provides a very helpful tool for structural analysis of thin films with fine grain structures. An illustration for the configuration of TKD in an SEM instrument is shown in Figure 20.

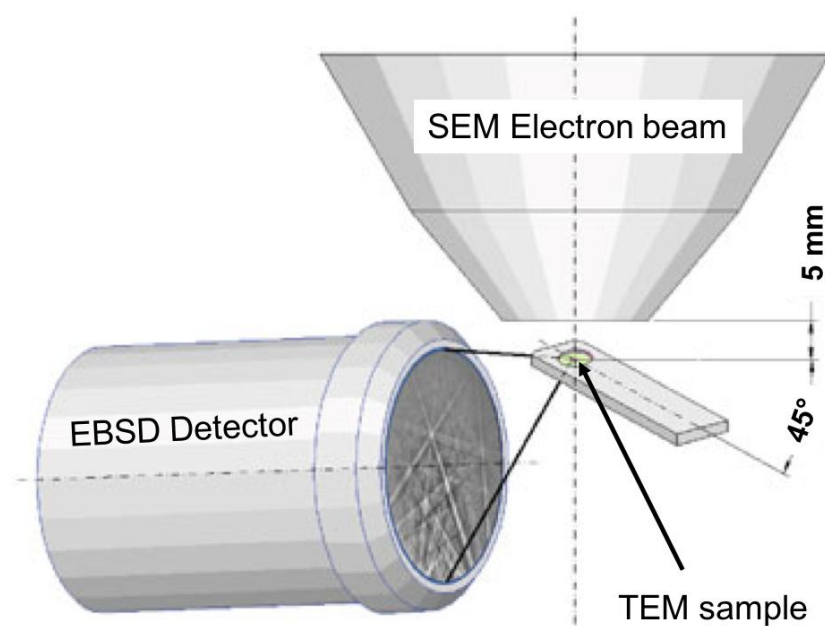


**Figure 20** Configuration for TKD in a SEM instrument. Taken from Ref. [84].

### ❖ Experimental

Ag/Al TEM samples were prepared using FIB and analyzed in the dual beam FIB/SEM instrument mentioned earlier in section 2.3.2, which is equipped with an EBSD detector (EDAX, Hikari). The TEM sample was positioned at an angle of 45 degrees from the horizontal plane normal to the main axis of the electron beam and using an acceleration voltage of 30 kV. The Kikuchi bands are indexed according to their miller indices and analyzed using the OIM 5.3 data collection software by EDAX.

For the scan analyses, one phase file was used for Ag and Al due to their same structure and similar lattice constant. Grain size (intercept length) and grain misorientation analyses were carried out on the thin films. Two clean up filters were used in the OIM data analysis software, namely; the confidence index filter ( $CI < 0.09$ ) and standardization filter (see Ref. [87] for filters details).

### 2.3.6. Atom probe tomography (APT)

APT is currently considered the most powerful analytical technique to characterize materials on the atomic scale in three dimensions. The technique is based on the field evaporation of surface atoms from a needle shaped tip with a sharp end-radius. Field evaporation is triggered via a standing electric voltage (DC) applied on the tip and superimposed by ultra-short pulses of either voltage or laser. Once surface atoms become ionized by the field they get accelerated and projected away from the tip towards a position sensitive detector. Two types of information are collected for each field evaporated atom reaching the detector, namely, the time of flight (TOF) and the two-dimensional coordinates of the hit on the detector, respectively. The TOF information is measured from the time a pulse is applied on the tip to the time an atom impacts the detector, which provides information on the elemental specie of the atom, while the coordinates of hits on the detector are used to build a virtual point cloud reconstruction representing the evaporated volume from the tip. It is generally understood that the field applied reduces an energy barrier for the surface atoms to become ionized, which using the simplest Müller's model [67] for field evaporation, named the *image hump* theory, the energy to remove an adatom from the surface and ionize it  $n$  times can be expressed as:

$$Q_0 = \Lambda_s + \sum_1^n I_i - n\phi_e \quad (40)$$

where  $\Lambda_s$  is the sublimation energy,  $I_i$  is the ionization energy, and  $\phi_e$  is the work function of the tip material. Based on this,  $Q_0$  can be calculated for various elements showing different field evaporation values for each element.

APT is optimal for carrying out chemical analysis at the sub-nm resolution in three dimensions, where the depth spatial resolution is less than 0.1 nm and a lateral resolution is of about 0.3 nm [88]. The detection efficiency is usually limited which impedes the technique to be suitable for full crystallographic characterization of crystalline materials, with some exception in a few materials. A simple schematic illustration of an APT setup is shown in Figure 21.

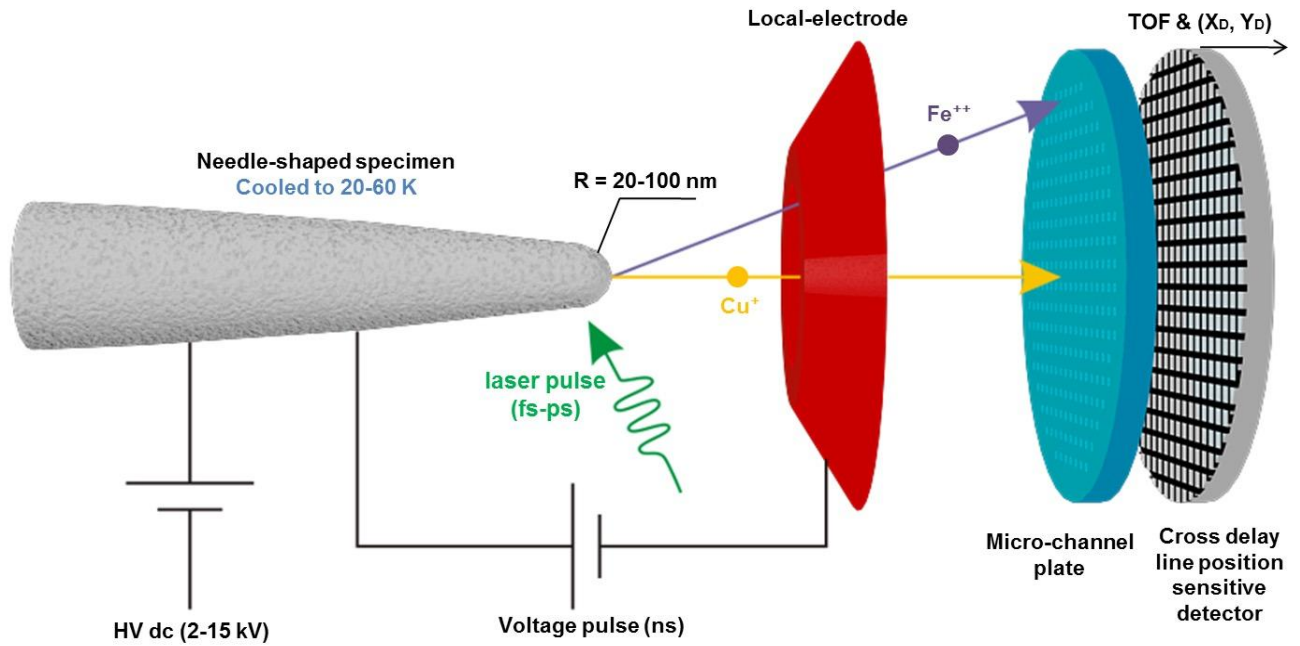


**Figure 21** Schematic illustration for a modern local electrode atom probe (LEAP) system.

## ❖ Experimental

APT samples of Ag/Al and Ru/Al were prepared using FIB (described in section 2.3.2) and measured in a LEAP 3000X HR CAMECA™ system. The measurements were carried out in voltage pulsing with a repetition rate of 200 kHz, 20-25% pulse fraction, a base temperature of 70-80 K and an evaporation rate of 3-5 atoms per 1000 pulses. The data were reconstructed and analyzed using the software IVAS 3.6.8 provided by CAMECA™. Proximity histograms (proxigrams) were used in some cases for analysis of interfaces where the local atomic neighborhood normal to a chosen iso-surface is calculated and plotted in one dimension [67]. Spatial distribution map (SDM) algorithm was used to precisely measure the lattice spacing within certain datasets, which is available in the IVAS software (details on SDM can be found in Ref. [89]).

## 3. Results

### 3.1. Ag/Al system

#### 3.1.1. As-deposited films

##### 3.1.1.1. Period investigation

Ag/Al multilayer thin films with Ag-rich composition (Ag:Al = 2:1) were investigated for the effects of the period thickness on the microstructure and interdiffusion. STEM and XRD results are presented here, followed by APT results in section 3.1.1.3. Figure 22 shows STEM images of the 10 nm and 200 nm periods deposited with 100 W sputtering power and 0.003 mbar argon pressure. In BF-STEM the Ag layers are in dark grey and Al layers are in light grey. Epitaxial growth can be clearly observed for all periods, and the shifts in the layer morphologies can be well correlated with each column of grains. The Ag and Al grains show columnar growth with most GBs extending vertically to the layers. The homologous temperature,  $T_h$ , for Ag is estimated at 0.24 and 0.26 for the low and high sputtering power, respectively, whereas for Al is estimated at 0.32 and 0.35 for the low and high sputtering power, respectively (calculated from Eq.36). Difference in the homologous temperatures for both elements is considered not to be significant. Grooves in the multilayers at the GB intersections were sometimes observed in the STEM images, which were more clearly seen in large periods. Nanotwins were clearly detected in the Ag grains (see Figure 22). The formation of twin boundaries in sputter deposited Ag is a common feature which occurs due to the low stacking fault energy of Ag (22 mJ/m<sup>2</sup>) [90]. Al on the other hand has high stacking fault energy (120-165 mJ/m<sup>2</sup>) [90] and does not easily form twin boundaries unless deformed or in nanocrystalline structure [91]. Nanotwins formed here in Al can be mainly induced by Ag layers, due to the coherent interfaces and the epitaxial relationship which allows lattice defects to penetrate between the layers. The penetration of twin boundaries across the layers is displayed more clearly in the TKD analysis in section 3.1.1.2. Such results have also been shown in detail by Bufford et al. for Ag/Al multilayer thin films deposited by magnetron sputtering [92].

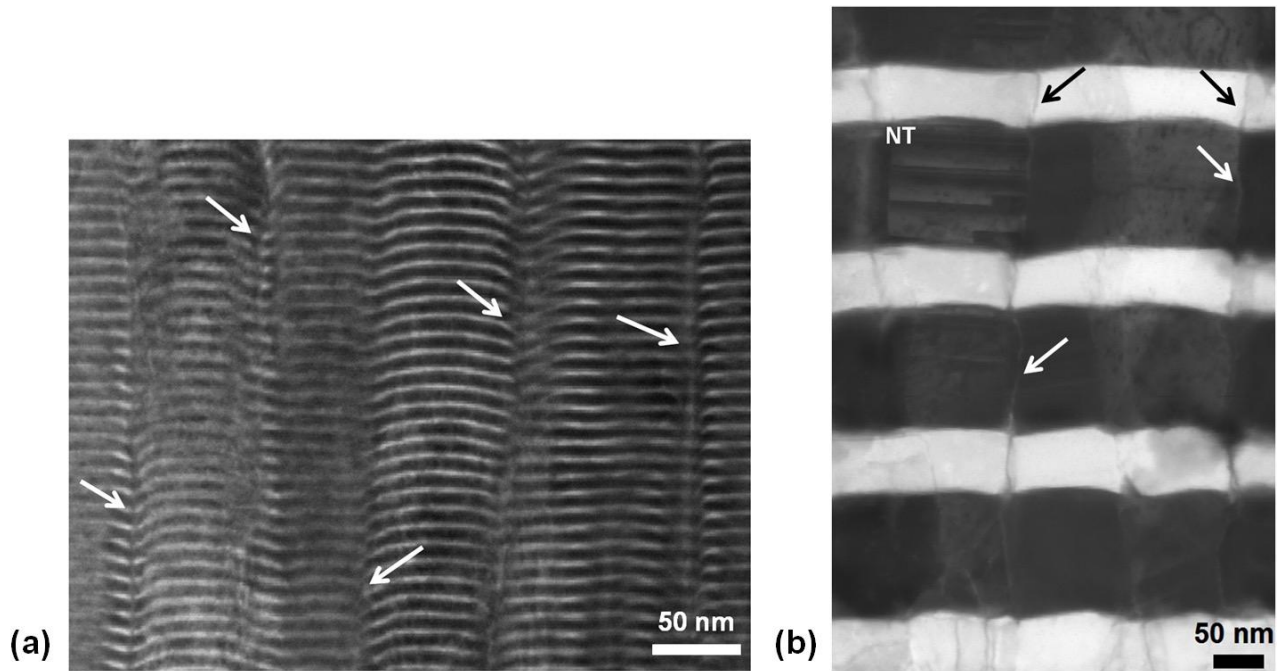


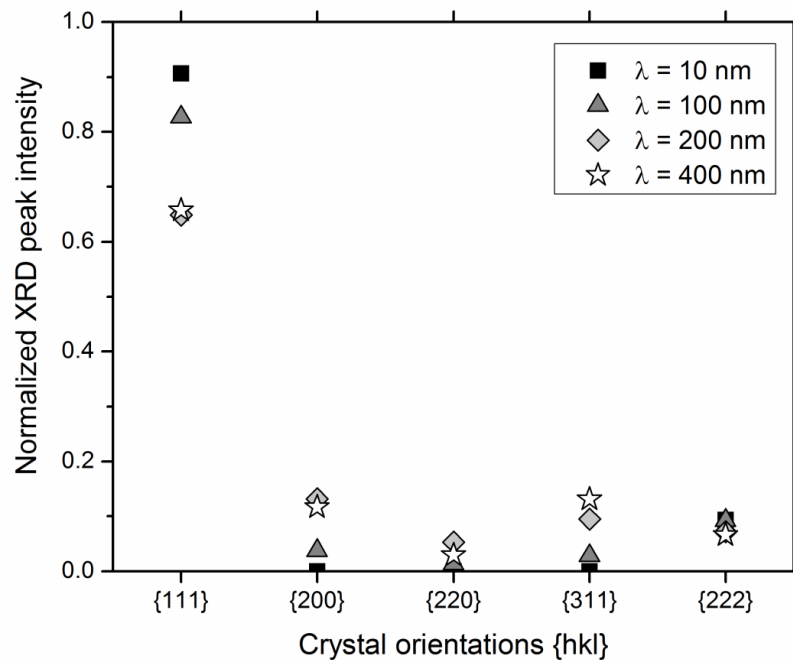
**Figure 22** BF-STEM for Ag/Al multilayer thin film of (a) 10 nm period and (b) 200 nm periods of Ag-rich composition. Vertical GBs are marked with arrows. One Ag grain showing nanotwins is marked by “NT” [93].

XRD measurements were carried out on the different multilayer periods deposited under the same conditions to study the structure of the phases and the changes in the texture. Due to the negligible difference in the lattice constants of Ag and Al, their diffraction peaks in the measurements overlap together. However, as a result of the strong epitaxial growth and nearly identical lattice constants, Ag and Al grains growing on top of each other share the same orientation. Therefore, the summation of the Ag and Al peaks is considered to represent the general texture in the films. The intensity of each diffraction peak is divided by the total intensity for all peaks resulting in the plot shown in Figure 23, representing the normalized XRD peak intensity ratios for the five crystal orientations as a function of the period. Generally, the films show a strong texture along the  $\{111\}$  orientation. Materials with fcc crystal structure synthesized by sputter deposition are well known to have a preferential orientation along the  $\langle 111 \rangle$  fiber texture as it is the lowest energy configuration for the growth of the films [17]. The comparison shows that the multilayers are less textured in thicker periods. Nevertheless, only slight differences are noticed between multilayers of 200 and 400 nm periods. The 10 nm periods have shown the strongest texturing, where an XRD diffraction pattern is shown in Figure 24, displaying only  $\{111\}$  and  $\{222\}$  peaks. It is generally understood that roughness can possibly rise with the individual film layer thickness due to combined effects of surface diffusion, grain growth, and stress, which influences the texture of the films [94]. Therefore, in the case here, slight roughness increase in larger periods is expected to cause the reduced fiber texture in such

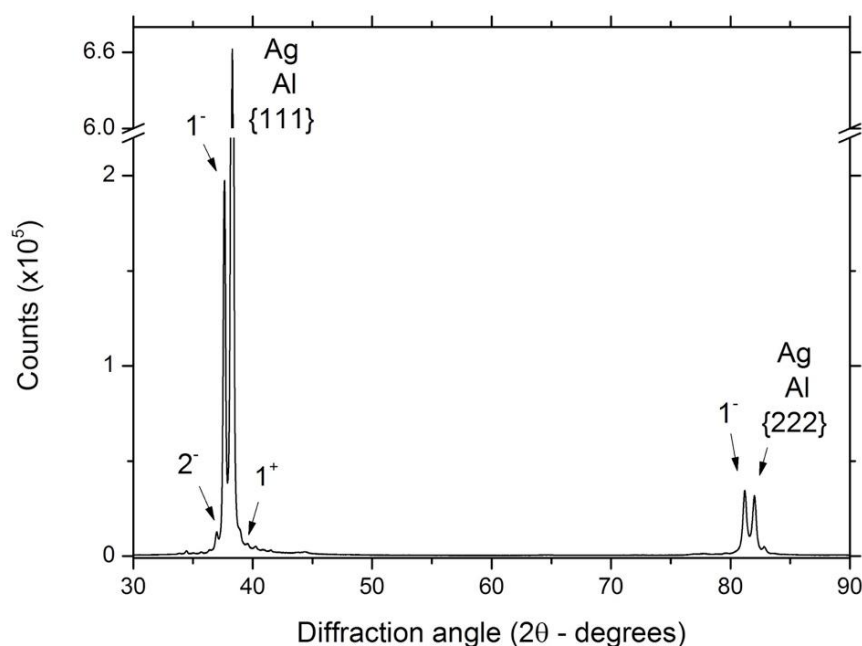
epitaxial films. Similar results were detected for Nb/Al and Ti/Al multilayer thin films, respectively [94]. It is important to mention that no peaks for intermetallic phases were detected in all these periods investigated in here of as-deposited condition. However, a specific feature was detected only for the 10 nm periods by XRD, which is satellite peaks. Satellite reflections in XRD appear due to the formation of a superlattice structure in the films. Since multilayers themselves are a periodicity in the microstructure, they produce satellite peak reflections when the period thickness becomes very low. Superlattice structures are generally ultra-thin multilayers which exhibit long range structural coherence, generally found in epitaxial thin films. The position of a satellite peak is defined by:

$$\frac{2 \sin \theta_{hkl}}{\lambda_x} = \frac{1}{\bar{d}} \pm \frac{n}{\lambda} \quad (41)$$

where  $\theta_{hkl}$  is the incidence angle,  $\lambda_x$  is the x-ray wavelength,  $\bar{d}$  is the average interplanar spacing,  $n$  is the satellite peak order, and  $\lambda$  is the bilayer period thickness of the multilayer [95]. It is important to add here that the interplanar distance measured for the overlapped peak {111} in the four periods was compared. The 100, 200, and 400 nm was measured to be  $2.357 \pm 0.005 \text{ \AA}$ , while the 10 nm period was  $2.349 \pm 0.005 \text{ \AA}$ , which are both extremely close to their bulk values ( $d_{\text{Ag}} \text{ bulk} = 2.359 \text{ \AA}$  and  $d_{\text{Al}} \text{ bulk} = 2.338 \text{ \AA}$ ). Therefore, negligible in-plane stresses can be expected in the thin films.



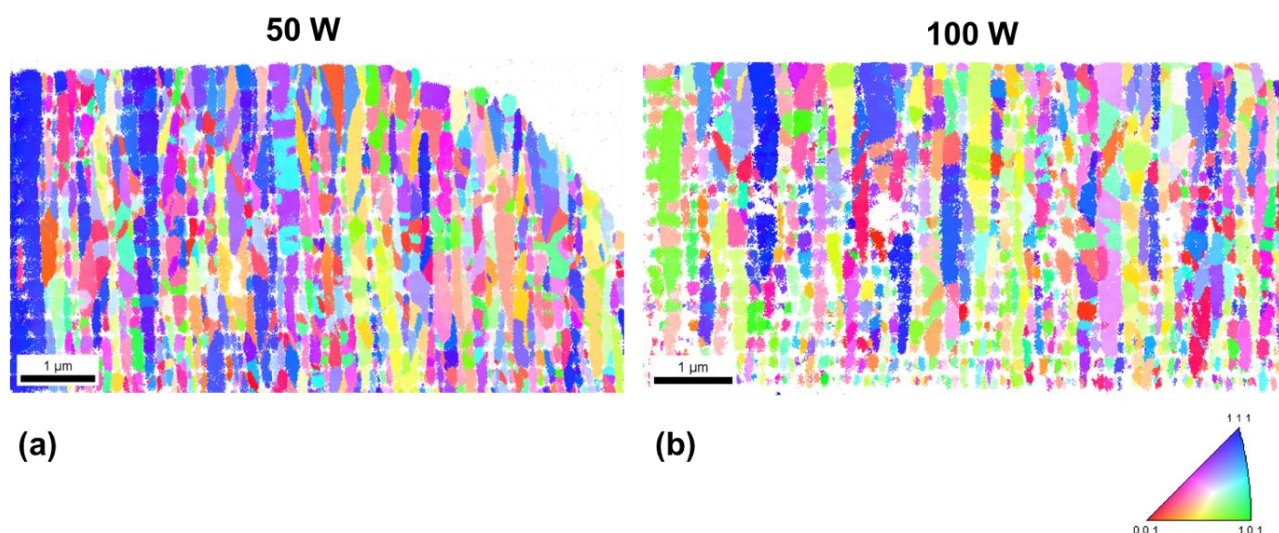
**Figure 23** Normalized XRD peak intensity for the fcc "Ag+Al" peaks as a function of the period thickness synthesized with the same deposition parameters [93].



**Figure 24** XRD measurement for Ag/Al multilayers of 10 nm period (Ag-rich composition). Satellite peaks are marked. The number refers to their order.

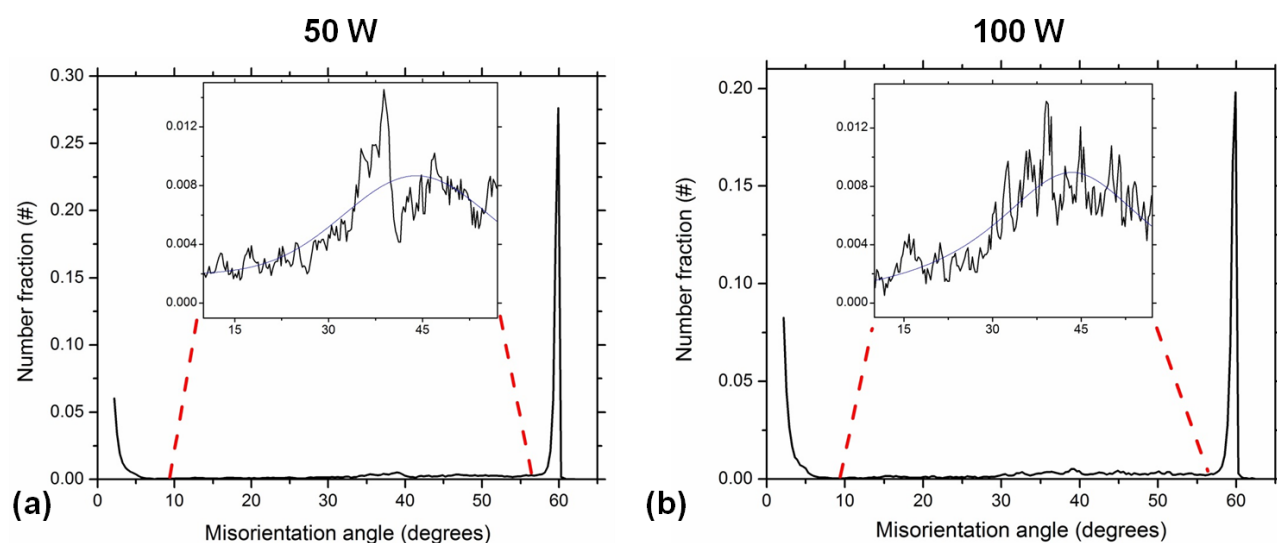
### 3.1.1.2. Sputtering power investigation

The microstructure and interdiffusion effects of the different periods deposited using low and high sputtering power are compared. TKD and XRD results are presented here, followed by APT results in section 3.1.1.3. STEM images of the multilayers of different periods deposited using different sputtering powers did not reveal any noticeable differences, therefore they are not shown here. TKD was used to study the differences in the microstructures using the different sputtering powers for the 200 nm period. Figure 25 shows the inverse pole figure maps for the two multilayers. Different orientations of the crystals can be observed in the TEM films, where the epitaxial relationship of the grains growing on top of each other is very clear. Many columns of grains can be observed having the same orientation together during growth with a several micrometers in length. The distribution of misorientation angles detected for each sample is plotted in Figure 26. Most of the boundaries are found at 60 degrees misorientation, which in fcc structures corresponds to twin boundaries around  $\langle 111 \rangle$ , defined as  $\Sigma 3$  twin boundaries and are coherent in nature [96]. This is followed by low angle boundaries and substructures (related to dislocation pile-ups), which are below 10 degrees misorientation. In between lies random high angle GBs which have shown higher distribution here between 33 to 55 degrees.

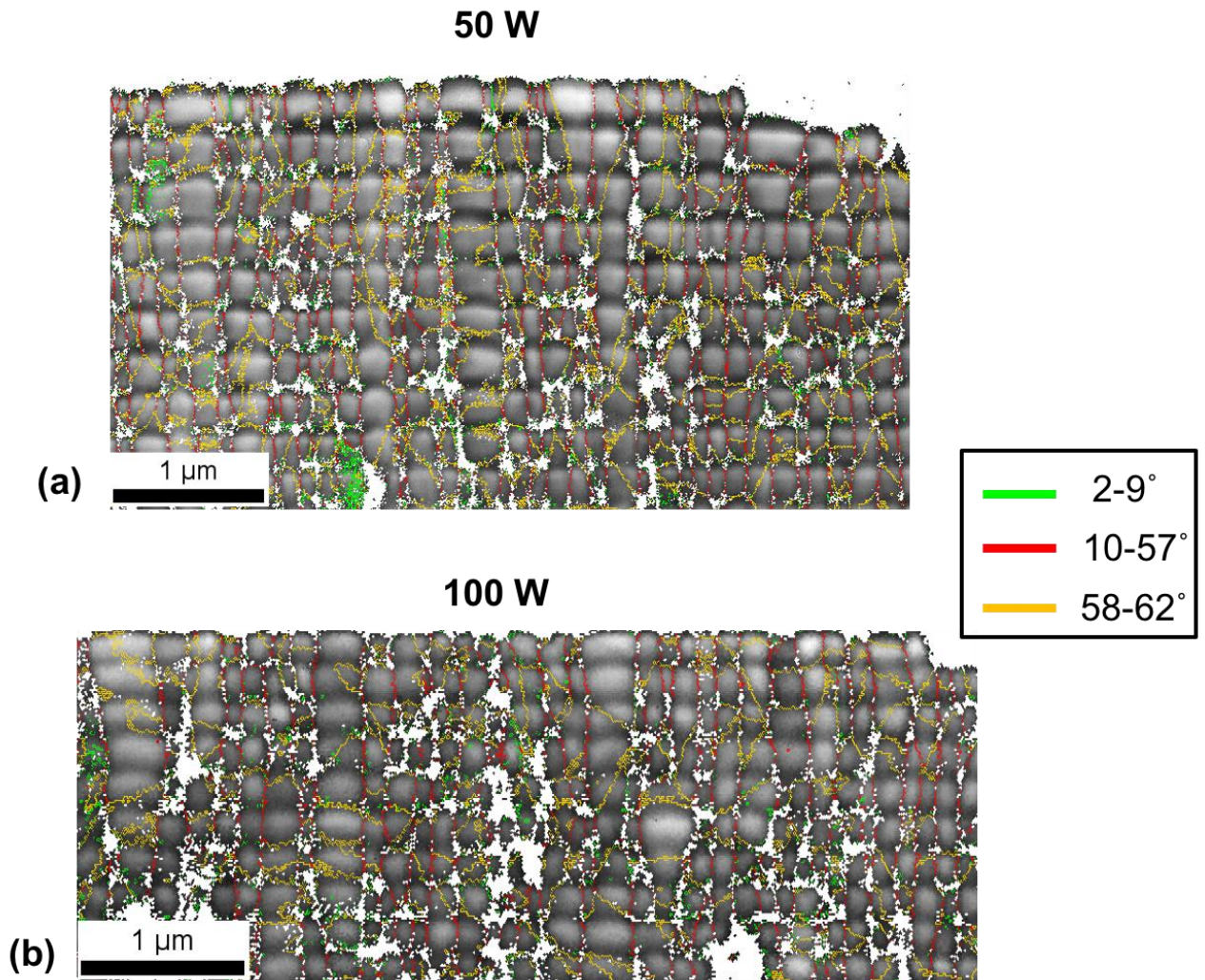


**Figure 25** TKD results showing the inverse pole figure for Ag/Al 200 nm period deposited using (a) low and (b) high sputtering powers. IPF legend shown on the bottom right. The orientations shown are measured in the direction normal to the multilayers (i.e. film growth direction).

The boundaries seen on the TEM foil are categorized into the three segments: low angle boundaries, high angle GBs, and the  $\Sigma 3$  twin boundaries. Using the OIM EBSD software these three boundaries are marked with three different colors and presented in Figure 27. It can be observed that the high angle GBs occupy the vertical boundaries to the multilayers, whereas the twin boundaries mostly exhibit certain angles from the vertical boundaries. Moreover, the penetration of the lattice defects through the multilayers becomes very clear.

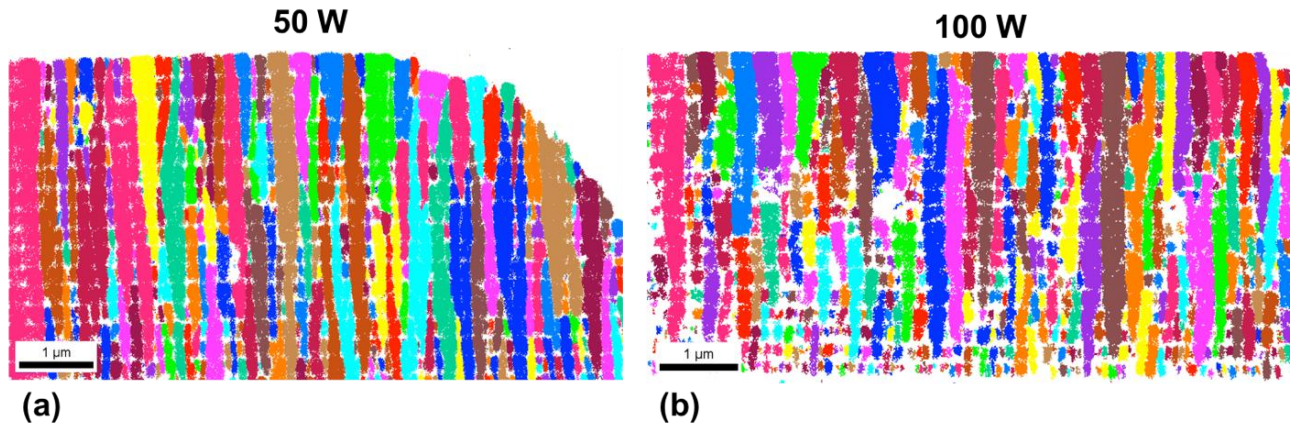


**Figure 26** Misorientation angle plots for the TKD analysis of the Ag/Al 200 nm period deposited using (a) low and (b) high sputtering powers. The inset shows a clearer distribution from 10-55 degrees. The blue lines are an average fitting to highlight the distribution.



**Figure 27** TKD analysis of the Ag/Al 200 nm period deposited using (a) low and (b) high sputtering powers. The three different boundaries are shown in three different colors as defined in the legend.

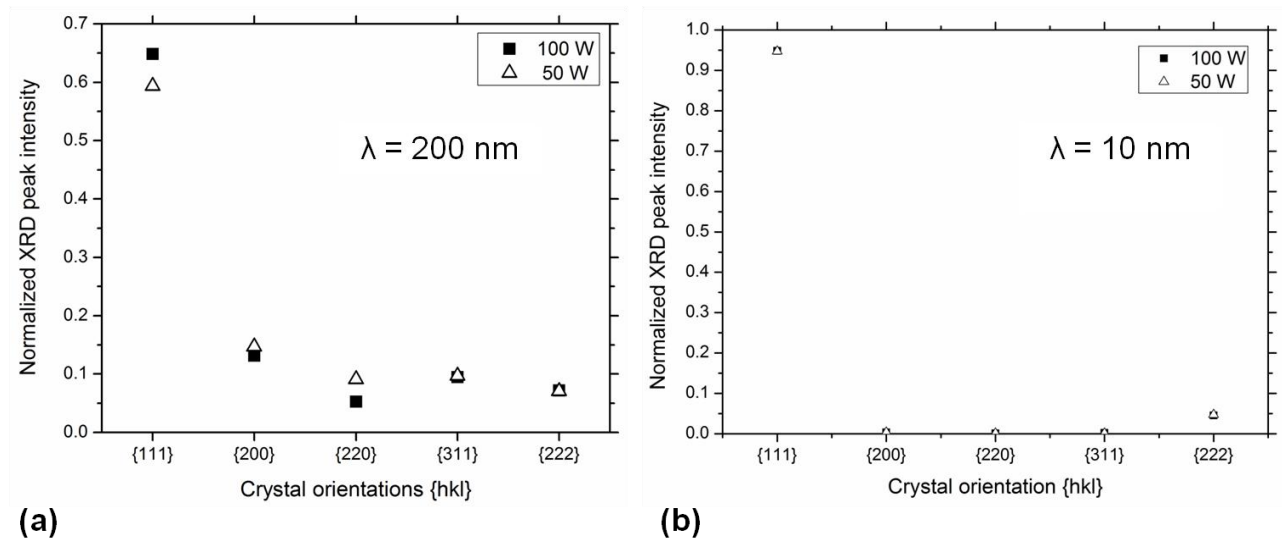
The fraction of twin boundaries in both samples was calculated to be around 50%, whereas the fraction of the high angle GBs was about 30% and low angle boundaries (including substructures) was almost 20%, respectively. Twin boundaries in these films are therefore the highest amount of crystalline boundaries in the structure. It can be therefore understood that many of the grain orientations shown in Figure 25 are due to the twin crystals in the microstructure. Therefore, using a unique color for every grain in the TEM sample (unique grain color) and subtracting out the twin boundaries, the two samples can be represented as shown in Figure 28. The columns of grains growing from bottom to top is more strongly displayed in this image. The lateral dimensions of the grains (intercept length) are measured for both sample and averaged. The average intercept length for the films deposited using 50 W was  $42 \pm 20$  nm and using 100 W was  $50 \pm 25$  nm, respectively.



**Figure 28** TKD analysis of the Ag/Al 200 nm period deposited using (a) low and (b) high sputtering powers. Unique color grain is used to display the columns of grains in the multilayer thin films while subtracting out the twin boundaries.

So far both samples have shown very similar structural properties using TKD analysis, however the multilayers deposited using higher sputtering power exhibit marginally wider grains. This can be expected due to the higher substrate temperatures during film growth that allows more surface diffusion and lateral growth of the islands during deposition. Such analysis is not possible to be carried out for the 10 nm period since the grains are too small for the resolution of TKD. It can be however expected that the sputtering power would induce similar changes in the average lateral dimensions of the grains as seen in the 200 nm period.

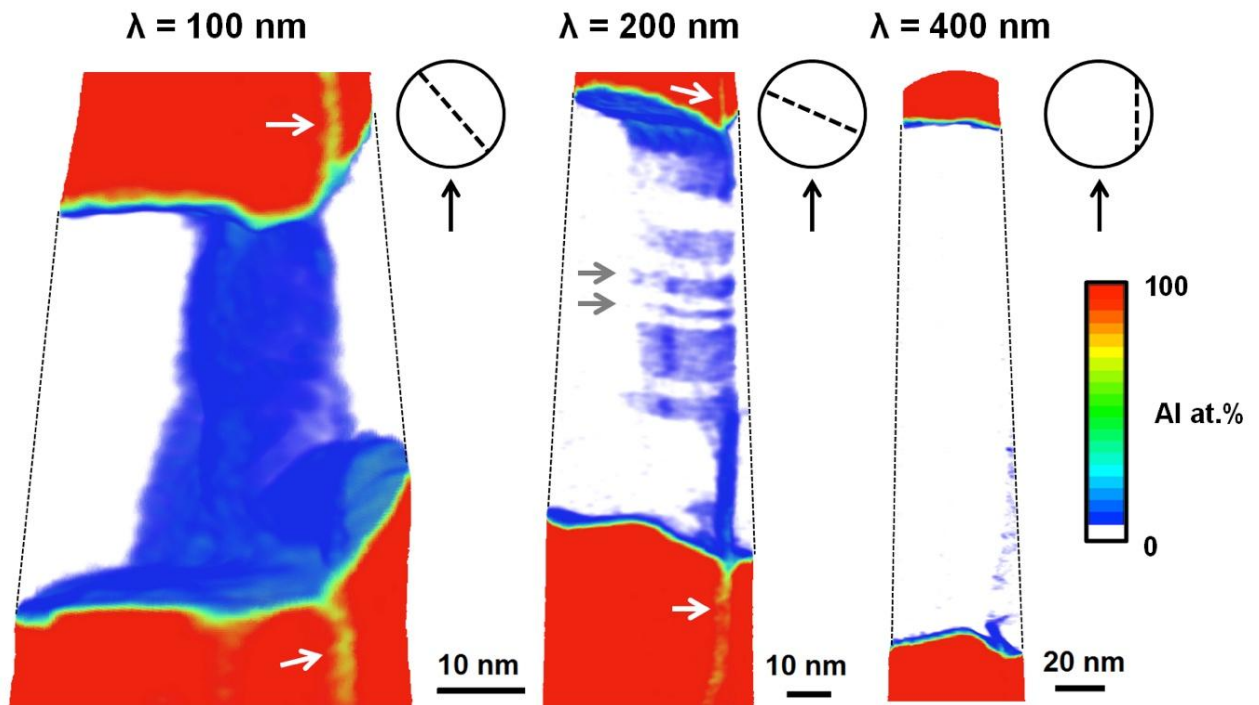
XRD measurements were carried out on the multilayer thin films deposited using the two different sputtering powers to study the influence on the film texture. Two periods were chosen for this investigation, the 10 nm and the 200 nm periods in both conditions, respectively. Figure 29 shows the normalized XRD peak intensity ratios for the two periods. A slight change in the film texture can be observed for the 200 nm period, while the 10 nm period have shown almost identical texture using both sputtering powers. The increased surface mobility at elevated substrate temperatures using high sputtering power can be understood to allow more atom movements on the surface and higher condensation at the lowest energy configuration, which is along the  $\langle 111 \rangle$  direction here. However, this effect is more visible for the 200 nm compared to the 10 nm period in the XRD measurements.



**Figure 29** Normalized XRD peak intensity for the fcc "Ag+Al" peaks for the Ag/Al multilayer thin films of (a) 200 nm periods and (b) 10 nm periods, synthesized using high and low sputtering powers, respectively [93].

### 3.1.1.3. APT analyses

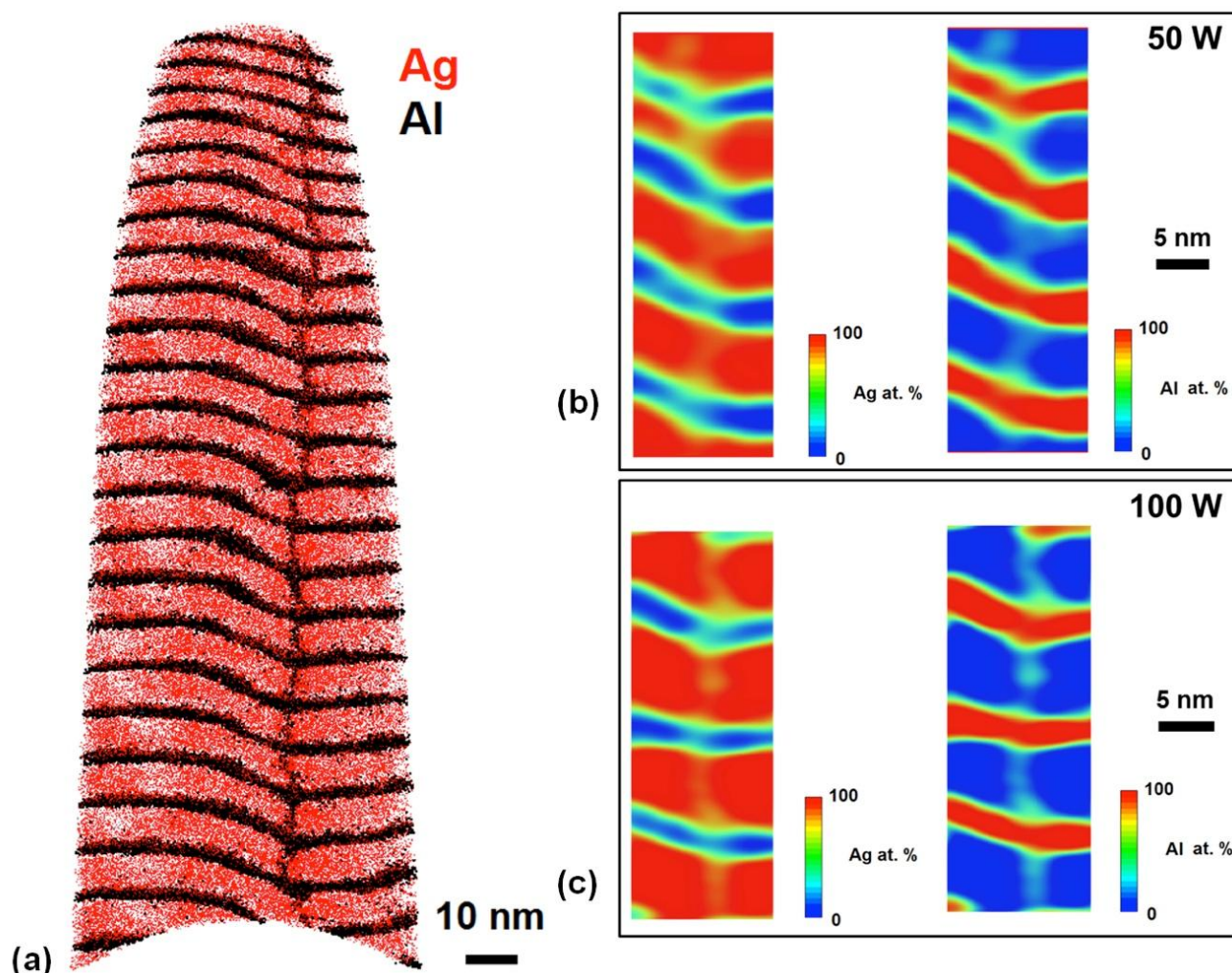
The different periods characterized in the previous two sections are further investigated using APT in order to study the influence of the period thickness and the sputtering power on the interdiffusion and concentration gradients at the phase boundaries. Figure 30 shows APT analyses for the multilayers of 100, 200, and 400 nm periods deposited with the same conditions using high sputtering power. In these analyses, the extent of Al diffusion along the Ag GBs is compared. The images represent 3D concentration maps of the Al distribution (Ag is transparent) where a vertical GB is located within each of the three reconstructions. The film with the period of 100 nm shows the highest extent of GB diffusion, with Al distributed along the entire GB plane in the Ag layer. The multilayer with 200 nm period shows Al diffusion to a lesser extent in the Ag GBs. Segregation along GB dislocations in the Ag layer can be clearly observed. In the film with a period of 400 nm GB diffusion is very limited. Al is detected with concentrations up to  $\sim 10$  at. % in the first approximately 20 nm of the GB on the Ag layer. At further distances from the Al bottom layer Al is detected only in small traces along the GB plane. It is important to add that Ag diffusion in the Al GBs is only detected for the films of 100 and 200 nm periods which is visible in Figure 30 as low Al concentrations at the GB plane in the Al layer.



**Figure 30** APT analyses for Ag/Al multilayer thin films of 100, 200, and 400 nm periods deposited using high sputtering power. GB diffusion of Al in the Ag layer is visualized using 3D concentration maps of Al concentration (Ag is transparent). The small dotted lines mark the borders of the reconstructions. The drawings on the top right of each reconstruction represent the position of the vertical GB plane along the main axes of the tips, and the black arrows mark the direction of view. Grey arrows mark GB dislocations, and white arrows mark Ag diffusion in the Al GBs [93].

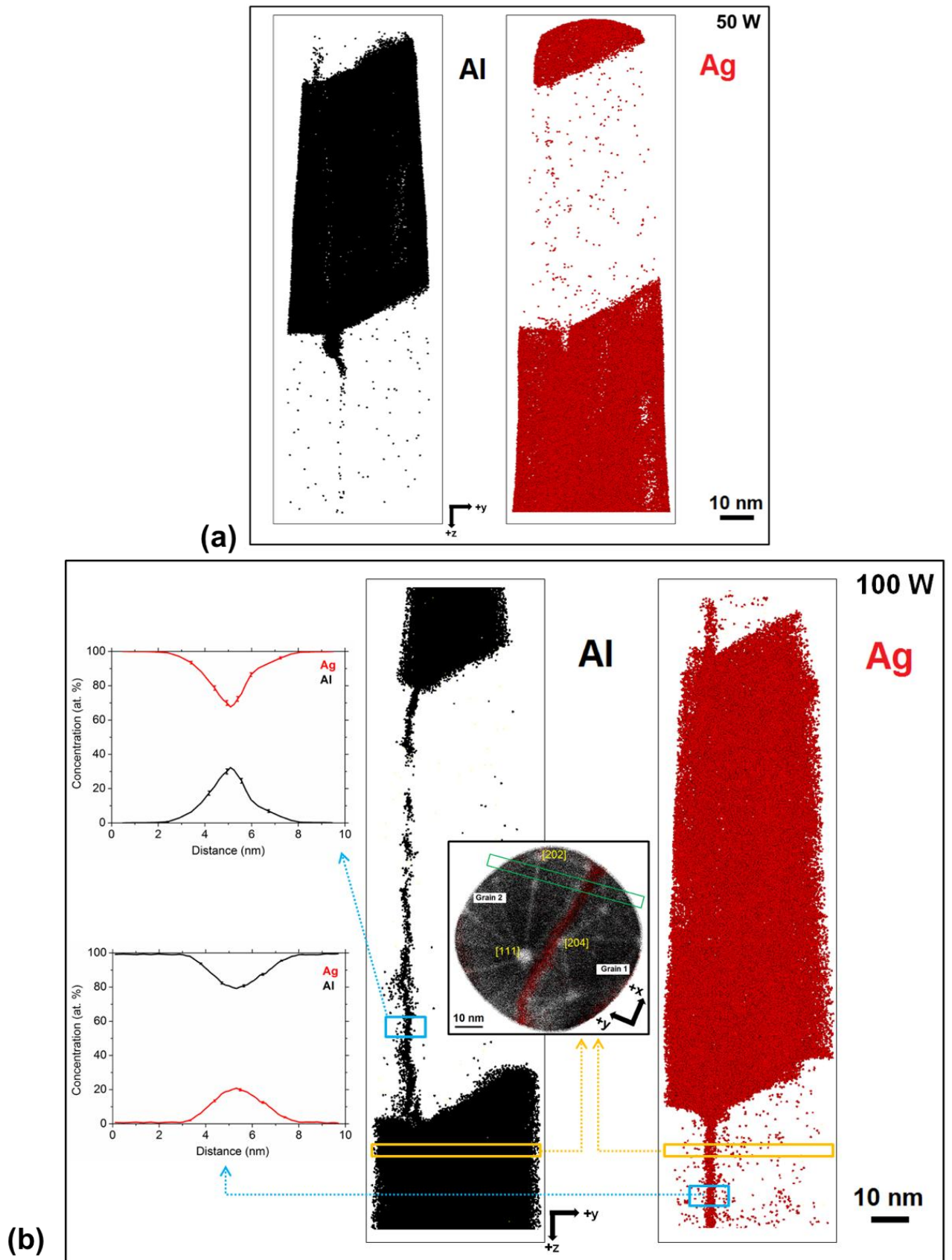
To compare the magnitude of interdiffusion as a function of sputtering power, only data for films of 10 and 200 nm periods are presented. The interdiffusion along the GBs and the layer interfaces (interfacial mixing) are analyzed separately. The two different sputtering powers reveal a significant effect on the GB diffusion in the 200 nm period compared to the 10 nm period. Figure 31(a) shows a 12 nm tomographic slice along a reconstruction from a multilayer of 10 nm period deposited with high sputtering power. Ag and Al atoms are presented, and a vertical GB displays strong interdiffusion. In Figure 31(b) and (c) Al diffusion in Ag GBs and Ag diffusion in Al GBs is shown to be active for both sputtering conditions. In contrast, for the multilayer of 200 nm periods, using low sputtering power only short GB diffusion lengths ( $\sim 10$  nm) are detected for Al in Ag GBs, as shown in Figure 32(a). For high sputtering power, both Al and Ag diffuse in the Ag and Al GBs, respectively, with diffusion lengths almost equal to the individual layer thicknesses. The 200 nm period, therefore, display significant GB diffusion and almost no lattice diffusion (leakage inside the grains), reflecting type C kinetics. This can be clearly observed in Figure 32(b) and is also seen in

Figure 30 in the image of the 200 nm period. The Al concentration in the Ag GBs reaches up to ~30 at. %, while Ag in the Al GBs reaches ~20 at. % as seen in Figure 32(b).



**Figure 31** APT analyses for Ag/Al multilayer thin films of 10 nm period. (a) 12 nm thick tomographic slice along a reconstruction from a sample deposited using high sputtering power. Ag and Al atoms are presented, and a vertical GB displays strong interdiffusion. (b) and (c) present local analyses from regions with a vertical GB from films deposited with low and high sputtering power, respectively. The data is presented using 2D concentration maps for Al and Ag separately [93].

Regarding the interfacial mixing, the Ag on Al and Al on Ag interfaces are analyzed separately. Furthermore, to avoid interfacial roughness inducing artifacts in the concentration gradients using conventional 1D concentration profile measurements, proxigrams are used instead, since they offer higher precision for concentration profiling across interfaces with irregular morphologies. Concentrations across eight interfaces are calculated, averaged, and plotted for each condition, as shown in Figure 33.



**Figure 32** APT reconstructions for Ag/Al multilayer thin films of 200 nm period sputtered with low and high sputtering power. Al and Ag atoms are shown separately from 8 nm thick tomographic slices in the  $x$ -axis direction of the reconstruction. A vertical GB is located in both reconstructions.

(a) At 50 W, very limited GB diffusion of Al in Ag GB and no Ag in Al GBs are detected, respectively. (b) At 100 W, Al is detected along Ag GBs with diffusion lengths as large as the Ag individual layer, likewise for Ag diffusion in Al GBs. Concentration profiles across the Al and Ag GBs are shown in the two left insets, respectively (regions marked with blue color). A cross section along the  $z$ -axis of the reconstruction in the Al bottom layer shows the crystallographic orientations of the two Al grains with Ag segregation at the GB (middle inset). A green rectangle marks the position of the tomographic slice in the  $xy$ -plane perspective [93].

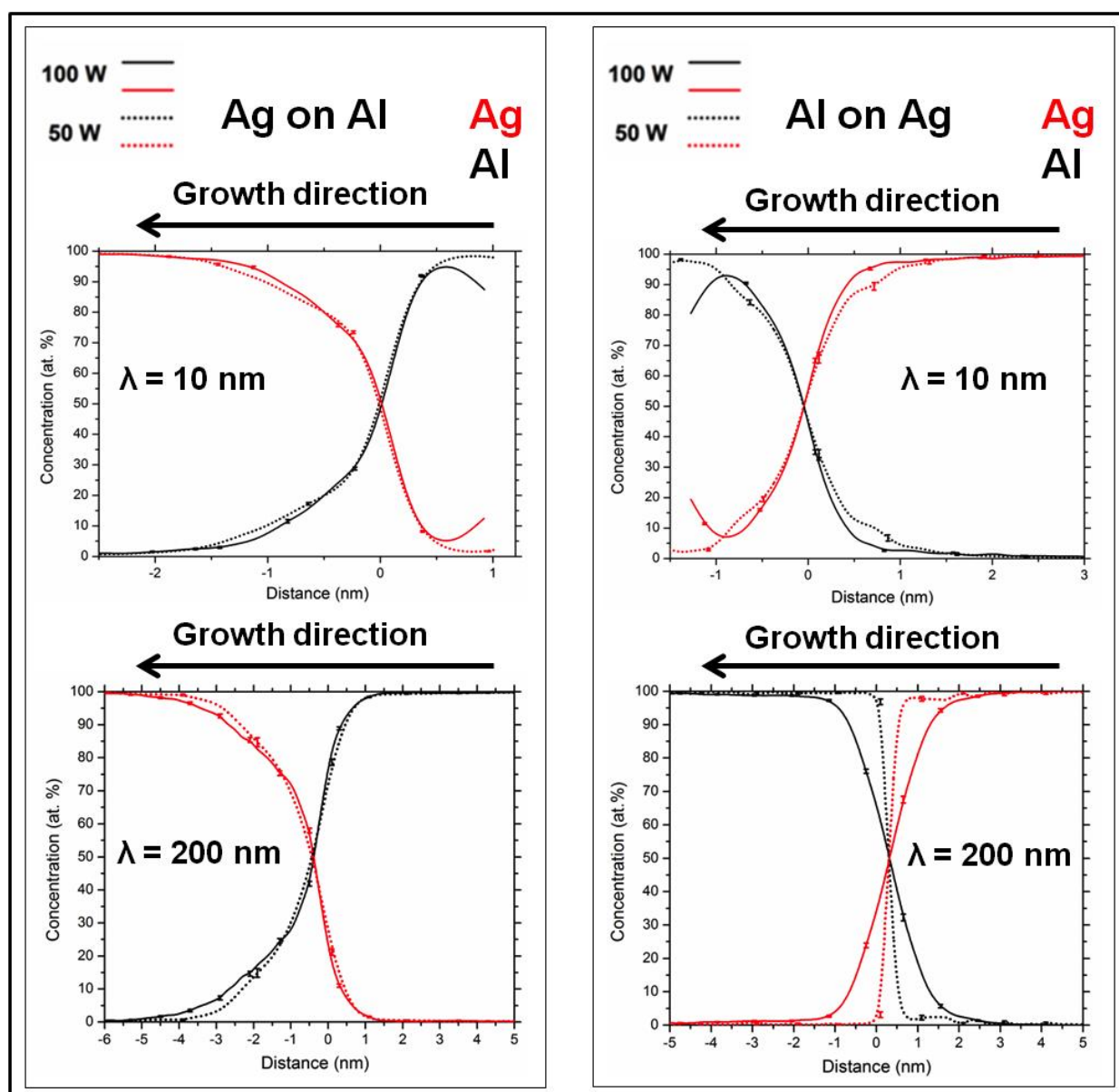


**Figure 33** Proxigram analyses for Ag on Al and Al on Ag interfaces, respectively, measured by APT for Ag/Al multilayer thin films of 10 and 200 nm periods in the as-deposited condition synthesized with low and high sputtering powers, respectively. The thin film growth direction is marked [93].

The zone of intermixing is about 1-3 nm thick depending on the condition. Three observations can be deduced from these analyses. First, if Ag is deposited on Al, the intermixing profile is observed to be asymmetric, while in the case of Al on Ag the profile is symmetric. Al is more enriched at the Ag side of the asymmetric interfaces. This behavior is identical for all the periods analyzed, independent from the sputtering conditions. Second, varying the sputtering power in the films of 200 nm period induces a total change in the zone of intermixing of ~1 nm for Ag on Al interfaces and ~2 nm for the Al on Ag interfaces, respectively. While for the multilayers of 10 nm period the Al layer shrinks by ~1 nm using high sputtering power. Third, the film of 10 nm period display an increase in Ag concentration within the Al layers from ~2 to ~8 at.% with increased sputtering power. Therefore, it can be understood that the small periods exhibit more mass transport inside the grains compared to the large periods.

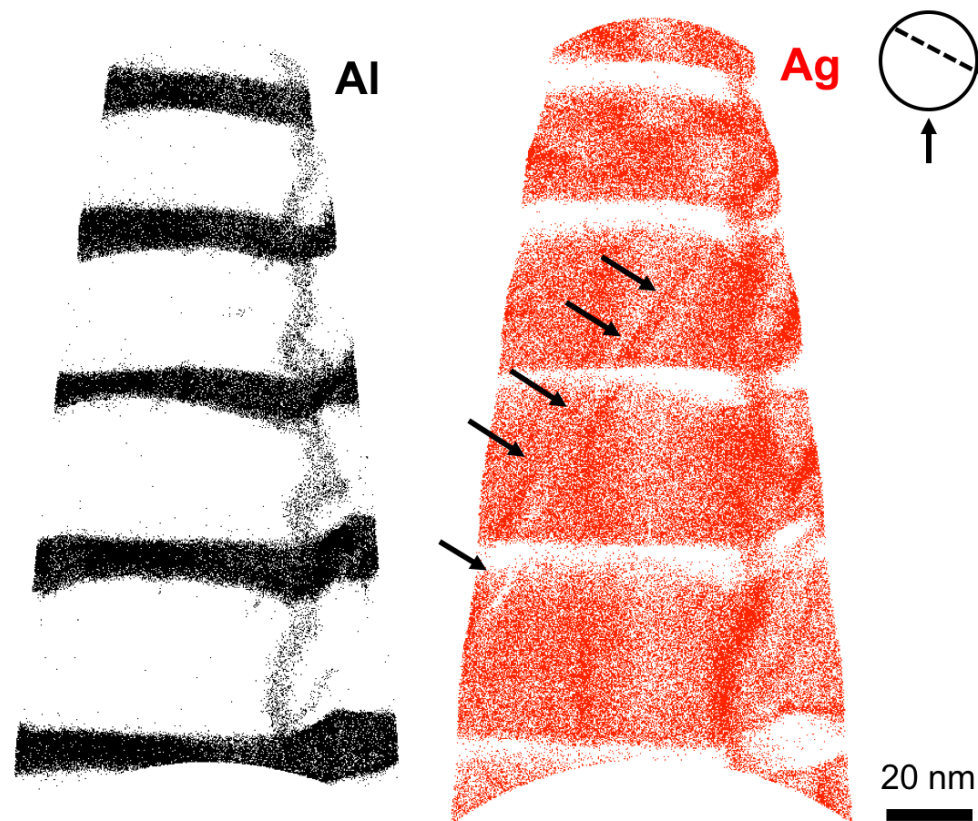


**Figure 34** APT reconstruction for Ag/Al multilayer thin films of 50 nm periods deposited using high sputtering power. Al and Ag atoms are shown separately from 8 nm thick tomographic slice along the main axis of the reconstruction. A vertical GB is located in both reconstructions showing solute atom segregations. The GB is seen relatively thick, this is because the GB plane is not perpendicular to the tomographic slice. The drawing on the tip right represents the position of the vertical GB plane along the main axis of the reconstruction and the black arrow marks the direction of view. Black

arrows in the reconstruction mark the diagonal twin boundary which is more clearly visible in the Ag layer.

Aside from the influence of period on interdiffusion, it is important to point out that almost no segregations were detected at the twin boundaries measured in APT. Figure 34 shows an APT reconstruction from a 50 nm period (Ag-rich composition deposited with 100 W sputtering power) which displays a twin boundary penetrating through the multilayer diagonally. Twin boundaries growing diagonally were shown in the TKD results in section 3.1.1.2. The lack of solute atoms segregations at these lattice defects is expected since such twin boundaries detected with TKD have shown to be coherent type of twin boundaries. Coherent twin boundaries exhibit a perfect fit for the atomic planes between the two crystals and have the lowest boundary energy compared to other boundaries [96]. Therefore, this result here offers a good agreement between the structural and chemical analysis.

#### **3.1.1.4. Sputtering gas pressure investigation**

The influence of the argon gas pressure used during film deposition on the microstructure of the thin films is studied using STEM and XRD analyses. The investigation was carried out on 200 nm periods which were deposited using high sputtering power (100 W) and three different argon gas pressures of 0.003, 0.01 and 0.06 mbar. Films deposited with 0.003 mbar were already shown in the sections above but will be also presented here for comparison purposes. Figure 35 shows STEM image of the 200 nm period sample as shown in Figure 22 but in lower magnification. A slight increase in the interfacial roughness in the film growth direction can be observed, nevertheless, the multilayer structure remains well defined. Figure 36 and Figure 37 show the 200 nm period deposited using 0.01 and 0.06 mbar pressure, respectively.

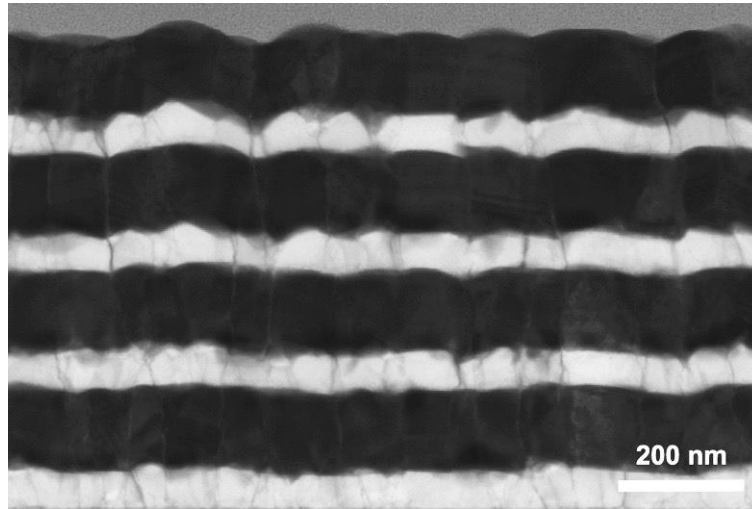


**Figure 35** BF-STEM for Ag/Al multilayer thin films of 200 nm period deposited with 0.003 mbar gas pressure and 100 W sputtering power.

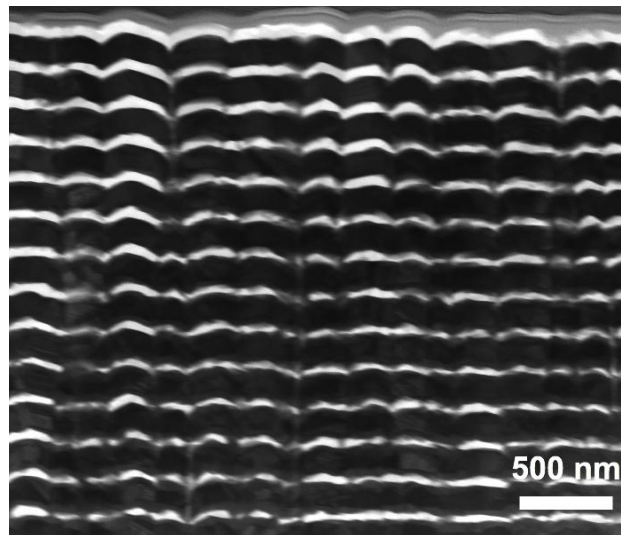


**Figure 36 (a)** BF-STEM for Ag/Al multilayer thin films of 200 nm period deposited with 0.01 mbar gas pressure and 100 W sputtering power.

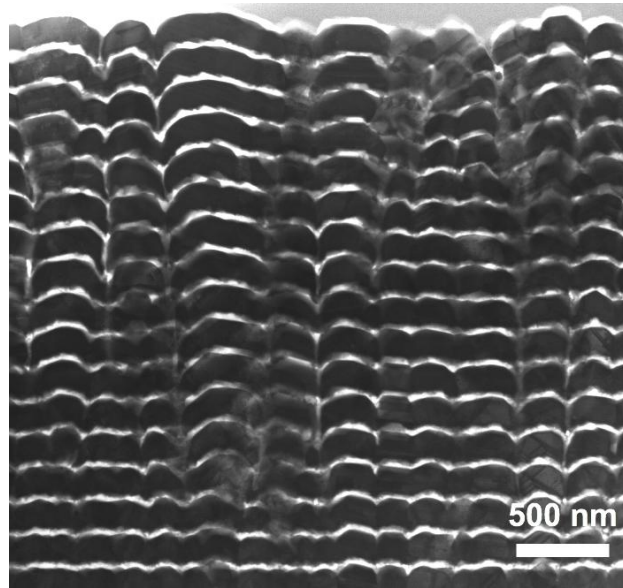


**Figure 37** (a) BF-STEM for Ag/Al multilayer thin films of 200 nm period deposited with 0.06 mbar gas pressure and 100 W sputtering power.

The influence of the sputtering gas pressure on the microstructure of the multilayers can be clearly visible. The roughness of the multilayers is generally increased using higher gas pressure. Moreover, a gradual rise in the roughness of the multilayers along the growth direction of the layers is also shown to increase with the gas pressure. Topographic defects are observed to form in the layers near the surface for the films deposited with 0.06 mbar, which are created as a result of the increased interfacial roughness (this phenomenon is explained in section 1.3). Such topographic defects are known to contribute majorly as fast diffusion paths for mass transport.

The increased roughness is expected to influence the texture of the parent phases in the multilayer thin films. Figure 38 displays the normalized XRD peak intensity ratios for five crystal orientations of “Ag+Al” phases for the 200 nm period films deposited with different gas pressure. Indeed, the plot shows that less texturing in the preferential {111} orientation occurs in the films deposited using higher gas pressures.

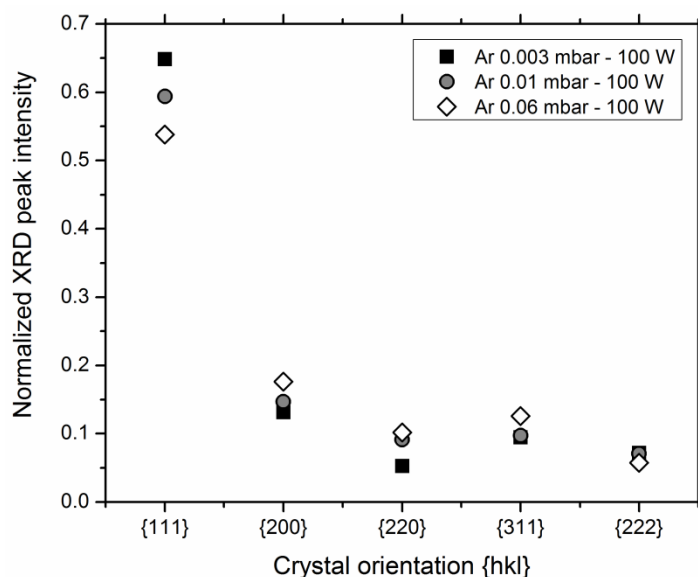


**Figure 38** Normalized XRD peak intensity for the fcc "Ag+Al" peaks of the 200 nm multilayer periods as a function of the gas pressure deposited using 100 W sputtering power.

### 3.1.1.5. Composition investigation in the 10 nm periods

The small periods of 10 nm with Ag-rich composition have shown the most interesting behavior concerning interdiffusion and phase formation, presented in section 3.1.2.3. Therefore, further investigation was carried out on the 10 nm period by additionally studying the influence of the composition on the interdiffusion and phase formation. STEM and XRD results are presented here, followed by APT results in section 3.1.1.6.

#### A. Al-rich composition

Figure 39 shows STEM images for the 10 nm period deposited by 50 W sputtering power and 0.003 mbar argon pressure in Al-rich composition. The sample showed higher interfacial roughness compared to the Ag-rich composition presented above. Increased roughness with the growth direction and formation of topographic defects in the microstructure are observed, respectively. The morphology of the multilayers within each column of grains also appear to be irregular, reflecting high roughness within the individual grains. Figure 40 shows an XRD measurement for this sample. Satellite peaks are also observed. Appearances of reflections of other crystal orientations than the {111} and {222} are detected. This can be directly related to the increased interfacial roughness which reduces the texturing along the  $\langle 111 \rangle$  direction. However, no peaks for intermetallic phases were detected here.

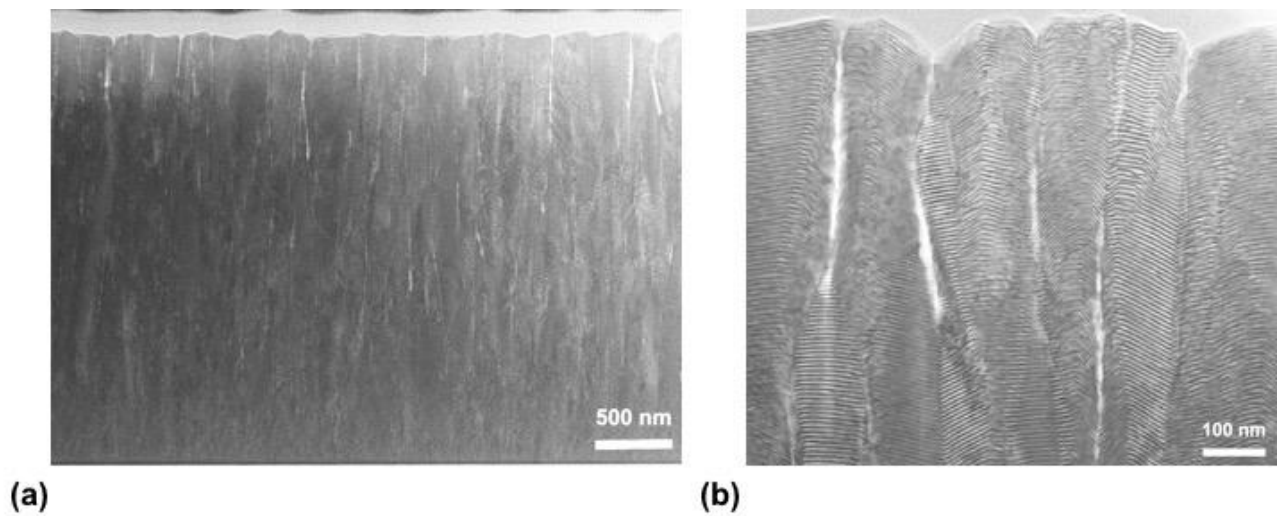


**Figure 39** BF-STEM for Ag/Al multilayer thin films of 10 nm period of Al-rich composition (Ag:Al ratio of 1:2) deposited with 50 W sputtering power and 0.003 mbar Argon pressure. (b) Higher magnification for the multilayers near the surface.

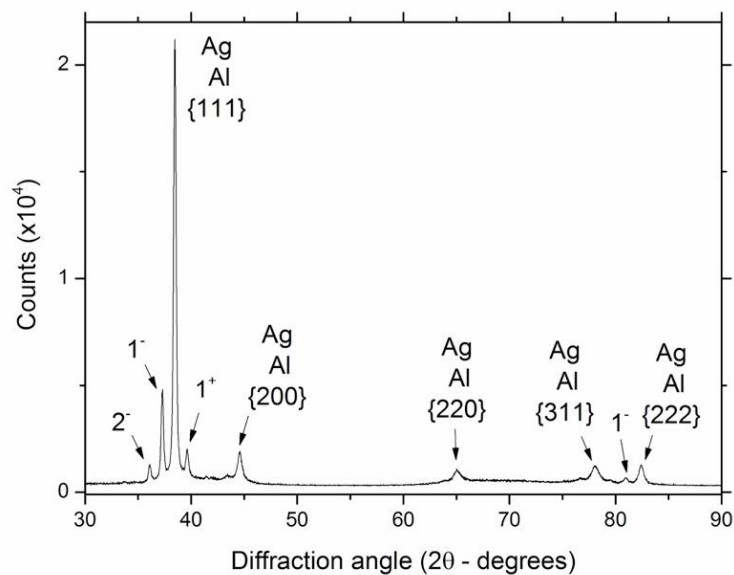
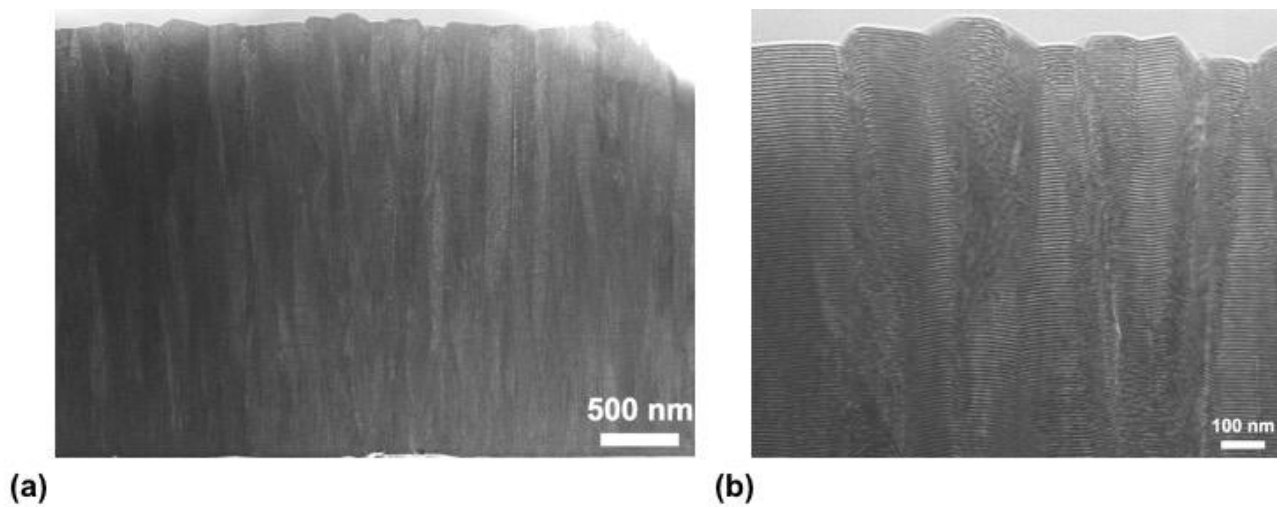


**Figure 40** XRD measurement for Ag/Al multilayer thin film of 10 nm period of Al-rich composition (Ag:Al ratio of 1:2) deposited with 50 W sputtering power and 0.003 mbar argon pressure. Satellite peaks are marked. The number refers to their order.

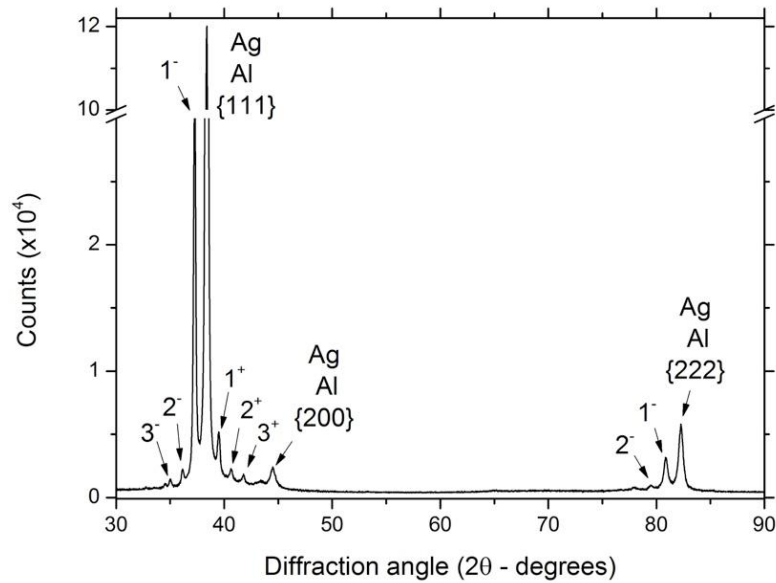
### B. Near 50:50 composition

Figure 41 shows STEM images for the 10 nm period deposited by 50 W sputtering power and 0.003 mbar argon pressure in near 50:50 composition. This sample also showed higher interfacial

roughness compared to the Ag-rich composition, but slightly less than the Al-rich composition. The increased roughness with the growth direction is also evident, along with some rare formations of topographic defects in the microstructure. The morphology of the multilayers within each column of grains also appear to be irregular, reflecting high roughness within the individual grains. Figure 42 shows an XRD measurement for this sample. Satellite peaks are also observed. Only one crystal orientation reflection other than the {111} and {222} is detected, that is the {200} orientation. This can be directly related to the degree of interfacial roughness which is qualitatively between the Ag-rich and Al-rich compositions. No diffraction peaks for intermetallic phases were detected here.



**Figure 41** BF-STEM for Ag/Al multilayer thin films of 10 nm period of near 50:50 composition deposited with 50 W sputtering power and 0.003 mbar Argon pressure. (b) Higher magnification for the multilayers near the surface.



**Figure 42** XRD measurement for Ag/Al multilayer thin film of 10 nm period of near 50:50 composition deposited with 50 W sputtering power and 0.003 mbar argon pressure. Satellite peaks are marked. The number refers to their order.

The growth behavior of these small periods is shown to be greatly dependent on the composition, where the Ag-rich composition offers minimal interfacial roughness and highest degree of texturing.

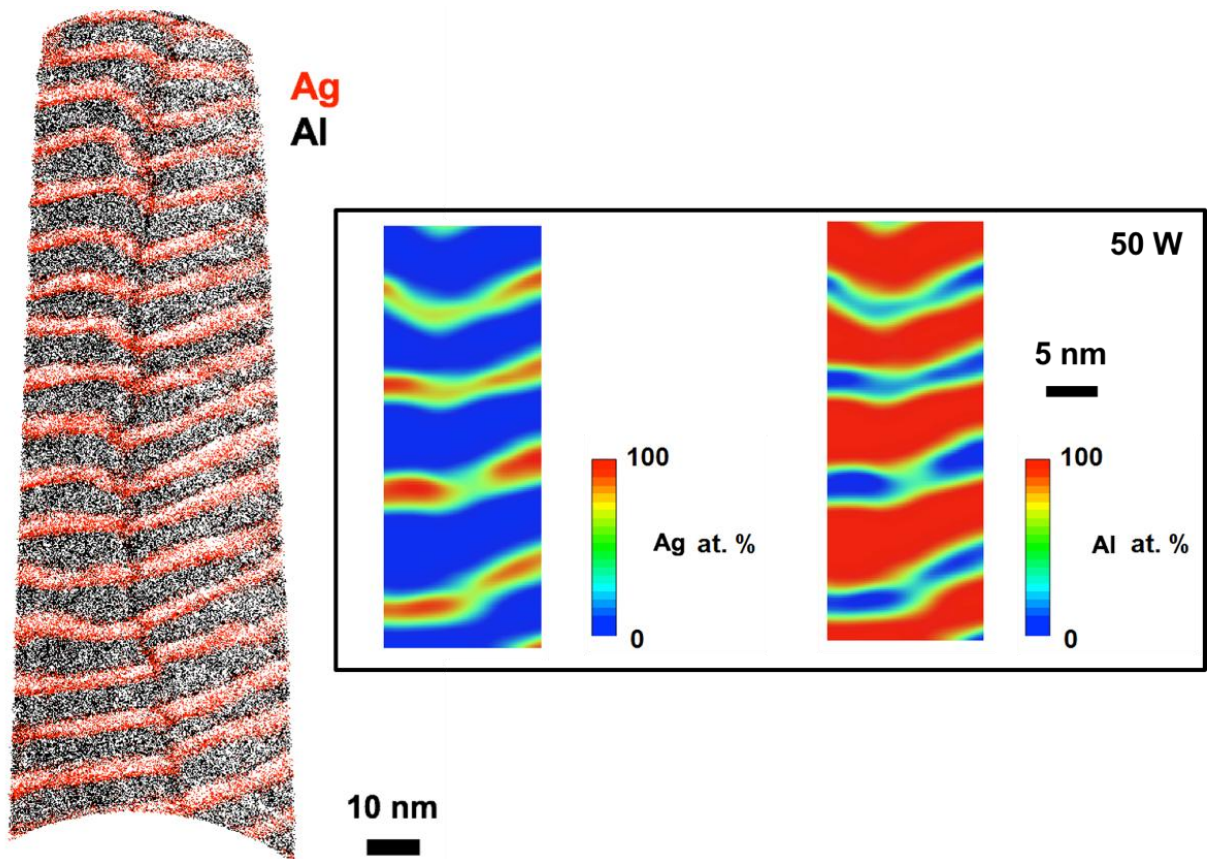
### 3.1.1.6. APT analyses

The Ag/Al 10 nm periods characterized in the previous section are further investigated using APT in order to study the influence of the nominal composition on the interdiffusion and concentration gradients at the phase boundaries. Interdiffusion along fast diffusion paths is analyzed as well as the interfacial mixing and the composition within the individual layers.

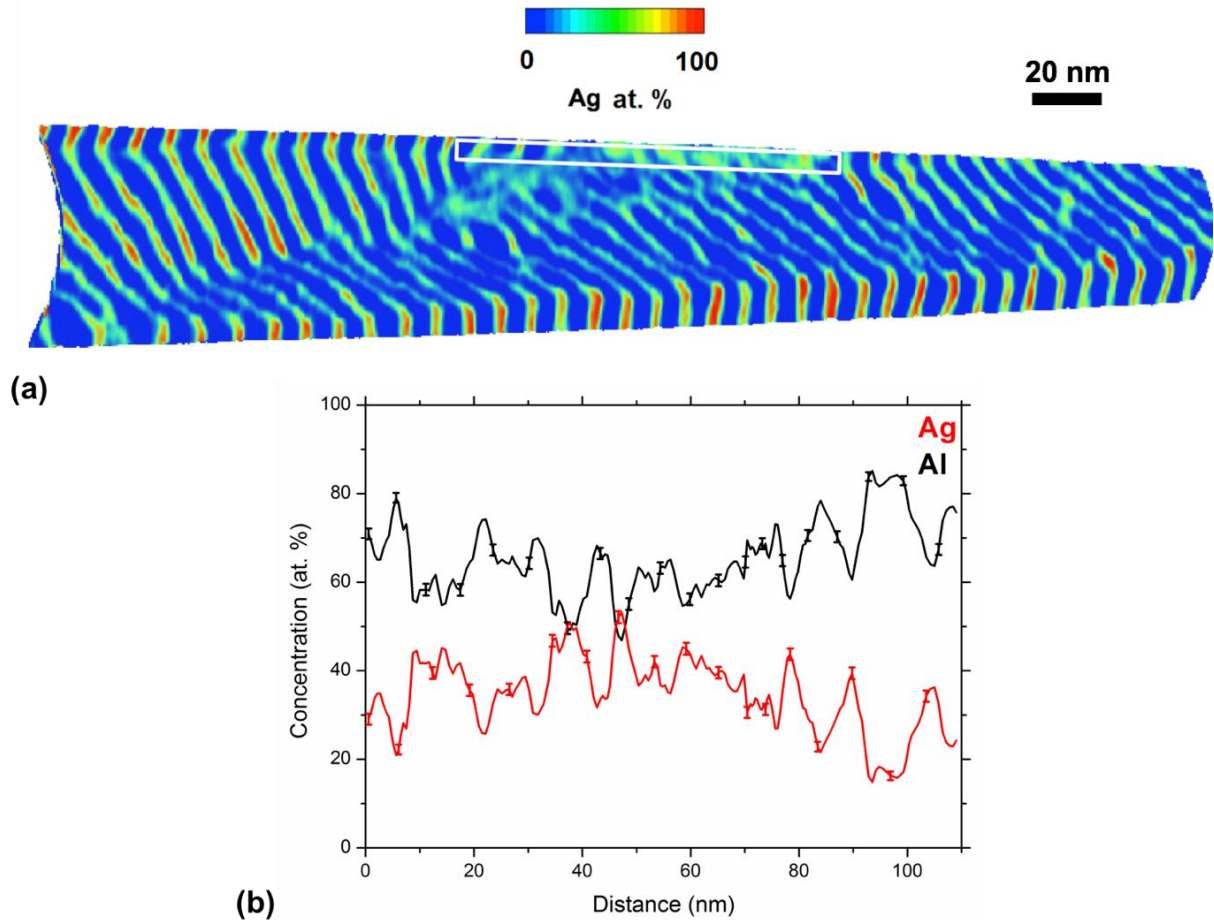
#### A. Al-rich composition

Figure 43 shows a 10 nm tomographic slice along a reconstruction from the 10 nm period with Al-rich composition. A vertical GB is located in the reconstruction which displays localized interdiffusion. In Figure 43 the segregation along the GB is highlighted using 2D concentration maps. It can be noticed that in this case here, Al is detected at the GBs of the Ag phase whereas almost no Ag is detected at the Al GBs. Although GBs display localized interdiffusion between the

layers, diffusion along fast diffusion paths was dominated by the topographic defects that have formed in these multilayer thin films as shown in Figure 44.



**Figure 43** APT analyses for Ag/Al of 10 nm period with Al-rich composition. (left) 10 nm thick tomographic slice along a reconstruction, Ag and Al atoms are presented, and a vertical GB displays localized interdiffusion. (right box) Local analyses from regions with a vertical GB using 2D concentration maps for Al and Ag separately.



**Figure 44** APT analyses for Ag/Al of 10 nm period with Al-rich composition. (a) A region along a topographic defect is visualized using 2D concentration maps of Ag concentration within a 10 nm tomographic slice in the reconstruction. The reconstruction is rotated 90 degrees with respect to the film growth direction. (b) 1-D concentration profile along the region marked with the white box.

APT has revealed here that the local regions observed with STEM (see Figure 39), where the multilayer structure collapses locally, referred to as tomographic defects, exhibit an immense degree of interdiffusion. As explained in sections 1.3 and 1.7.2, such regions act as extremely fast diffusion paths where the diffusivity rates approach surface diffusion. It is shown in Figure 44(b) that a solid solution of the alloy exists at such regions, approaching a 50:50 composition. Nevertheless, it is important to emphasize that no intermetallic phases were detected in these samples using XRD, as was shown in Figure 40. The XRD results neither show high background levels near the peaks to indicate amorphous phases. Therefore, the high intermixing induced at the topographic defects can be considered to form a supersaturated solid solution having an fcc structure.

Regarding the interfacial mixing across the multilayers at regions distant from the tomographic defects or GBs, proxigram analysis was used. The Ag on Al and Al on Ag interfaces are analyzed separately. Concentrations across eight interfaces are calculated, averaged, and plotted as shown in Figure 45.

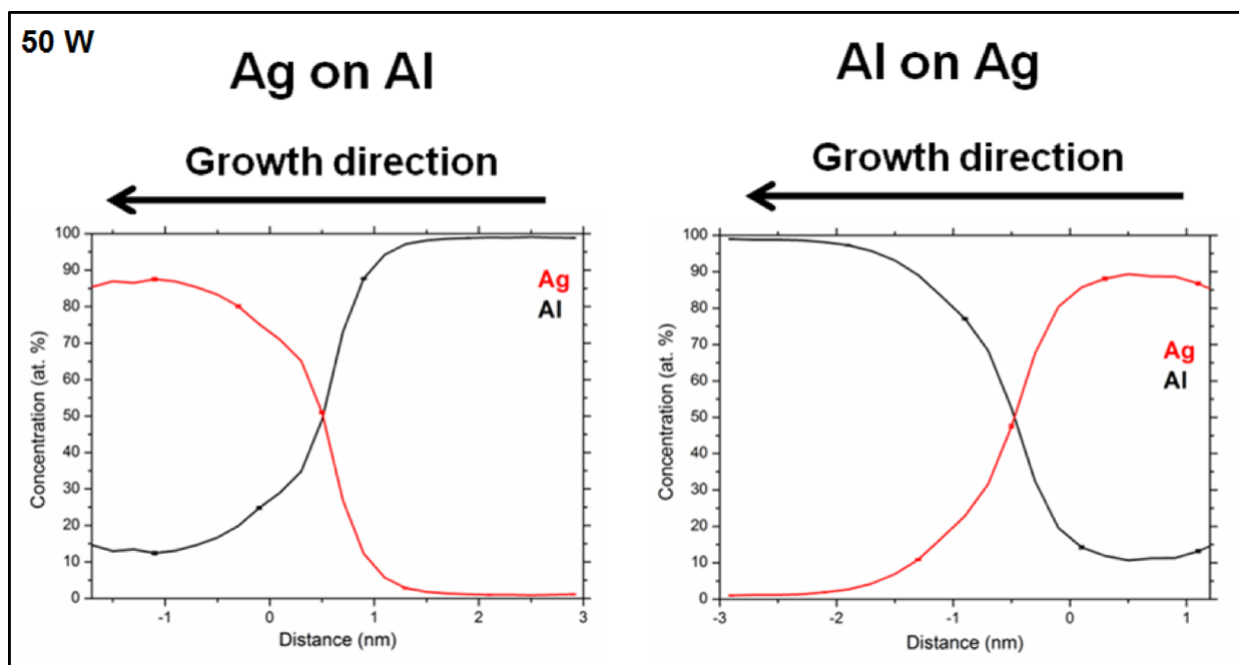


**Figure 45** Proxigram analyses for Ag on Al and Al on Ag interfaces, respectively, measured by APT for Ag/Al multilayer thin films of 10 periods with Al-rich composition. The thin film growth direction is marked.

The results for the proxigram analysis shows very interesting behavior, which strongly contrasts the results seen in the Ag-rich thin films of the same period thickness (see Figure 33). Two observations can be deduced from the proxigram analyses. First, the interfaces of Ag deposited on Al, display a symmetric concentration profile, while for the Al on Ag interfaces they show an asymmetric one, which is exactly the opposite of what is observed in the Ag-rich thin films (Figure 33). The second, and the most interesting result, is that the mass-transport in the interior of the grains occurs here in the thinner Ag parent layers with concentrations reaching up to ~13 at.% Al. The Ag-rich films in comparison, show an amount of ~ 2 at. % of Ag in the Al layers (at 50 W sputtering power). It can be therefore understood that the diffuser direction has reversed by reversing the Ag:Al composition ratio for these multilayers thin films of small periods. However, the case here of Al-rich composition exhibits significantly higher mass-transport of solute atoms inside the grains, which is within the thinner layers of Ag (thinner compared to the Al layers).

## B. Near 50:50 composition

Figure 46 shows a 10 nm tomographic slice along a reconstruction from the 10 nm period with near 50:50 composition. A vertical GB is located in the reconstruction which displays localized interdiffusion. In Figure 46 the segregation along the GB is highlighted using 2D concentration maps. Similar to the Al-rich composition, Al is detected at the GBs of the Ag phase whereas almost no Ag is detected at the Al GBs. Apart from GB diffusion, topographic defects which form in these multilayer thin films (see Figure 41) were detected with APT and reveal a network of fast-diffusion paths (see Figure 47), which is like those found in the multilayer thin film of Al-rich composition of 10 nm period.

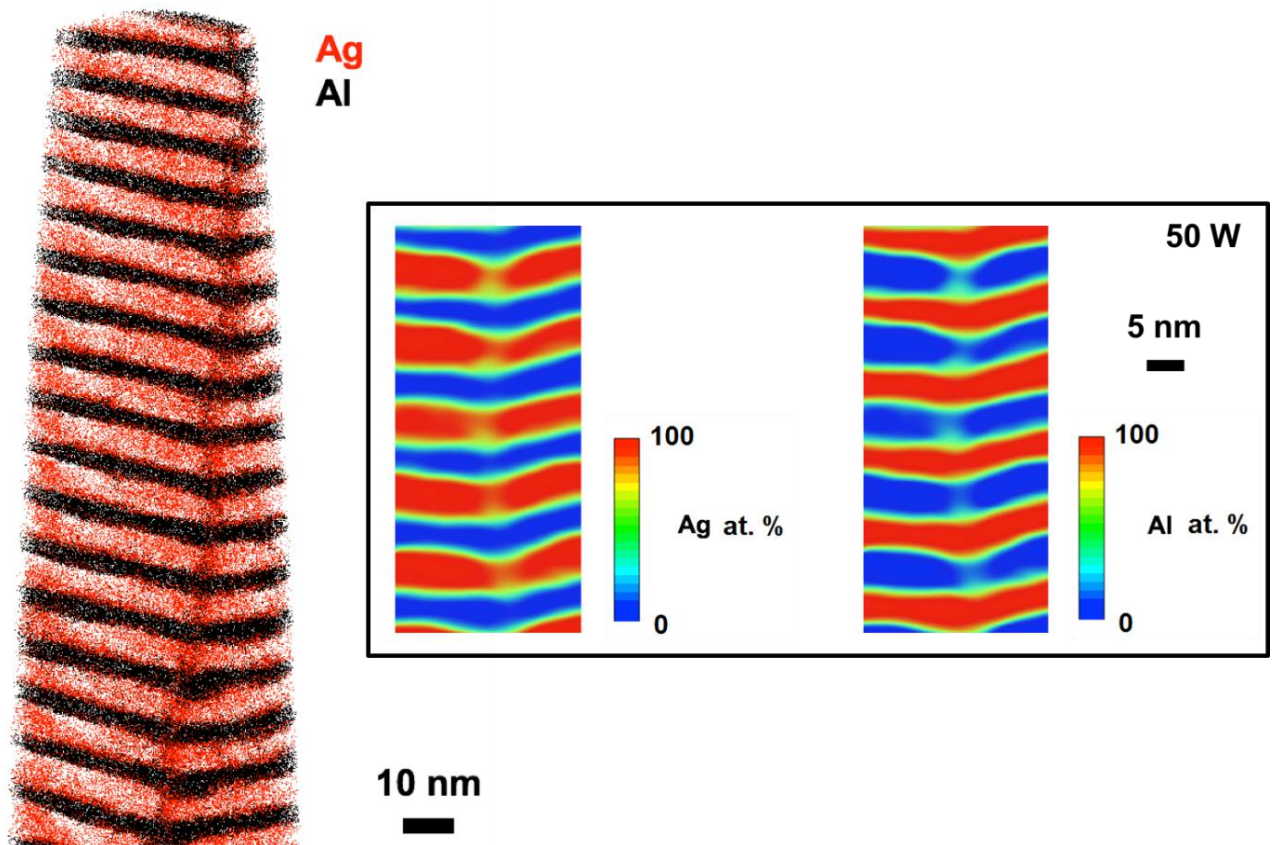


**Figure 46** APT analyses for Ag/Al of 10 nm period with near 50:50 composition. (left) 10 nm thick tomographic slice along a reconstruction, Ag and Al atoms are presented, and a vertical GB displays localized interdiffusion. (right box) Local analyses from regions with a vertical GB using 2D concentration maps for Al and Ag separately.

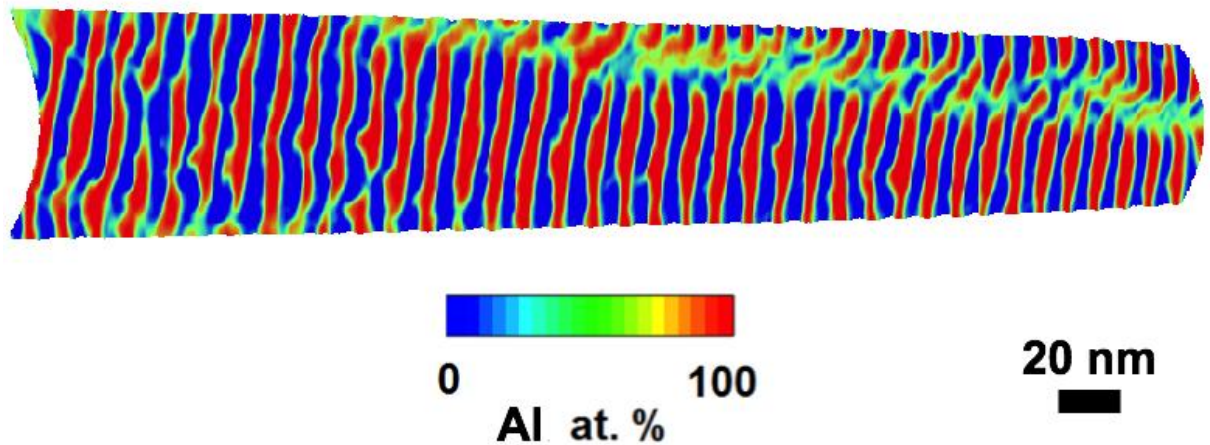


**Figure 47** APT analyses for Ag/Al of 10 nm period with near 50:50 composition. A region along a topographic defect is visualized using 2D concentration maps of Al concentration within a 10 nm tomographic slice in the reconstruction. The reconstruction is rotated 90 degrees with respect to the film growth direction.

The high interfacial roughness within the multilayers can be more clearly observed by APT in the Figure 47, compared to the STEM imaging. The same behavior was observed in the APT datasets of the Al-rich composition. In this near 50:50 composition the concentrations along the tomographic defects have also shown similar results to the Al-rich thin films (similar to Figure 44(b)) and is therefore are not presented here. Again, the XRD analysis of these thin films have not revealed any peaks for intermetallic phases neither any indications for an amorphous phase. Therefore, similarly to the Al-rich thin films, a supersaturated solid solution is expected to form along the topographic defects in the microstructure. Regarding the interfacial mixing across the multilayers at regions distant from the tomographic defects or GBs, proxigram analysis was also used. The Ag on Al and Al on Ag interfaces are analyzed separately. Concentrations across eight interfaces are calculated, averaged, and plotted as shown in **Figure 48**. The proxigram analysis in the films here reveals very interesting behaviors. Three observations can be deduced from the proxigram analyses. First, no clear dissimilarity is observed regarding the concentration gradients for the interfaces of Ag on Al and the Al on Ag, respectively. Second, the mass-transport of solute atoms in the interior of the grains occurs in the both phases simultaneously. Third, the concentration of the Al solute atoms in the Ag layers is  $\sim 7$  at.%, whereas the concentration of Ag solute atoms in the Al layers is  $\sim 5$  at.% (at 50 W sputtering power). It can be therefore understood that the diffusion occurs here in both directions, in contrast with the diffusion behavior found in the Ag-rich and Al-rich multilayer thin films of 10 nm period.

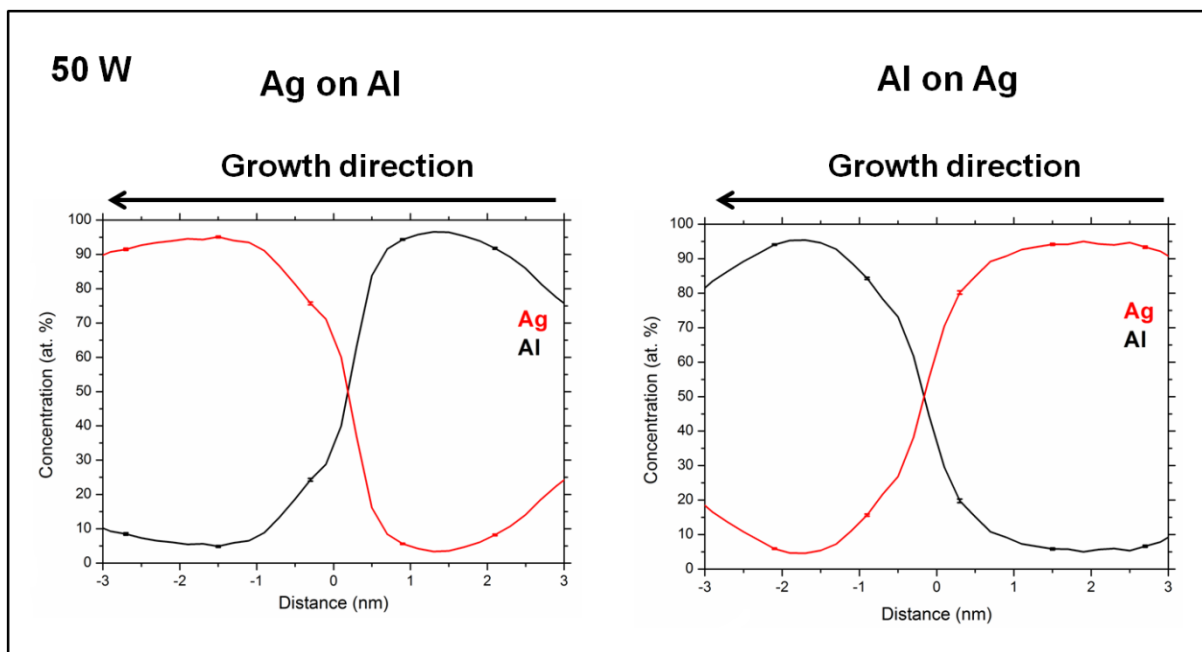


**Figure 48** Proxigram analyses for Ag on Al and Al on Ag interfaces, respectively, measured by APT for Ag/Al multilayer thin films of 10 periods with near 50:50 composition. The thin film growth direction is marked.

### 3.1.2. Thermally treated films

#### 3.1.2.1. Period and sputtering power investigation

The multilayer thin films of Ag-rich composition deposited in different period thicknesses and sputtering powers were analyzed in the DSC. Figure 49 shows the calorimetric response of the multilayer periods of different periods deposited using low sputtering power. The enthalpies of reactions (calculated from the whole signal) for each period in both sputtering powers is plotted in the inset of Figure 49. The thin films of 10 nm period exhibit the earliest exothermic heat release that starts at about 350 K which becomes larger in magnitude as the temperature increases until a sharp exothermic event occurs at 393 K. For larger periods, the exothermic reaction shift to higher temperatures and the reaction occurs within a broader temperature range. For the multilayers of 100 nm period a single broad peak even marks the formation of the  $\text{Ag}_2\text{Al}$   $\gamma$  phase (see section 3.1.2.2), whereas for the films of 200 and 400 nm periods the overall reaction displays two and three successive signals, respectively. The calorimetric behavior here can be related to the two-step growth model (see section 1.5). By comparing the plot for the enthalpies of reactions it is clear to observe that the heat release gradually increases (higher negative value) with the period thickness. Moreover,

the films deposited with low sputtering power displayed more negative enthalpy values compared to the films deposited with high sputtering power. The films of 100, 200, and 400 nm periods show a difference of almost 2 kJ g-atom<sup>-1</sup>, while the multilayers of 10 nm period exhibit a very small difference of about 0.30 kJ g-atom<sup>-1</sup>. Using four various heating rates, the activation energies for the reactions were calculated for each period using A Kissinger-like analysis [97] applied on the onset temperature values of the reactions. The resulting activation energy for the 10 nm period was calculated to be 1.07 eV for both sputtering conditions, while the films of 100, 200 and 400 nm periods have shown a range from 1.15 to 1.30 eV. The values calculated for the 100-400 nm periods agree with activation energy reported by Baglin et al. [98] and Weaver et al. [99] of 1.20 for Ag<sub>2</sub>Al  $\gamma$  phase formation in Ag/Al bilayer thin films with individual layer thicknesses of 190 and 460 nm.

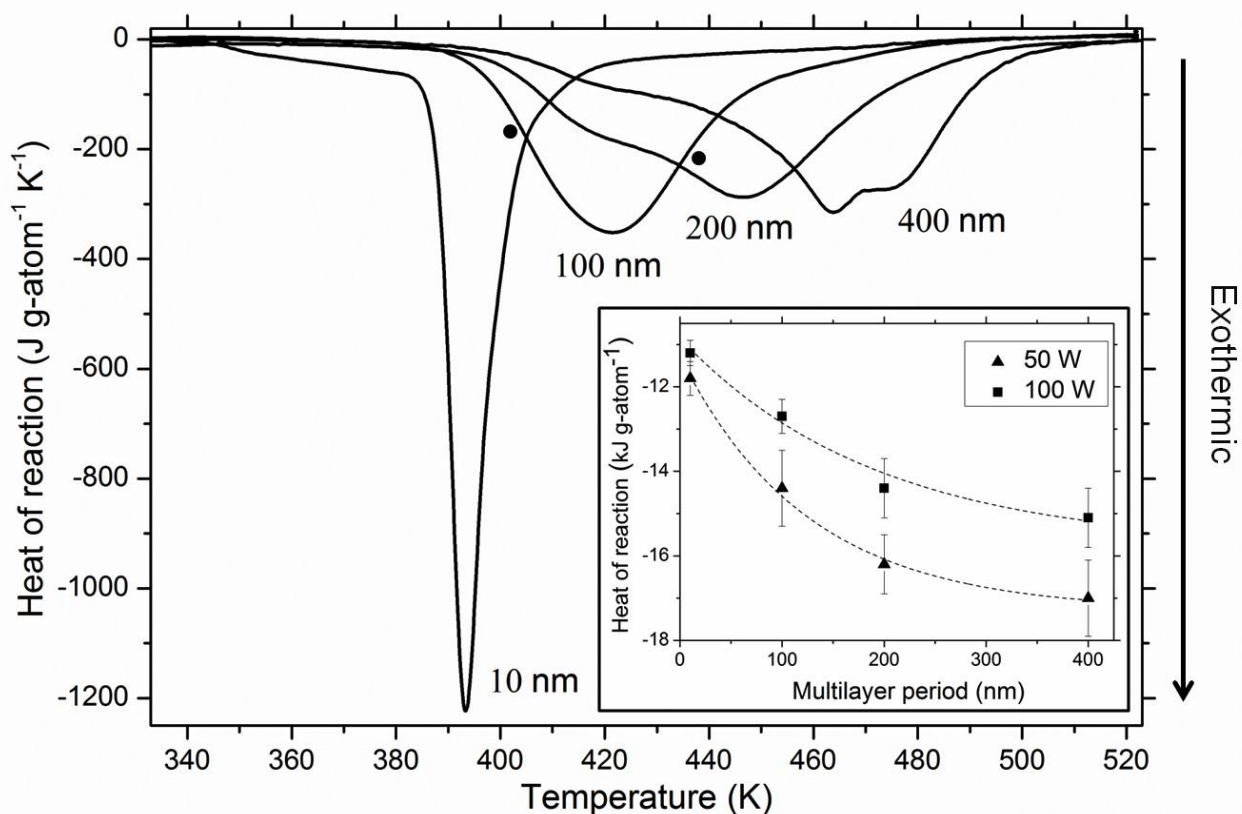


**Figure 49** DSC scans with heating rate of 0.33 K.s<sup>-1</sup> for the different Ag/Al multilayer periods deposited using low sputtering power (50 W). The two black dots mark the temperatures for APT/TEM investigations shown in section 3.1.2.2. The inset shows the heat of reaction in different periods for both sputtering conditions. The dotted lines are an exponential fit as a guide to the eye for highlighting the relationship for the heat of reaction as a function the period thicknesses [93].

Intermetallic phases formed by thermal treatment were studied using XRD, TEM and APT. The mechanism of phase formation and the microstructural evolution is studied via ramp annealing of the free standing multilayer thin films in the DSC to a specified temperature then the samples are instantly cooled with a rate of  $3.33 \text{ K.s}^{-1}$ , and the microstructure is subsequently investigated. The results are presented in the two following sections.

### **3.1.2.2. Phase formation in the 100 nm periods**

The multilayer of 100 nm period was chosen for this investigation rather than 200 or 400 nm periods in order to attain more interfaces within the restricted APT dataset volume, for satisfactory statistics of the reactant products. Ag/Al multilayer thin films of 100 nm period deposited at low sputtering power were ramp-annealed with a heating rate of  $0.33 \text{ K.s}^{-1}$  in the DSC to three different temperatures: at the beginning, near the end, and after the exothermic event, respectively. The two temperatures at the exothermic event are marked on the DSC scan of the 100 nm period in Figure 49, which are at 398 K and 435 K, respectively.

#### **A. Early stage of the exothermic reaction**

The initial stage of the reaction is investigated, which is chosen at 398 K that is a few degrees above the onset of the main exothermic peak (see Figure 49). Figure 50 shows an XRD measurement for the sample ramp-annealed to 398 K. The formation of the  $\text{Ag}_2\text{Al}$   $\gamma$  hcp phase can be clearly observed. Certainly, Ag/Al multilayers deposited on Si (100) substrates exhibited a different texture than the films deposited on Cu, nevertheless, the product (intermetallic phase) from the multilayer reaction should not be affected. TEM analysis was carried out on the same sample in order to investigate the nucleation sites of the new compound phase. Figure 51 shows a magnified TEM image at a region along one of the vertical GBs within the sample. The nucleation and growth of the new intermetallic phase is clearly visible at the vertical GB region. Furthermore, the new phase is observed to grow across the Al layers, i.e. across both layer interfaces of the Al phase.

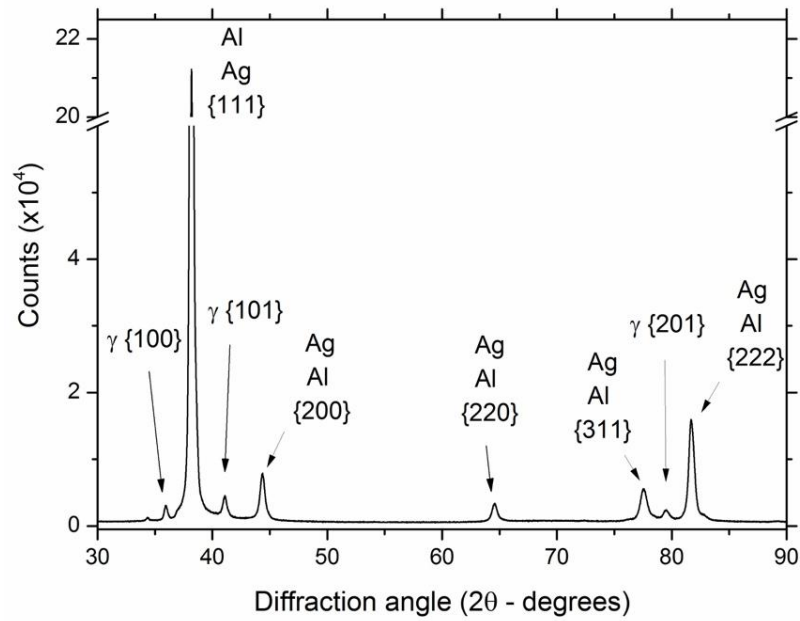


**Figure 50** XRD measurement for Ag/Al multilayer thin film of 100 nm period deposited at low sputtering power, ramp annealed to 398 K and subsequently cooled.

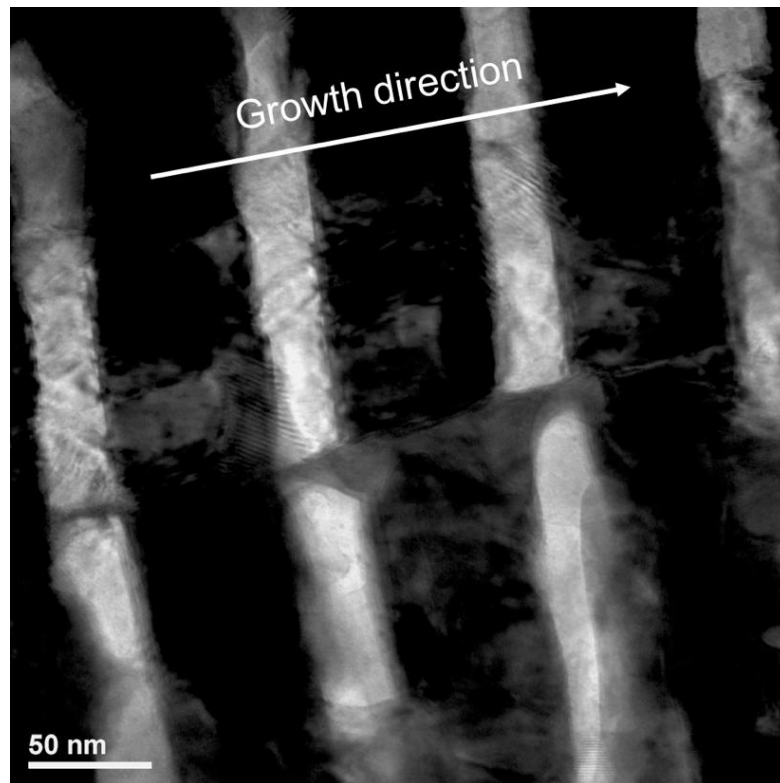


**Figure 51** BF-TEM image for Ag/Al multilayer thin film of 100 nm period deposited at low sputtering power, ramp-annealed to 398 K and subsequently cooled. The intermetallic phase appears along a vertical GB region.

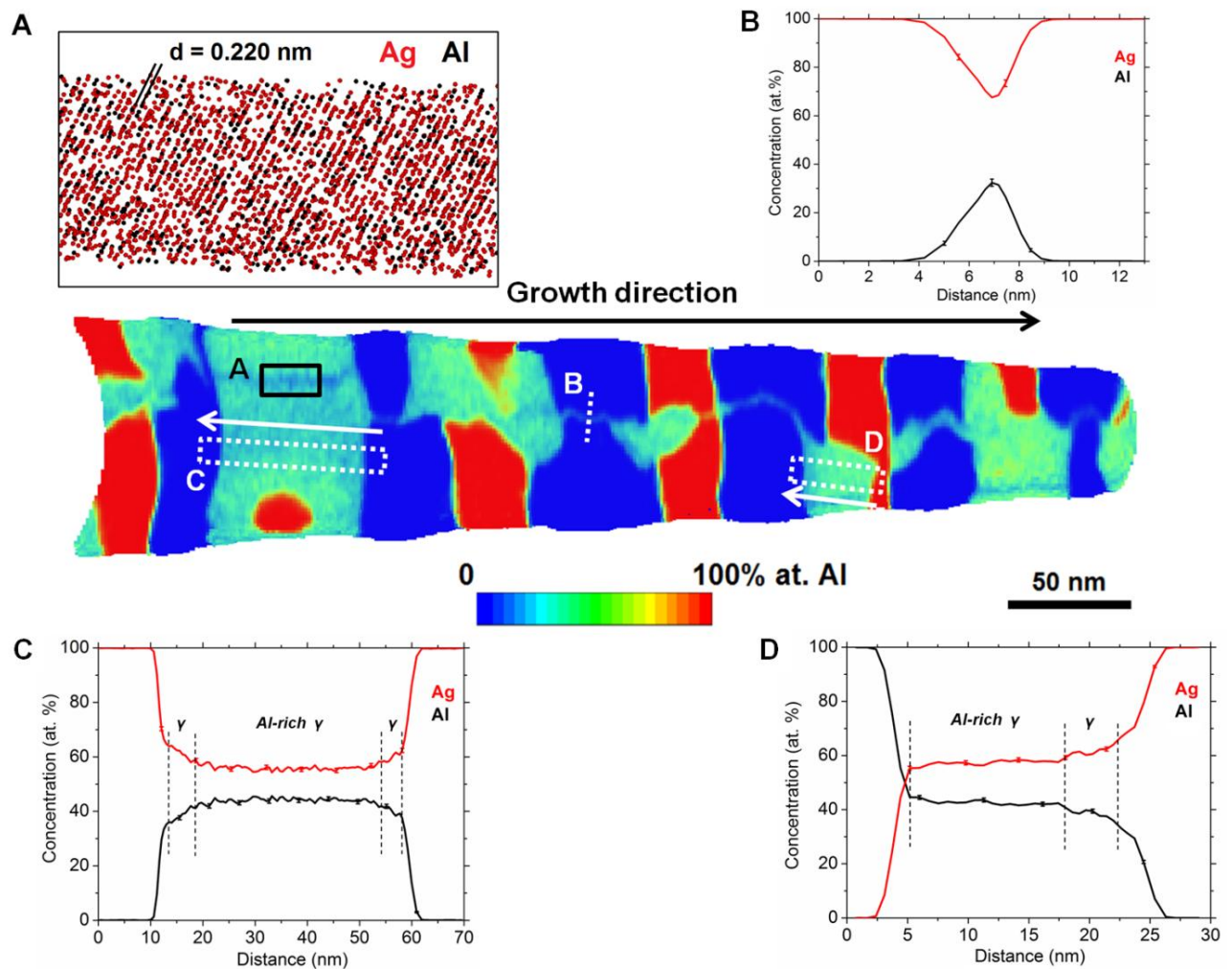


**Figure 52** APT analysis for Ag/Al multilayer thin films of 100 nm period ramp-annealed to 398 K. A 2D concentration map is presented for Al within 8 nm thick tomographic slice from the reconstruction. The thin film growth direction is marked. Inset A represents a crystallographic pole from the intermetallic phase which displays Al and AG lattice planes. Inset B shows a 1D concentration profile across a GB in a Ag layer. Insets C and D show 1D concentration profiles from the regions marked. Corresponding compositions for equilibrium  $\gamma$  phase and Al-rich  $\gamma$  phase are marked [93].

Figure 52 shows an APT reconstruction of the same sample condition at a region of preferential nucleation along a vertical GB, as detected by TEM in Figure 51. The APT data show that the  $\text{Ag}_2\text{Al}$   $\gamma$  intermetallic phase has formed predominantly at the intercepting point between the GBs and the layers interfaces, and has grown more intensely surrounding the Al parent phases. A crystallographic pole (inset A in Figure 52) detected in the intermetallic  $\gamma$  phase shows Al and Ag atoms lying on the same lattice planes with lattice spacing of 0.220 nm, which corresponds to a  $\langle 101 \rangle$  direction in the

$\text{Ag}_2\text{Al}$  hcp crystal structure, measured using SDM algorithm. It is important to note that the interfacial mixing of the Ag and Al parent phases remain unchanged as shown in Figure 53, almost identical to the profiles of the as-deposited condition of the 200 nm period presented in Figure 33 in section 3.1.1.3. It is also important to mention that the concentrations of both diffusing species (Al and Ag) in the GBs of the parent phases (Al and Ag) at such annealing temperature are less than or equal to the concentration values reported in the GBs of the 200 nm period in the as deposited condition synthesized with high sputtering power, presented in Figure 32(b) in section 3.1.1.3.

The inset C in Figure 52 shows 1D concentration profile extracted within the dataset that runs through an extended  $\gamma$  phase region between two Ag layers, in which most of Al has been consumed. It can be seen that the Al composition of the intermetallic phase reaches a value of about 43 at. % ( $\text{Ag}_{57}\text{Al}_{43}$ ). The Al content is close but somewhat higher (1-2 at.%) than the solubility limit of the equilibrium  $\text{Ag}_2\text{Al}$   $\gamma$  in the phase diagram according to Refs. [65], [100], [101]. Towards both interfaces a concentration gradient is observed that reflects the equilibrium solubility range (35-41 at. % Al) of the  $\gamma$  phase in the phase diagram. Inset D in Figure 52 shows a profile from pure Al through the  $\gamma$  phase and into Ag. This profile is in good agreement with the Ag-Al phase diagram. A large step in concentration from pure Al to Al-rich  $\gamma$  phase is followed by a broad gradient from 43 to 35 at. % Al and drops to pure Ag. It should be stated that to this point the whole reaction appears to be dominated by Al diffusion leading to the suppression of the  $\text{Ag}_3\text{Al}$   $\mu$  phase.

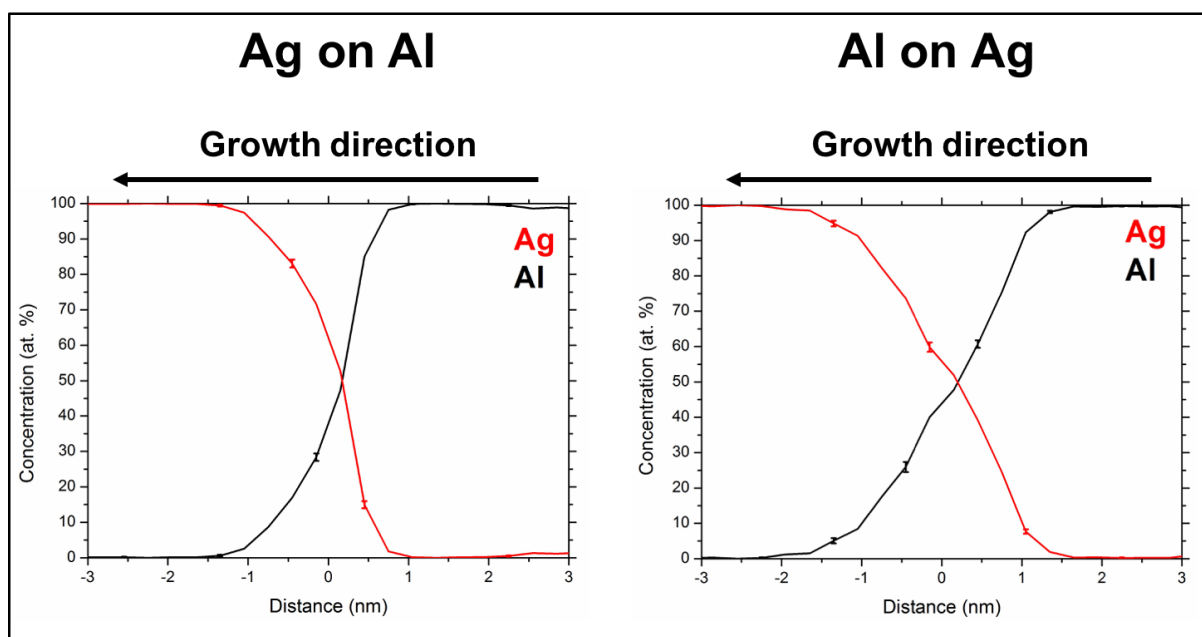


**Figure 53** Proxigram analyses for Ag on Al and Al on Ag interfaces, respectively, measured by APT for Ag/Al multilayer thin films of 100 periods ramp-annealed to 398 K.

### B. Near-end stage of the exothermic reaction

A later stage of the reaction is investigated, chosen at 435 K, which is before the end of the main exothermic peak (see Figure 49). APT analyses were carried out on this sample in order to unveil the evolution of the compositions and microstructure at the atomic level. Figure 54 shows an APT reconstruction from such sample. Three composition groups can be observed in the APT measurements of this sample condition. The first group consists of unreacted Ag areas (dark blue color in Figure 54). The second group is the Al-rich  $\text{Ag}_2\text{Al}$   $\gamma$  phase (dark orange color in Figure 54). This phase has grown extensively and represents the major fraction within the volumes measured in this sample condition. The third group is categorized as fine nanosize multiphase regions with compositions ranging between 14 and 40 at. % Al (light blue to dark yellow colors in Figure 54). No Al parent phase is observed in the APT measurements of this sample condition. At this stage, the film displays a multilayer structure, composed of Al enriched  $\text{Ag}_2\text{Al}$  islands and unreacted Ag phases surrounded by fine nanosize multiphase regions. Apparently, in these regions a competition between stable, metastable, and energetically similar phases takes place on a nanometer scale.

A crystallographic pole along two Al rich  $\text{Ag}_2\text{Al}$  grains of the same orientation and a grain of the fine nanosize multiphase region lying in between is presented in inset A (see Figure 54). The pole reveals the same ordering of Al and Ag planes along the three grains. The Al enriched  $\text{Ag}_2\text{Al}$  grains have d-

spacing of 0.220 nm, while the intermediate grain shows d-spacing of 0.195 nm. The concentration within this intermediate grain exhibits a value of 20-25 at.% Al (see inset C in Figure 54) which fits within the solubility range of the  $\text{Ag}_3\text{Al}$   $\mu$  phase, therefore, the d-spacing can correspond to  $\langle 222 \rangle$  crystal orientation in a complex cubic  $\beta\text{-Mn}$  structure (A13 structure). The concentration profile in inset B of Figure 54 is similar to that of Figure 52 C and D but only somewhat shallower and represents the existence range of the  $\gamma$  before the concentration drops to pure Ag. In some other parts in the reconstruction, particles of about 10 nm in size show a constant concentration of  $\sim 15$  at.% Al (see inset D in Figure 54) that matches the composition of a metastable  $\text{Ag}_5\text{Al}$  phase, according to Ref. [69], [102].

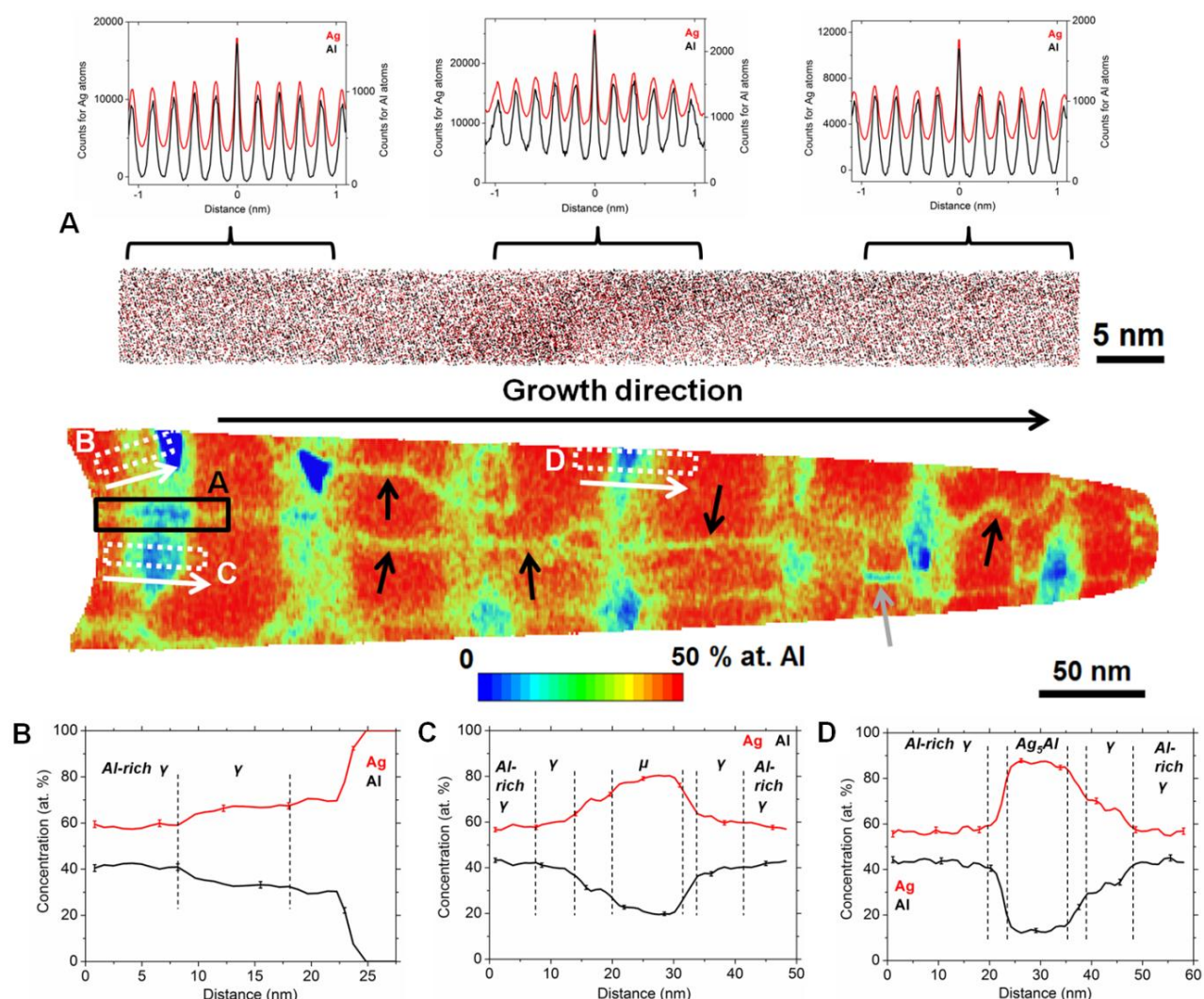


**Figure 54** APT analysis for Ag/Al multilayers of 100 nm period ramp-annealed to 435 K. 2D concentration map is presented for Al within 8 nm thick tomographic slice from the reconstruction. The thin film growth direction is marked. Black arrows mark GBs in the Al-rich  $\gamma$  phase and a grey arrow marks a clear crystallographic pole. Inset A shows a crystallographic pole along three grains.

SDM analysis from the middle grain shows smaller d-spacing (see text). Insets B, C, and D show 1D concentration profiles from the regions marked. Corresponding compositions for equilibrium  $\mu$  phase, equilibrium  $\gamma$  phase, and Al-rich  $\gamma$  phase are marked [93].

### C. After the exothermic reaction

The 100 nm period multilayer thin films were ramp-annealed to 533 K in the DSC which is a temperature above the complete exothermic reaction. The sample was then analyzed using XRD and APT. Figure 55 shows an XRD analysis of the sample which displays only the  $\text{Ag}_2\text{Al}$   $\gamma$  (hcp) intermetallic product phase. A minor peak for either Ag, Al, or both phases is detected here indicating that some traces of unreacted parent phase(s) remain at the respective annealing temperature for this multilayer period. Figure 56 shows an APT reconstruction from such sample. The APT analysis reveals that the  $\text{Ag}_2\text{Al}$   $\gamma$  intermetallic phase exhibits a homogenous concentration of 38 at.% Al and 62 at.% Ag across the whole sample. Such value fits within the equilibrium solubility range of the  $\gamma$  phase. It is worth noting here that the composition of the  $\gamma$  intermetallic phase measured by APT within all measurements have shown fluctuations on the very fine scale (1-3 nm).

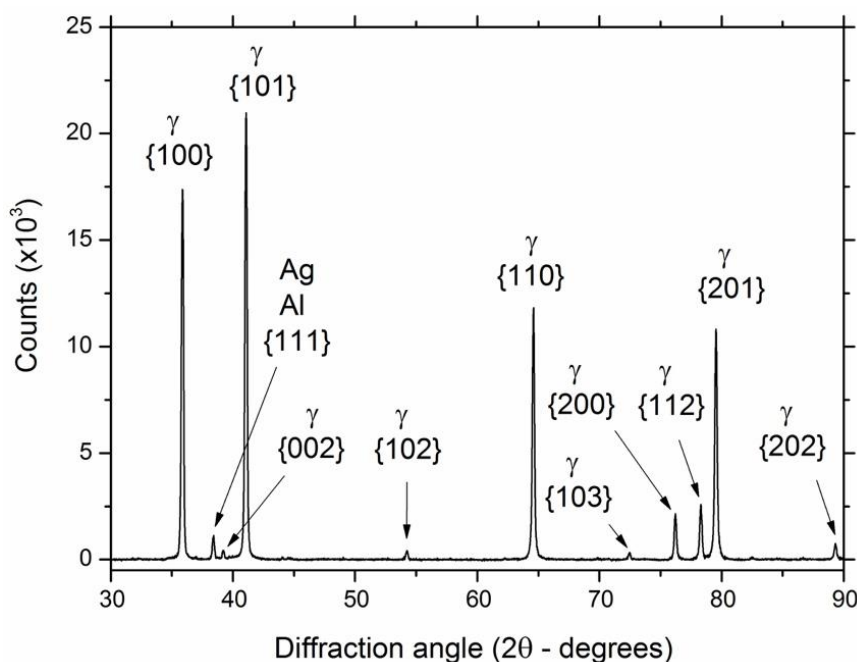


**Figure 55** XRD measurement for Ag/Al multilayer thin films of 100 nm period ramp annealed to 533 K (after the DSC exothermic peak) [93].

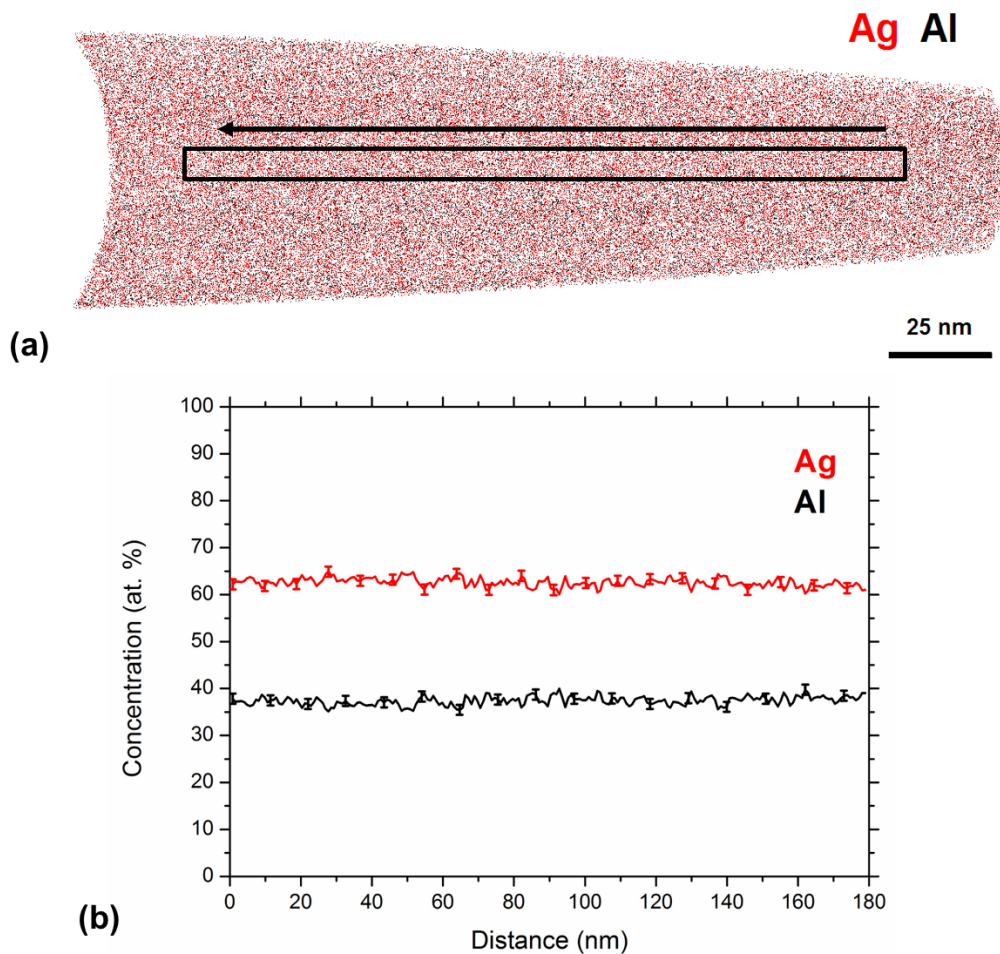


**Figure 56** APT analysis for Ag/Al multilayer thin films of 100 nm period ramp annealed to 533 K. (a) 20 nm tomographic slice in the reconstruction showing both Al and Ag atoms, respectively. (b) 1D concentration profile along the region marked in black in the reconstruction. The arrow marks the direction of the 1D measurement.

### 3.1.2.3. Phase formation in the 10 nm periods

The 10 nm period were deposited in three different compositions as was shown in section 3.1.1, where their structure and interdiffusion behavior in as-deposited condition were compared. Figure 57 shows the calorimetric response of the films in the three different compositions deposited at low sputtering power. The DSC scan for the Ag-rich composition is already shown in Figure 49, but plotted here again for comparison.

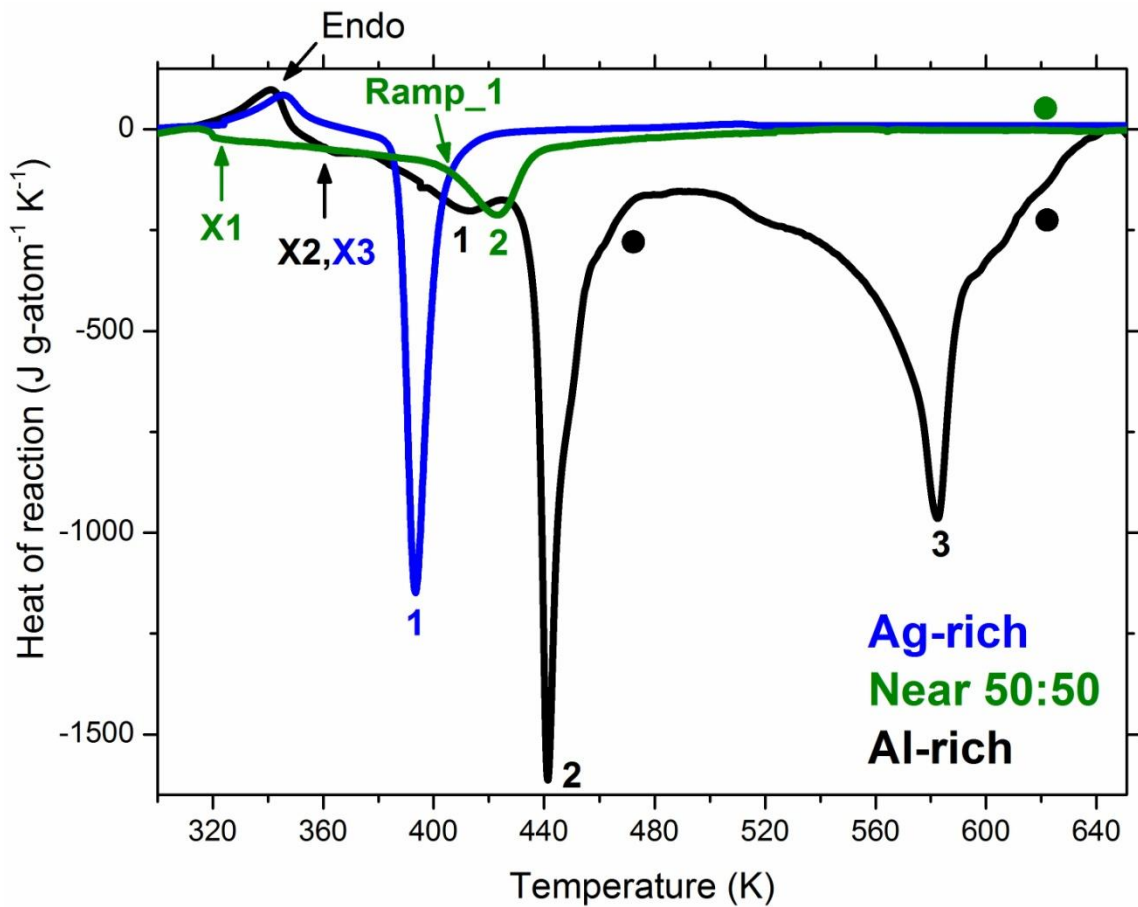


**Figure 57** DSC scans with heating rate of  $0.33 \text{ K}\cdot\text{s}^{-1}$  for the Ag/Al 10 nm periods deposited using low sputtering power (50 W) in three different compositions. The arrows marking X1-X3 mark the early broad exothermic events in each composition. The numbers in colors mark the main exothermic peaks for each composition. The arrow marking “Ramp\_1” for the near 50:50 composition as well as dots for the near 50:50 composition and the Al-rich composition mark the temperatures chosen for microstructural investigations of the reactions. The arrow marking ”Endo” marks an endothermic event that occasionally appeared in some DSC measurements of the Ag/Al multilayer thin films.

The Al-rich composition has shown three exothermic peaks. The first peak is at about 417 K, the second one is at about 444 K, and the third one is around 585 K, respectively (marked by black numbers in Figure 57). A small broad heat release is detected before the first peak in each composition, which occurs earliest in the near 50:50 sample (marked by X1-X3 in Figure 57). An endothermic event around 340 K was often detected in some DSC measurements which is expected to form due to evaporation of condensed water on the cooled films. The near 50:50 composition has shown one main exothermic peak at about 425 K. The enthalpy for the first main exothermic peak in

all compositions was calculated to be around  $-12 \text{ kJ.g-atom}^{-1}$ . The phase formation and nucleation behavior in each of the three conditions were compared by combining calorimetric and microstructural analysis.

### **A. Ag-rich composition**

To investigate the reaction mechanism in the 10 nm period of Ag-rich composition the films were annealed isothermally for 2 hours at 323 K under vacuum. Isothermal treatment was chosen here to elucidate the early stages of the reaction, given the fact that when these films are ramp-annealed in the DSC they show a narrow DSC exothermic peak where the multilayers are expected to exhibit a spontaneous reaction leading a rapid and complete transformation to the hcp intermetallic phase.

Figure 58 shows an APT analysis of the 10 nm of Ag-rich composition after isothermal treatment. The analyzed volume represents a snapshot during the phase transformation reaction in the film. The propagation direction of the reaction detected within this reconstruction is opposite to the film growth direction, and it is possible to study the phase formation evolution. Inspecting the 2D concentration map and the 1D concentration profile measurement, several observations can be reported. At a first glance, it is clear that the multilayer structure starts to collapse at a region where the morphology of the layers is interrupted by a vertical GB. Thus, it can be assumed that the collapse of the multilayer structure predominantly initiates at the GB region. This is highly expected since strong interdiffusion is detected at the GBs directly after deposition (see Figure 31). Remarkably, if it comes to the layered structure distant from the GB, the concentration profile of Figure 58(b) reveals that the Ag diffuses into the thin Al layers, whereas no Al diffuses into the Ag layers. In fact, in the Ag layers, the composition is still at 100 at.% Ag, while in the Al layers various concentrations between 60 and 80 at. % Al are detected which must be fcc solid solution, since no other phases appear in that composition range in the phase diagram.

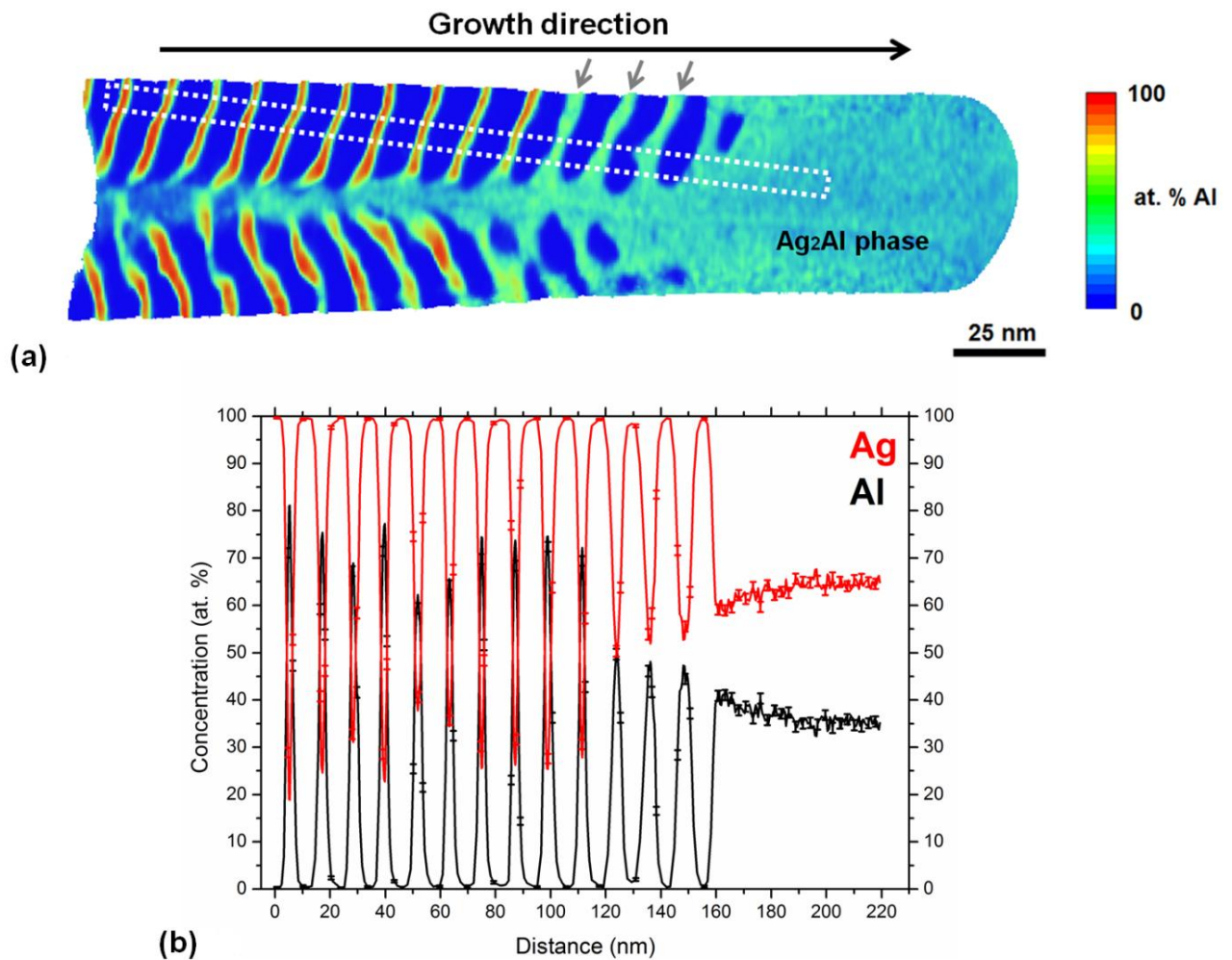
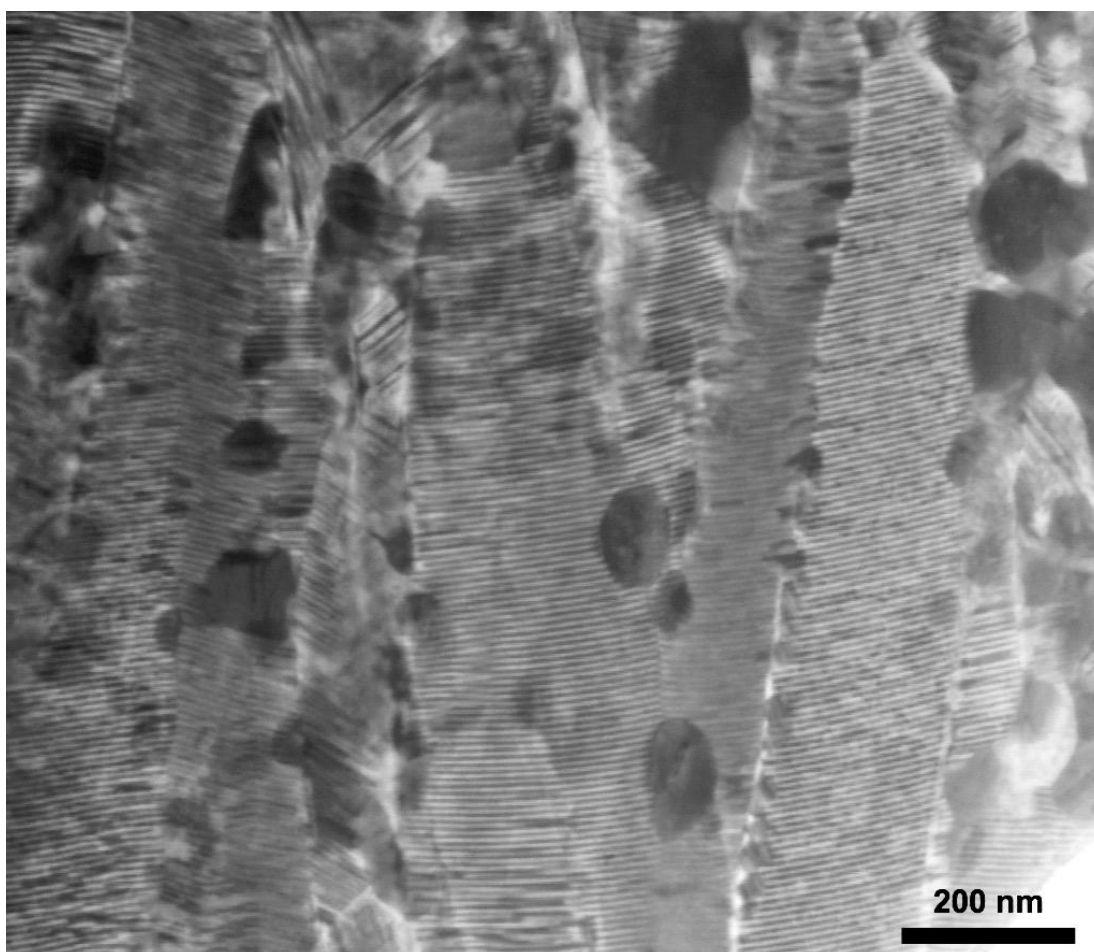


**Figure 58** APT analysis for Ag/Al multilayer thin films of 10 nm period (Ag-rich composition) after isothermal treatment. (a) 2D concentration map for Al within 8 nm thick tomographic slice from the reconstruction. The thin film growth direction is marked. Grey arrows mark three thickened layers reflecting nucleation and growth (b) 1D concentration profile along the region marked [93].

It is also interesting that some supersaturated Al layers become thicker below concentrations of about 51 at.% Al (marked by grey arrows in Figure 58(a)). This indicates the formation of a transient metastable intermetallic  $\text{Ag}_{50}\text{Al}_{50}$  phase, which has been predicted from theoretical considerations [102]. Consumption of the Ag layers follows, until the homogenous intermetallic  $\text{Ag}_2\text{Al}$   $\gamma$  phase is finally attained. The intermetallic phase reaches a constant composition of  $\sim 35$  at. % Al, which lies within the solubility range of the equilibrium  $\text{Ag}_2\text{Al}$   $\gamma$  phase, and matches the total nominal composition of the deposited thin film. Note the concentration gradient within the  $\text{Ag}_2\text{Al}$   $\gamma$  phase at the proximity of the multilayer region (see Figure 58(b)). This gradient reflects the existence range of the  $\gamma$  phase from 35 to 41 at.% Al in the phase diagram, as the  $\gamma$  is collecting Ag from the remaining Ag parent phase.

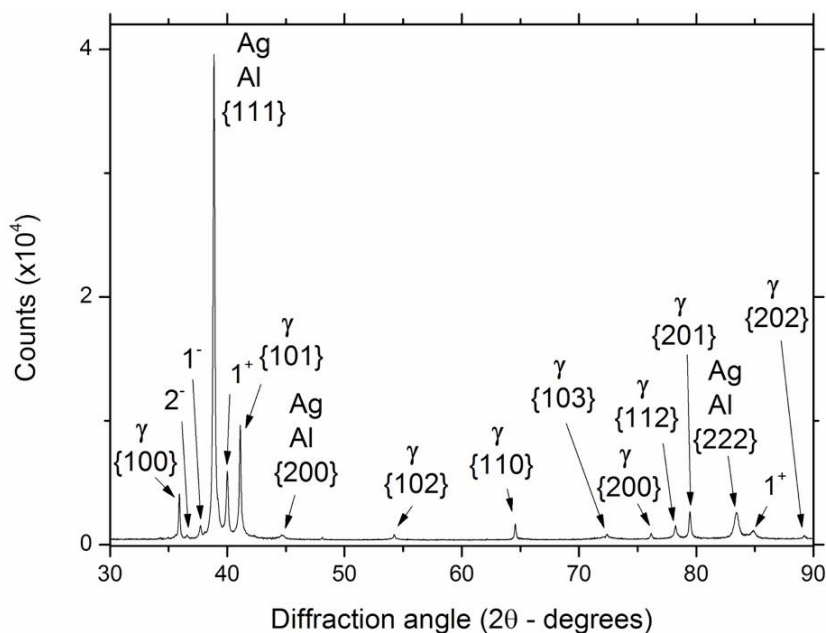
## B. Al-rich composition

The product after the second exothermic peak detected for the 10 nm period of Al-rich composition is investigated. For this investigation, the films were ramp-annealed in the DSC to a temperature above the exothermic peak (480 K), which is marked by the first black dot shown in Figure 57, and the microstructure was consequently studied. Figure 59 shows the STEM results from thin films after ramp-annealing to such temperature. Surprisingly, a multilayer structure is still detected in most of the sample. A new phase is seen in STEM to have nucleated along the boundaries separating the columns of grains within the structure, that are namely the vertical GBs as well as the topographic defects, which were observed in the as-deposited condition (see Figure 39). Furthermore, some fringe-like features were observed that appear to form diagonally with respect to the film growth direction.



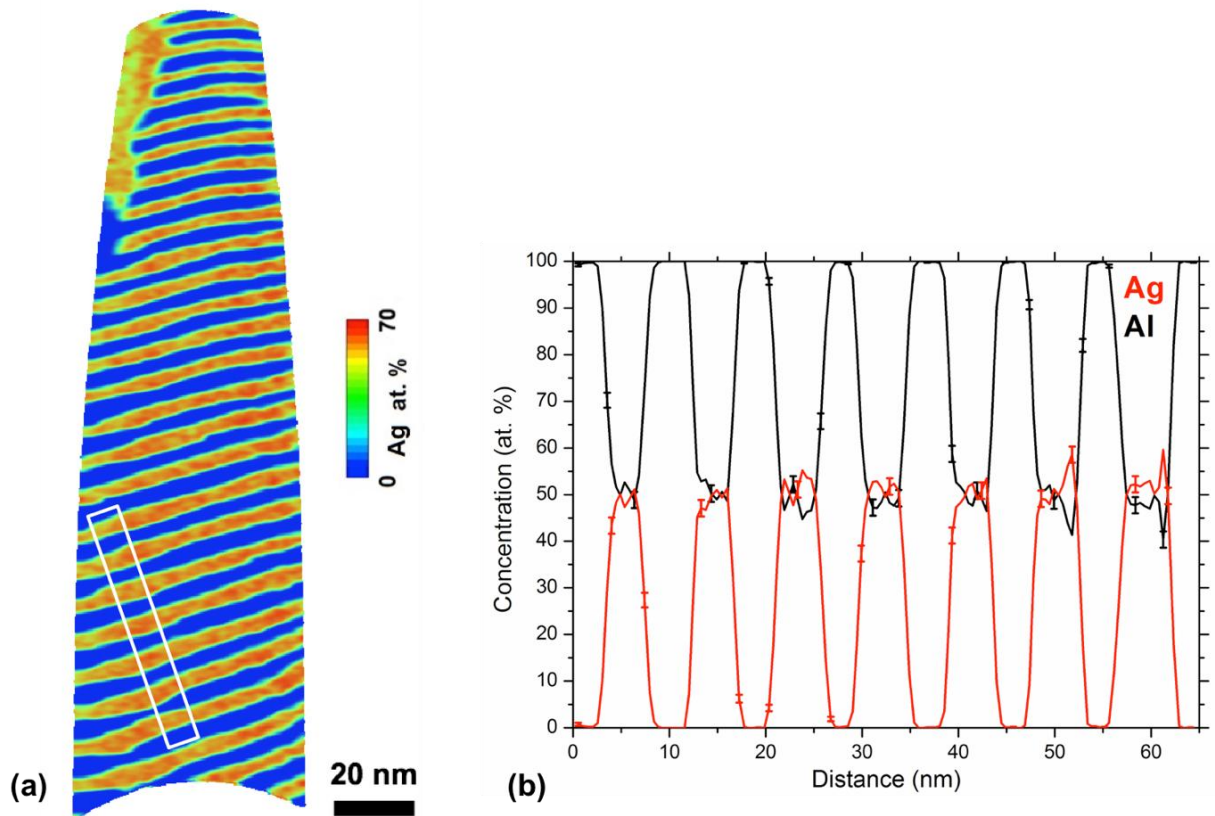
**Figure 59** BF-STEM for Ag/Al multilayer thin films of 10 nm period of Al-rich composition ramp-annealed to a temperature of 480 K (after 2<sup>nd</sup> DSC peak).

Figure 60 shows an XRD analysis of such sample condition. Diffraction peaks for the  $\gamma$  (hcp) phase were detected as well as Ag+Al peaks. Satellite peaks were also detected in this sample confirming that a superlattice structure is still existent after ramp-annealing to 480 K. No other intermetallic phases were detected in this sample condition. Therefore, so far, the exothermic peak can be understood to be the heat release due to the nucleation and growth of the  $\gamma$  (hcp) phase.



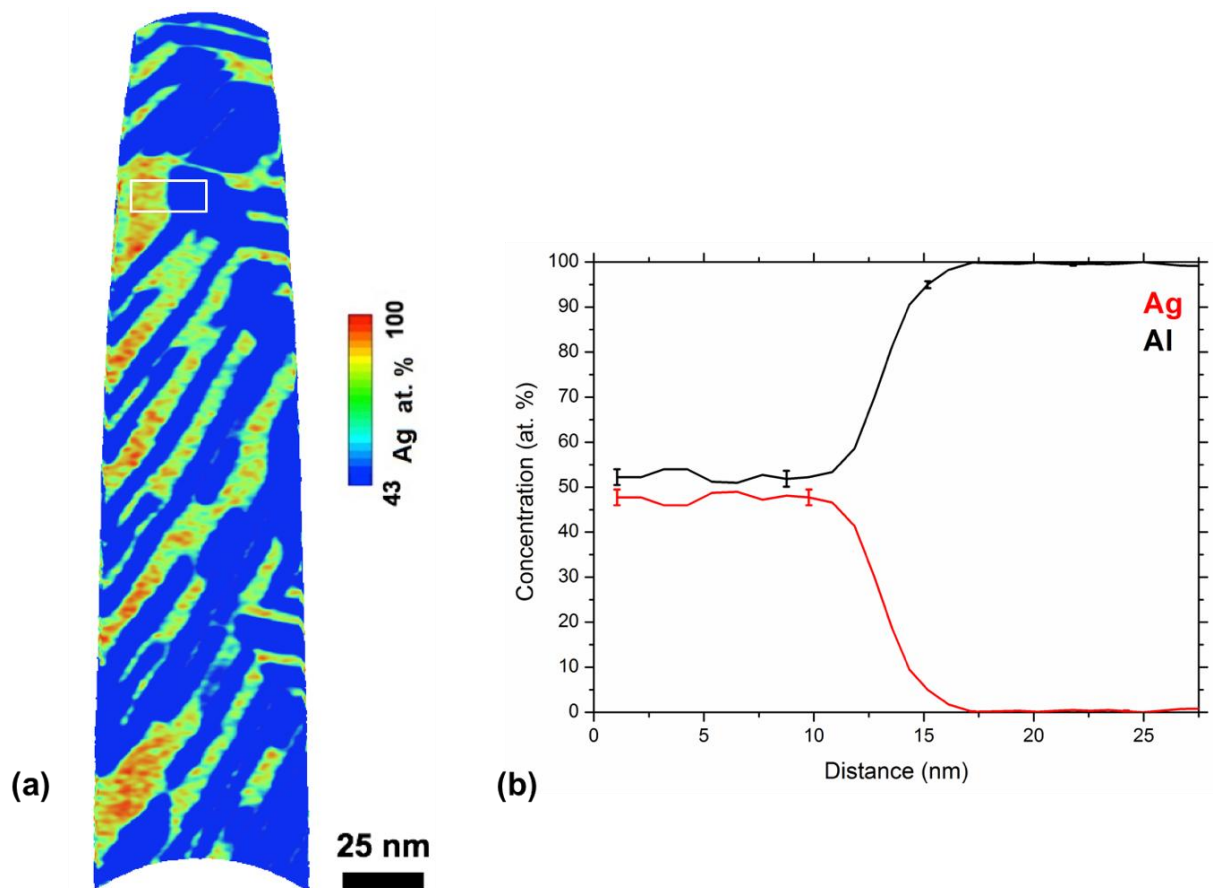
**Figure 60** XRD measurement for Ag/Al multilayer thin film of 10 nm period of Al-rich composition ramp-annealed to a temperature of 480 K (after 2<sup>nd</sup> DSC peak). Satellite peaks of Ag/Al diffraction peaks are marked. The number refers to their order.

Figure 61 shows an APT analysis from the same sample. The dataset displays the multilayer structure seen by STEM imaging. The multilayer consists of pure Al layers and an intermetallic phase exhibiting a 50:50 composition of Ag:Al. The intermetallic phase is shown to have formed where all Ag parent phases existed of this sample. Moreover, the thickness of the Al and AgAl layers are identical, showing that the intermetallic phase nucleated in the diffused Ag parent phases and has grown in thickness from about 3 nm up to 5 nm. Moreover, the reconstruction has also shown an island of AgAl intermetallic phase next to the multilayers, which agrees with the phases seen at the boundaries separating the columns of grains detected by STEM. It is worth noting that the composition of the AgAl phase has shown some fine fluctuations inside the layers as well as in the islands. Several APT datasets analyzed from this sample condition have displayed the same results.



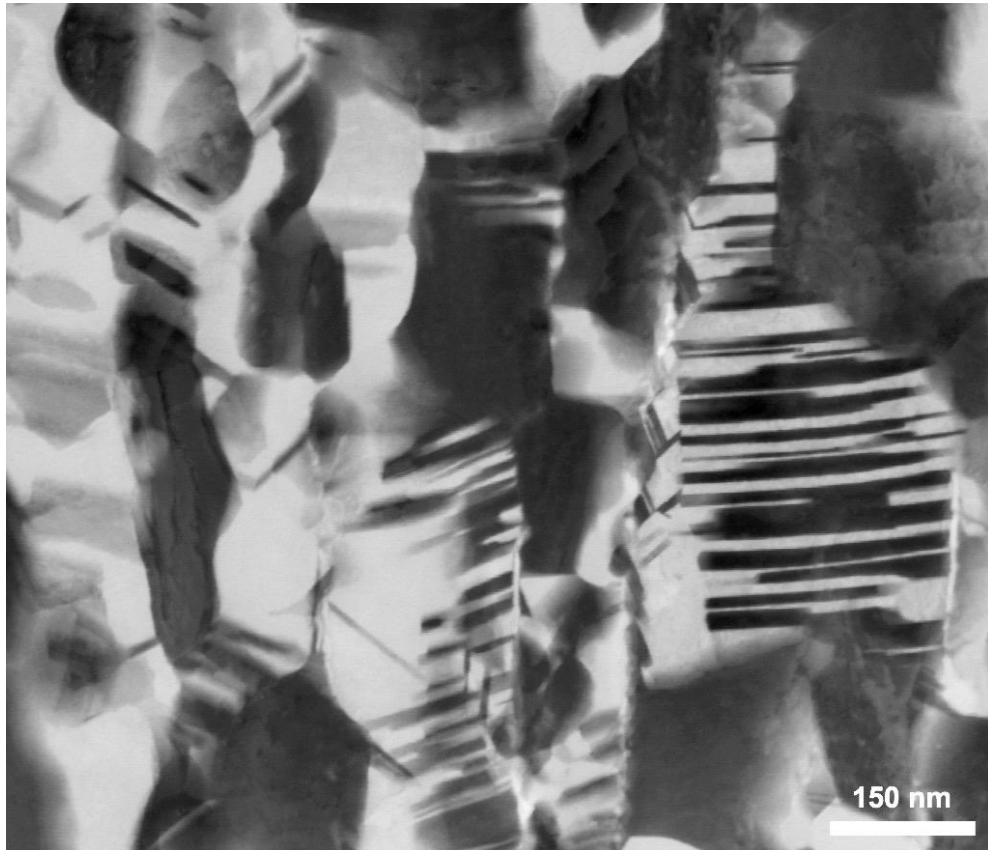
**Figure 61** APT analysis for Ag/Al multilayer thin films of 10 nm period of Al-rich composition ramp-annealed to a temperature of 480 K (after 2<sup>nd</sup> DSC peak). (a) 2D concentration map for Ag within 10 nm thick tomographic slice from the reconstruction. (b) 1D concentration profile from the region marked in the reconstruction.

Figure 62 shows an APT analysis from the same sample, but from a region where diagonal fringe-like features exist (see Figure 59). The reconstruction displays the same two phases as detected in the multilayer regions, namely; pure Al phase and a 50:50 AgAl phase with fine fluctuations in the composition. The phases are present in islands and in layers, respectively. The thin layers of the intermetallic phase are connected to thicker layers. It can be therefore understood that the intermetallic phase grows while maintaining its layered structure, and during growth it coalescences with other layered structures to form thicker layers. The interfaces between the Al and the intermetallic phase were relatively sharp (~1 nm thick) in all the APT measurements for this condition. Eight APT datasets were measured from this sample with relatively large volumes (40-60 million atoms detected) where only these two phases were detected. It can be therefore understood that the intermetallic phase detected exhibits the structure of the  $\text{Ag}_2\text{Al}$   $\gamma$  (hcp) phase detected by XRD but with composition of 50:50 AgAl. Thus, this confirms the formation of the metastable intermetallic  $\text{Ag}_{50}\text{Al}_{50}$  phase of hcp structure, which is predicted from theoretical considerations [102].



**Figure 62** APT analysis for Ag/Al multilayer thin films of 10 nm period of Al-rich composition ramp-annealed to a temperature of 480 K (after 2<sup>nd</sup> DSC peak). (a) 2D concentration map for Ag within 8 nm thick tomographic slice from the reconstruction. (b) 1D concentration profile from the region marked in the reconstruction.

The product of the third exothermic peak detected for the 10 nm period of Al-rich composition is investigated. For this investigation, the films were ramp-annealed in the DSC to a temperature above the third exothermic peak (620 K), which is marked by the second black dot shown in Figure 57, and the microstructure was consequently studied. Figure 63 shows the STEM results from multilayer thin film after ramp-annealing to such temperature. Large grains of Al seen in light grey color along with large grains of the intermetallic hcp phase seen in dark grey color. Layer structures were still detected in the sample with various thicknesses for each of the phases, respectively, but relatively thicker compared the layers observed after the second exothermic peak. It is also worth noting that gradients in the contrast within many grains were detected. Figure 64 shows an XRD analysis for such sample condition. Diffraction peaks for the  $\gamma$  (hcp) phase were detected as well as Al (fcc) peaks. No satellite peaks were detected, neither any intermetallic phases other than the  $\gamma$  (hcp) phase.



**Figure 63** BF-STEM for Ag/Al multilayer thin films of 10 nm period of Al-rich composition ramp-annealed to a temperature of 620 K (after 3<sup>rd</sup> DSC peak).

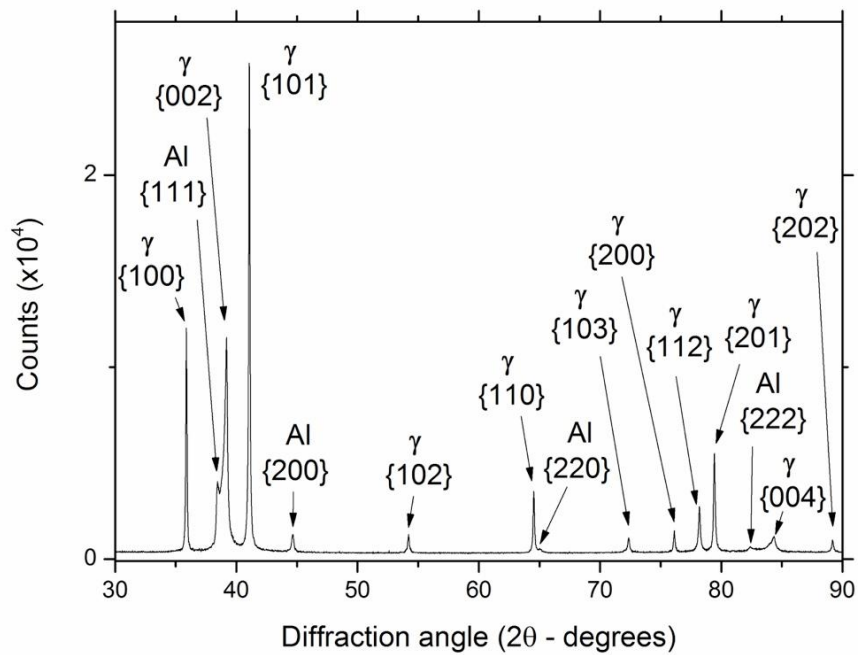


**Figure 64** XRD measurement for Ag/Al multilayer thin film of 10 nm period of Al-rich composition ramp-annealed to a temperature of 620 K (after 3<sup>rd</sup> DSC peak).

Figure 65 shows APT analysis from the same sample. The composition of the intermetallic phase was inhomogeneous, where it showed in some regions to exhibit a 50:50 composition while in some other regions was slightly more Ag-rich (55 at.% Ag, 45 at.% Al). The layer structures and the large grains of both phases seen in STEM were detected by APT. However, fine clusters of Ag were observed in the Al grains, which are expected to be early formation of GP zones, which can be seen in Figure 65(b) as fluctuations in the concentrations within the Al grain. Therefore, the third exothermic peak is understood to be heat release due to the coalescence of the phases as well as nucleation of GP zones in the fcc Al phase.

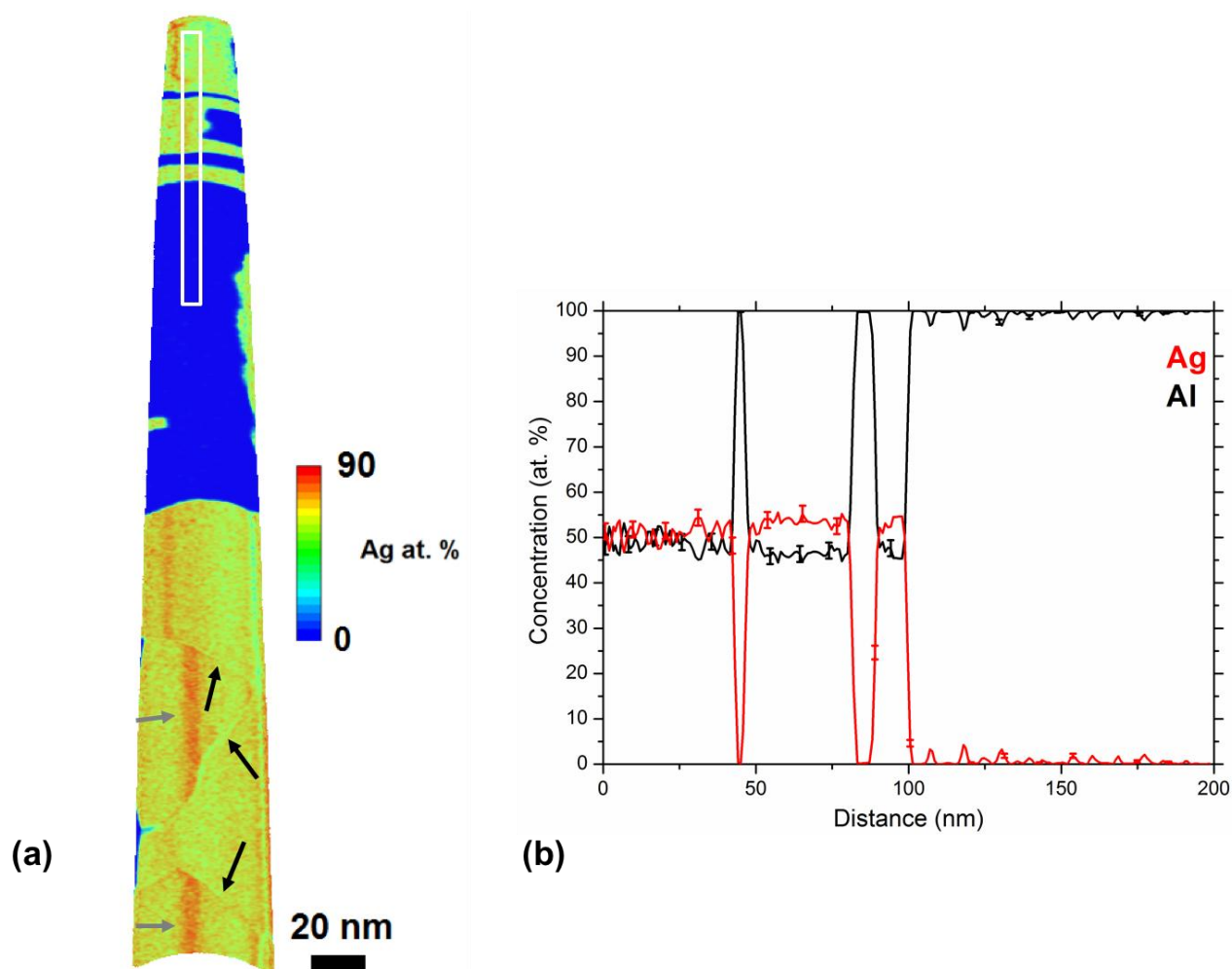


**Figure 65** APT analysis for Ag/Al multilayer thin films of 10 nm period of Al-rich composition ramp-annealed to a temperature of 620 K (after 3<sup>rd</sup> DSC peak). (a) 2D concentration map for Ag within 8 nm thick tomographic slice from the reconstruction. Black arrows mark GBs in the hcp phase and grey arrows mark regions of crystallographic poles (b) 1D concentration profile from the region marked in the reconstruction.

### C. Near 50:50 composition

Based on the results of the Al-rich composition, the exothermic peak observed in films with near 50:50 composition is expected also to be heat release due to the formation of the intermetallic hcp phase, with either 50:50 composition or closer to the equilibrium stoichiometry of the  $\gamma$  phase. The mechanism for the phase formation is more of interest to study here, since in the as-deposited condition interdiffusion occurs in both the Ag and Al parent phases, respectively. The films were ramp-annealed in the DSC to 405 K which is an early stage of the exothermic reaction (marked by “Ramp\_1” in Figure 57), and the microstructure was consequently studied. Figure 66 shows the STEM results of the thin films after ramp-annealing to such temperature. The nucleation and growth of an intermetallic phase is again evident to form at the vertical GBs and the tomographic defects in the microstructure. Most of the sample volume is still in the multilayer structure. Figure 67 shows an XRD measurement of this sample condition. One relatively small diffraction peak for the intermetallic  $\gamma$  phase is detected. Satellite peaks were detected which highlight the superlattice structure in the sample.

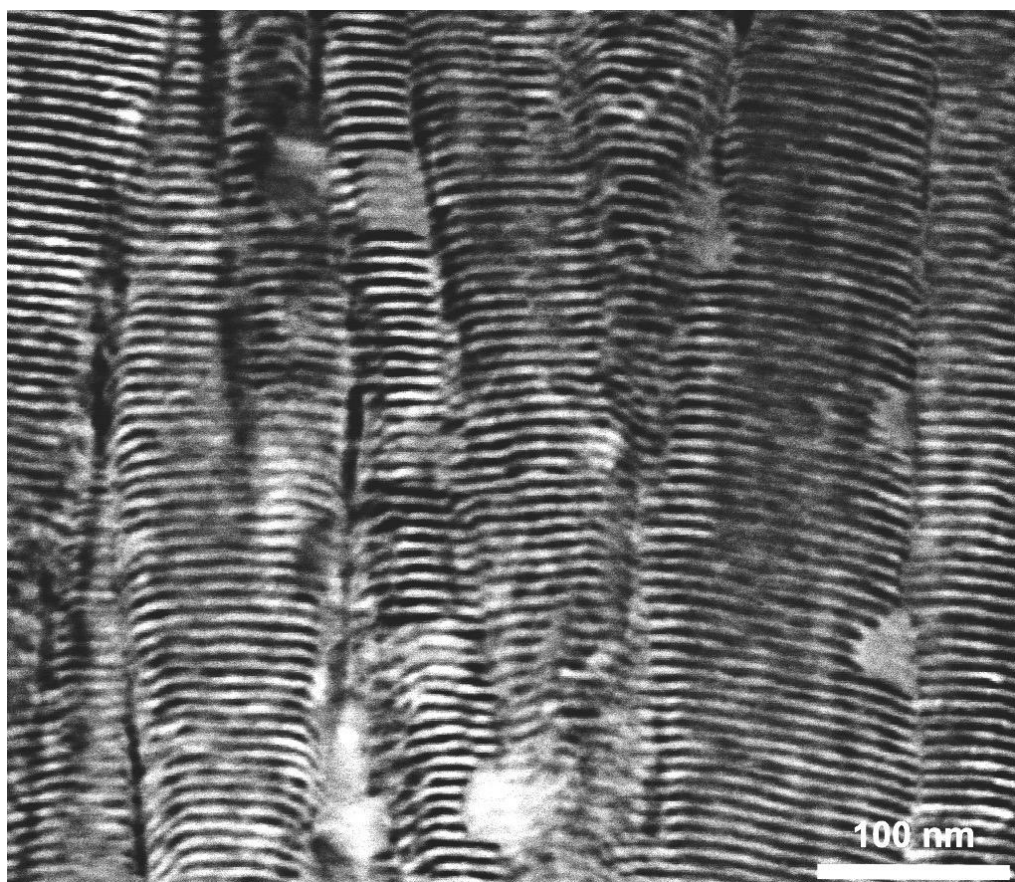


**Figure 66** HAADF-STEM for Ag/Al multilayer thin films of 10 nm period with near 50:50 composition ramp-annealed to a temperature of 405 K.

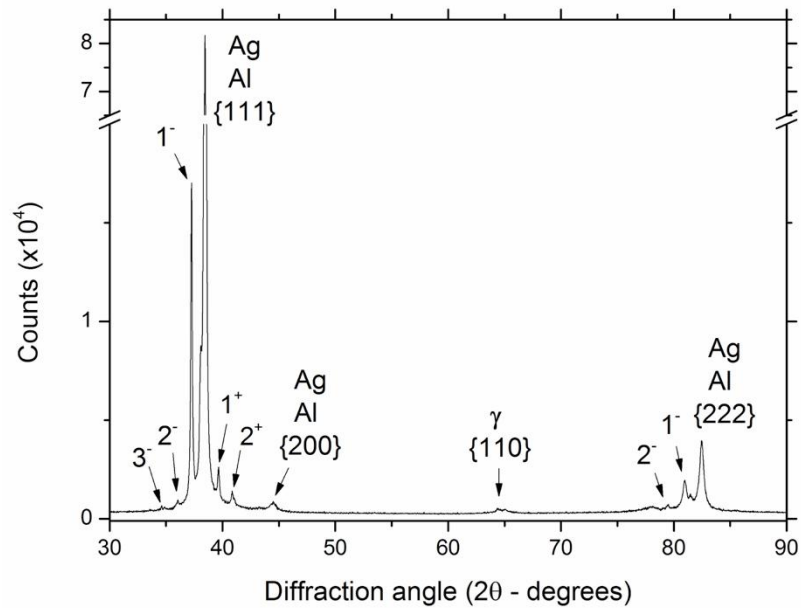


**Figure 67** XRD measurement for Ag/Al multilayer thin film of 10 nm period with near 50:50 composition ramp-annealed to a temperature of 405 K. Satellite peaks of Ag+Al diffraction peaks are marked. The number refers to their order.

Figure 68 shows an APT analysis from the multilayer region of the same sample. Interdiffusion is observed to occur in both the Al and the Ag layers, respectively. The interdiffusion appears strongly inhomogeneous along the phase boundary interfaces. The mass transport seems to be facilitated along line defects within the microstructure which offer faster diffusion compared to lattice diffusion. Hence, 1D-profile measurements across the multilayers were not carried out here to avoid averaging out the local interdiffused regions at the phase boundaries. Figure 69 shows an APT analysis from a region where the intermetallic phase has formed as shown in Figure 66. The APT analysis reveals that the phase formed exhibits a 50:50 composition similarly to the composition of the intermetallic phase formed in the films with the Al-rich composition. However, here the reaction occurs simultaneously in both parent phases. The interdiffusion behavior observed in the as-deposited case is therefore maintained by annealing the films up to a point where intermetallic phase nucleates and both layers become consumed by the new growing intermetallic phase. Nevertheless, the Ag layers seem to get consumed slightly faster than the Al layers (see inset A in Figure 69).

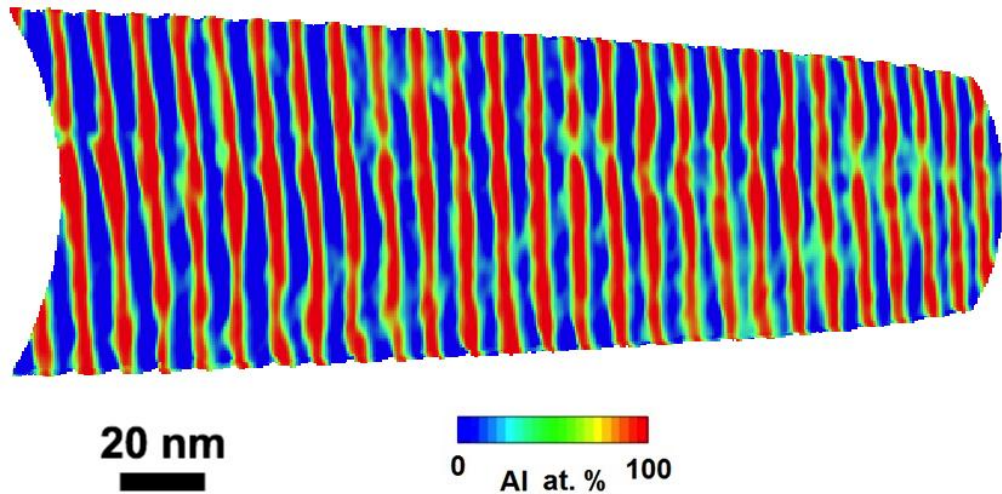


**Figure 68** APT analysis for Ag/Al multilayer thin films of 10 nm period with near 50:50 composition ramp-annealed to a temperature of 405 K. The image shows a 2D concentration map for Al within 8 nm thick tomographic slice of the reconstruction in the multilayer region.

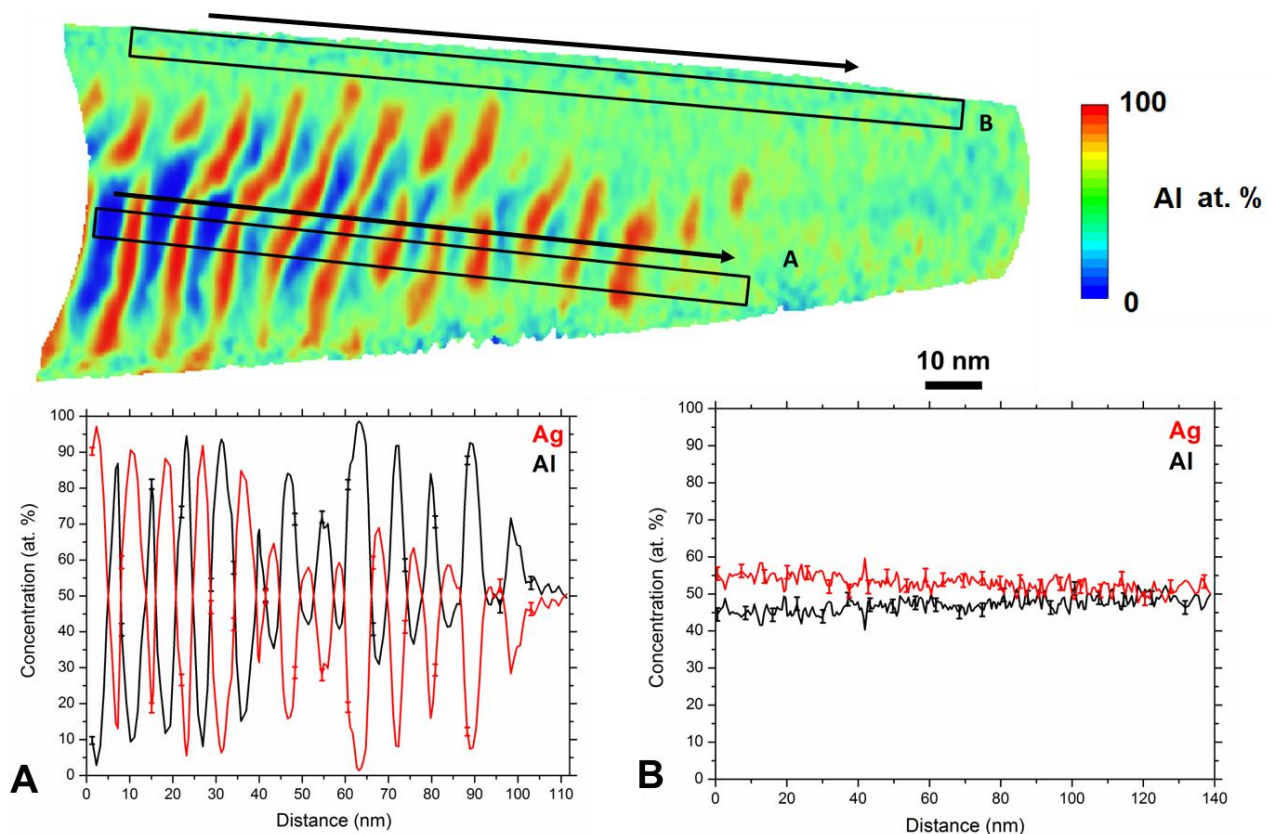


**Figure 69** APT analysis for Ag/Al multilayer thin films of 10 nm period with near 50:50 composition ramp-annealed to a temperature of 405 K. The image shows a 2D concentration map for Al within 8 nm thick tomographic slice of the reconstruction in a region where the intermetallic phase is observed to nucleate and grow. The two insets at the bottom show 1D concentration profiles from the two regions marked. The arrow shows the direction of the profile measurement.

It was of interest to study the condition of these films after ramp-annealing to considerably higher temperatures above the exothermic peak. The films were ramp-annealed in the DSC to a temperature of 620 K, and the microstructure was consequently studied. Figure 70 shows a STEM image of the microstructure after ramp-annealing to such temperature. Most of the structure shows the intermetallic phase in dark grey color with some grains of Al seen in light grey color. Within the intermetallic phase, some layers are detected which appear to be diffused, which are expected to be precipitations of the equilibrium  $\text{Ag}_2\text{Al}$  phase within the metastable  $\text{AgAl}$  intermetallic phase. Al was also detected in fringe-like features within the microstructure. Therefore, some Al remain unreacted at higher temperature which is understood to be related to the minor Al enrichment of these films and the fact of the miscibility gap existent in the Al-rich region of the phase diagram, as well as Al diffusing out of the 50:50 metastable phase at high temperatures (see discussion below). The columnar structure is still evident as well as the topographic defects. Figure 71 shows an XRD measurement from the same sample condition. The analysis confirms that only the Al fcc phase and  $\gamma$  hcp phase exist in the sample, respectively. No satellite peaks were detected for the fcc structure.

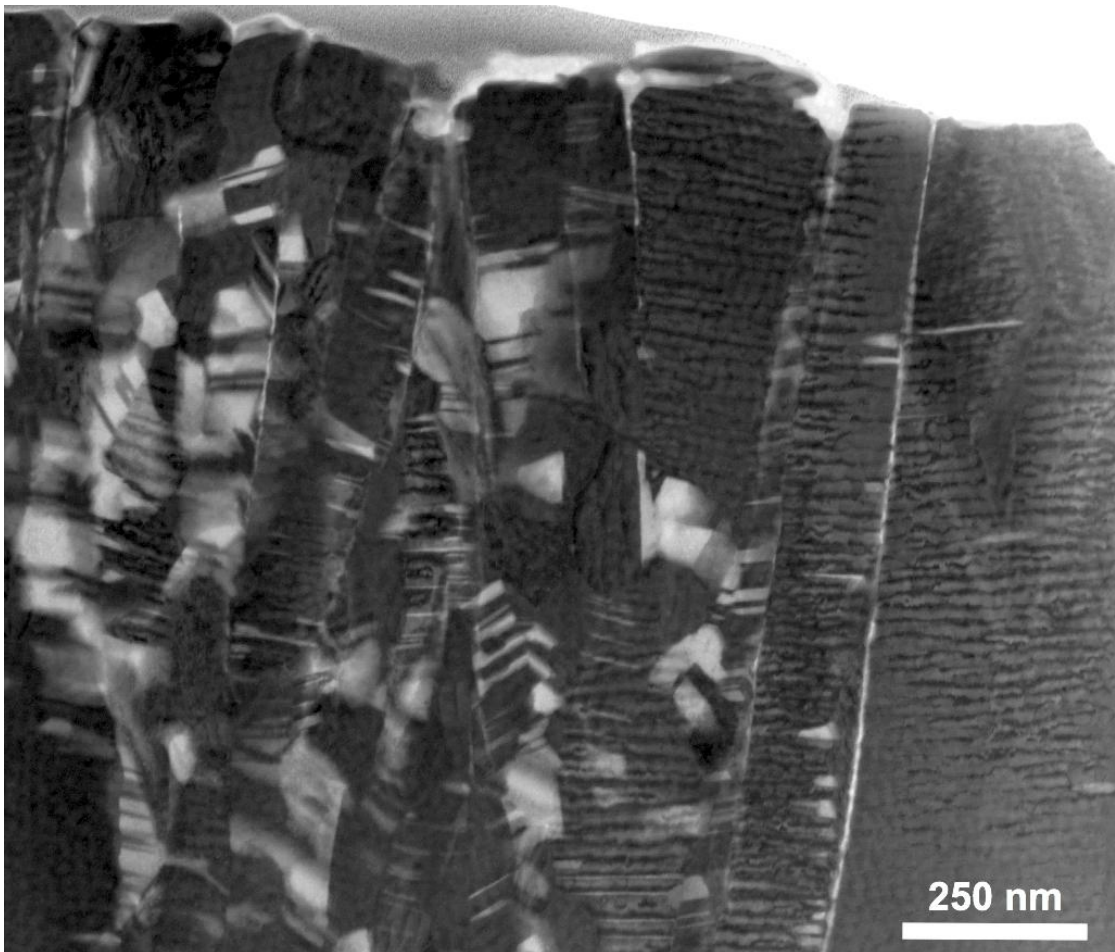


**Figure 70** BF-STEM for Ag/Al multilayer thin films of 10 nm period with near 50:50 composition ramp-annealed to a temperature of 620 K.

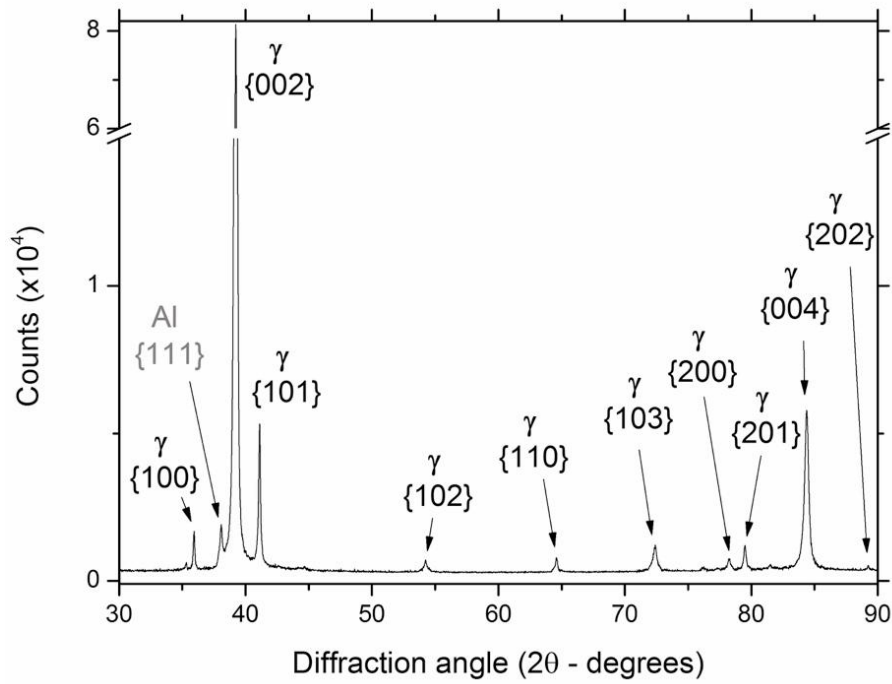


**Figure 71** XRD measurement for Ag/Al multilayer thin film of 10 nm period with near 50:50 composition ramp-annealed to a temperature of 620 K.

## 3.2. Ru/Al system

As mentioned in section 1.10, the investigation of interdiffusion and phase formation in the Ru/Al system was carried out within limited extent, due to some constraints in extracting high quality datasets via APT. However, some valuable results were collected which highlight the kinetics in this system in the as-deposited condition and during the early phase formation, respectively.

### 3.2.1. As-deposited films

#### 3.2.1.1. Multilayer thin films

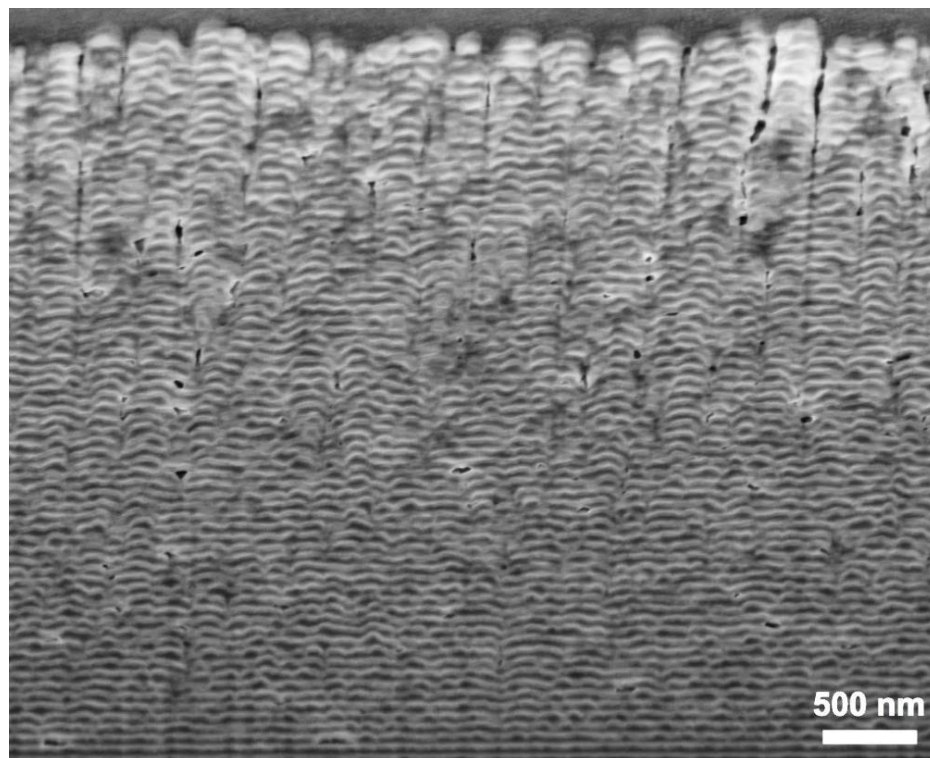


**Figure 72** SEM image for Ru/Al multilayers of 44 nm bilayer period.

Figure 72 shows a cross section for Ru/Al multilayers of 44 nm bilayer period imaged by SEM. In bright contrast are the Al layers and in dark contrast are the Ru layers, respectively. Columnar growth is hardly observed in the multilayers. However, columnar growth is known to exist in the growth of such multilayers but disappears after a critical period thickness (about 4.5 nm) due

increase in the roughness [41]. It is also known that the growth direction of the Ru layers is along the  $\langle 0001 \rangle$  hexagonal close packed (hcp) direction while the Al layers grow along the  $\langle 111 \rangle$  fcc direction, respectively [41]. The homologous temperature,  $T_h$  (calculated from Eq. 36) for Al is calculated to be 0.38 and for Ru to be 0.13, respectively, estimating the substrate temperature here to be around 353 K. Difference in the homologous temperatures for both elements is considered to be large in this case. High interfacial roughness of the multilayers can be clearly observed which increases gradually along the growth direction. After a certain distance from the substrate the disorder in the multilayer structure becomes significantly high that most layers get disconnected in the lateral direction and high density of topographic defects develop in the microstructure. Pores were also observed in the films as a result of the high disorder in the multilayer structure. APT analysis was carried out on these multilayer thin films to determine the interdiffusion behavior.

Figure 73 shows an APT analysis of the same sample condition. Only two layers are detected in the reconstruction. The layer interface detected appears diagonal in the reconstruction and is not perpendicular to the main tip axis which is due to the high disordered structure of the multilayers as seen in Figure 72. It was generally not possible to collect large datasets from the Ru/Al multilayer thin films due to premature fractures of the tips near the interfaces during field evaporation, which can occur here to two main reasons, firstly due to dynamic changes in the end tip during field evaporation, and secondly due to the high concentration of voids expected here at the interfaces in these films as a result of the film growth behavior. Furthermore, the quality of the measurements is insufficient to carry out analysis across the interfaces for precisely quantifying the interfacial mixing. This is primarily due to local magnification effects and ion-trajectory aberrations that occur because of strong differences in the field evaporation values of Ru and Al, respectively ( $F_{\text{Ru}} = 41 \text{ V/nm}$ ,  $F_{\text{Al}} = 19 \text{ V/nm}$  [67]). Low density of Ru atoms can be observed in the topographic slice shown in Figure 73 compared to Al atoms, which highlights the uneven field evaporation rate of ions across both layers. Reconstruction artifacts induced because of field evaporation differences and dynamic changes in the end tips shapes during measurements are explained below (section 3.2.1.2). Nevertheless, the reconstructions revealed clear results regarding GB diffusion, where Al segregations were detected along GBs in the Ru layers (see Figure 73). The same behavior was detected in the 66, and 88 nm periods as well (not shown here). The Ru layers have displayed very fine crystal structures compared to Al, where several GBs are detected within the reconstructions. Precise quantification of the segregations at the GBs in the APT reconstructions was not possible to be provided due to the field evaporation artifacts. However, the extension of the Al diffusion in the Ru GBs was significant compared to the thickness of the individual layers.

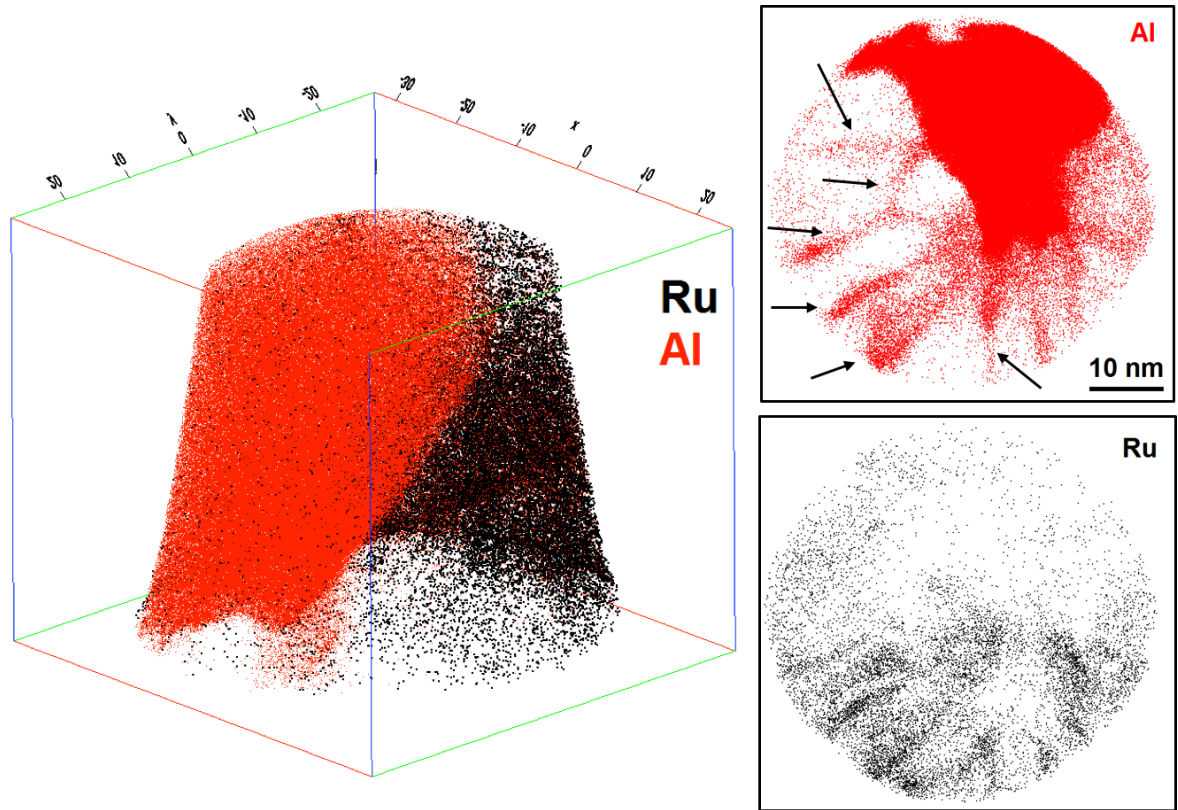


**Figure 73** APT analysis for Ru/Al multilayers of 44 nm period. The two insets on the left represent a 8 nm thick tomographic slice along the main axis of the tip. Al and Ru atoms are shown separately. GBs are marked by black arrows.

### 3.2.1.2. Local magnification effects

Being solely based on the projection of ions from the surface of a sharp tip in APT, the quality of the field desorption map on the detector is extremely sensitive to the shape of the end-tip curvature, as well as the field evaporation rate of the ions from the surface of the tip. The electric field on the end-tip can be directly related to the end-tip radius by the simple equation:

$$F_{elect.} = \frac{V_{tip}}{k_f R_{tip}} \quad (42)$$

where  $V_{tip}$  is the applied voltage on the tip,  $k_f$  is the shape factor constant, and  $R_{tip}$  is the end-tip radius. The field on the tip is therefore enhanced for smaller radius values. If the tip is composed of a multiphase material in which a significant difference in the field evaporation values for the individual

phases exists ( $\Delta F_{elect.} > 20\%$  [103]), therefore the phase with lower field evaporation value would evaporate at a faster rate compared to the other phase. This condition instantly develops irregular curvatures at the end-tip, where local field enhancements occur due to the local protrusions at the tip surface. Furthermore, a step on the tip surface is created along the interface between the phase retained on the surface (high field phase) and the protruded phase (low field phase). This induces trajectory aberrations of the ions evaporating along such steps. Hence, segregations or concentration gradients measured across the interfaces can be strongly inaccurate using standard reconstruction algorithms which assume constant tip geometry throughout the measurement. Beside reconstruction artifacts originating from ion-trajectory aberrations, the irregular surface developed on the tip also leads to local stress enhancements which results in less stable samples and premature fractures during measurements. APT samples are normally under high mechanical stresses that is associated with the high applied voltages, where stresses can be generally in the range from a few hundred MPa up to a few GPa [104]. Irregular tip shapes are more susceptible to premature fracture due to stress enhancements at the deformed steps. Moreover, tips with high residual stresses, high concentration of voids, structural defects and a generally brittle nature are also likely to fail rapidly during APT measurements. Further information regarding reconstruction artifacts and limitations of the APT technique is available in Refs. [67], [105].

### **3.2.1.3. Trilayer thin films**

To improve yield and collect more data from the interfaces, it was necessary at least to minimize the roughness of the interfaces. Flatter layers are more likely to produce stable APT measurements due to reduced voids at the interfaces during film growth. However, local magnification issues cannot be circumvented, interfaces become blurred in the datasets and the tips can anyhow fracture under extreme deformations during measurements.

Investigating trilayer thin films has produced more successful results in comparison to multilayers. Figure 74 shows a TEM image from the trilayer sample where in dark contrast is the Ru layers and in bright contrast is the Al layer. The layer interfaces appear relatively flat compared to the interfaces detected in the multilayer samples. However, the morphology of the Al on Ru interface appears slightly different compared to the Ru on Al interface. The bottom interface is somewhat rough compared to the upper one, where the fine grain structure of the Ru layer is observed to induce such

rough interface. The grain structure in the Al layers appears to be coarser compared to the Ru layers, which clearly influences the morphology of the upper interface.

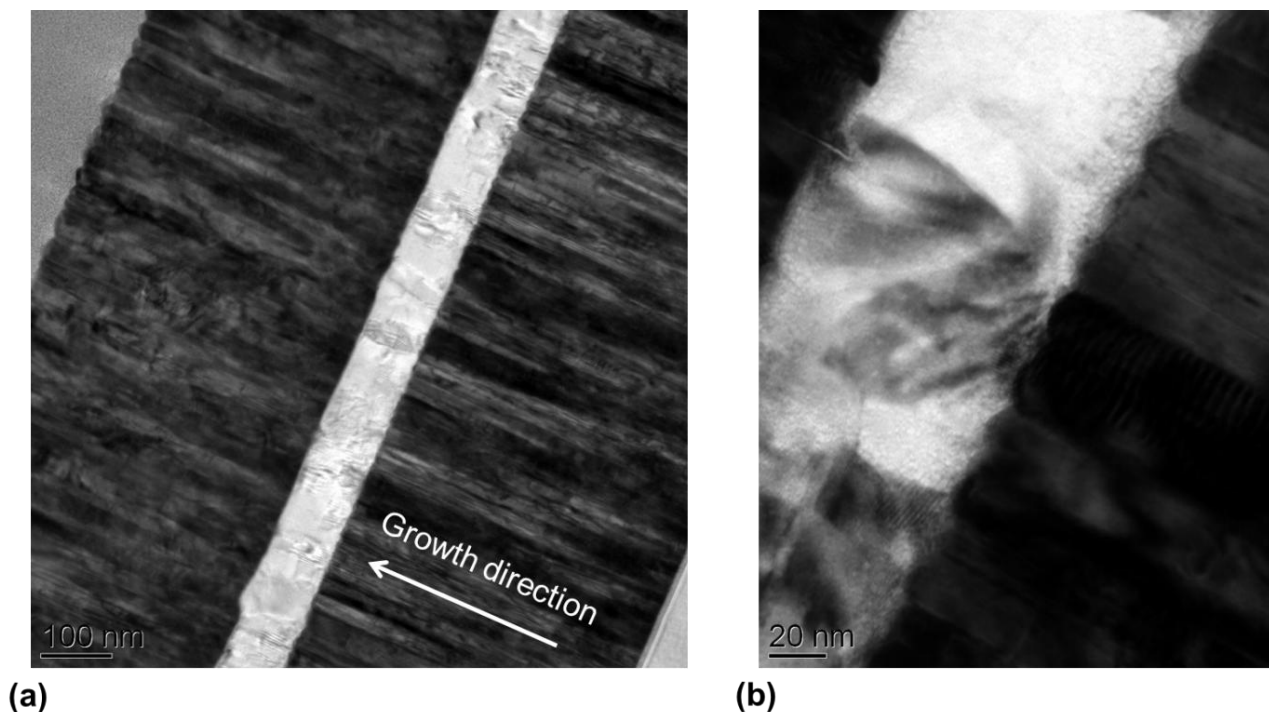


**Figure 74** BF-TEM for the Ru/Al trilayer structure. (a) An overview of the layers, (b) magnified image of the layer interfaces.

The APT analysis of such sample has revealed different characteristics for both interfaces concerning the interdiffusion, as shown in Figure 75. Although the reconstructions include artifacts at the layer interfaces due to some instability in the field evaporation rates for Ru and Al layers during the measurements, some qualitative information is still possible to extract from the datasets regarding interdiffusion. The top interface is observed to be relatively sharp, whereas the bottom interface is diffused. Three successful APT measurements from such sample have shown identical results. Interdiffusion at the bottom interface was observed to be localized along the GBs in the Ru layer, where Al segregations are detected. Therefore, this shows a similarity regarding interdiffusion as in the multilayer samples. However, for the trilayer thin film it was possible to differentiate the interdiffusion behavior for the interfaces of the Ru grown on Al and the Al grown on Ru, respectively. The segregations of Al in the Ru GBs was found to extend up to approximately 15 nm in length, and showing additional segregations along the triple junctions in the fine grain structures of the Ru layers. No Al was detected at the GBs of the top Ru layer, indicating that Al diffuses only

downwards along the GBs of the Ru layers. Furthermore, no Ru was detected to diffuse in the grain or along the GBs in the Al layer.

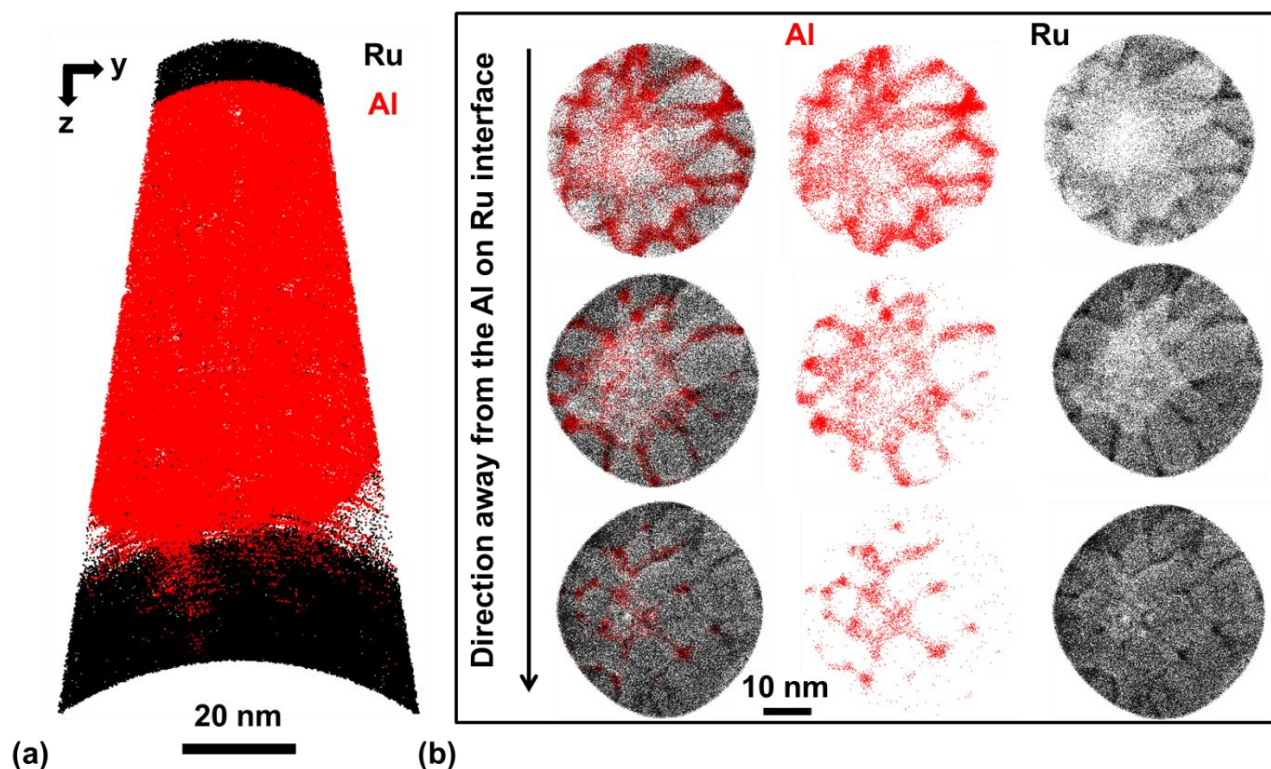


**Figure 75** APT analysis for the Ru/Al trilayer structure. (a) 12 nm topographic slice in the reconstruction showing Ru and Al atoms. (b) Three topographic slices along the z-direction in the interdiffused part of the bottom Ru layer where each slice is 5 nm thick, Ru and Al atoms are shown together as well as separately, for visualization purposes.

### 3.2.2. Thermally treated films

To investigate the mechanism of the early phase formation and the developments of the interdiffusion within this system with temperature, the films were thermally treated and the microstructure was afterwards analyzed. The trilayer thin films were used for this investigation since they provided more successful results using APT in the as-deposited condition, and can therefore provide a clear reference for the condition of the films before annealing. Unfortunately, the weight of the trilayer thin film was too little to provide good quality measurement data in the DSC (at least 5 mg is required). The DSC was used however to provide highly controlled heating conditions of the trilayer thin films. The films were ramp-annealed in the DSC at 0.33 K/s to four specific

temperatures and held at such temperatures for 10 minutes then the films were subsequently cooled. The four annealing temperatures chosen were 573, 593, 613, and 633 K, respectively. The as-mentioned temperatures were selected based on previous works on Ru/Al multilayer thin films with period thickness of 88nm which have shown the formation of the first intermetallic phase to appear around such temperatures [75], [76]. Each of the samples annealed in the DSC were analyzed with STEM. Figure 76 shows the STEM images of the samples after each annealing condition. The samples annealed to 573 and 593 K have not shown any obvious differences compared to the as-deposited condition. However, the sample annealed at 613 K displayed clear indications for the formation of a new phase within the Al layer. The new phase is seen to grow along the GBs in the Al parent phase, and appears to form at both layer interfaces (the Ru on Al interface and the Al on Ru interface, respectively). The new phase is observed to grow strongly in the Al layer and totally absent in the Ru layers. The sample annealed at 633 K displayed slightly additional growth of the new phase within the Al layer, where grains of the new phase intersect and reach a total thickness equivalent to the thickness of the Al layer.

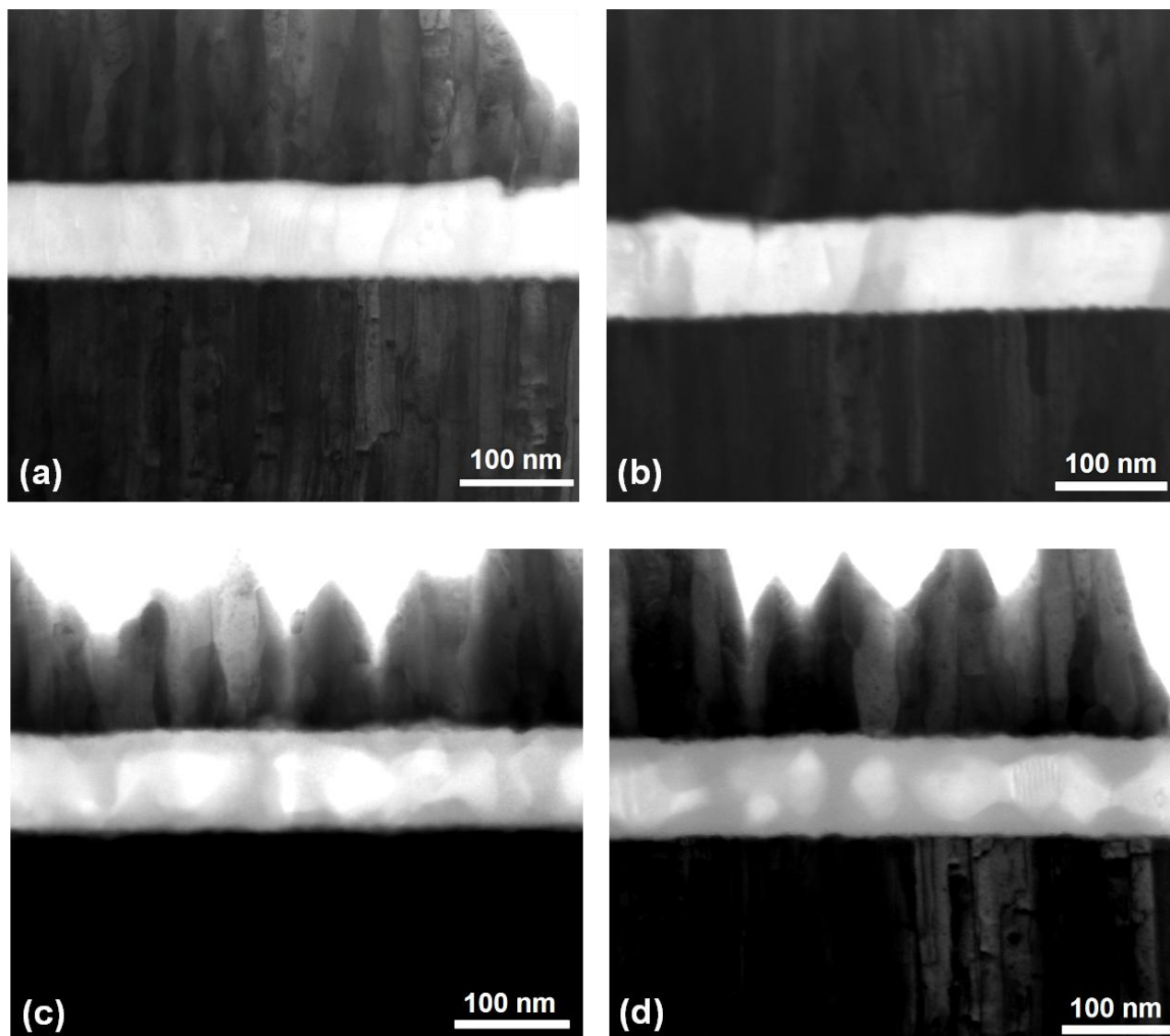


**Figure 76** BF-STEM images of the Ru/Al trilayer thin film annealed to four different temperatures: (a) 573 K, (b) 593 K, (c) 613 K, and (d) 633 K.

The trilayer thin film sample annealed at 633 K was analyzed by APT to study the composition of the new phase and the interdiffusion behavior. Figure 77 displays an APT reconstruction highlighting the growth of the new phase in the Al layer. The volume captured in the APT reconstruction shows the new phase growing at the bottom part of the Al layer, however, it is understood from the STEM that the new phase nucleates at both layer interfaces and grows within the Al layer. The APT analysis further confirmed that the new phase is found to grow in the Al layer and the Ru layers remain almost unaffected. The compound phase appears to grow deeper along the GB regions in the Al phase. It therefore becomes understandable that the new phase nucleates via the diffusion of Ru in the Al GBs, and grows extensively along the Al GBs before the grains coalesce together and a continuous layer is formed.

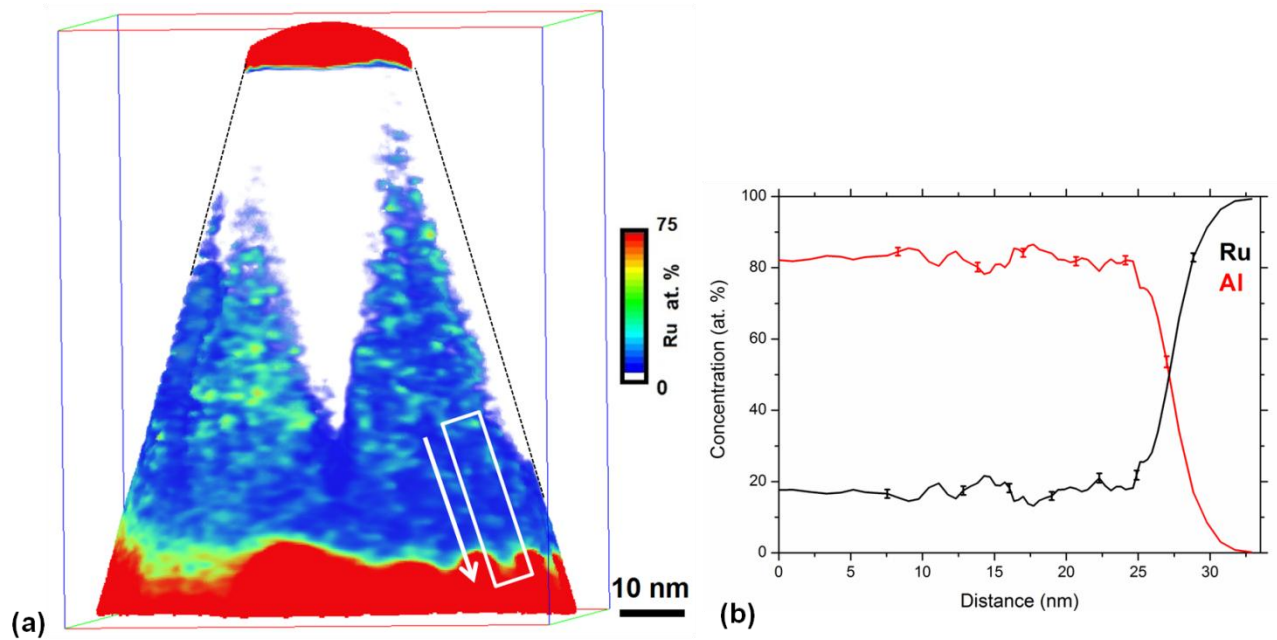


**Figure 77** APT analyses for Ru/Al trilayer thin film annealed to 633 K. (a) The new intermetallic phase formed in the Al layer is visualized using 3D concentration map of Ru concentration (pure Al parent phase is transparent). The small dotted lines mark the borders of the reconstructions. (b) 1D concentration profile along the region marked in the reconstruction. The white arrow marks the direction of the profile measurement.

The intermetallic phase measured by APT has shown a concentration of about 17 at.% Ru and 83 at.% Al, which almost fits the composition of the  $\text{RuAl}_6$  phase. Such phase is expected to be the first phase to form according to previous studies for the phase formation by annealing Ru/Al multilayer thin films [75]–[77]. The composition in the new phase has shown very fine compositional fluctuations and compared to the stoichiometric equilibrium value of this intermetallic phase (~15 at.% Ru) it appears to be slightly more Ru-enriched, which indicates supersaturation in the new phase. Results for off-stoichiometric values of this intermetallic phase showing Ru-enriched compositions measured by APT were previously reported in Ref. [77].

## 4. Discussions

### 4.1. Ag/Al investigation

A wide range of experimental data was collected on Ag/Al multilayer thin films concerning the interdiffusion behaviors, the effect of deposition parameters, as well as the kinetics and nature of chemical reactions. In addition to the kinetic effects caused by high interfacial densities in thin films, it is also necessary to consider the influence of the texture of the as-deposited film on the reaction kinetics, which in some cases can have major contribution. Greer [53] for example has demonstrated that interdiffusion rates can vary by up to one order of magnitude between (111) and (200) grown Ag/Au multilayer thin films, which is expected to be caused by non-identical diffusivities and movements of different GB types. It was shown here for Ag/Al that the texture can vary depending on the period as well as the sputtering power. Although some minor microstructural variations can affect the interdiffusivities in the thin films, the observed changes in the enthalpy values as a function of the period thickness and sputtering power can be mainly attributed to the significant differences in the extent of interdiffusion during deposition, especially along GBs. Similar to the concept of concentration gradient preparation (explained in section 1.4), the formation of local interdiffused regions offers favorable sites for nucleation and consequently reduce the remaining heat of the reaction that gets released for the phase transformation. The reactant volumes (i.e. layer thicknesses) and diffusion distances in the Ag/Al polycrystalline thin films investigated here have shown to be the main contributing factors on the kinetics. Multilayers of miscible elements with columnar grown and relatively low interfacial roughness favor such relationship, since the grain sizes can be comparable to the individual layer thicknesses. The result shown for the enthalpy-period relationship (see inset in Figure 49) is similar to the enthalpy-period relationship reported for Ni/Al multilayer thin films by Michaelsen et al. [45]. The increased interdiffusion found here in the smaller periods supports their suggestions for the existence of such an enthalpy-period relationship. For thinner layers the vertical dimensions of the grains are reduced which is understood to intensify the effective GB diffusivity [57].

The relatively low reaction temperatures compared to other metallic multilayers of miscible elements demonstrate the high atomic mobility in this system, which is clearly evident from the degree of interdiffusion during deposition. It is also obvious, due to the fact that slight change in the substrate

temperature of (~25 K) using different sputtering powers during deposition has induced a strong result on the interdiffusion and the heat of reaction for the intermetallic phase formation in the multilayer thin films. It is reported in literature that the activation energy for GB self-diffusion in Al is lower than in Ag (0.6 and 0.9 eV, respectively [98]), leading to Al diffusion along Ag GBs during annealing. Diffusion of Al in the Ag GBs and diffusion of Ag in the Al GBs was detected using APT. However, the diffusion of Al in the Ag GBs was indeed observed to be more pronounced.

Concentration gradients across the phase boundary interfaces were shown to depend on the sputtering power which is likely due to the substrate temperature that can influence the intermixing at the interfaces. However, for the Ag-rich multilayers, asymmetric concentration profiles were detected for the Ag/Al phase boundary interfaces (see Figure 33), which is a common feature observed in metallic multilayer thin films [106]. A few reasons can cause such an effect. First, Ag and Al exhibit different surface energies which influence the growth of the interface during deposition. Fcc Al has lower surface energies than fcc Ag [107], thus, more Al atoms are expected to segregate on the Ag surfaces during growth and eventually diffuse into the first few Ag monolayers as more Ag atoms impact the surface. This behavior has been detected and simulated in several metallic multilayer thin film systems synthesized by PVD techniques, as reported in Refs. [79], [106], [108]. Such non-equilibrium segregation effects at interfaces during film deposition can be referred to as *dynamic segregation* [109]. Moreover, both elements have different cohesive energies, which are also ascribed to affect the interface growth behavior. Buchanan et al. [106] have investigated the interfacial thickness in numerous aluminum-transition metal multilayers, and proposed that the cohesive energy of the transition metals is a correlating parameter to describe the interfacial thickness variations. According to their study, elements with lower cohesive energies show thicker intermixed lengths ( $E_c(\text{Ag}) < E_c(\text{Al})$  at 300 K).  $E_c$  values for Ag and Al are 2.85 and 3.36 eV, respectively [107]. They have also reported thicker Ag on Al interfaces compared to Al on Ag interfaces using grazing-incidence x-ray reflectometry [106]. Furthermore, Ag is a heavier element compared to Al and has three times higher sputtering rate [110], leading to more intensive ion bombardments on the Al surface during growth, resulting in increased intermixing. The films of different compositions studied in the 10 nm period show contrary results regarding the asymmetry of the concentration gradients to what is found in the Ag-rich films. This can be related to the significantly increased roughness in these thin films inducing different shadowing effects during film growth which influences the concentration gradients. The interfacial mixing in the Ag-rich films agrees with literature where the quality of the multilayer structure was very good (relatively flat layers). Nevertheless, the results on the phase formation in this Ag/Al thin film system suggest that not so much the concentration

gradient but rather the amount of local supersaturation of the terminal solid solutions that promote the nucleation of the intermetallic phase at the layer interfaces or at the GBs (nucleation discussed below).

The increased roughness detected in the 10 nm period deposited with different compositions (Al-rich or near 50:50 composition) is due to the film growth behavior which is influenced by the thickness of the Ag layers. According to an experimental study by Fournée et al. [111] for the growth of Ag/Al bilayer thin films, it was shown that the film growth mode of Ag layer switches from a rough 3D growth mode to a smooth 2D growth mode above approximately five monolayer thickness. This is due to interfacial strain that gets relieved by Shockley partial domains which develop above a specific layer thickness and consequently the film becomes relaxed. This displays perfect agreement with the results of the work here. In the 10 nm period with Ag-rich composition the individual Ag film thickness is approximately 7 nm, and consequently the multilayer displayed very low roughness. Depositing multilayer with lower Ag content (thinner Ag film thickness) the roughness starts to rise, especially for the Al-rich composition where the individual Ag film thickness is approximately 3 nm thick. The rise in the roughness in the epitaxial multilayer thin films has demonstrated its influence on the interdiffusion by creating topographic defects in the microstructure which contribute majorly as fast-diffusion paths as was observed in the analysis of the 10 nm period in as-deposited condition with Al-rich or near 50:50 composition.

A significant rise in the multilayer roughness was also observed for the 200 nm period deposited with high sputtering gas pressure. The rise in roughness here occurs due to reduced surface mobility of adatoms of both Ag and Al, which arrive with lower incident energy as a result of additional bombardments with the gas atoms in the chamber. The adatoms condense quickly on the surface and less adatoms re-arrange in preferential condensation or orientations sites. This is also evident from the reduced texture observed by increasing the gas pressure. The rise in roughness lead to the formation of topographic defects in the microstructure, which based on the APT analysis carried out in the 10 nm period of high roughness, it can be predicted that the 200 nm periods deposited with high gas pressure exhibit strong interdiffusion at the topographic defects. The investigation of the gas pressure therefore demonstrates the control of the deposition parameters on the mass transport in the multilayer thin films.

The APT investigation of the 10 nm period of different composition in the as-deposited condition has effectively demonstrated the effect of the gradient energy on interdiffusion in very thin layers. As suggested by Cook and Hilliard [25] as well as Greer [20], and simulated by Hentschel et al. [112], the role the gradient energy on interdiffusion becomes significant in multilayer wavelengths below 10 nm thick. Mass transport is observed to be higher in the very thin individual layers (below 6 nm) of the Ag/Al multilayer, either for Ag or Al. When both Ag and Al layers are almost of the same thickness of approximately 5 nm (near 50:50 composition), interdiffusion during deposition occurs in both phases. Rise of interfacial stresses in ultrathin multilayer films can also induce such effects, such as in Cu/Ni multilayers thin films for example [113], however, interfacial stresses are considered insignificant in this Ag/Al system due to their similar lattice constants, which was also supported by comparing d-spacing values measured in XRD to bulk values, that displayed very minor differences. Hence, the effect of the increased mass transport inside the grains of the 10 nm periods can be strongly attributed to the gradient energy effect. The initial interdiffusion behavior after deposition observed in the 10 nm periods has shown a clear relationship on the microstructural and phase evolution during annealing of the films (nucleation discussed below). It is important to point out that although the high interdiffusion measured in the 10 nm period by APT, no intermetallic phases were seen in the XRD measurements of the films in the as-deposited condition. The amount of Ag and Al found inside the grains is above the solubility limit of the fcc phases at such temperatures according to the equilibrium conditions. This reflects that both fcc structures exhibit a large degree of supersaturation in the as-deposited state. According to Wang et al. [114] impurity diffusion coefficient of Al in pure Ag is slightly higher compared to Ag in pure Al, which can explain the higher content of Al found in the Ag grains for the Al-rich composition compared to the content of Ag in Al grains for the Ag-rich composition in the 10 nm periods. The increased degree of interdiffusion in the small 10 nm periods clarifies also the small difference in the enthalpy values as a function of sputtering power (see inset of Figure 49) and lower activation energy compared to larger periods of the Ag-rich composition. Reflectivity measurements performed by Weaver and Brown [99] on Ag/Al films synthesized by vacuum evaporation with different layer thicknesses showed increased diffusivities for smaller layer thickness, as they reported that diffusivity increases by up to one order of magnitude in layers smaller than 100 nm thickness.

#### **A. Nucleation and phase evolution in the 10 nm period**

In the DSC measurements of the 10 nm period, an early broad exothermic event was detected for all the compositions, especially in the films with near 50:50 composition which have shown the broad exothermic event starting at a lower temperature. This early heat release before the narrow exothermic event is a common observation in miscible metallic multilayer thin films, where it is discussed as interdiffusion or formation of an amorphous phase followed by “homogenous” nucleation of the intermetallic phase [47], [48], [115], [116]. Based on the APT investigation of the 10 nm periods after thermal treatment, the early broad exothermic event certainly appears to be interdiffusion leading to precipitation reactions at the GBs as well as further mass transport inside the grains to form a supersaturated solid solution. The subsequent narrow exothermic event is a spontaneous reaction caused by nucleation of the  $\gamma$  hcp phase from the supersaturated solid solution. Therefore, the nucleation mode here can be described to be a polymorphic one for all compositions. However, the product of the reaction, the phase evolution, and the microstructural evolution by annealing the films is different for each of the three compositions investigated.

In the films of Ag-rich composition, Ag atoms start to diffuse in the thinner Al layers during deposition, assisted by the gradient energy effect. In the Ag-Al phase diagram, Al-rich Ag-Al solid solutions are unstable below the solvus line and decompose, where a miscibility gap exists within the  $\alpha$  phase [100], [101]. This is reflected in Figure 78, which shows a plot of the Thermo-Calc calculations for the  $\alpha$ ,  $\mu$ , and  $\gamma$  free energy curves at 323 K (calculated from Ref. [117], [118]), where the unstable region in the  $\alpha$  phase is marked. Spinodal decomposition is known to occur in Al-rich Ag-Al alloys [100], [119], and is expected to take place in the Al layers as Ag diffuses and supersaturates the Al. Indeed, an inhomogeneous concentration distribution is detected within the Al rich layers (see Figure 58). The early reaction follows the arrows numbered “1” marked along the  $\alpha$  curve, representing a supersaturation reaction (see Figure 78), where Ag diffuses into the  $\alpha$ -Al phase. According to the  $T_0$  concept [120], the  $\text{Ag}_2\text{Al}$   $\gamma$  hcp phase should nucleate by polymorphic mode only below the Al concentration of 46 at. %, where a sufficient driving force exists for the polymorphic nucleation. The fact that the nucleation occurs earlier, at about 51 at. % Al (realized by the sudden thickening of the layers), points out that a  $\text{Ag}_{50}\text{Al}_{50}$  metastable phase forms briefly as a transient phase before the equilibrium  $\gamma$  appears. This is also supported by the detection of such metastable phase in the annealed 10 nm period of different compositions (discussed below). Once the  $\gamma$  phase has nucleated, the remaining pure Ag layers can be consumed. It is important to add that the  $\gamma$  phase precipitates also in the GB regions during the early stages of the reactions (see center of the reconstruction shown in Figure 58). Here the segregation leads to a local saturation up to the value

above the  $T_0(1)$  followed by polymorphic  $\gamma$  phase formation. This is likely to be the dominant nucleation process for larger periods as well (discussed below). Although for the reaction of Ag/Al multilayers thin films Al is known to diffuse faster in the Ag layers [66], [98], [121], the opposite is found in this case here, which is understood to be caused by enhancement of interdiffusion in the Al layers by the gradient energy effect. Schleiwies et al. [121] have also shown strong diffusion of Ag in very thin Al layer (6 nm thick) deposited between relatively thicker Ag layers, using tomographic atom probe (TAP) analysis.

The reaction pathway in the Al-rich composition of the 10 nm periods is the opposite to the case found for the Ag-rich composition. The supersaturation of the  $\alpha$ -Ag phase occurs by Al diffusing in the Ag layers during deposition and the diffusion continues further during annealing, assisted by the gradient energy effect. The pathway for this reaction is marked the arrow numbered “2” in Figure 78. The supersaturation is likely to continue further beyond the  $T_0(2)$  where the equilibrium phases  $\mu$  and  $\gamma$  become suppressed. The suppression of these equilibrium phases is supported by the concentrations detected at the tomographic defects which lie within the stoichiometric values of the equilibrium phases, but structural analysis via XRD has shown no evidence for formation of the intermetallic equilibrium phases. Thus, the Al is expected to accumulate in the fcc Ag layers till a concentration beyond  $T_0(1)$  where the  $Ag_{50}Al_{50}$  metastable phase nucleates by polymorphic mode. The reaction at the tomographic defects and vertical GBs is believed to occur here slightly before the reaction in the layers. Therefore, the first exothermic peak in the DSC measurement (peak marked 1 in black in Figure 57) is considered to be the formation of the new phase at the tomographic defects and vertical GBs, while the second exothermic peak (peak marked 2 in black in Figure 57) is the formation of the new phase throughout all the supersaturated layers. The metastable phase exhibits similar hcp structure as the equilibrium  $\gamma$  phase, as reported in Ref. [102]. A recent XRD experimental study carried out by Mao et al. [122] on Ag-Al thin films with a wide range of compositional gradient have also shown  $\gamma$  hcp peak reflections in the films with composition range of 46-54 at.% Al. Experimental evidence for non-stoichiometric composition of the  $\gamma$  hcp phase with higher Al content were also reported in different studies [123], [124]. After the reaction of all the Ag layers the interdiffusion rate in the system drops due to the miscibility gap in the Al-rich region. By further annealing the microstructure evolves by grain boundary migration [125] where layers of Al and the metastable phase coalesce and grow, maintaining sharp interfaces together. During growth, the layers move and re-arrange in the microstructure, in which some layers were observed to have diagonal configurations after the second exothermic event. As the layers continue to coalesce by

annealing, the superlattice structure fades away since the layers become thicker, whereas some parts exhibit further growth into full grown islands for both phases, respectively. At elevated temperatures Ag becomes more soluble in the  $\alpha$ -Al terminal phase, according the equilibrium conditions (see phase diagram in Figure 13), hence, traces of Ag begin to dissolve in the Al grains, which is likely to explain the formation of early clusters of GP zones detected in Al after the third exothermic event. In some parts of the intermetallic phase more Ag-rich compositions were measured showing concentrations of about 55 at. % Ag, which indicates a tendency in the system to form the equilibrium  $\text{Ag}_2\text{Al}$   $\gamma$  hcp at elevated temperatures from within the metastable phase. This requires Al to diffuse out of the metastable phase for the equilibrium phase to form. This was also clearly visible in the STEM images of the 10 nm period films of near 50:50 composition ramp-annealed to 620 K (discussed below).

The reaction in the films with near 50:50 composition was shown to occur in both parent phases simultaneously. The individual layer thickness for the Al and Ag phases was approximately 5 nm thick where enhancement in the diffusion due to the gradient energy effect occurred in both phases. The reaction pathway occurs again by supersaturation in the fcc phases where Al diffuses in the Ag phase and Ag diffuses in the Al phase, respectively. The pathway for this reaction is marked by arrows numbered “3” in Figure 78. The supersaturation continues slightly beyond the intersection of the gibbs free energy curves of the  $\alpha$ -fcc and the metastable hcp  $\text{Ag}_{50}\text{Al}_{50}$  metastable (hypothetical curve), where polymorphic nucleation of the  $\text{Ag}_{50}\text{Al}_{50}$  phase occurs. Such behavior of the reaction in this case here appears to induce a broader and smaller exothermic peak compared to the Ag-rich and Al-rich compositions. However, due to the fact that the films were not exactly 50:50 composition but slightly more Al-rich (~55 at.% Al), not all the layers reacted forming the  $\text{Ag}_{50}\text{Al}_{50}$  phase. Unreacted Al layers were detected at higher annealing temperatures which again occurs due to the miscibility gap in the Al-rich region of the phase diagram added to the fact that Al would diffuse out of the metastable phase at higher temperature for the precipitations of the stable  $\text{Ag}_2\text{Al}$   $\gamma$  hcp phase. Indeed, diffused layer features were observed in the intermetallic phase at 620 K, which is expected to be the precipitation of the equilibrium  $\gamma$  at elevated temperatures from within the metastable phase. APT analysis in the Al-rich films at elevated temperatures supports this, as areas of Ag-rich compositions were detected within the hcp phase (see Figure 65(b)).

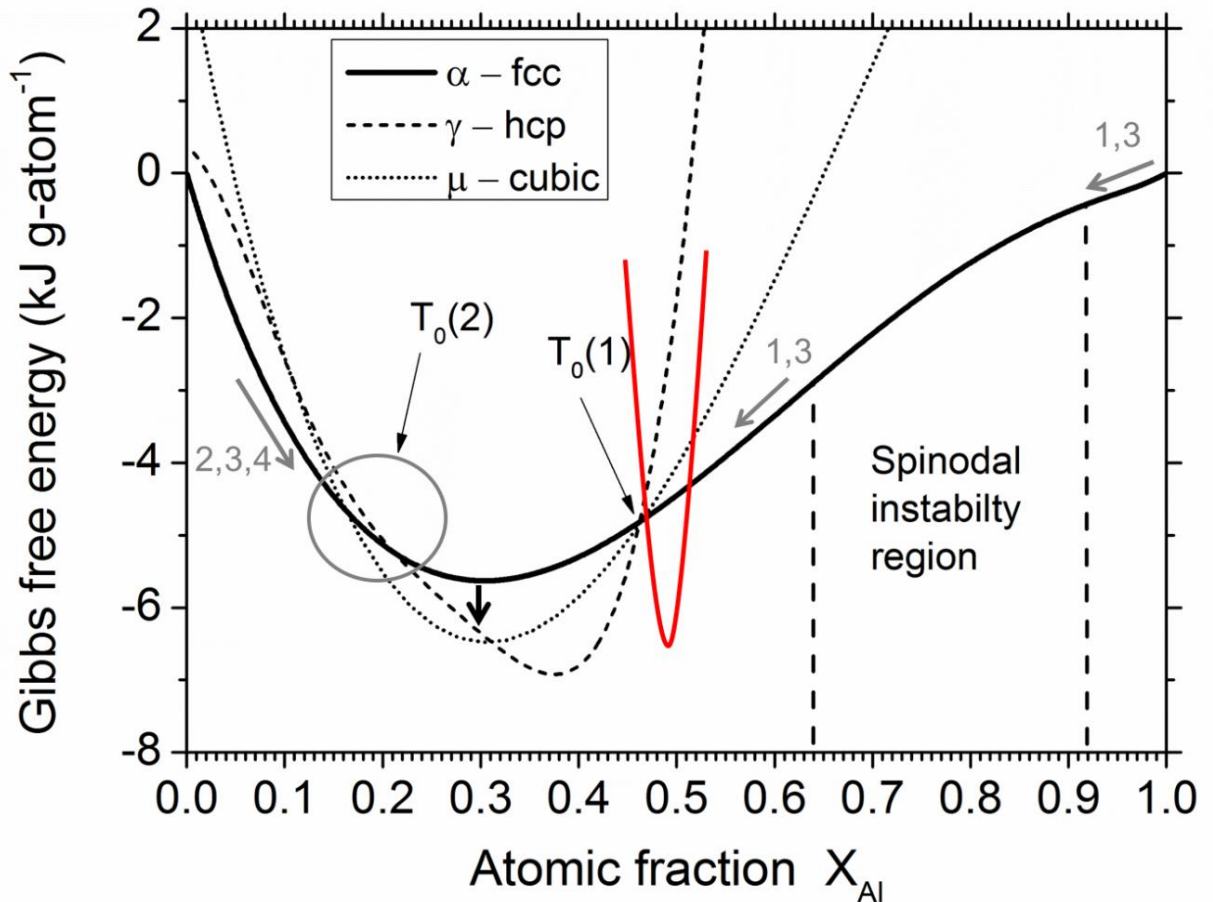


**Figure 78** Thermo-Calc plot from CALPHAD thermodynamic values of Ag-Al system (calculated from Refs. [117], [118]) at 323 K showing the  $\alpha$ ,  $\mu$ , and  $\gamma$  free energy curves. A hypothetical curve is added for the metastable hcp AgAl phase (in red color). The grey arrows mark the path for the supersaturation reactions. The numbers on the arrows refer to the specific reaction described in the text. The thick black arrow presents the polymorphic reaction occurring in the multilayer of 100 nm period (free energy curves are very similar in the temperature range of 300-473 K).

The formation of the metastable hcp AgAl phase agrees with literature reporting the formation of such phase as precipitates at GP zones in a supersaturated fcc matrix [102], [123]. However, the results here show a large volume of the product metastable phase which is expected to be formed due to the enhanced kinetics in ultrathin multilayer films.

## B. Nucleation and phase evolution in the 100 nm period

The reaction in the 100 nm periods (Ag-rich composition) is dominated by nucleation of the  $\text{Ag}_2\text{Al}$   $\gamma$  hcp phase at junctions of GBs with the layer interfaces through segregation at these triple points (see Figure 52). The same is expected for the larger periods (200 and 400 nm). As heat is applied to the films, interdiffusion initiates along GBs. Al starts to diffuse in the Ag GBs, and Ag proceeds at a slower rate in the Al GBs. The concentration of the diffuser increases up to a certain limit, where the GBs become saturated. Out of all the APT measurements carried out, the highest diffuser concentration detected was  $\sim 20$  at. % Ag in the Al GBs and  $\sim 30$  at.% Al in the Ag GBs. These concentrations do not present sufficient supersaturation to promote polymorphic nucleation. Thus, the nucleation is confined to the junctions between GBs and layer interfaces, where sufficient supersaturation can occur and diffusion controlled growth is not restricted. The formation of Al-rich  $\gamma$  phase and rapid dissolution of the Al parent phases indicates asymmetric diffusion rates of Ag and Al in  $\gamma$  phase, where Al diffuses faster than Ag, reflecting some Kirkendall effect [28]. Certainly, asymmetric diffusion of Ag and Al in  $\gamma$  intermetallic phase was reported by Minamino et al. [126] in Ag/Al diffusion couples, with diffusion coefficients measured to be  $D_{\text{Ag}} = 5.41 \times 10^{-13} \text{ m}^2\text{s}^{-1}$  and  $D_{\text{Al}} = 1.14 \times 10^{-12} \text{ m}^2\text{s}^{-1}$  (at 773 K, under no applied pressure), respectively. At higher temperatures where all (or most) of the Al parent phase has been incorporated into the Al-rich  $\gamma$  phase, Al starts to diffuse out of the  $\gamma$  phase towards the Ag parent phase and supersaturating it (see Figure 54). Now, on the Ag-rich side local polymorphic nucleation of the  $\mu$  phase or the  $\gamma$  phase from the supersaturated  $\alpha$  phase becomes possible beyond  $T_0(2)$ . Along this reaction direction (marked by arrow numbered “4” in Figure 78) other Ag-rich metastable phases are also possible to form, such as  $\text{Ag}_5\text{Al}$  displayed in inset D of Figure 54.  $T_0(2)$  is therefore presented as an area of probable intercepts of the Gibbs free energy curves (see Figure 78). Indeed, compositions and structural information fitting to a coherent  $\mu$  phase were detected within the fine nanosize multiphase regions at 435 K (see insets A and C in Figure 54).  $\text{Ag}_5\text{Al}$  (or other metastable phases) and  $\mu$  are therefore competing with the  $\gamma$  phase at this stage of the reaction in the Ag-rich areas of the microstructure and are likely to form simultaneously at different locations. Fine-nanosize multiphase regions were also reported in other studies on Ag/Al thin film reactions [98], [99], [121], and specifically along the  $\text{Ag}_2\text{Al}/\text{Ag}$  interfaces during the growth of  $\text{Ag}_2\text{Al}$   $\gamma$  phase in diffusion couples [127]. Hence, these regions are predicted to form during the dissolution of Ag and reaction with the  $\gamma$  phase. When all the parent phases react, the composition of the  $\gamma$  phase exhibits a homogenous concentration fitting to the equilibrium range (see Figure 56).

A schematic representation of the reaction in Ag/Al multilayers of period thickness 100-400 nm range is shown in Figure 79. This sequence of reactions occurs within a single exothermic event for the multilayer of 100 nm period, which is expected to consist of three events sequentially overlapped in a short temperature range (see Figure 49). The first exothermic event is considered to be diffusion along the GBs and nucleation of the  $\gamma$  phase, the second is isotropic growth of the  $\gamma$  phase and the third is likely to be the heat released during the fine nanosize multiphase formations and diffusion in the  $\gamma$  phase. The analysis at 398 K for the multilayer of 100 nm period is suggested to be at a reaction stage between the first and second overlapped exothermic events. Therefore, a certain similarity is found with the two-stage growth model for the reaction mechanism in miscible multilayer thin films. However, the growth of the compound phase here is found to grow in all directions and not confined in the vertical or lateral directions. Moreover, the segregation and nucleation at the GB junctions is the active mechanism in this system, which agrees with previous studies on Ag/Al bilayer reactions [98], [128]. It is important to mention that phase competition as well as phase suppression were experimentally detected for all period thicknesses which most likely arise from the asymmetric diffusion rates of the phases during reaction that have demonstrated a vibrant effect on the phase evolution.

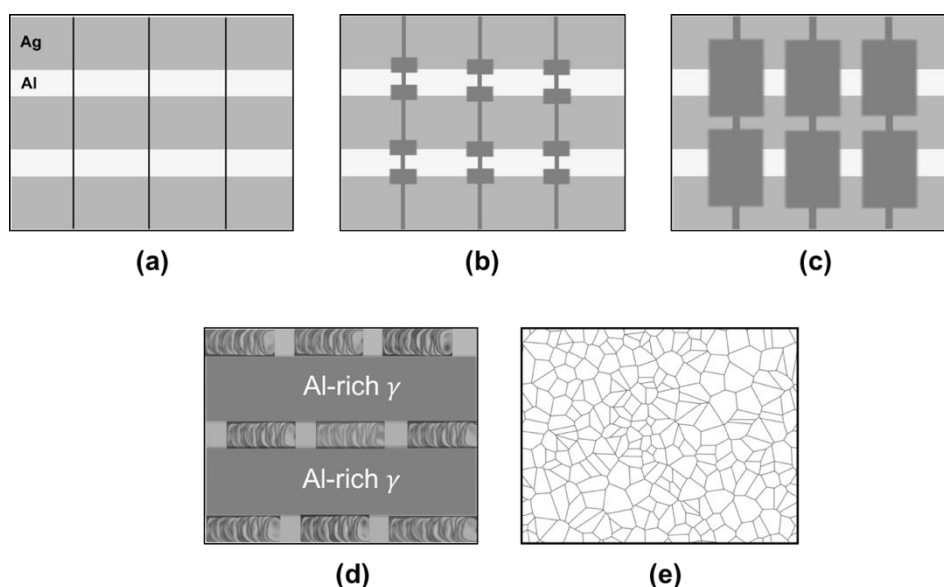


**Figure 79** A schematic representation of the sequence of reactions in Ag/Al multilayer thin films with 100-400 nm periods under slow heating. (a) As-deposited condition, (b) GB diffusion and nucleation of the  $\gamma$  phase along the GB intersections with layer interfaces, (c) isotropic growth of the Al-rich  $\gamma$  phase, (d) a multilayer structure composed of large Al-rich  $\gamma$  phase islands and parent Ag

phases along with fine nanosize multiphase regions (most of Al parent phases are consumed here), (e) Stoichiometric  $\gamma$ -hcp homogenous phase [93].

#### **4.2. Ru/Al investigation**

The large difference in the melting points of Ru and Al is also seen to have its effects on thin film deposition by PVD. The low homologous temperature estimated for the Ru films indicates low adatom mobility during film growth which explains the fine grain structure observed in the Ru layers, fitting to a 'zone 1' according to structure zone models [62], [63]. The low adatom mobility can also lead to the thin films exhibiting a 3D growth mode as the islands are not mobile enough to sufficiently grow in the lateral direction (parallel to the substrate) [59]. The Al layers on the other hand have a higher estimated homologous temperature which indicates higher adatom mobility during growth in comparison to Ru which explains the coarser grain structure in Al. The growth of the Al layers is therefore expected to have 2D growth mode due to the increased mobility of the Al adatoms. This also clarifies the differences observed for the Ru on Al interfaces compared to the Al on Ru interfaces which can be related to the different grain structures for each of the layers, respectively. The increasing roughness, formation of pores, and disorder of the multilayer structure along the growth direction is a manifestation of both metals exhibiting different film growth modes. It is as well affected by the nature of the layer interfaces which is incoherent, where no crystallographic relationship is known to exist between the layers.

The diffusion of Al downwards (towards the substrate) into the Ru layer can be understood as well to be a result of the high mobility during deposition of Al adatoms in comparison to Ru. The segregations of Al in the Ru GBs is therefore induced by non-equilibrium kinetics, which can also be referred to as dynamic segregations during film growth [109]. According to a study carried out by Buchanan et al. [106] on various Al-transition bilayer thin films deposited by magnetron sputtering and examined via X-ray reflectometry, Ru/Al bilayer thin films were shown to exhibit asymmetric intermixing along the phase boundaries. They reported that the intermixing length of Ru on Al is thicker than the Al on Ru layer, 5.2 and 0.8 nm, respectively [106]. This asymmetry is expected due to differences in the cohesive and surface energy values for both metals, respectively. Specifically, the surface energy of the Al is much lower along the growth direction compared to Ru [107], [129]. This would induce more segregations of Al into the Ru layers as Ru adatoms arrive onto Al. However, according to the APT results here, the upper interface in the trilayer film (Ru on Al) seemed relatively sharp in the reconstructions (see Figure 75). This is understood to be affected by

artifacts in the reconstruction due to the field evaporation from a high field phase to a low field phase [103]. No analysis was carried out here to quantify interfacial mixing for such reason, and according to literature [106], the Ru on Al interface is expected to be more diffused. The existence of segregations of Al at Ru GBs is not affected by the field differences, especially since the field evaporation goes from a low field phase into a high field phase, yet measuring the quantity of segregation at the GBs can show minor errors (such minor errors are fully described in Ref. [105]).

The analysis of the trilayer thin film after annealing suggests that Ru atoms diffuse into the Al layers, specifically by GB diffusion, for the new phase to nucleate. According to Gusak et al. [33], [130], the formation of the new phase as a result of GB wetting occurs via polymorphic mode where the solid solution at the interdiffused region at the GB plays the role of a supersaturated parent metastable phase. The RuAl<sub>6</sub> phase can be understood to nucleate via polymorphic mode after a sufficient amount of Ru supersaturates the Al phase. There are no impurity diffusion coefficients found in literature for the Ru-Al system, nevertheless, it is understood that the diffusivity of metals with low melting point is higher than metals of higher melting point [23], specifically along GBs. It can be therefore predictable that Al diffusion in Ru would be faster than Ru in Al due to the significantly lower melting point of Al compared to Ru. Nevertheless, the nucleation occurs after sufficient Ru atoms diffuse into Al layers, simply due to the fact that intermetallic phases exist only at the Al-rich area in the phase diagram. The nucleus here is expected to form in the Al layer, along the intersection of the Al GBs with the Ru layer, where it forms at both layer interfaces (Ru on Al and Al on Ru). The RuAl<sub>6</sub> is the Al-richest equilibrium intermetallic phase found in the phase diagram and is commonly reported to form as an initial phase by annealing Ru/Al multilayers with periods above 22 nm [75]. In periods below 22 nm the B2-RuAl phase directly forms [41], [74], which can be understood to be caused by stronger interdiffusion in smaller periods (as seen in the Ag/Al results), where intermediate Al-rich intermetallic phases become suppressed during the reaction.

The formation of the RuAl<sub>6</sub> is reported to occur at slightly lower temperatures (around 576 K) in the multilayer thin films [75] compared to the trilayer thin film structure studied here. This can be related to the topographic defects and the high amount of disorder found in the multilayer structure where strong interdiffused regions in the as-deposited state exist, thus less energy is required for nucleation to occur. It worth to mention that Ru/Al multilayer thin films are possible to be deposited with improved multilayer structural quality (lower roughness) as shown in Ref. [77], which requires

increasing the sputtering power. However, according to the APT results shown here, additional dynamic segregations can be expected in such conditions.

## 5. Conclusions

The investigation here demonstrates the necessity of combining local chemical analysis along with crystallographic analysis to fully comprehend behaviors of mass transport and phase formations in multilayer thin films. Atomic scale analysis was shown to be extremely essential to elucidate the thermodynamic characteristics of multilayer thin films. Supersaturation of phases is likely to occur in thin films due to their high density of point defects compared to bulk. Off-stoichiometric values commonly reported in literature for the growing intermetallic phase can surely be influenced by the decay of other compound intermediate phases, but as seen here, it can be also affected by supersaturations effects and asymmetric diffusion rates of parent phases in the growing phase. However, it is important to mention that Ag/Al system can exhibit additional supersaturation due to the strong similarity in the structural properties of the parent phases.

Concentration gradients at layer interfaces in thin films can be influenced by four different factors, namely, the solubility of both phases together, non-equilibrium segregations during deposition, equilibrium transport through and across the layer interfaces, as well as interfacial and external stresses. The results of the Ag/Al system have shown effects for the second and third factors, respectively. Differences in surface energies and cohesive energies were attributed to dissimilarities in concentration gradients at the both layer interfaces (Ag on Al and Al on Ag), representing non-equilibrium segregation effects. Whereas, increased substrate temperatures (higher sputtering power) induce broader layer interfaces representing equilibrium transport at the interface. It is important to remember that transport through the interfaces depends on the nature of the phase boundaries. Incoherent interfaces, can likely exhibit higher atomic transport through the phase boundary, which is an important aspect to be aware of considering the analysis carried out here for the coherent interfaces of the Ag/Al system. Some disagreements with the two-step growth model regarding the growth behavior of the early compound phase (also observed in other experimental studies [46], [121]), can be ascribed to dissimilar transport regimes at different types of interfaces as well as the density of GBs in the microstructure.

For the first time, the relationship between interdiffusion and period thickness is experimentally shown here using local chemical analysis, which supports suggestions found in literature for common calorimetric results of miscible metallic multilayer thin films as a function of the period. The increase of interdiffusion in the Ag/Al multilayers is found to be confined along the lattice defects in the microstructure showing Type C diffusion which act as fast-diffusion paths and play a vital role in the nucleation and the diffusion controlled growth of the compound phase during annealing. The effective GB diffusivity in thin films is an important variable, which is affected by the dimensions of the grains and reactant volume, respectively. The structural properties of the GBs can also influence the diffusivity rates. Lattice defects in Ru/Al were also shown to contribute in the enhancement of interdiffusion during deposition as well as the nucleation and growth behavior of the  $\text{RuAl}_6$  intermetallic phase.

In Ag/Al multilayers of Ag-rich composition, segregation at interfaces induces local supersaturation up to a concentration, where polymorphic nucleation of the  $\gamma$  intermetallic phase is possible. Due to the rapid kinetics in the small periods, this condition is reached within the thin diffused layers resulting in high density of nucleation sites, added to precipitation reactions at the interdiffused GBs. This together leads to a quick formation of stoichiometric  $\gamma$  phase as a final phase throughout the film. In larger periods, the kinetics is more sluggish in comparison and the nucleation condition is reached only at the GB junctions with parent interfaces.

The gradient energy effect on interdiffusion was observed for small periods of Ag/Al, where the mass transport was shown to increase in films under 6 nm thickness. This shows good agreement with literature studies that anticipate such behavior. The results reveal unique kinetics in the small periods where the pathway of the early phase formation reaction is strongly dependent on the thickness of the individual layers. Hence, the results demonstrate fundamental properties for diffusion kinetics in ultrathin multilayer films which are essential for understanding the thermal and structural stability of such films.

The behavior of the film growth for the binary metallic layers and the deposition parameters used have shown massive contribution to the quality of the multilayer structure which is directly connected to the interdiffusion behavior. The interplay between multilayer structure, interdiffusion,

nucleation, and phase growth was exclusively displayed in the investigation of the Ag/Al system. Rise in roughness may lead to formation of topographic defects in the microstructure which were shown to be highly intermixed regions and offer preferential nucleation sites for early phase formation. Reduced quality of the multilayer structure due to different dynamics of the film growth may cause some limitations in the practical applications of multilayer thin films.

The APT results have revealed that several intermetallic phases briefly nucleate during a single exothermic event seen in the DSC scans, where such intermetallic phases can be metastable or equilibrium phases. Asymmetric diffusion rates of parent and intermediate phases were shown to have a significant effect on the phase evolution, as seen in the reactions of Ag/Al multilayers thin films of 100 nm period. In alloys with more complex phase diagrams than the Ag/Al system, asymmetric diffusion rates of individual phases during annealing of multilayers, are therefore expected to have a key role in the criteria of phase selection and phase sequence, respectively.

The atomic scale analysis carried out on Ag/Al multilayer thin films gave rise to questions regarding the effects of interface types on the concentration gradient development during deposition and annealing. Different vacancy interactions and interfacial stresses known to exist for semi-coherent and incoherent phase boundaries can impact the kinetic regimes of the system as well as the early phase growth behavior. APT technique offers great capability to investigate the local chemistry at the interfaces in 3D, but the quality of the datasets is highly sensitive to artifacts during field evaporation. For future work, it would be very interesting to carry out an alike study on a miscible metallic multilayer system of semi-coherent or incoherent phases boundaries with similar field evaporation values for the binary phases. Experimental analyses employed on the atomic scale for different multilayer systems have an extremely high potential to improve our understandings of reaction kinetics in thin film structures.

## Appendix A1 – Stress effects on concentration gradients in thin films

### Interfacial stress effects on interdiffusion

Larché and Cahn [21], [131] have focused on defining interdiffusion effects resulting from non-hydrostatic stresses in crystalline structures. Deformation is modelled as a material coordinate system based on Lagrangean multipliers which models solid state diffusion in a network of substitutional and interstitial atoms as well as vacancies within a lattice under stress. The model was applied for studying stress effects at a phase boundaries. An interface is calculated under mechanical equilibrium between two phases,  $\alpha$  and  $\beta$ , respectively. The interface is then plotted with and without the self-stress induced by the composition change across the interface, where self-stress is referred to the stress resulting only from composition heterogeneity. The interface can be calculated using two equations at the equilibrium state. The first equation describes the compositional field at the mechanical equilibrium state using thermochemical quantities and the second equation considers the effect of the nature of the phase boundary (incoherent boundary in the case here) on the composition gradient. Elastic constants are assumed to be unchanged with the composition. Neither externally applied stresses nor residual stresses are considered here, only the self-stress generated by concentration distribution at the interface. The two equations are:

$$\mu_1^{0\alpha} - \mu_2^{0\alpha} + RT \ln \frac{\tilde{\gamma}_1^\alpha \tilde{c}^\alpha}{\tilde{\gamma}_2^\alpha (1 - \tilde{c}^\alpha)} - V_0'^\alpha \eta^\alpha T_{kk}^\alpha = \mu_1^{0\beta} - \mu_2^{0\beta} + RT \ln \frac{\tilde{\gamma}_1^\beta \tilde{c}^\beta}{\tilde{\gamma}_2^\beta (1 - \tilde{c}^\beta)} - V_0'^\beta \eta^\beta T_{kk}^\beta \quad (43)$$

$$\begin{aligned} & \mu_2^{0\alpha} + RT \ln[\tilde{\gamma}_2^\alpha (1 - \tilde{c}^\alpha)] + V_0'^\alpha \left[ -\frac{1}{2} \frac{v^\alpha}{E^\alpha} (T_{kk}^\alpha)^2 + \frac{1 + v^\alpha}{2E^\alpha} T_{ij}^\alpha T_{ij}^\alpha + \tilde{c}^\alpha \eta^\alpha T_{kk}^\alpha \right] \\ & = \mu_2^{0\beta} + RT \ln[\tilde{\gamma}_2^\beta (1 - \tilde{c}^\beta)] + V_0'^\beta \left[ -\frac{1}{2} \frac{v^\beta}{E^\beta} (T_{kk}^\beta)^2 + \frac{1 + v^\beta}{2E^\beta} T_{ij}^\beta T_{ij}^\beta + \tilde{c}^\beta \eta^\beta T_{kk}^\beta \right] \end{aligned} \quad (44)$$

in which,

$$T_{kk}^\alpha = 2Y^\alpha \eta^\alpha (\tilde{c}^\alpha - c_0^\alpha), \quad (45)$$

$$T_{kk}^\beta = 2Y^\beta \eta^\beta (\tilde{c}^\beta - c_0^\beta) \quad (46)$$

where,

$$Y = \frac{E}{(1 - \nu)} \quad (47)$$



The influence of the composition change on the common tangent construction for both phases can be presented as in Figure 81. The free energy curves are shifted with a value equivalent to the elastic energy per mole (Hemholtz free energy per mole,  $\hat{f}$ ), that is:

$$\hat{f}_{el} = \frac{V'_0 E}{1 - \nu} \eta^2 (\bar{c}^\alpha - c_0^\alpha)^2 \quad (48)$$

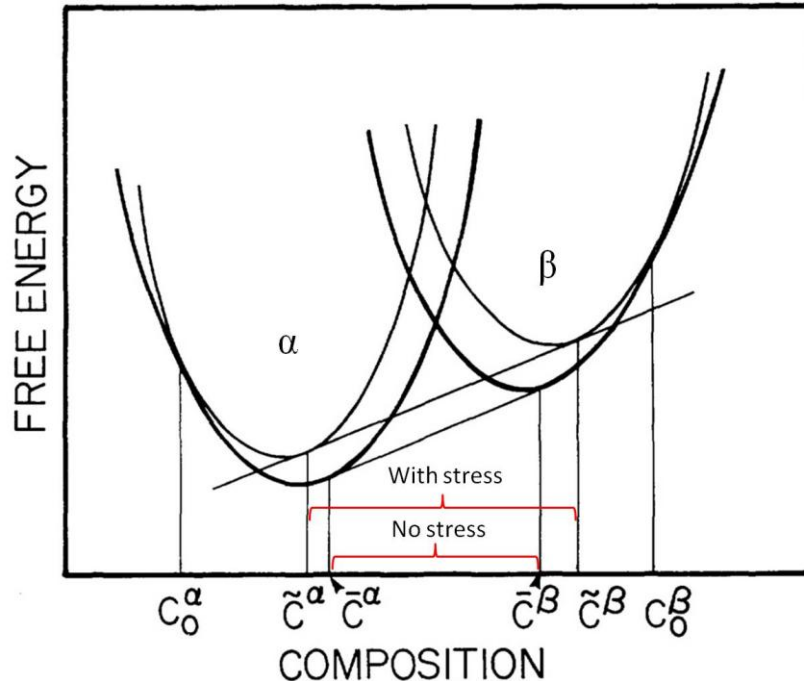


**Figure 81** Common tangent construction for the free energy curves of phase  $\alpha$  and phase  $\beta$  with and without the composition gradient stress showing the change in the equilibrium concentration values at the interface show in Figure 80. Taken from Ref. [21].

It is important to mention that the model above does not consider changes in the elastic constants with composition, neither external pressure (volumetric stresses), and neither composition dependent mobilities of the phases. It only solves the interface change based on the thermo-mechanical equilibrium. Interfacial stresses in thin films commonly show broader interfaces. Chakraborty [132] has used the Lahn & Cahn SID theory to calculate interdiffusion in Pd-Cu bilayer thin films and has shown enhanced intermixing taking self-stresses into account, which further increases considering stress gradients from the substrate. Shifts in the free energy curves of phases near a phase boundary due to the self-stress could generally therefore impose some effects on compositional gradients between two phases in a layered structure.

## References

- [1] M. Ohring, *Materials Science of Thin Films, Second Edition*. 2001.
- [2] J. E. Greene, “Tracing the 5000-year recorded history of inorganic thin films from ~3000 BC to the early 1900s AD,” *Appl. Phys. Rev.*, vol. 1, no. 4, p. 41302, 2014.
- [3] H. Lechtman, “Pre-Columbian surface metallurgy,” *Sci. Am.*, vol. 250, no. 6, pp. 56–63154, 1984.
- [4] A. Volta, “On the Electricity Excited by the Mere Contact of Conducting Substances of Different Kinds,” *Philos. Trans. R. Soc. London*, vol. 1, p. 403, 1800.
- [5] W. R. Grove, “On the Electro-Chemical Polarity of Gases,” *Philos. Trans. R. Soc. London*, vol. 142, no. January, pp. 87–101, 1852.
- [6] T. Young, “An Essay on the Cohesion of Fluids,” *Philos. Trans. R. Soc. London*, vol. 95, no. 0, pp. 65–87, 1805.
- [7] A. Wright, “On a new process for the electrical deposition of metals, and for constructing metal-covered glass specula,” *J. Franklin Inst.*, vol. 104, no. 4, pp. 242–251, 1877.
- [8] M. N. Baibich, J. M. Broto, A. Fert, F. N. Van Dau, F. Petroff, P. Eitenne, G. Creuzet, A. Friederich, and J. Chazelas, “Giant magnetoresistance of (001)Fe/(001)Cr magnetic superlattices,” *Phys. Rev. Lett.*, vol. 61, no. 21, pp. 2472–2475, 1988.
- [9] I. K. Schuller, S. Kim, and C. Leighton, “Magnetic superlattices and multilayers,” *J. Magn. Mater.*, vol. 200, no. 1, pp. 571–582, 1999.
- [10] E. Ehrmann-Falkenau and A. Wagendristel, “Influence of the Grain-Boundary Structure on the Rate of Mixing in Thin Polycrystalline Films,” *Phys. stat. sol.*, vol. 60, p. 427, 1980.
- [11] D. L. Beke, G. A. Langer, G. Molnár, G. Erdélyi, G. L. Katona, A. Lakatos, and K. Vad, “Kinetic pathways of diffusion and solid-state reactions in nanostructured thin films,” *Philos. Mag.*, pp. 1–11, 2012.
- [12] N. Zotov and A. Ludwig, “Atomic mechanisms of interdiffusion in metallic multilayers,” *Mater. Sci. Eng. C*, vol. 27, no. 5–8 SPEC. ISS., pp. 1470–1474, 2007.
- [13] A. V Chadwick, “Diffusion in Nanocrystalline Solids,” *Diffus. Fundam.*, vol. 2, no. 1, pp. 1–22, 2005.
- [14] R. Würschum, S. Herth, and U. Brossmann, “Diffusion in Nanocrystalline Metals and Alloys—A Status Report,” *Adv. Eng. Mater.*, vol. 5, no. 5, pp. 365–372, 2003.
- [15] C. V. Thompson and R. Carel, “Stress and grain growth in thin films,” *J. Mech. Phys. Solids*, vol. 44, no. 5, pp. 657–673, 1996.

- [16] D. M. Mattox, *Handbook of Physical Vapor Deposition ( PVD ) Processing Second edition*. William Andrew, 2010.
- [17] K. S. Sree Harsha, *Principles of Vapor Deposition of Thin Films*. Elsevier, 2006.
- [18] K. C. Russell, "Grain boundary nucleation kinetics," *Acta Metall.*, vol. 17, no. 8, pp. 1123–1131, 1969.
- [19] S. Labat, P. Gergaud, O. Thomas, B. Gilles, and A. Marty, "Interdependence of elastic strain and segregation in metallic multilayers : An x-ray diffraction study of „ 111 ... Au / Ni multilayers," *J. Appl. Phys.*, vol. 87, no. 3, pp. 1172–1181, 2000.
- [20] A. L. Greer, "Diffusion and reactions in thin films," *Appl. Surf. Sci.*, vol. 86, no. 1–4, pp. 329–337, 1995.
- [21] F. C. Larche and J. W. Cahn, "The interaction of composition and stress in crystalline solids.," *J. Res. Natl. Bur. Stand. (1934).*, vol. 33, no. 3, p. 467, 1984.
- [22] Y. Kuru, M. Wohlschlägel, U. Welzel, and E. J. Mittemeijer, "Interdiffusion and stress development in Cu-Pd thin film diffusion couples," *Thin Solid Films*, vol. 516, no. 21, pp. 7615–7626, 2008.
- [23] H. Mehrer, *Diffusion in Solids*. Springer, 2007.
- [24] J. W. H. Cahn John E., "Free Energy of a Nonuniform System. I. Interfacial Free Energy," *J. Chem. Phys.*, vol. 28, no. 2, pp. 258–267, 1958.
- [25] H. E. Cook and J. E. Hilliard, "Effect of gradient energy on diffusion in gold-silver alloys," *J. Appl. Phys.*, vol. 40, no. 5, pp. 2191–2198, 1969.
- [26] H. E. Cook, D. de Fontaine, and J. E. Hilliard, "A Model for diffusion on cubic lattices and its application to the early stages of ordering," *Acta Metall.*, vol. 17, p. 765, 1969.
- [27] A. C. Lewis, D. Josell, and T. P. Weihs, "Stability in thin film multilayers and microlaminates: The role of free energy, structure, and orientation at interfaces and grain boundaries," *Scr. Mater.*, vol. 48, no. 8, pp. 1079–1085, 2003.
- [28] A. Paul, T. Laurila, V. Vuorinen, and S. V. Divinski, *Thermodynamics , Diffusion and the Kirkendall Effect in Solids*. Springer, 2014.
- [29] A. Gusak, *Diffusion-controlled solid state reactions*. 2010.
- [30] J. Philibert, "Reactive Diffusion in thin films," *Defect Diffus. Forum*, vol. 53, pp. 74–81, 1991.
- [31] F. M. d'Heurle, "Nucleation of a new phase from the interaction of two adjacent phases: Some silicides," *J. Mater. Res.*, vol. 3, no. 1, pp. 167–195, 1988.
- [32] U. Gösele and K. N. Tu, "Growth kinetics of planar binary diffusion couples: 'Thin-film case' versus 'bulk cases,'" *J. Appl. Phys.*, vol. 53, no. 4, pp. 3252–3260, 1982.
- [33] A. M. Gusak, F. Hodaj, and A. O. Bogatyrev, "Kinetics of nucleation in the concentration

- gradient,” *J. Phys. Condens. Matter*, vol. 13, no. 12, pp. 2767–2787, 2001.
- [34] G. V. Kidson, “Some aspects of the growth of diffusion layers in binary systems,” *J. Nucl. Mater.*, vol. 3, no. 1, pp. 21–29, 1961.
- [35] F. Hodaj and A. M. Gusak, “Suppression of intermediate phase nucleation in binary couples with metastable solubility,” *Acta Mater.*, vol. 52, no. 14, pp. 4305–4315, 2004.
- [36] A. Gusak and K. P. Gurov, “Peculiarities of Intermediate Phase Nucleation in the Process of Chemical Diffusion,” *Solid State Phenom.*, vol. 23–24, pp. 117–122, 1992.
- [37] P. J. Desré and A. R. Yavari, “Suppression of crystal nucleation in amorphous layers with sharp concentration gradients,” *Phys. Rev. Lett.*, vol. 64, no. 13, pp. 1533–1536, 1990.
- [38] F. Hodaj and P. J. Desré, “Effect of a sharp gradient of concentration on nucleation of intermetallics at interfaces between polycrystalline layers,” *Acta Mater.*, vol. 44, no. 11, pp. 4485–4490, 1996.
- [39] K. R. Coffey and K. Barmak, “A new model for grain boundary diffusion and nucleation in thin film reactions,” *Acta Metall. Mater.*, vol. 42, no. 8, pp. 2905–2911, 1994.
- [40] K. R. Coffey, L. A. Clevenger, K. Barmak, D. A. Rudman, and C. V. Thompson, “Experimental evidence for nucleation during thin-film reactions,” *Appl. Phys. Lett.*, vol. 55, no. 9, pp. 852–854, 1989.
- [41] N. Zotov, K. Woll, and F. Mücklich, “Phase formation of B2-RuAl during annealing of Ru/Al multilayers,” *Intermetallics*, vol. 18, no. 8, pp. 1507–1516, 2010.
- [42] C. Bergman, E. Emeric, G. Clugnet, and P. Gas, “Kinetics of Reactive Diffusion in Al/Co Multilayers,” *Defect Diffus. Forum*, vol. 194–199, pp. 1533–1538, 2001.
- [43] G. Lucadamo, K. Barmak, S. Hyun, C. Cabral, and C. Lavoie, “Evidence of a two-stage reaction mechanism in sputter deposited Nb/Al multilayer thin-films studied by in situ synchrotron X-ray diffraction,” *Mater. Lett.*, vol. 39, no. 5, pp. 268–273, 1999.
- [44] P. Zieba, “Diffusion along Migrating Grain Boundaries,” *Interface Sci.*, vol. 11, pp. 51–58, 2003.
- [45] C. Michaelsen, K. Barmak, and T. P. Weihs, “Investigating the thermodynamics and kinetics of thin film reactions by differential scanning calorimetry,” *J. Phys. D. Appl. Phys.*, vol. 30, no. 23, pp. 3167–3186, 1997.
- [46] T. Jeske, M. Seibt, and G. Schmitz, “Microstructural influence on the early stages of interreaction of Al/Ni-investigated by TAP and HREM,” *Mater. Sci. Eng. A*, vol. 353, no. 1–2, pp. 105–111, 2003.
- [47] A. S. Edelstein, R. K. Everett, G. Y. Richardson, S. B. Qadri, E. I. Altman, J. C. Foley, and J. H. Perepezko, “Intermetallic phase formation during annealing of Al/Ni multilayers,” *J. Appl.*

- Phys.*, vol. 76, no. 12, pp. 7850–7859, 1994.
- [48] E. Ma, C. V. Thompson, and L. a. Clevenger, “Nucleation and growth during reactions in multilayer Al/Ni films: The early stage of Al<sub>3</sub>Ni formation,” *J. Appl. Phys.*, vol. 69, no. 4, pp. 2211–2218, 1991.
- [49] J. Horváth, R. Birringer, and H. Gleiter, “Diffusion in nanocrystalline material,” *Solid State Communications*, vol. 62, no. 5, pp. 319–322, 1987.
- [50] K. Barmak, C. Michaelsen, and G. Lucadamo, “Reactive phase formation in sputter-deposited Ni/Al multilayer thin films,” *J. Mater. Res.*, vol. 12, no. 1, pp. 133–146, 1997.
- [51] E. Illeková, J. C. Gachon, A. Rogachev, H. Grigoryan, J. C. Schuster, A. Nosyrev, and P. Tsygankov, “Kinetics of intermetallic phase formation in the Ti/Al multilayers,” *Thermochim. Acta*, vol. 469, no. 1–2, pp. 77–85, 2008.
- [52] L. Fister and C. David, “Controlling Solid-State reaction mechanisms using diffusion length in ultrathin-film superlattice composites,” *J. Am. Chem. Soc.*, vol. 114, no. 8, pp. 4639–4644, 1992.
- [53] A. L. Greer, “Interdiffusion in Metallic Multilayers,” *Defect Diffus. Forum*, vol. 143–147, pp. 557–568, 1997.
- [54] J. M. Roussel and P. Bellon, “Interface sharpening and broadening during annealing of Cu Ni multilayers: A kinetic Monte Carlo study,” *Phys. Rev. B - Condens. Matter Mater. Phys.*, vol. 73, no. 8, pp. 1–13, 2006.
- [55] A. Peteline, S. Peteline, and O. Oreshina, “Triple junction diffusion: Experiments and models,” *Defect and*, vol. 194–199, pp. 1265–1270, 2001.
- [56] I. V. Belova, T. Fiedler, N. Kulkarni, and G. E. Murch, “The Harrison diffusion kinetics regimes in solute grain boundary diffusion,” *Philos. Mag.*, vol. 92, no. 14, pp. 1748–1763, 2012.
- [57] I. V. Belova and G. E. Murch, “Diffusion in Nanocrystalline Materials,” *J. Phys. Chem. Solids*, vol. 64, pp. 873–878, 2003.
- [58] N. Kaiser, “Review of the fundamentals of thin-film growth,” *Appl. Opt.*, vol. 41, no. 16, pp. 3053–3060, 2002.
- [59] C. V Thompson, “Structure evolution during processing of polycrystalline films,” *Mater. Sci.*, vol. 30, pp. 159–90, 2000.
- [60] H. Li, J. Zhu, S. Zhou, Z. Wang, H. Chen, P. Jonnard, K. Le Guen, and J. M. André, “Zr/Mg multilayer mirror for extreme ultraviolet application and its thermal stability,” *Appl. Phys. Lett.*, vol. 102, no. 11, 2013.
- [61] A. S. Ramos and M. T. Vieira, “Intermetallic compound formation in Pd/Al multilayer thin

- films,” *Intermetallics*, vol. 25, pp. 70–74, 2012.
- [62] A. Anders, “A structure zone diagram including plasma-based deposition and ion etching,” *Thin Solid Films*, vol. 518, no. 15, pp. 4087–4090, 2010.
- [63] J. A. Thornton, “Influence of apparatus geometry and deposition conditions on the structure and topography of thick sputtered coatings,” *J. Vac. Sci. Technol.*, vol. 11, no. 4, p. 666, 1974.
- [64] D. Depla and S. Mahieu, *Reactive Sputter Deposition*, vol. 109. Springer, 2008.
- [65] A. J. McAlister, “The Ag-Al ( Silver-Aluminum ) System,” *Bull. Alloy phase Diagr.*, vol. 8, no. 6, 1987.
- [66] R. Roy and S. K. Sen, “Calorimetric and other studies of intermetallic phase formation in Ag/Al bilayer thin films,” *J. Mater. Sci.*, vol. 27, no. 22, pp. 6098–6104, 1992.
- [67] B. Gault, M. Moody, J. M. Cairney, and S. P. Ringer, *Atom Probe Microscopy*. Springer, 2012.
- [68] R. Erni, H. Heinrich, and G. Kostorz, “On the internal structure of Guinier-Preston zones in Al-3 at.% Ag,” *Philos. Mag. Lett.*, vol. 83, no. 10, pp. 599–609, 2003.
- [69] S. Y. Yu, B. Schönfeld, and G. Kostorz, “Diffuse x-ray scattering of Ag – 13.4 at. % Al,” *Phys. Rev. B*, vol. 56, no. 14, pp. 8535–8541, 1997.
- [70] F. Mücklich and N. Ilić, “RuAl and its alloys. Part I. Structure, physical properties, microstructure and processing,” *Intermetallics*, vol. 13, no. 1 SPEC. ISS., pp. 5–21, 2005.
- [71] F. Mücklich, N. Ilić, and K. Woll, “RuAl and its alloys, Part II: Mechanical properties, environmental resistance and applications,” *Intermetallics*, vol. 16, no. 5, pp. 593–608, 2008.
- [72] S. A. Anderson and C. I. Lang, “Thermal Conductivity of Ruthenium Aluminide (RuAl),” *Scr. Mater.*, vol. 38, no. 3, pp. 493–497, 1998.
- [73] I. D. Bleskov, É. I. Isaev, and Y. K. Vekilov, “Electronic structure and ground state parameters of Ru<sub>1-x</sub>Me<sub>x</sub>Al refractory alloys,” *Phys. Solid State*, vol. 52, no. 9, pp. 1803–1809, 2010.
- [74] M. A. Guitar, H. Aboufadel, C. Pauly, P. Leibenguth, S. Migot, and F. Mücklich, “Production of single-phase intermetallic films from Ru-Al multilayers,” *Surf. Coatings Technol.*, vol. 244, pp. 210–216, 2014.
- [75] K. Woll, “Festkörper- und selbstfortschreitende Reaktionen in Multilagen zur RuAl-Dünnschichtsynthese,” University of Saarland, 2012.
- [76] K. Woll, R. K. S. Chinnam, and F. Mücklich, “Thin-Film Synthesis and Cyclic Oxidation Behavior of B<sub>2</sub>-RuAl,” *Mater. Res. Soc.*, vol. 1128, pp. 1128-U06-10, 2009.
- [77] C. Pauly, K. Woll, B. Bax, and F. Mücklich, “The role of transitional phase formation during ignition of reactive multilayers,” *Appl. Phys. Lett.*, vol. 107, no. 11, 2015.

- [78] S. N. Prins, L. A. Cornish, W. E. Stumpf, and B. Sundman, “Thermodynamic assessment of the Al-Ru system,” *Calphad Comput. Coupling Phase Diagrams Thermochem.*, vol. 27, no. 1, pp. 79–90, 2003.
- [79] X. W. Zhou, H. N. G. Wadley, R. a. Johnson, D. J. Larson, N. Tabat, a. Cerezo, a. K. Petford-Long, G. D. W. Smith, P. H. Clifton, R. L. Martens, and T. F. Kelly, “Atomic scale structure of sputtered metal multilayers,” *Acta Mater.*, vol. 49, no. 19, pp. 4005–4015, 2001.
- [80] R. Guinebretiere, *X-ray Diffraction by Polycrystalline Materials*. ISTE, 2007.
- [81] C. A. Volkert and A. M. Minor, “Focused Ion Beam Microscopy and Micromachining,” *MRS Bull.*, vol. 32, no. 5, pp. 389–399, 2007.
- [82] K. Thompson, D. Lawrence, D. J. Larson, J. D. Olson, T. F. Kelly, and B. Gorman, “In situ site-specific specimen preparation for atom probe tomography,” *Ultramicroscopy*, vol. 107, no. 2–3, pp. 131–139, 2007.
- [83] B. Fultz and J. Howe, *Transmission Electron Microscopy and diffractometry of materials*, 4th ed. Springer, 2013.
- [84] S. Suzuki, “Features of transmission EBSD and its application,” *Jom*, vol. 65, no. 9, pp. 1254–1263, 2013.
- [85] K. Babinsky, R. De Kloe, H. Clemens, and S. Primig, “A novel approach for site-specific atom probe specimen preparation by focused ion beam and transmission electron backscatter diffraction,” *Ultramicroscopy*, vol. 144, pp. 9–18, 2014.
- [86] R. R. Keller and R. H. Geiss, “Transmission EBSD from 10 nm domains in a scanning electron microscope,” *J. Microsc.*, vol. 245, no. 3, pp. 245–251, 2012.
- [87] EDAX, *OIM Analysis 5.3 (Manual)*. TexSEM Laboratories, 2007.
- [88] D. N. Seidman, “Three-Dimensional Atom-Probe Tomography: Advances and Applications,” *Annu. Rev. Mater. Res.*, vol. 37, no. 1, pp. 127–158, 2007.
- [89] B. P. Geiser, T. F. Kelly, D. J. Larson, J. Schneir, and J. P. Roberts, “Spatial distribution maps for atom probe tomography,” *Microsc. Microanal.*, vol. 13, no. 6, pp. 437–447, 2007.
- [90] D. Bufford, Z. Bi, Q. X. Jia, H. Wang, and X. Zhang, “Nanotwins and stacking faults in high-strength epitaxial Ag/Al multilayer films,” *Appl. Phys. Lett.*, vol. 101, no. 22, 2012.
- [91] M. Chen, E. Ma, K. J. Hemker, H. Sheng, Y. Wang, and X. Cheng, “Deformation Twinning in Nanocrystalline Aluminum,” *Science (80-. )*, vol. 300, no. 5623, pp. 1275–1277, 2003.
- [92] D. Bufford, Y. Liu, Y. Zhu, Z. Bi, Q. X. Jia, H. Wang, and X. Zhang, “Formation Mechanisms of High-density Growth Twins in Aluminum with High Stacking-Fault Energy,” *Mater. Res. Lett.*, no. November, pp. 1–10, 2013.
- [93] H. Aboulfadl, I. Gallino, R. Busch, and F. Mücklich, “Atomic scale analysis of phase

- formation and diffusion kinetics in Ag/Al multilayer thin films,” *J. Appl. Phys.*, vol. 120, no. 19, p. 195306, 2016.
- [94] G. Lucadamo, K. Barmak, and K. P. Rodbell, “Texture in Ti/Al and Nb/Al multilayer thin films: Role of Cu,” *J. Mater. Res.*, vol. 16, no. 5, pp. 1449–1459, 2001.
- [95] E. E. Fullerton and I. K. Schuller, “Structural refinement of superlattices from X-Ray Diffraction,” vol. 45, no. 16, pp. 9292–9310, 1992.
- [96] D. A. Porter and K. E. Easterling, *Phase Transformations in Metals and Alloys*. 1992.
- [97] H. E. Kissinger, “Reaction kinetics in differential thermal analysis,” *Anal. Chem.*, vol. 29, no. 11, pp. 1702–1706, 1957.
- [98] J. E. E. Baglin, F. M. D’Heurle, and W. N. Hammer, “The interaction process for Ag-Al polycrystalline thin-film couples,” *J. Appl. Phys.*, vol. 50, no. 1, pp. 266–275, 1979.
- [99] C. Weaver and L. C. Brown, “Diffusion in evaporated films of silver–aluminium,” *Philos. Mag.*, vol. 17, no. 149, pp. 881–897, 1968.
- [100] K. T. Moore, W. C. Johnson, J. M. Howe, H. I. Aaronson, and D. R. Veblen, “On the interaction between Ag-depleted zones surrounding  $\gamma$  plates and spinodal decomposition in an Al-22 at.% Ag alloy,” *Acta Mater.*, vol. 50, no. 5, pp. 943–956, 2002.
- [101] C. Li, C. Niu, Z. Du, C. Guo, and Y. Jing, “The thermodynamic analysis of GP zones in aged-supersaturated Al-Ag alloys,” *Calphad Comput. Coupling Phase Diagrams Thermochem.*, vol. 34, no. 1, pp. 120–128, 2010.
- [102] N. Zarkevich and D. Johnson, “Predicted hcp Ag-Al metastable phase diagram, equilibrium ground states, and precipitate structure,” *Phys. Rev. B*, vol. 67, no. 6, pp. 1–8, 2003.
- [103] C. Oberdorfer and G. Schmitz, “On the Field Evaporation Behavior of Dielectric Materials in Three-Dimensional Atom Probe: A Numeric Simulation,” *Microsc. Microanal.*, vol. 17, no. 1, pp. 15–25, 2010.
- [104] C. K. S. Moy, G. Ranzi, T. C. Petersen, and S. P. Ringer, “Macroscopic electrical field distribution and field-induced surface stresses of needle-shaped field emitters,” *Ultramicroscopy*, vol. 111, no. 6, pp. 397–404, 2011.
- [105] C. Oberdorfer, S. M. Eich, and G. Schmitz, “A full-scale simulation approach for atom probe tomography,” *Ultramicroscopy*, vol. 128, pp. 55–67, 2013.
- [106] J. D. R. Buchanan, T. P. a. Hase, B. K. Tanner, P. J. Chen, L. Gan, C. J. Powell, and W. F. Egelhoff, “Anomalously large intermixing in aluminum–transition-metal bilayers,” *Phys. Rev. B*, vol. 66, no. 10, p. 104427, 2002.
- [107] H. W. Sheng, M. J. Kramer, a. Cadien, T. Fujita, and M. W. Chen, “Highly optimized embedded-atom-method potentials for fourteen FCC metals,” *Phys. Rev. B - Condens. Matter*

- Mater. Phys.*, vol. 83, no. 13, pp. 1–20, 2011.
- [108] X. W. Zhou and H. N. G. Wadley, “Atomistic simulation of the vapor deposition of Ni/Cu/Ni multilayers: The effects of adatom incident energy,” *J. Appl. Phys.*, vol. 84, no. 4, pp. 2301–2315, 1998.
- [109] T. Bigault, F. Bocquet, S. Labat, O. Thomas, and H. Renevier, “Interfacial structure in (111) Au:Ni multilayers investigated by anomalous x-ray diffraction,” *Phys. Rev. B*, vol. 64, no. 12, p. 125414, 2001.
- [110] M. P. Seah, “Pure element sputtering yields using 500–1000 eV argon ions,” *Thin Solid Films*, vol. 81, no. 3, pp. 279–287, 1981.
- [111] V. Fournée, J. Ledieu, T. Cai, and P. Thiel, “Influence of strain in Ag on Al(111) and Al on Ag(100) thin film growth,” *Phys. Rev. B*, vol. 67, no. 15, pp. 3–6, 2003.
- [112] M. Hentschel, M. Bobeth, G. Diener, and W. Pompe, “On the short-time compositional stability of periodic multilayers,” *Thin Solid Films*, vol. 354, no. 1, pp. 267–275, 1999.
- [113] M. C. Benoudia, F. Gao, J. M. Roussel, S. Labat, M. Gailhanou, O. Thomas, D. L. Beke, Z. Erdélyi, G. Langer, A. Csik, and M. Kis-Varga, “Thermoelasticity and interdiffusion in CuNi multilayers,” *Phys. Rev. B - Condens. Matter Mater. Phys.*, vol. 85, no. 23, pp. 1–7, 2012.
- [114] C. Wang, C. Zhuang, J. Han, and X. Liu, “Assessment of the atomic mobilities for binary Al-Ag fcc alloys,” *Calphad*, vol. 37, pp. 145–150, 2012.
- [115] C. Michaelsen, G. Lucadamo, and K. Barmak, “The early stages of solid state reactions in Ni/Al multilayer films,” *J. Appl. Phys.*, vol. 80, no. 12, pp. 6689–6698, 1996.
- [116] M. H. da Silva Bassani, J. H. Perepezko, A. S. Edelstein, and R. K. Everett, “Initial Phase Formation During Interdiffusion Reactions,” *Scr. Mater.*, vol. 37, no. 2, pp. 227–232, 1997.
- [117] A. T. Dinsdale, “SGTE data for pure elements,” *Calphad*, vol. 15, no. 4, pp. 317–425, 1991.
- [118] S. S. Lim, P. L. Rossiter, and J. E. Tibballs, “Assessment of the Al-Ag binary phase diagram,” *Calphad*, vol. 19, no. 2, pp. 131–141, 1995.
- [119] Y. Gao, Z. Luo, S. Zhang, and C. Huang, “Phase-Field simulation of solute precipitations around the gamma phase in Al-Ag alloy,” *Acta Metall. Sin.*, vol. 46, no. 12, pp. 1473–1480, 2010.
- [120] R. Busch, F. Gärtner, C. Borschers, P. Haasen, and R. Bormann, “Microstructure development during rapid solidification of highly supersaturated Cu-Co alloys,” vol. 43, no. 9, pp. 3467–3475, 1995.
- [121] J. Schleiweis and G. Schmitz, “Thin film interreaction of Al/Ag analyzed by tomographic atom probe,” *Mater. Sci. Eng. A*, vol. 327, no. 1, pp. 94–100, 2002.
- [122] F. Mao, M. Taher, O. Kryshnal, A. Kruk, A. Czyska-Filemonowicz, M. Ottosson, A. M.

- Andersson, U. Wiklund, and U. Jansson, "Combinatorial Study of Gradient Ag-Al Thin Films: Microstructure, Phase Formation, Mechanical and Electrical Properties," *ACS Appl. Mater. Interfaces*, vol. 8, no. 44, pp. 30635–30643, 2016.
- [123] K. T. Moore and J. M. Howe, "Characterization of  $\gamma$  plate-shaped precipitates in an Al-4.2 at.% Ag alloy - growth kinetics, solute field, composition and modeling," *Acta Mater.*, vol. 48, no. 16, pp. 4083–4098, 2000.
- [124] J. Schleiwies, "NANOANALYSE HÖCHSTER AUFLÖSUNG VON METALLISCHEN SCHICHTSYSTEMEN," Göttingen University, 2001.
- [125] G. Gottstein and L. Shvindlerman, *Grain boundary migration in Metals*, 2nd ed., vol. 31, no. C. CRC, 2010.
- [126] Y. Minamino, T. Yamane, S. Ueno, M. Koizumi, N. Ogawa, and M. Shimada, "Effect of high pressure on react diffusion in Al-Ag system," *Met. Sci.*, vol. 18, no. 8, pp. 419–426, 1984.
- [127] Y. Wang, G. Luo, L. Li, Q. Shen, and L. Zhang, "Formation of intermetallic compounds in Mg–Ag–Al joints during diffusion bonding," *J. Mater. Sci.*, vol. 49, no. 20, pp. 7298–7308, 2014.
- [128] A. Wagendristel, H. Bangert, and W. Tonsern, "Diffusional alloying in polycrystalline Ag-Al thin film couple studied by means of Keissig X-ray interference," *Surface*, vol. 86, pp. 68–74, 1979.
- [129] W. Hu, B. Zhang, B. Huang, F. Gao, and D. J. Bacon, "Analytic modified embedded atom potentials for HCP metals," *J. Phys. Condens Matter*, vol. 13, pp. 1193–1213, 2001.
- [130] A. M. Gusak and A. V. Nazarov, "On the description of solid state amorphizing reactions," *J. Phys. Condens. Matter*, vol. 4, no. 20, pp. 4753–4758, 1992.
- [131] F. C. Larche and J. W. Cahn, "The effect of self-stress on diffusion in solids," *Acta Metall.*, vol. 30, no. 10, pp. 1835–1845, 1982.
- [132] J. Chakraborty, "Diffusion in Stressed Thin Films Universität Stuttgart März 2005 Diffusion in Stressed Thin Films," no. 161, 2005.